

Doctoral Dissertation

Measurement of the Higgs boson production in the
 $H \rightarrow WW^* \rightarrow \ell\nu\ell\nu$ decay with the ATLAS detector at the LHC

Graduate School of Science, Kobe University

Tomoe Kishimoto

January, 2015

Abstract

This thesis reports a measurement of the Higgs boson production in the $H \rightarrow WW^* \rightarrow \ell\nu\ell\nu$ decay with the ATLAS detector at the LHC. The measurement of the production and decay rate of the Higgs boson provides an essential confirmation of the Standard Model of the particle physics. The ratio of the observed to expected values of the production and decay rate is defined as “signal strength” of the Higgs boson. For a Higgs boson mass of $m_H = 125.36$ GeV, the signal strength measured from a data sample corresponding to an integrated luminosity of 20.3 fb^{-1} at $\sqrt{s} = 8$ TeV proton-proton collisions is $1.07^{+0.18}_{-0.18}$ (stat.) $^{+0.22}_{-0.19}$ (syst.), where the result is obtained by focusing the gluon-gluon fusion production mode of the Higgs boson. The observed signal strength is consistent with the Standard Model prediction. The significance of a data excess over expected number of backgrounds corresponds to 4.5 standard deviation. The measurement is performed with a data-driven background estimation technique called OS-SS method, which reduces systematic uncertainties on background predictions. The combined result with the vector-boson fusion production mode and another data sample corresponding to an integrated luminosity of 4.5 fb^{-1} at $\sqrt{s} = 7$ TeV is also reported.

Contents

1	Introduction	5
2	The Higgs boson	7
2.1	Theoretical background	7
2.1.1	The Higgs mechanism	7
2.1.2	Production and decay of the Higgs boson	11
2.1.3	Possible new phenomena revealed by Higgs boson measurements	16
2.2	Status of Higgs boson measurements	19
2.3	Analysis overview	21
3	The Large Hadron Collider	26
3.1	The LHC detectors	27
3.2	Luminosity determination	28
3.3	Physics runs in 2010–2012	29
3.4	Particle production rates in hadron colliders	29
4	The ATLAS detector	33
4.1	Definition of coordinates	35
4.2	Magnets	36
4.2.1	Central solenoid	36
4.2.2	Barrel and endcap toroids	37
4.3	Inner trackers	37
4.3.1	Silicon-pixel vertex-detector	38
4.3.2	Semi conductor tracker	38
4.3.3	Transition radiation tracker	40
4.4	Calorimeters	40
4.4.1	Electromagnetic calorimeter	41
4.4.2	Hadronic calorimeter	41
4.5	Muon spectrometers	44
4.5.1	Monitored Drift Tube	44
4.5.2	Cathode Strip Chamber	45
4.5.3	Resistive Plate Chamber	46
4.5.4	Thin Gap Chamber	48
4.6	Trigger and data acquisition system	49
4.6.1	Level 1 trigger system	50
4.6.2	HLT and DAQ system	51

5	Data samples	53
5.1	Collision data	53
5.2	Monte Carlo samples	54
5.2.1	Signal samples	55
5.2.2	Background samples	60
5.2.3	Monte Carlo event weights	62
6	Object reconstruction and selection	65
6.1	Charged track and vertex	65
6.2	Electron reconstruction	68
6.3	Muon reconstruction	70
6.4	Jet reconstruction	72
6.5	Missing transverse energy reconstruction	74
6.6	Object selection	75
7	Event selection	82
7.1	Pre-selections	82
7.2	Selection for $n_j = 0$ category	86
7.3	Selection for $n_j = 1$ category	87
7.4	Selection for $n_j \geq 2$ ggF-enriched category	90
8	Background estimation	96
8.1	W +jets background	97
8.1.1	The extrapolation factor method	97
8.1.2	Validation of the method using same-sign lepton sample	105
8.2	QCD background	106
8.3	<i>Other</i> VV background	113
8.3.1	The OS-SS method	113
8.3.2	Monte Carlo validation	119
8.4	Z +jets background	123
8.4.1	p_T^Z reweighting	125
8.4.2	$Z \rightarrow \tau\tau$ background	126
8.4.3	$Z \rightarrow ee/\mu\mu$ background	130
8.5	Top background	133
8.5.1	Estimation of background normalization for $n_j = 0$ category	133
8.5.2	b -tag extrapolation for $n_j = 1$ category	136
8.5.3	Control region for $n_j \geq 2$ ggF-enriched category	138
8.6	WW background	139
8.6.1	WW control region	140
8.6.2	Theoretical uncertainty in extrapolation	141
8.7	Other backgrounds	145
9	Signal extraction and uncertainties	147
9.1	Fit regions	147
9.2	Likelihood function and test statistic	151
9.3	Uncertainties	153

10 Results	155
10.1 Event yields and distributions	155
10.2 Fit results	155
11 Discussion	164
11.1 Comparison with the different background estimation	164
11.2 7 TeV (2011) analysis	165
11.3 VBF analysis	167
11.4 Combined results	168
11.5 Comparisons with the CMS results	170
12 Conclusion	172
A Appendix	183
A.1 Selection for the VBF analysis	183

Chapter 1

Introduction

What are the ultimate constituents of matter? How do they interact with each other? Particle physics is the most ambitious and organized research to answer these questions. Since the discovery of the electron, especially in the last fifty years, the particle physics has been developed rapidly in theories and experiments. This led to the construction of the Standard Model (SM) of the particle physics in 1970s. In the SM, the material in the universe is made up of fermions. The fermions are composed of quarks and leptons of three generations, where each generation consists of two types of quarks and leptons. The interactions between elemental particles are mediated by gauge bosons, which are formulated in a frame of the gauge theory. Three types of interactions, electromagnetic, strong and weak interactions, are distinguished in the SM. The gauge bosons associated with the interactions are photons (electromagnetic), gluons (strong) and W or Z bosons (weak). Gravitational interaction is not included in the SM since the gravitational forces are insignificant on the scale of the particle physics in the energy range we consider.

In a simple gauge theory, the gauge bosons are required to be massless in order to keep the invariance under gauge transformations. However, it is inconsistent with a fact that the weak interaction is the short-range force. The UA1 and UA2 experiments at the CERN SPS proton-antiproton collider have also confirmed by direct measurements that the W and Z bosons are massive. Higgs mechanism was introduced into the theory in order to explain these masses. In this mechanism, the W and Z bosons obtain their masses by interacting with the non-zero Higgs field as a consequence of the spontaneous symmetry breaking of the vacuum of the Higgs field. An important consequence of the mechanism is a prediction of the existence of a “Higgs boson” corresponding to the Higgs field. Thus, many efforts over 40 years to discover the Higgs boson was started. At the beginning of the 21st century, the Higgs boson was the last unobserved fundamental particle predicted in the SM.

The Large Hadron Collider (LHC) at European Organization for Nuclear Research (CERN) is the world’s largest proton-proton collider, accelerating bunch of protons to 7 TeV and resulting in the center of mass energy of 14 TeV in its design. The LHC came into operation in 2010. The previous highest energy collider, Tevatron at Fermilab, produced proton-antiproton collisions at 2 TeV. The LHC thus increases the collision energy significantly to raise production rates of particles, the Higgs boson being the main example, and is capable of producing heavy particles predicted in theories beyond the SM. At one of four collision points at the LHC, a general purpose detector, A Toroidal LHC ApparatuS (ATLAS), is installed to perform various physics studies, such as searches for the Higgs boson, searches for new phenomena, as well as measurements of the SM processes. Also the Compact Muon Solenoid (CMS) detector is installed at another collision point with the same motivation.

On 4 July 2012, the ATLAS and CMS experiments at the LHC announced that a new particle was observed in the mass region around 125 GeV. It has been confirmed that this particle is consistent with the Higgs boson. Figure 1.1 shows an event display of Higgs boson candidates. This discovery of the Higgs boson opens a new era at the LHC, where the properties of the Higgs boson, such as the production cross section and branching fractions, in other words, couplings to other SM particles, are precisely measured. Many theories beyond the SM predict deviations of the production and decay rate of the Higgs boson from the SM by introducing new particles. Therefore, the measurement of the production and decay rate gives constraints to the theoretical models, or may lead to the discovery of new physics beyond the SM.

The sequential decay $H \rightarrow WW^* \rightarrow \ell\nu\ell\nu$ is a sensitive experimental channel to measure the Higgs boson production and decay rate, where ℓ is an electron or muon, since the decay branching ratio of the Higgs boson to WW^* at the observed mass is the second largest next to $H \rightarrow b\bar{b}$ decay and it is comparatively easy to detect the leptons in the final state with high resolutions. This thesis presents the measurement results of the Higgs boson production through this $H \rightarrow WW^* \rightarrow \ell\nu\ell\nu$ decay channel. The ratio of the observed to expected values of the production and decay rate predicted by the SM, defined as “signal strength”, is one of the central results in this thesis.

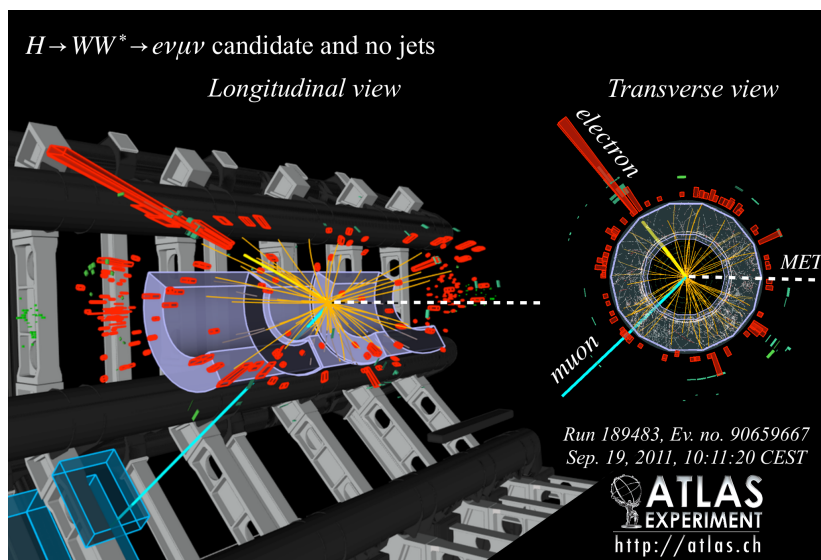


Figure 1.1: Event display of a $H \rightarrow WW^* \rightarrow e\nu\mu\nu$ candidate event. The event was recorded by ATLAS on 2011-09-19, 10:11:20 CEST in run number 189483 as event number 90659667. Electron track is colored light yellow and its energy deposit is shown with red box. Muon track is colored light blue. Neutrinos are represented by missing transverse momentum (dotted line) that points away from the $e\mu$ system.

This thesis is organized as follows. Chapter 2 provides theoretical and experimental aspects of the Higgs boson. Chapter 3 and 4 briefly summarize the LHC and ATLAS detector. Chapter 5 describes data and simulation samples used in the analysis. Chapter 6 shows object reconstructions using the ATLAS detector and their performances. Chapter 7 summarizes selection of events. Chapter 8 discusses the modeling of background processes. The extraction procedure of the signal and results are presented in Chapter 9 and 10. Chapter 11 discusses combined results with other analyses using different data samples. Chapter 12 gives conclusions.

Chapter 2

The Higgs boson

The Standard Model of particle physics (SM) has been very successful in describing the elementary particles and their interactions in the nature. All elementary particles predicted by the SM have been conclusively discovered. The SM particles are summarized in table 2.1. In the SM, all matters in the universe consist of spin-1/2 quarks and leptons, which are the sources of interactions mediated by spin-1 gauge bosons. These bosons are required to be massless in order to keep the gauge invariance under local gauge transformations. While the photon and gluon are massless as expected, the W and Z bosons have been confirmed that they are massive particles [1,2]. The Higgs mechanism [3,4], which breaks the electroweak symmetry [5] and gives the masses to the W and Z gauge bosons, is introduced into the theory in order to explain the measurements. As a consequence, the existence of a Higgs boson was predicted in the Higgs mechanism. The particle consistent with this Higgs boson has been discovered by the ATLAS and CMS experiments in 2012 [6,7]. The measurement of this Higgs boson properties provides an essential confirmation of the SM, and distinguishes different theoretical scenarios.

In this chapter, how the mass of the gauge bosons comes out by the Higgs mechanism is described in section 2.1, together with the production and decay of the Higgs boson at the LHC, and possible new phenomena in the Higgs boson production. Section 2.2 provides the status of Higgs boson measurement in ATLAS. Section 2.3 gives an overview of the analysis using the $H \rightarrow WW^* \rightarrow \ell\nu\ell\nu$ decay channel.

2.1 Theoretical background

2.1.1 The Higgs mechanism

The electroweak standard model is based on a gauge theory with the symmetry group $SU(2) \otimes U(1)$, and describes the electromagnetic and weak interactions mediated by the corresponding gauge bosons: massless photon for the electromagnetic interaction and massive W and Z bosons for the weak interaction. For $U(1)$ gauge theory as an example, the invariant kinetic term of the gauge boson, is given by:

$$\mathcal{L}_{kin} = -\frac{1}{4}F_{\mu\nu}F^{\mu\nu}, \quad (2.1)$$

where:

$$F_{\mu\nu} = \partial_\mu A_\nu - \partial_\nu A_\mu. \quad (2.2)$$

Table 2.1: The Standard Model particles.

	Name	Charge [e]	Spin	Mass [GeV]	
Quark:	1st generation	up u	+2/3	1/2	$\sim 3 \times 10^{-3}$
		down d	-1/3	1/2	$\sim 4 \times 10^{-3}$
	2nd generation	charm c	+2/3	1/2	1.29
		strange s	-1/3	1/2	$\sim 95 \times 10^{-3}$
	3rd generation	top t	+2/3	1/2	173
		bottom b	-1/3	1/2	4.2
Lepton:	1st generation	electron e^-	-1	1/2	511×10^{-6}
		electron neutrino ν_e	0	1/2	$< 2 \times 10^{-9}$
	2nd generation	muon μ^-	-1	1/2	106×10^{-3}
		muon neutrino ν_μ	0	1/2	$< 0.17 \times 10^{-3}$
	3rd generation	tau τ^-	-1	1/2	1.78
		tau neutrino ν_τ	0	1/2	$< 15.5 \times 10^{-3}$
Gauge boson	photon γ	0	1	0	
	gluon g	0	1	0	
	Z boson Z^0	0	1	80.39	
	W boson W^\pm	± 1	1	91.19	
Higgs boson	Higgs boson H	0	0	125.36	

\mathcal{L}_{kin} is invariant under the transformation: $A_\mu(x) \rightarrow A_\mu(x) - \partial_\mu \eta(x)$ for any space-time x and arbitrary function of $\eta(x)$. If a mass term for the gauge boson is naively added to the Lagrangian as follows:

$$\mathcal{L}_{kin} = -\frac{1}{4}F_{\mu\nu}F^{\mu\nu} + \frac{1}{2}m^2 A_\mu A^\mu, \quad (2.3)$$

it is soon found out that the mass term violates the local gauge symmetry. The $U(1)$ gauge symmetry thus requires the gauge boson to be massless. This logic can be extended to the case of $SU(2) \otimes U(1)$ gauge theory, where gauge bosons (i.e. γ , W and Z) are also required to be massless. The following describes how the W and Z bosons obtain their masses through the Higgs mechanism.

In the Higgs mechanism, a $SU(2)$ doublet of complex scalar fields $\phi^0(x)$ and $\phi^+(x)$ is introduced as follows:

$$\phi(x) = \begin{pmatrix} \phi^+(x) \\ \phi^0(x) \end{pmatrix} = \frac{1}{\sqrt{2}} \begin{pmatrix} \phi_1(x) + i\phi_2(x) \\ \phi_3(x) + i\phi_4(x) \end{pmatrix}. \quad (2.4)$$

A Lagrangian \mathcal{L}_{scaler} , which is $SU(2) \otimes U(1)$ gauge invariant for the scalar fields is given by:

$$\mathcal{L}_{scaler} = (D_\mu \phi)^\dagger (D_\mu \phi) - V(\phi). \quad (2.5)$$

The covariant derivative of ϕ is:

$$D_\mu \phi = (\partial_\mu + i\frac{g}{2}\sigma^i W_\mu^i + i\frac{g'}{2}B_\mu)\phi, \quad (2.6)$$

where W_μ^i and B_μ are, respectively, the $SU(2)$ and $U(1)$ gauge bosons. The scalar potential $V(\phi)$ is represented as:

$$V(\phi) = \mu^2 \phi^\dagger \phi + \lambda (\phi^\dagger \phi)^2. \quad (2.7)$$

Vacuum stability demands λ to be greater than zero. If $\mu^2 > 0$, the potential $V(\phi)$ has the minimum value at $\phi = 0$ and preserve the symmetries of the Lagrangian. However, if $\mu^2 < 0$, the minimum point shifts to:

$$\phi^\dagger \phi = -\frac{\mu^2}{2\lambda} = \frac{v^2}{2}, \quad (2.8)$$

and the field ϕ acquires a nonzero vacuum expectation value. The potential takes the form as shown in figure 2.1. There is an infinite number of states with the minimum energy satisfying $\phi^\dagger \phi = v^2/2$ due to the symmetry form of the $V(\phi)$. Here, a vacuum expectation value of ϕ can be chosen as:

$$\langle \phi \rangle = \frac{1}{\sqrt{2}} \begin{pmatrix} 0 \\ v \end{pmatrix}. \quad (2.9)$$

This choice of a particular vacuum state corresponds to a spontaneous symmetry breaking, that is the symmetry of the Lagrangian becomes hidden by the choice. Only a neutral scalar field can acquire a vacuum expectation value in order to keep the conservation of the electric charge. Thus, the ϕ^0 is to be interpreted as the neutral component of the doublet, which is invariant under a new $U(1)$ symmetry. As a result, the photon is still massless after the spontaneous symmetry breaking.

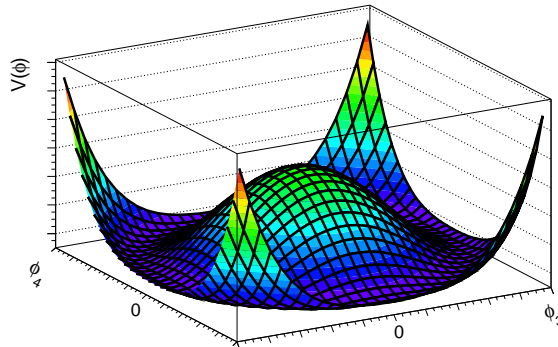


Figure 2.1: The Higgs potential for a complex scalar field with $\mu^2 < 0$ and $\lambda > 0$.

The W and Z gauge boson masses can now be generated. It is convenient to parameterize $\langle \phi \rangle$ in the unitary gauge as follows:

$$\phi(x) = \frac{1}{\sqrt{2}} \begin{pmatrix} 0 \\ v + h(x) \end{pmatrix}. \quad (2.10)$$

The Lagrangian \mathcal{L}_{scalar} can be written by substituting equation 2.10 as follows:

$$\mathcal{L}_{scaler} = \left| \left(\partial_\mu + i\frac{g}{2}\sigma^i W_\mu^i + i\frac{g'}{2}B_\mu \right) \frac{1}{\sqrt{2}} \begin{pmatrix} 0 \\ v+h \end{pmatrix} \right|^2 - V(\phi_0) \quad (2.11)$$

$$= \frac{1}{2}(\partial_\mu h)(\partial^\mu h) - \lambda v^2 h^2 + \frac{v^2}{8} [g^2 ((W_\mu^1)^2 + (W_\mu^2)^2) + (gW_\mu^3 - g'B_\mu)^2] + (\mathcal{O}(h^2) \text{ and } h\text{-mixed terms}). \quad (2.12)$$

The first term of equation 2.12 is the kinetic term of the Higgs boson. The second term corresponds to the mass of the Higgs boson:

$$m_H = v\sqrt{2\lambda}. \quad (2.13)$$

The charged vector boson, W_μ^\pm , and its complex conjugate are defined as:

$$W_\mu^\pm \equiv \frac{1}{\sqrt{2}}(W_\mu^1 \mp iW_\mu^2). \quad (2.14)$$

Thereby the g^2 term in equation 2.12 becomes:

$$\frac{1}{2} \left(\frac{gv}{2} \right)^2 W_\mu^\dagger W^\mu, \quad (2.15)$$

and yielding the W mass:

$$m_W = \frac{gv}{2}. \quad (2.16)$$

The two remaining neutral gauge bosons, Z and A , are defined as follows:

$$Z_\mu \equiv \frac{1}{\sqrt{g^2 + g'^2}}(gW_\mu^3 - g'B_\mu) \text{ with mass } m_Z = \frac{v}{2}\sqrt{g^2 + g'^2}, \quad (2.17)$$

$$A_\mu \equiv \frac{1}{\sqrt{g'^2 + g^2}}(gW_\mu^3 + g'B_\mu) \text{ with mass } m_A = 0. \quad (2.18)$$

In a summary, the Lagrangian \mathcal{L}_{scaler} describes a theory with one real scalar, three massive vector and one massless vector bosons. Three massive vector bosons are to be identified with the W^\pm and Z bosons, one massless vector boson is the photon and the single remaining massive scalar boson corresponds to the Higgs bosons. Thus, the masses of the W^\pm and Z bosons are explained by introducing the Higgs mechanism. The existence of the Higgs boson is predicted by the theory as a consequence.

The VVh and $VVhh$ terms in equation 2.12, where $V = W^\pm, Z$, give rise to triple and quartic couplings between one or two Higgs bosons and the gauge bosons. For example, WWh and $WWhh$ terms can be written as follows with equation 2.14:

$$\frac{1}{4}g^2 v W_\mu^- W^{+\mu} h + \frac{1}{8}g^2 W_\mu^- W^{+\mu} h h. \quad (2.19)$$

Therefore, the coupling strength at the WWh vertex is predicted as:

$$g_{hWW} = \frac{1}{2}g^2 v = 2\frac{m_W^2}{v}. \quad (2.20)$$

The observation and measurement of the coupling of the Higgs boson to WW thus provide an essential confirmation of the Higgs mechanism. Fermions masses are also explained thorough the

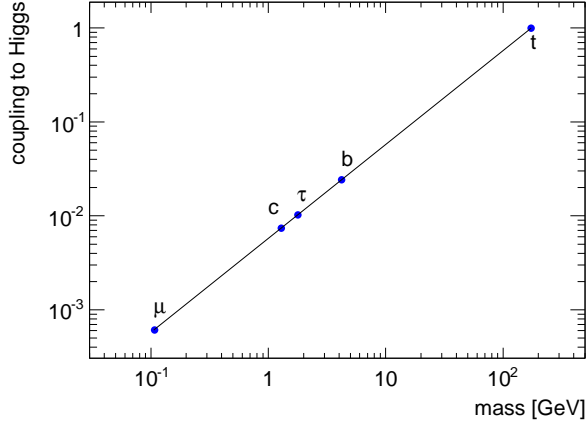


Figure 2.2: Higgs boson couplings to each fermion predicted in the Standard Model, where $v = 263$ GeV.

Higgs mechanism by introducing an arbitrary Yukawa coupling constant $\lambda_f = \sqrt{2}m_f/v$, which is proportional to its mass m_f as shown in figure 2.2.

To summarize the section, the complete Lagrangian in the electroweak standard model is expressed in the following:

$$\begin{aligned}
 \mathcal{L} = & -\frac{1}{4}\mathbf{W}_{\mu\nu} \cdot \mathbf{W}^{\mu\nu} - \frac{1}{4}B_{\mu\nu} \cdot B^{\mu\nu} & \left\{ \begin{array}{l} W^\pm, Z \text{ and } \gamma \text{ kinetic energies,} \\ \text{and self interactions} \end{array} \right. \\
 & + \bar{L}\gamma^\mu \left(i\partial_\mu - g\frac{1}{2}\boldsymbol{\sigma} \cdot \mathbf{W}_\mu - g'\frac{Y}{2}B_\mu L \right) & \left\{ \begin{array}{l} \text{Leptons and quarks kinetic} \\ \text{energies, and interactions} \\ \text{with } W^\pm, Z \text{ and } \gamma \end{array} \right. \\
 & + \bar{R}\gamma^\mu \left(i\partial_\mu - g'\frac{Y}{2}B_\mu R \right) & \\
 & + \left| \left(i\partial_\mu - g\frac{1}{2}\boldsymbol{\sigma} \cdot \mathbf{W}_\mu - g'\frac{Y}{2}B_\mu L \right) \phi \right|^2 - V(\phi) & \left\{ \begin{array}{l} W^\pm, Z, \gamma \text{ and Higgs masses,} \\ \text{and couplings to Higgs} \end{array} \right. \\
 & -(G_1\bar{L}\phi R + G_2\bar{L}\phi_c R + h.c.). & \left\{ \begin{array}{l} \text{Leptons and quarks masses,} \\ \text{and couplings to Higgs} \end{array} \right.
 \end{aligned} \tag{2.21}$$

2.1.2 Production and decay of the Higgs boson

This subsection describes the production of the Higgs boson at the LHC and its decay. The leading production modes of the Higgs boson at the LHC consist of gluon-gluon fusion (ggF), vector-boson fusion (VBF), and associate production with W/Z (VH) and with a pair of top quarks (ttH). Figure 2.3 shows Feynman diagrams for these production processes. The estimation of these production cross sections at the LHC relies on detailed calculations. Considering a simple process in electroweak interactions as an example, $e^+e^- \rightarrow e^+e^-$, the cross section is calculable in a perturbative way. The perturbative field theory allows level by level calculation of particle interactions. The lowest level (Leading Order, LO) of the process has only two diagrams as shown in figure 2.4. The precision of the calculation can be improved by including the next-to-leading order (NLO) and the next-to-next-to-leading order (NNLO) diagrams. In elec-

troweak couplings, the LO calculation provides a good precision since the coupling constant α is small ($\sim 1/137$). However, the calculation at the LHC requires further theoretical treatments because the proton is a composite particle. The cross section calculation for collisions between proton i and j can be written as follows:

$$\sigma = \underbrace{\sigma_{ij \rightarrow X}}_{\text{short-distance}} \times \underbrace{\int f(x_i, Q^2) dx_i \cdot \int f(x_j, Q^2) dx_j}_{\text{long-distance}}. \quad (2.22)$$

The calculation can be separated into two parts: one is short-distance part, which is calculable in the perturbative theory described above, and the other is long-distance part, which is not calculable. The short-distance part describes the parton scattering with a large momentum transfer Q^2 , i.e. $gg \rightarrow H$, where the perturbative calculation is possible thanks to the smallness of the strong coupling constant ($\alpha_s \ll 1$) at a high energy region. The long-distance part describes probabilities to find the initial partons within protons, which is modeled by the parton distribution function (PDF), $f(x, Q^2)$, where x is a momentum fraction of the parton in proton. The PDFs are parameterized based on mainly data from experiments at HERA [8] and Tevatron [9, 10]. For example, figure 2.5 shows the PDFs modeled with MSTW2008 program [18].

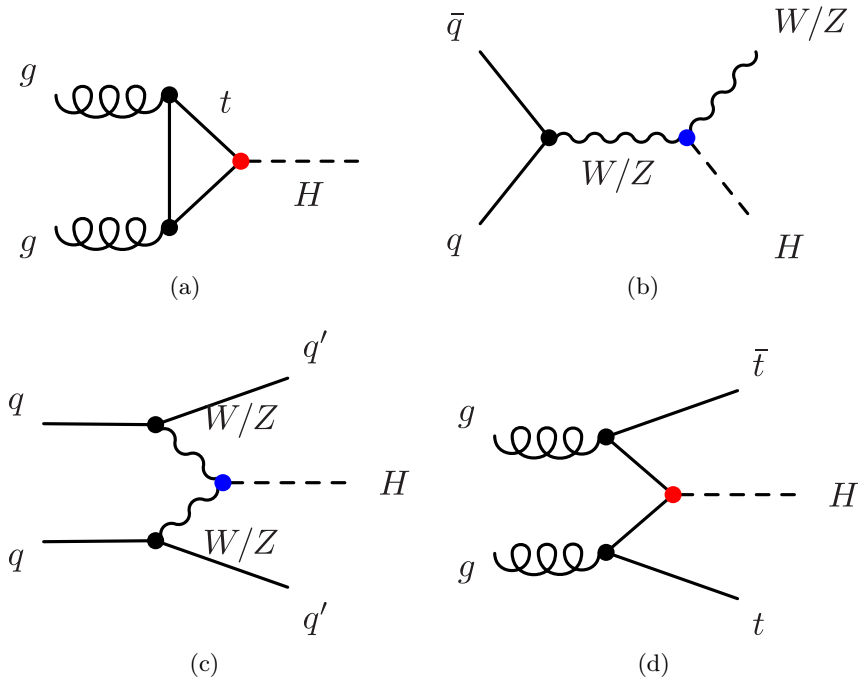


Figure 2.3: Feynman diagrams of production processes of the SM Higgs boson. (a) gluon-gluon fusion, (b) associate production with W/Z , (c) vector-boson fusion and (d) associate production with a pair of top quarks. Blue (red) dots indicate the Higgs boson coupling to the vector bosons (fermions).

The calculation of the Higgs boson production cross section has been performed within the LHC Higgs Cross Section Working Group [11, 12]. Figure 2.6 shows the evaluated production cross sections for each production mode as a function of Higgs boson mass.

- $gg \rightarrow H$ (ggF):

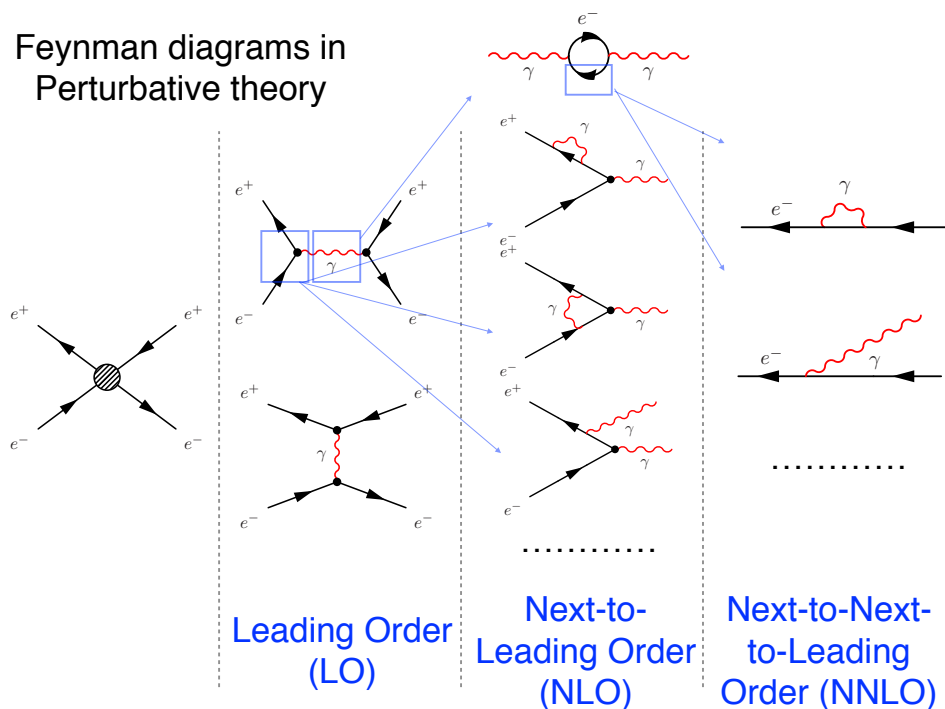


Figure 2.4: Feynman diagrams in perturbative theory for $e^+e^- \rightarrow e^+e^-$ process.

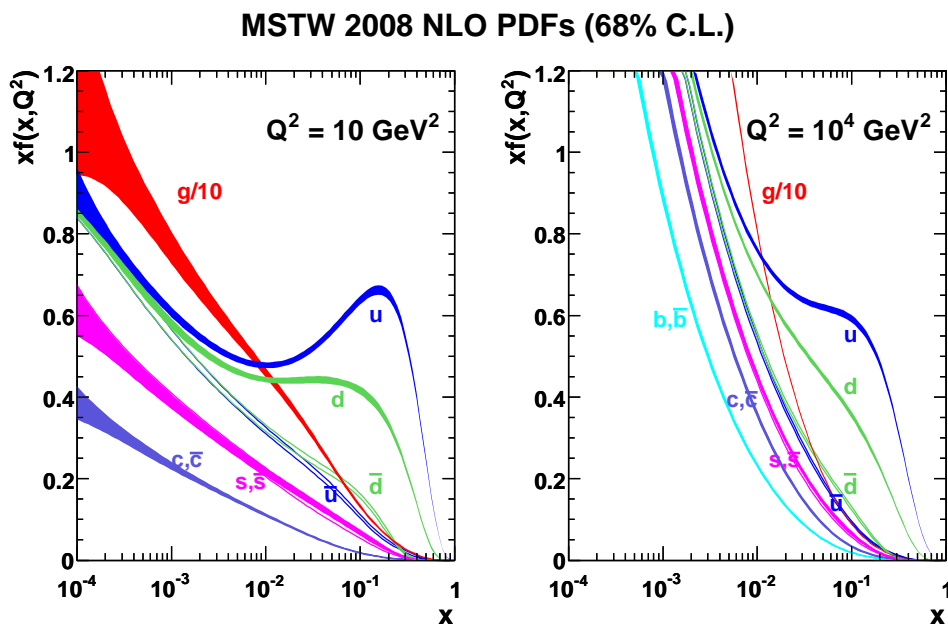


Figure 2.5: Parton distribution functions modeled by MSTW2008 at $Q^2 = 10 \text{ GeV}^2$ and $Q^2 = 10^4 \text{ GeV}^2$ [18].

The ggF process is the dominant Higgs boson production mode at the LHC. The ggF production proceeds dominantly through a top quark loop. The production can also proceed by a bottom quark loop, though this process is suppressed by m_b^2/m_t^2 because the Higgs boson couplings to the fermions are proportional to the square of the mass of fermions. The production cross section has been calculated at NNLO in QCD [13] and NLO in electroweak couplings [14, 15]. Resummation of the soft QCD radiation has been performed at next-to-next-to-leading log (NNLL) [16]. An uncertainty related to the perturbative calculation in QCD is derived by varying renormalization and factorization scales [17] by factor half and two (called QCD scale). The renormalization scale is introduced to the perturbative calculation to cancel infinities due to the ultraviolet divergence. The factorization scale defines the border between the short- and long-distance part. The maximum deviation in the QCD scale is taken as the uncertainty, and it is 7.5%. The PDF is modeled with the MSTW2008. The PDF uncertainty of 7.2% is estimated using the corresponding 68% C.L. band from the MSTW2008 sets (see figure 2.5).

- $qq \rightarrow qqV^*V^* \rightarrow qqH$ (VBF):

The VBF process is the second contribution to the Higgs boson production, where quarks radiate virtual vector bosons, which then annihilate to produce the Higgs boson. The VBF is characterized and effectively discriminated from other SM processes, including the other Higgs production processes, by tagging the two quarks in the final state as jets. The VBF production cross section has been calculated at NNLO in QCD by VBF@NNLO program [19]. Electroweak correction is evaluated at NLO with HAWK program [20]. The calculation has a 0.2% uncertainty from the QCD scale and a leading uncertainty of 2.7% due to modeling of PDFs.

- $q\bar{q} \rightarrow V^* \rightarrow VH$ (VH):

The Higgs boson is emitted from the Z or W boson in this process (Higgs-strahlung). The VH process is effectively discriminated from the QCD process by using the $W \rightarrow \ell\nu$ and $Z \rightarrow \ell\ell$ signatures. The total cross section has been computed at NNLO in QCD and NLO in electroweak couplings with VH@NNLO program [21].

- $gg, qq \rightarrow t\bar{t}H$ ($t\bar{t}H$):

The Higgs boson is produced in the association with a top-quark pair. The $t\bar{t}H$ process can provide information about the top-Higgs Yukawa coupling without the loop of other quarks. However, the production rate is found to be small compared to the other production modes described above. The total production cross section has been evaluated at NLO in QCD [22].

The Higgs boson decays rapidly into other particles after its production. The Standard Model can predict the decay process of the Higgs boson if the mass is given. For example, if the coupling of the Higgs boson to WW is provided as equation 2.20, the partial Higgs boson width $\Gamma_{H \rightarrow WW}$ at the lowest order is given as follows:

$$\Gamma_{H \rightarrow WW} = \frac{g^2}{64\pi} \frac{m_H^3}{m_W^2} \sqrt{1 - \frac{4m_W^2}{m_H^2}} \left(1 - \frac{m_W^2}{m_H^2} + \frac{12m_W^2}{m_H^2} \right). \quad (2.23)$$

Also the Higgs boson can couple and decay to the other gauge bosons. At tree level, the decays $H \rightarrow WW$ and $H \rightarrow ZZ$ are possible, while at one-loop the decays $H \rightarrow gg$, $\gamma\gamma$ and γZ occur. The decays to fermions are also possible at tree level; they are predominant processes with a mass below the WW threshold ($m_H \sim 160$ GeV). The branching fraction with higher-order

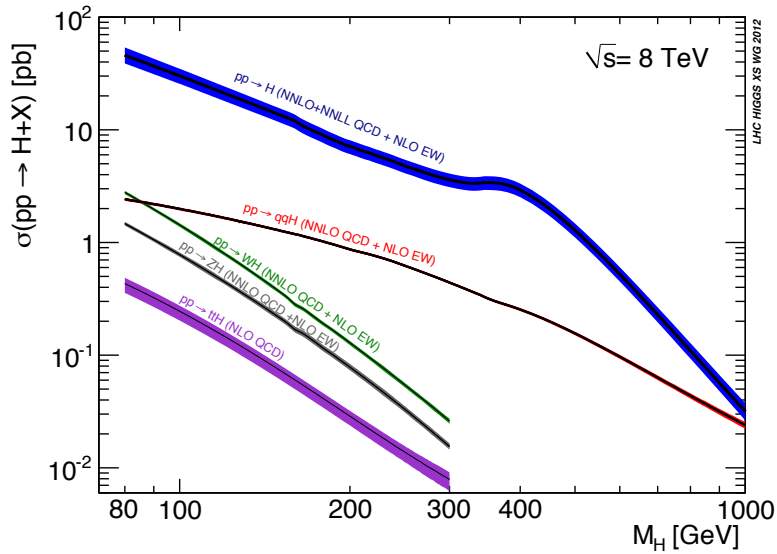


Figure 2.6: Standard Model Higgs boson production cross sections at $\sqrt{s} = 8 \text{ TeV}$ [11].

corrections is shown in figure 2.7 as a function of the Higgs boson mass. The branching ratios are also calculated within the LHC Higgs Cross Section Working Group using PROPHECY4f [23] and HDECAY [24] programs.

Accessing individual decay channels by the experiment allows for measurements of absolute Higgs boson couplings, as well as constraining the overall Higgs boson decay width. The main decay channels for Higgs boson studies performed at ATLAS are summarized in the following.

- $H \rightarrow b\bar{b}$:
The $H \rightarrow b\bar{b}$ is the dominant decay mode at $m_H \sim 125 \text{ GeV}$. However, it is not feasible to observe the signal in the ggF production mode because of high QCD backgrounds. The VH production with the $W \rightarrow \ell\nu$ and $Z \rightarrow \ell\ell$ decays can be efficiently used for triggering and background reduction purposes.
- $H \rightarrow WW$:
The $H \rightarrow WW$ has the second largest branching ratio, and can keep the purity by selecting the $WW \rightarrow \ell\nu\ell\nu$ decay even in the ggF production mode. The $H \rightarrow WW$ thus provides strong constraints on the couplings to the vector bosons. Analysis of the $H \rightarrow WW^* \rightarrow \ell\nu\ell\nu$ mode is described in detail through this thesis.
- $H \rightarrow \tau\tau$:
The $H \rightarrow \tau\tau$ has the branching ratio of about 6%. It is an important channel to demonstrate the presence of direct couplings of the Higgs boson to fermions together with the $H \rightarrow b\bar{b}$ and its proportionality to mass. All combinations of leptonic ($\tau \rightarrow \ell\nu\bar{\nu}$ with $\ell = e, \mu$) and hadronic ($\tau \rightarrow \text{hadrons } \nu$) tau decays are used. The understanding of the irreducible $Z/\gamma^* \rightarrow \tau\tau$ background is a key for this channel.
- $H \rightarrow ZZ$:
The branching ratio of the $H \rightarrow ZZ$ ($< 0.03\%$) is smaller than the other leading decay modes. Nevertheless, the $H \rightarrow ZZ \rightarrow 4\ell$ provides a good sensitivity for the measurement of the Higgs boson properties due to its high signal-to-background ratio. Since the four-leptons in the final state can be detected with high resolutions, a clear peak of the invariant

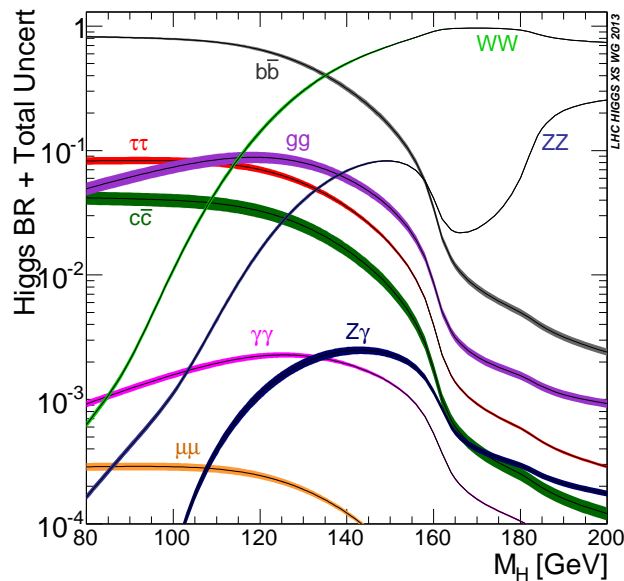


Figure 2.7: Standard Model Higgs boson decay branching ratios [11].

mass of the Higgs boson is observed as shown in figure 2.8. The largest background comes from ZZ^* production (red histogram in the figure) in this analysis.

- $H \rightarrow \gamma\gamma$:
The $H \rightarrow \gamma\gamma$ decay occurs with a factor of ten reduction in the branching ratio compared to the $H \rightarrow ZZ$. The sensitivity of the measurement is driven by the performance of the photon reconstruction. The good diphoton invariant mass resolution of the ATLAS makes it possible to separate the signal from the large continuum background.

2.1.3 Possible new phenomena revealed by Higgs boson measurements

The Standard Model, despite its many successes, does not yet provide a complete description of the universe. The “hierarchy problem” is an open issue regarding the naturalness of the Higgs boson mass. The physical Higgs boson mass, which is observed by the experiment, includes corrections via contributions of the loop diagrams as shown in figure 2.9. These contributions give the quadratic divergence, $\delta m_H^2 \sim \Lambda^2$, in the Higgs boson mass term. Λ is the cut-off momentum scale up to where the SM is valid. Considering the SM is valid up to the Planck scale ($\Lambda \sim 10^{18}$ GeV), the given correction is to be also $\mathcal{O}(10^{18}$ GeV). This means the bare Higgs boson mass and the correction are tuned to generate the physical Higgs boson mass $\mathcal{O}(10^2$ GeV). Thus, the possible existence of additional new particles and interactions is motivated in order to cancel the contribution of the SM particles. Also there are other open questions, such as the nature of the dark matter, that the SM is not able to answer. Therefore, observation of new phenomena at the LHC is highly hoped to understand the particle physics beyond the Standard Model.

The following subsection explains two possible scenarios, where the Higgs boson production deviates from the SM prediction and the precise measurement of the properties of the Higgs boson is motivated.

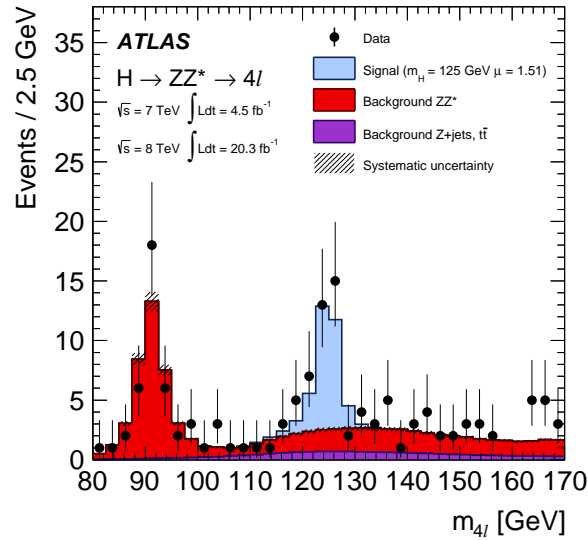


Figure 2.8: The distribution of the four-lepton invariant mass, $m_{4\ell}$, of the selected candidates (filled circles) compared to the expected signal and background contributions (filled histograms). The signal expectation shown is for a mass hypothesis of $m_H = 125$ GeV and normalized to the data [25].

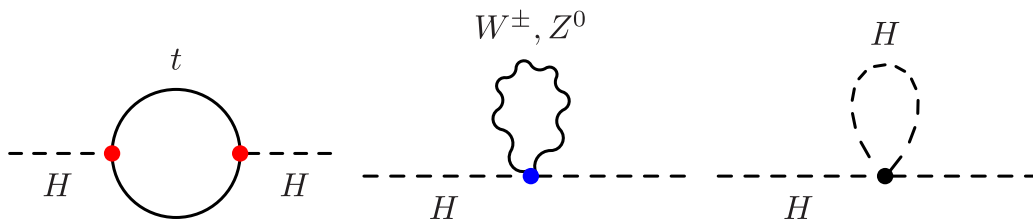


Figure 2.9: Three main Feynman diagrams, which contribute to the Higgs boson mass correction.

Simplified MSSM

Supersymmetry [26–34] provides a means to solve the hierarchy problem by introducing superpartners. Superpartners are hypothetical elementary particles originated from an idea of new symmetry between the fermions and bosons. The radiative correction of the superpartner to the Higgs boson mass is considered to cancel those of the SM particle. The Minimal Supersymmetric Standard Model (MSSM) [35–39] extends the SM by introducing superpartners for every fermions and gauge bosons, whose spin differ by one half compared to the corresponding SM particles. In this extension, the Higgs sector consists of two scalar doublet fields H_u and H_d that leads to five Higgs states, two CP-even h and H , a CP-odd A and two charged H^\pm bosons. Superpartners for these Higgs bosons are also introduced. The observed Higgs boson can be considered as the lightest MSSM Higgs boson h . The mass mixing matrix for the CP-even Higgs bosons, \mathcal{M}_s , is described by two parameters: the ratio of the two vacuum expectation values, $\tan\beta$, and the mass of A , m_A , as follows:

$$\begin{aligned} \mathcal{M}_s = & (m_Z + \delta_1) \begin{pmatrix} \cos^2 \beta & -\cos \beta \sin \beta \\ -\cos \beta \sin \beta & \sin^2 \beta \end{pmatrix} \\ & + m_A \begin{pmatrix} \sin^2 \beta & -\cos \beta \sin \beta \\ -\cos \beta \sin \beta & \cos^2 \beta \end{pmatrix} + \begin{pmatrix} 0 & 0 \\ 0 & \frac{\delta}{\sin^2 \beta} \end{pmatrix}, \end{aligned} \quad (2.24)$$

where δ_1 and δ are radiative corrections involving primarily top quarks and stops (superpartner of top).

The couplings in a simplified MSSM model can be obtained from this mass mixing matrix as follows [40, 41]. The eigenvalues of the mass matrix correspond to the mass of h and H . The eigenvalue is evaluated at observed $m_h \sim 125$ GeV to obtain δ as function of m_A and $\tan\beta$:

$$\frac{\delta}{\sin^2 \beta} = \frac{m_h^2(m_A^2 + m_Z^2 - m_h^2) - m_A^2 m_Z^2 \cos^2(2\beta)}{m_Z^2 \cos^2 \beta + m_A^2 \sin^2 \beta - m_h^2}, \quad (2.25)$$

where δ_1 is neglected because it is a sub-leading correction. Substituting equation 2.25 into equation 2.24, the mass of H and the mixing angle α , $h = \cos \alpha H_d + \sin \alpha H_u$ and $H = -\sin \alpha H_d + \cos \alpha H_u$, are fully described by the m_A and $\tan\beta$ as follows:

$$m_H^2 = \frac{(m_A^2 + m_Z^2 - m_h^2)(m_Z^2 \cos^2 \beta + m_A^2 \sin^2 \beta) - m_A^2 m_Z^2 \cos^2(2\beta)}{m_Z^2 \cos^2 \beta + m_A^2 \sin^2 \beta - m_h^2} \quad (2.26)$$

$$\alpha = -\arctan \left(\frac{(m_Z^2 + m_A^2) \cos \beta \sin \beta}{m_Z^2 \cos^2 \beta + m_A^2 \sin^2 \beta - m_h^2} \right). \quad (2.27)$$

The Higgs boson couplings to the up-type (κ_u) and down-type (κ_d) fermions and to the vector bosons (κ_V), as ratios to the corresponding SM expectations, are given by:

$$\kappa_V = \frac{s_d(\tan \beta, m_A) + \tan \beta s_u(\tan \beta, m_A)}{\sqrt{1 + \tan^2 \beta}}, \quad (2.28)$$

$$\kappa_u = s_u(\tan \beta, m_A) \frac{\sqrt{1 + \tan^2 \beta}}{\tan \beta}, \quad (2.29)$$

$$\kappa_d = s_d(\tan \beta, m_A) \sqrt{1 + \tan^2 \beta}. \quad (2.30)$$

where s_u and s_d are:

$$s_u = 1/\sqrt{1 + \frac{(m_A^2 + m_Z^2)^2 \tan^2 \beta}{(m_Z^2 + m_A^2 \tan^2 \beta - m_h^2(1 + \tan^2 \beta))^2}}, \quad (2.31)$$

$$s_d = \frac{(m_A^2 + m_Z^2) \tan \beta}{m_Z^2 + m_A^2 \tan^2 \beta - m_h^2(1 + \tan^2 \beta)} s_u. \quad (2.32)$$

Thus, deviations of the couplings from the SM predictions, which sizes depend on the parameter of m_A and $\tan\beta$, are expected in this MSSM model. The precise measurement of the Higgs boson production and decay can constrain these parameters and is capable of observing the deviations if this model describes the nature.

Higgs portal of dark matter

Many ‘‘Higgs portal’’ models [42–46] introduce an additional weakly-interacting massive particle (WIMP) as a dark matter candidate, where the WIMP is assumed to interact very weakly with the SM particles, except for the Higgs boson. This interaction introduces an additional decay mode ($H \rightarrow \chi\bar{\chi}$) and makes a deviation of the total width of the Higgs boson from the SM expectation. For example, the ratio of the total width of the Higgs boson to the SM expectation, $\Gamma_h/\Gamma_{h,SM}$, is given in this model with the following assumptions.

The couplings of the Higgs boson to massive particles other than the WIMP are assumed to be equal to the SM predictions. Effective couplings to photons, κ_γ , and gluons, κ_g , are introduced to absorb the possible contributions of new particles through the decay loop. The Higgs boson production modes are assumed to be the same as the SM. Then, $\Gamma_h/\Gamma_{h,SM}$ is described as:

$$\kappa_h = \Gamma_h/\Gamma_{h,SM} = \sum_i \kappa_i^2 / (1 - \text{BR}_{\text{invisible}}), \quad (2.33)$$

$$\sum_i \kappa_i^2 = 0.0023 \times \kappa_\gamma^2 + 0.085 \times \kappa_g^2 + 0.91, \quad (2.34)$$

where $\text{BR}_{\text{invisible}}$ is the branching ratio of the Higgs boson to invisible final states, i.e. the WIMP. The branching ratios of the Higgs boson with $m_H = 125.5$ GeV to photons, gluons and sum of the other particles are 0.0023, 0.085 and 0.91, respectively [11]. The parameters of κ_γ , κ_g and $\text{BR}_{\text{invisible}}$ can be obtained by fitting the measured production and decay rates of all the channels.

2.2 Status of Higgs boson measurements

In this thesis, the measurement of the Higgs boson production using the $H \rightarrow WW^* \rightarrow \ell\nu\ell\nu$ decay channel is described. Results of the Higgs boson measurements using the other decay channels in ATLAS are briefly provided in this section.

Higgs boson mass

The $H \rightarrow ZZ^* \rightarrow 4\ell$ and $H \rightarrow \gamma\gamma$ decay modes allow to perform the Higgs boson mass measurement since their all final products can be detected with high resolutions. The measurements

have been performed using the proton-proton collision data sample corresponding to an integrated luminosity of 25 fb^{-1} at center-of-mass energies of 7 TeV and 8 TeV (see chapter 3). Figure 2.8 and 2.10 (a) show the obtained invariant mass distributions for the $H \rightarrow ZZ^* \rightarrow 4\ell$ and $H \rightarrow \gamma\gamma$ channels, respectively. There are clear peaks around $m_H \sim 125 \text{ GeV}$ due to the presence of the Higgs boson. Profile likelihood fits are performed on the invariant mass distributions to determine the Higgs boson mass [47], that results are shown in figure 2.10 (b). The best fit values are:

$$\begin{aligned}
 m_H &= 124.51 \pm 0.52(\text{stat.}) \pm 0.06(\text{syst.}) = 124.51 \pm 0.52 & (H \rightarrow ZZ^* \rightarrow 4\ell) \\
 m_H &= 125.98 \pm 0.42(\text{stat.}) \pm 0.28(\text{syst.}) = 125.98 \pm 0.50 & (H \rightarrow \gamma\gamma) \\
 m_H &= 125.36 \pm 0.37(\text{stat.}) \pm 0.18(\text{syst.}) = 125.36 \pm 0.41 & (\text{Combined})
 \end{aligned}$$

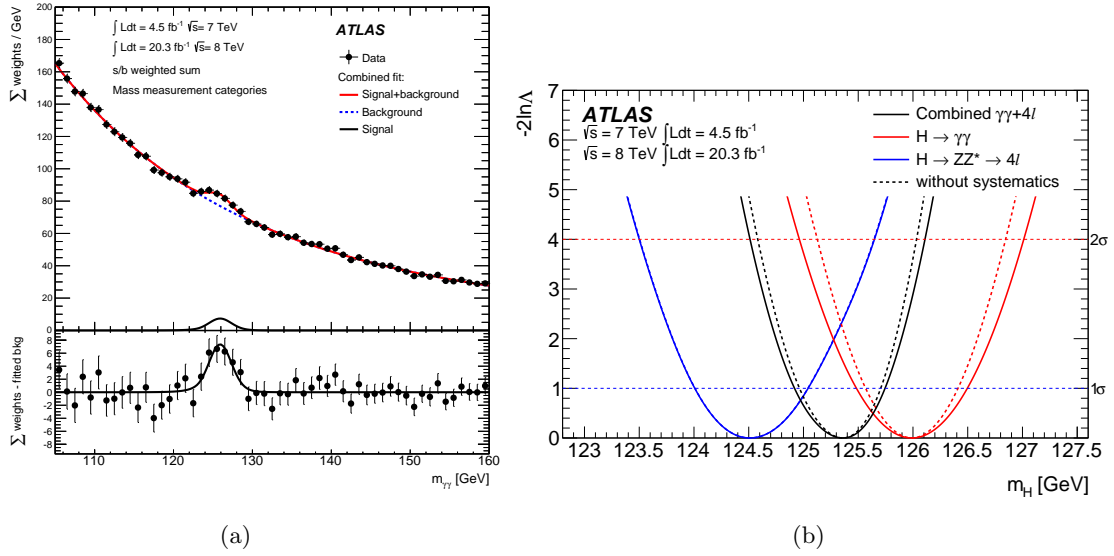


Figure 2.10: (a) The distribution of the di-photon invariant mass, $m_{\gamma\gamma}$, of the $H \rightarrow \gamma\gamma$ analysis. Different categories are summed together with a weight given by the signal-to-background ratio in each category. The fitted signal plus background is shown, along with the background-only component of this fit [47]. (b) Value of the profile likelihood, $-2\ln\Lambda$, as a function of m_H for the individual $H \rightarrow \gamma\gamma$ and $H \rightarrow ZZ^* \rightarrow 4\ell$ channels and their combination [47].

Signal strength

The signal strength of the Higgs boson, which is defined as the ratio of the observed production and decay rate to the expected rate by the SM, is measured using various decay modes. A measurement of the signal strength being zero means no signals in the data, and one corresponds to the same size as the expected yield in the SM. The measurements have been performed using the 7 TeV and 8 TeV data samples at the observed Higgs boson mass $m_H = 125.36 \text{ GeV}$. Figure 2.11 summarizes the observed signal strength for the $H \rightarrow ZZ^* \rightarrow 4\ell$, $H \rightarrow \gamma\gamma$, $H \rightarrow b\bar{b}$ and $H \rightarrow \tau\tau$ channels. No significant deviations from the SM expectations have been observed in these decay channels.

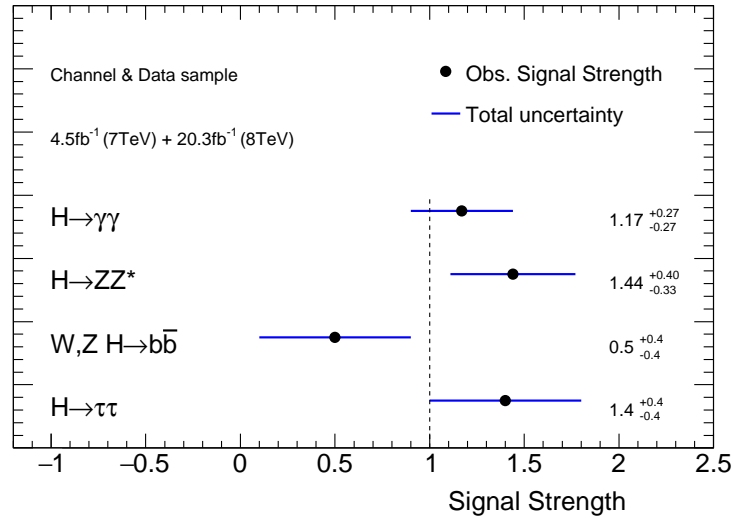


Figure 2.11: Summary of the observed signal strengths. The signal strength are measured at $m_H = 125.36$ GeV in ATLAS [48].

2.3 Analysis overview

The Higgs signal strength, μ , is measured using the $H \rightarrow WW^* \rightarrow \ell\nu\ell\nu$ decay mode and given as a result in this thesis. The measurement is performed at the observed Higgs boson mass $m_H \sim 125$ GeV. An overview of the analysis presented in this thesis is described in this section. The analysis follows the steps shown in figure 2.12.

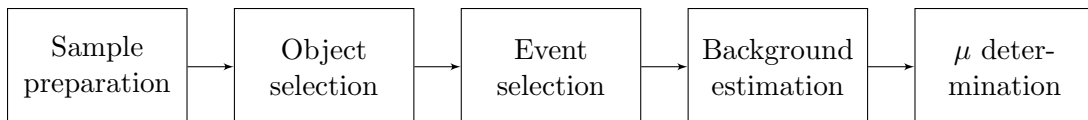


Figure 2.12: Analysis flow.

Sample preparation

This analysis uses the data collected by the ATLAS in year 2012, which corresponds to an integrated luminosity of 20.3 fb^{-1} at 8 TeV (denoted as “8 TeV data”). The particle production processes summarized in table 2.2 are considered as backgrounds in the analysis. Features of the signal and background processes are summarized in the following:

- **Signal:** Figure 2.13 (a) shows a Feynman diagram of signal processes (ggF production). An opposite-charge lepton pair and a large missing energy due to the presence of the neutrinos are observed in an event.
- **WW:** The non-resonant WW production such as shown in figure 2.13 (b) has the same final state with the signal process. The WW production is the dominant source of the background.

Table 2.2: Background processes to the $H \rightarrow WW^* \rightarrow \ell\nu\ell\nu$ measurement. Irreducible backgrounds have the same final state with the signal, other backgrounds are shown with features that lead to this final state.

Processes	Feature(s)
WW	Irreducible
$Other VV$	$\left\{ \begin{array}{l} W\gamma \\ W\gamma^*, WZ \text{ and } ZZ \end{array} \right.$ γ misidentified as e Unidentified leptons
$t\bar{t}$, single top (Top)	Unidentified b quarks
Z +jets	$\left\{ \begin{array}{l} Z/\gamma^* \rightarrow ee/\mu\mu \\ Z\gamma^* \rightarrow \tau\tau \rightarrow \ell\nu\ell\nu \end{array} \right.$ Misreconstructed ν Irreducible
W +jets	jet misidentified as lepton
Multi-jets (QCD)	jet misidentified as lepton, misreconstructed ν

- **Other VV:** The diboson production other than the WW process is denoted as “*Other VV*”, which consists of the $W\gamma, W\gamma^*, WZ$ and ZZ processes. The $W\gamma^*$ and WZ productions shown in figure 2.13 (c) contribute as backgrounds when one of the leptons in the final state is not identified. The $ZZ \rightarrow 4\ell$ process becomes a background when two leptons are not identified together with a mis-measurement of the missing energy. In case of the $ZZ \rightarrow \ell\nu\ell\nu$ process, the same final state with the signal is observed. The $W\gamma$ process becomes a background when the γ is misidentified as an electron.
- **Top:** The top-quark pair production, $t\bar{t}$, shown in figure 2.13 (d), becomes a background when the b -quarks are not identified. The single top-quark production consists of the top-quark production associated with a W boson, tW , and also associated with quarks, $t\bar{b}$ and $tq\bar{b}$. The tW process contributes as a background when the b -quark in the $t \rightarrow Wb \rightarrow \ell\nu b$ decay is not identified. The $t\bar{b}$ and $tq\bar{b}$ processes become backgrounds when the the b -quarks are not identified and jets are misidentified as a lepton.
- **Z+jets:** The Drell-Yan production with jets shown in figure 2.13 (e) can be separated to two processes by the decay mode. The $Z/\gamma^* \rightarrow ee/\mu\mu$ process becomes a background with a mis-measurement of the missing energy. The $Z/\gamma^* \rightarrow \tau\tau \rightarrow \ell\nu\ell\nu$ process has the same final state as the signal.
- **W+jets:** The W boson production with jets shown in figure 2.13 (e) becomes a background when the jets are misidentified as a lepton and the W decays leptonically.
- **QCD:** The multi-jet production is referred as “QCD” production in this thesis. The QCD process as shown in figure 2.13 (f) becomes a background when the jets are misidentified as two leptons.

To assess the data behavior, Monte Carlo (MC) simulations are prepared for the signal and background processes. The preparation of these signal and background MC samples, as well as the data, are described in chapter 5.

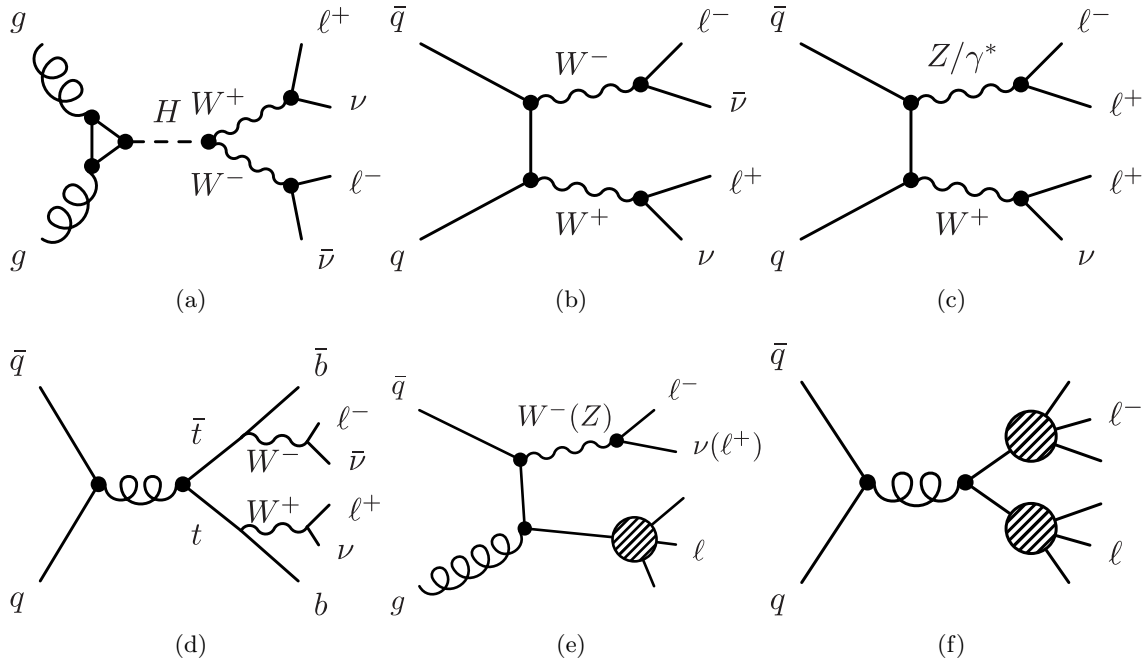


Figure 2.13: Feynman diagrams of production processes of the signal and backgrounds. (a) ggF H , (b) WW , (c) $WZ/W\gamma^*$, (d) $t\bar{t}$, (e) W +jets/ Z +jets, (f) QCD.

Object selection

Leptons, jets and missing energy in an event are reconstructed using the specific algorithms in ATLAS. These reconstructed objects are required to satisfy several quality selections to control misidentifications. The object reconstruction and selection are described in chapter 6.

Event selection

Selections based on the event topology are applied to reject the backgrounds. The background composition depends on the observed number of jets in the final state and the flavor of leptons ($e\mu$ or $ee/\mu\mu$). For example, the $t\bar{t}$ process tends to be reconstructed with two jets due to the presence of the b -quarks, and the $Z \rightarrow ee/\mu\mu$ process has the same flavor of the leptons in the final state. The analysis is thus categorized by the jet multiplicity and the flavor of leptons in order to optimize the event selections. The categorization is summarized in figure 2.14. They are divided into two main classes, ggF -enriched and VBF -enriched. The Higgs boson production modes, which are targeted in the analysis, are the ggF and VBF . The other production modes are still statistically limited in the available data. The Higgs boson production in the $n_j = 0$ and $n_j = 1$ categories are dominated by the ggF process. However, both the ggF and VBF processes are observable in the $n_j \geq 2$ category. To assess the individual production mode, the $n_j \geq 2$ category is divided into ggF -enriched and VBF -enriched samples by event selections based on the VBF topology. The event selection is described in detail in chapter 7.

Background estimation

Majority of the backgrounds are modeled using the MC simulations with a data-based normalization, or using the data directly to be free from the uncertainties as much as possible. These

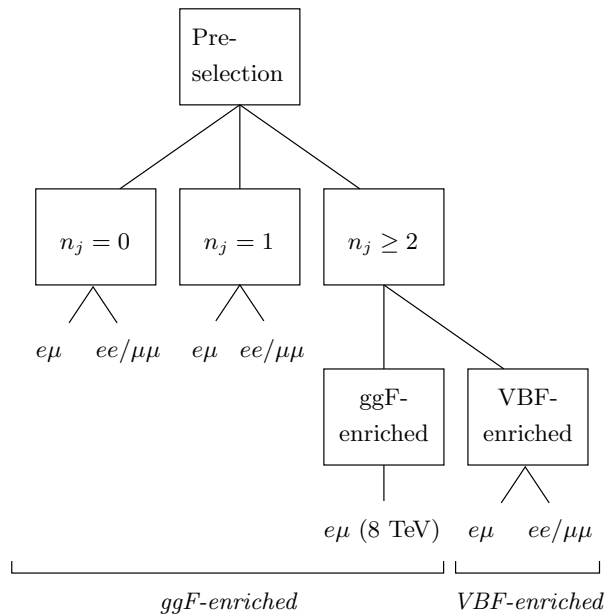


Figure 2.14: Analysis categorization based on the jet multiplicity and the lepton flavor, where n_j is the number of identified jets in an event.

background estimation techniques are described in chapter 8.

Signal strength determination

In the final step of the analysis, a profile likelihood fit is performed in order to extract the signal from the background, and measure the signal strength μ . All signal production modes are treated together with one parameter of the interest of μ . The fit is performed on the “transverse mass” (m_T) distribution. Because of the two neutrinos in the final state, it is not possible to fully reconstruct the invariant mass of the Higgs boson. However, m_T can be calculated without the unknown longitudinal neutrino momenta:

$$m_T = \sqrt{(E_T^{\ell\ell} + p_\nu^{\nu\nu})^2 + |\mathbf{p}_T^{\ell\ell} + \mathbf{p}_T^{\nu\nu}|^2}, \quad (2.35)$$

where $E_T^{\ell\ell} = \sqrt{(p_T^{\ell\ell})^2 + m_{\ell\ell}^2}$. $\mathbf{p}_T^{\ell\ell}$ ($\mathbf{p}_T^{\nu\nu}$) is the vector sum of the leptons (neutrinos) transverse momenta, and $p_T^{\ell\ell}$ ($p_T^{\nu\nu}$) is its magnitude. The signal process provides a different m_T shape from those of the other background sources since the signal m_T has an upper bound at the Higgs boson mass. Thus, the m_T distribution provides the highest discrimination power to distinguish the signal and background. Details of the fitting procedure are given in chapter 9.

The analysis and its results for the ggF-enriched category using the 8 TeV data, which is the most sensitive category, are described in the main body of this thesis (chapter 5–10). In order to improve the precision of the signal strength measurement with the currently available data, the signal acceptance has been increased by loosening the object and event selections compared to previous measurements [49]. For example, the threshold on the subleading lepton transverse momentum, $p_T^{\ell 2}$, has been lowered from 15 to 10 GeV. However, this approach requires to control increasing backgrounds as well, especially backgrounds originating from the W +jets and

Other VV productions, which dominate about 50% of the total background in this additional kinematic region of $10 < p_{\text{T}}^{\ell\ell} < 15$ GeV. The following studies have been performed on these backgrounds:

- Development of a data-driven method called “OS-SS method”,
- Construction of validation regions for the *Other VV* background.

The OS-SS method, which is described in section 8.3.1, uses the data directly to estimate the *Other VV* and part of the *W+jets* backgrounds in the $e\mu$ sample, that results in a reduction of systematic uncertainties. The *Other VV* background in the $ee/\mu\mu$ samples are estimated by the MC simulations in this analysis. Thus, the validities of the *Other VV* models have been investigated using dedicated validation regions, which are described in section 8.3.2. These studies are keys of this analysis.

Analyses of the other categories (i.e. VBF-enriched, 7 TeV data corrected in 2011) are briefly described in chapter 11, where combined results are also given.

Chapter 3

The Large Hadron Collider

The Large Hadron Collider (LHC) is the world's largest proton-proton collider constructed at European Organization for Nuclear Research (CERN), where bunches of protons are accelerated to 7 TeV and collide head-on at center-of-mass energy at 14 TeV in its design. The LHC can reach unexplored energy scale (TeV) for various physics studies. Figure 3.1 shows a schematic view of the accelerator complex at the CERN. The LHC is supplied with protons from the injection chain; LINAC2 – PS-BOOSTER – PS – SPS. The protons, which are yielded from hydrogen gas, are pre-accelerated in LINAC2 up to a kinetic energy of 50 MeV. The PS-BOOSTER accelerates them to 1.4 GeV for the injection into the PS. The PS not only accelerates the proton beam to a total energy of up to 26 GeV but also prepares the bunch structure for the LHC. They are transferred to the SPS which finally accelerates the beam to the LHC injection energy of 450 GeV. The SPS was operated as a proton-antiproton collider in 1980's, and it contributed the discovery of the W and Z bosons.

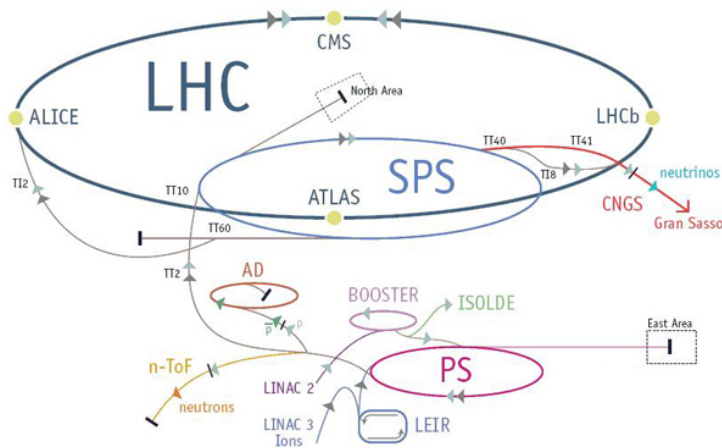


Figure 3.1: Schematic view of the CERN accelerator complex.

The main ring of the LHC is installed into the circular tunnel, which is almost 27 km in circumference and about 100 meters underground. The beam line is composed of accelerating cavities, super-conducting NbTi bending magnets and quadrupoles for beam control. The LHC accelerates the proton beam, which consists of 2808 bunches at full intensity. Each bunch contains about 10^{11} protons, then provides proton-proton collisions with a center-of-mass energy of 14 TeV and a very high number of collisions per unit time and area (luminosity, see section 3.2).

The LHC design parameters are summarized in table 3.1.

Table 3.1: The LHC design parameters [50].

Proton energy	7 TeV
Peak luminosity	$1.0 \times 10^{34} \text{ cm}^{-2}\text{sec}^{-1}$
Luminosity lifetime	10 hours
Number of bunches	2808
Bunch interval	24.95 nsec
Number of protons	1.15×10^{11} / bunch
Bunch length	77 mm
Beam radius	15.9 μm
Beam crossing angle	300 μrad

3.1 The LHC detectors

There are four collision points at the LHC. Accordingly, four particle detectors have been constructed in underground caverns. They are designed to record the particles originated from the collisions to perform various physics studies. Schematic overviews of the detectors are shown in figures 3.2 and 4.1.

- **ATLAS (A Toroidal LHC ApparatuS)**
The ATLAS is a general purpose detector that surrounds the collision point to record the particles coming from the collisions. The measurements such as the Higgs boson production and decay, also other SM processes, searches for new phenomena as well, are performed. Details of the detector are described in chapter 4.
- **CMS (Compact Muon Solenoid)**
The CMS is also a general purpose detector. A feature of the CMS detector is a very strong superconducting magnet of 4 Tesla magnetic field to perform precise momentum measurements for charged particles at very high momentum. This magnet is the largest solenoid of its type ever constructed. The tracker and calorimeter detectors are designed to be placed inside the coil, resulting in the overall detector is “compact” compared to detectors of similar weight.
- **LHCb**
The main purpose of the LHCb detector is to record the particles from B meson decays. A B meson contains a b quark and an anti- b quark, and its rare decays may be affected from the loop contributions from beyond SM particles. The LHCb detector is designed to reflect the fact that the B mesons and their decay particles are likely to stay close to the line of the beam pipe with a large boost. Thus, the detector stretches for 20 meters along the beam line covering the pseudorapidity (η , see section 4.1) of $2.0 < \eta < 5.0$, with its subdetectors stacked behind each other.
- **ALICE (A Large Ion Collider Experiment)**
The ALICE detector is optimized to study the nucleus-nucleus interactions, where the

formation of a new phase of matter, the quark-gluon plasma, is expected. The ALICE detector is designed to cope with the high particle densities in the nucleus-nucleus collisions. High detector granularity, low transverse momentum threshold of $p_T^{\min} \sim 0.15$ GeV and good particle identification capabilities up to 20 GeV are available.

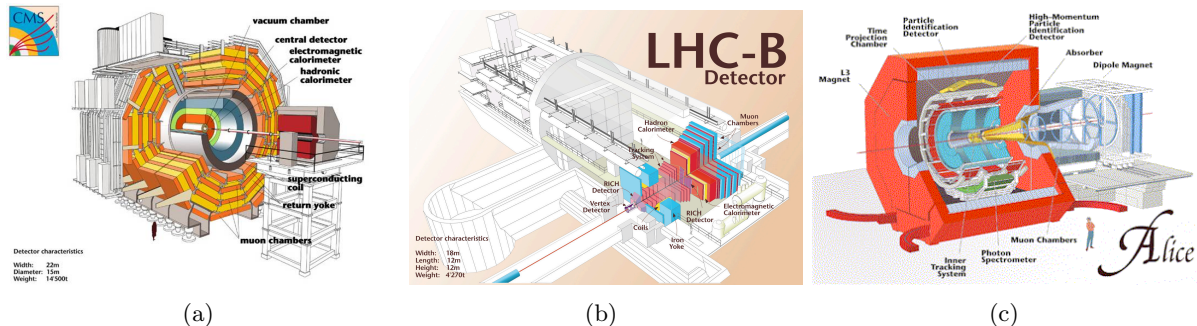


Figure 3.2: Schematic views of the detectors at the LHC. (a) CMS detector, (b) LHCb detector, (c) ALICE detector.

3.2 Luminosity dermiantion

One of the important parameters of colliders, luminosity \mathcal{L} , is introduced in this section. The number of events per second generated in the collisions, N , is given by:

$$N = \mathcal{L} \times \sigma, \quad (3.1)$$

where σ is the cross section for the process under study. The luminosity \mathcal{L} of a proton-proton collider can be expressed as follows [51]:

$$\mathcal{L} = \frac{\mu n_b f_r}{\sigma_{\text{inel}}}, \quad (3.2)$$

where μ is the average number of inelastic scattering per bunch crossing, f_r is the revolution frequency and n_b is the number of bunch pairs colliding per revolution. σ_{inel} is the proton-proton inelastic cross section. An experiment can measure the observed interaction rate per crossing, μ_{vis} , with several detectors and phase spaces. The luminosity can then be written as:

$$\mathcal{L} = \frac{\mu_{\text{vis}} n_b f_r}{\sigma_{\text{vis}}}, \quad (3.3)$$

where $\sigma_{\text{vis}} = \epsilon \sigma_{\text{inel}}$ is the total inelastic cross section multiplied by the efficiency of the particular detectors and phase spaces. The σ_{vis} may be obtained from the beam parameters directly. The absolute luminosity can be written in terms of the beam parameters as:

$$\mathcal{L} = \frac{n_b f_r n_1 n_2}{2\pi \Sigma_x \Sigma_y}, \quad (3.4)$$

where n_1 and n_2 are the number of protons per bunch, and Σ_x and Σ_y are the beam sizes of horizontal and vertical directions at the interaction point. The Σ_x and Σ_y are measured using

dedicated beam-separation scans, known as Van de Meer scans [52]. Combining equations 3.3 and 3.4, the σ_{vis} is given as:

$$\sigma_{\text{vis}} = \mu'_{\text{vis}} \frac{2\pi\Sigma_x\Sigma_y}{n_1n_2}, \quad (3.5)$$

where μ'_{vis} is the number of interactions when the $n_{1,2}$ and $\Sigma_{x,y}$ are determined. Now, the instantaneous luminosity at the operation is obtained by just counting μ_{vis} since other parameters in equation 3.3 are known.

3.3 Physics runs in 2010–2012

The LHC started proton-proton collisions for physics studies on 30 March 2010. The center-of-mass energy was 7 TeV and an integrated luminosity of 48.1 pb^{-1} was delivered in 2010. These data allowed to study the production of the W and Z bosons. One of the main features of operations in 2011 and 2012 was that a high bunch intensity (protons per bunch) was achieved. This gave a good instantaneous luminosity performance. The integrated luminosities of 4.46 fb^{-1} with 7 TeV and 22.8 fb^{-1} with 8 TeV were delivered. The data collected in 2011 and 2012 allows to measure the Higgs boson production over the various decay modes, and are called as “Run1 data” in this thesis. Figure 3.3 (a) shows the delivered luminosity versus time for 2010, 2011 and 2012, including Pb-Pb collisions. The peak instantaneous luminosity in 2012 reached to $7.73 \times 10^{33} \text{ cm}^{-2}\text{s}^{-1}$ as shown in figure 3.3 (c), and about five times larger data compared to 2011 were provided. However, this also led to considerable amount of interactions per bunch crossing (pileup) as shown in figure 3.3 (b). The pileup is one of the main challenges for triggers, data processing, as well as physics analyses at the hadron colliders.

3.4 Particle production rates in hadron colliders

Figure 3.4 shows the prediction of production cross sections for some benchmark processes at proton-proton and proton-antiproton colliders as a function of the center-of-mass energy. Processes proceeding via strong interactions have a much larger cross section than electroweak processes. It can be seen that the Higgs boson production is more than ten order of magnitude smaller than the total cross section. Therefore, the detectors are required to have capabilities to handle the total events rate, which is dominated by low- p_T inelastic (QCD) events, and to distinguish the signal in interest from other processes.

As seen in section 2.3, many of electroweak and QCD processes present in the SM could contribute to the $H \rightarrow WW^* \rightarrow \ell\nu\ell\nu$ analysis as backgrounds. Measurements of the production cross sections, which are fundamental parameters at the collider, for various SM processes have been performed by the ATLAS. Figure 3.5 shows a summary of SM production cross section measurements compared to the corresponding theoretical expectations. The observed data agree well with the expectations at NLO or higher order. This shows that the production processes in the SM are well understood in general.

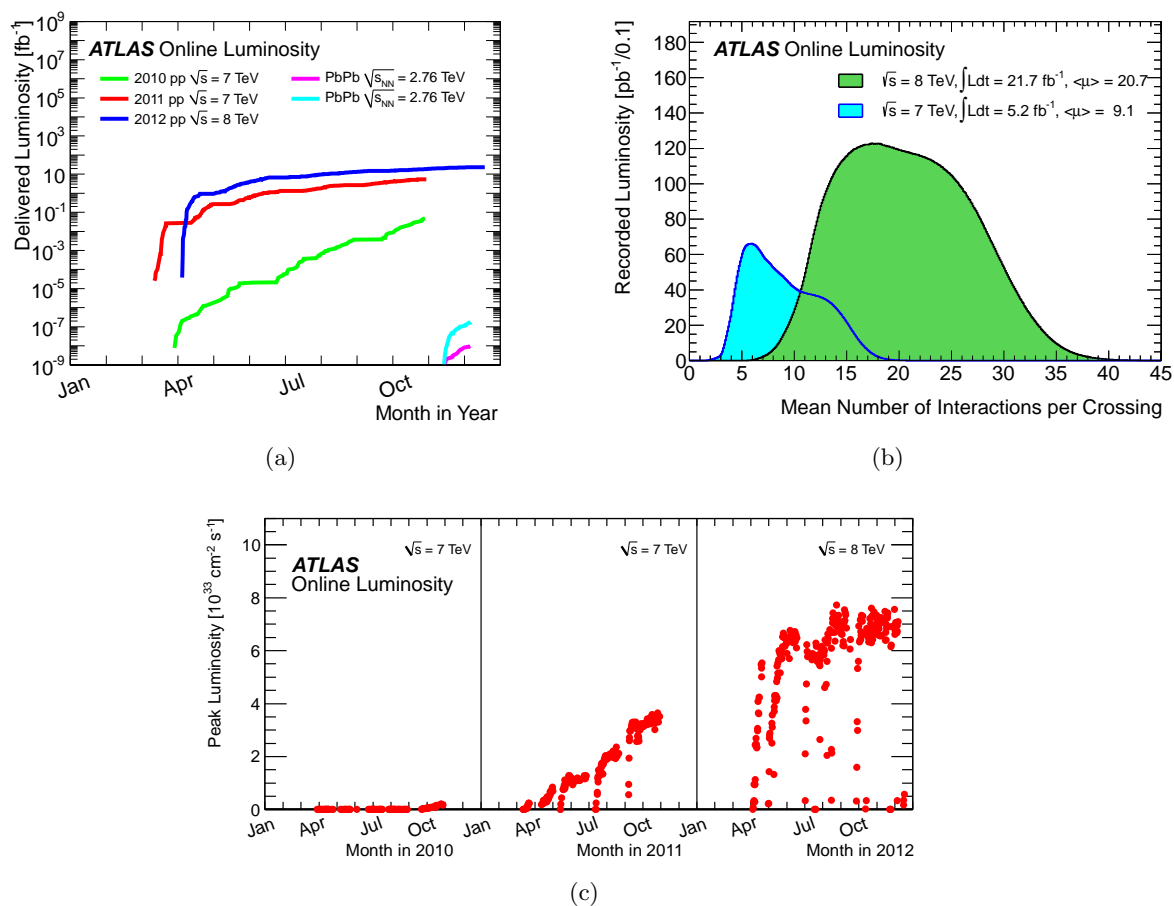


Figure 3.3: (a) Cumulative luminosity versus day delivered to ATLAS during stable beams and for proton-proton and Pb-Pb collisions in 2010, 2011 and 2012. (b) luminosity-weighted distribution of the mean number of interactions per crossing for the 2011 and 2012 data. (c) Peak instantaneous luminosity per day versus time during the proton-proton runs of 2010, 2011 and 2012 [53].

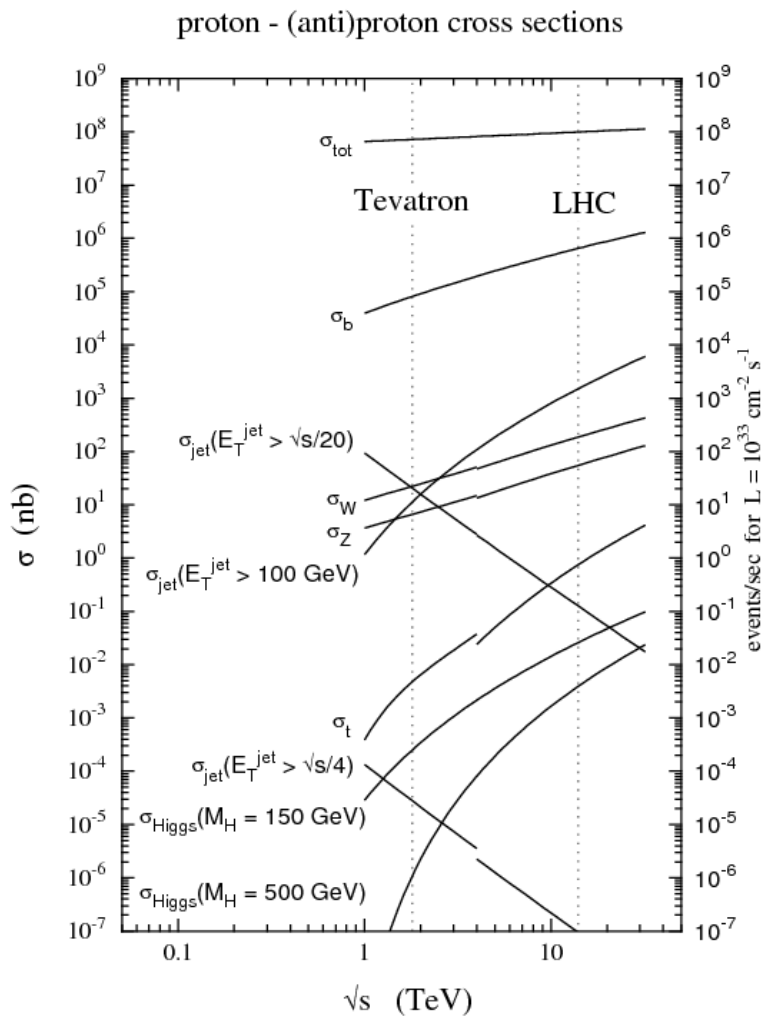


Figure 3.4: Predicted cross sections of proton-(anti)proton collisions as a function of center-of-mass energy. The energies at the Tevatron and LHC are indicated [54].

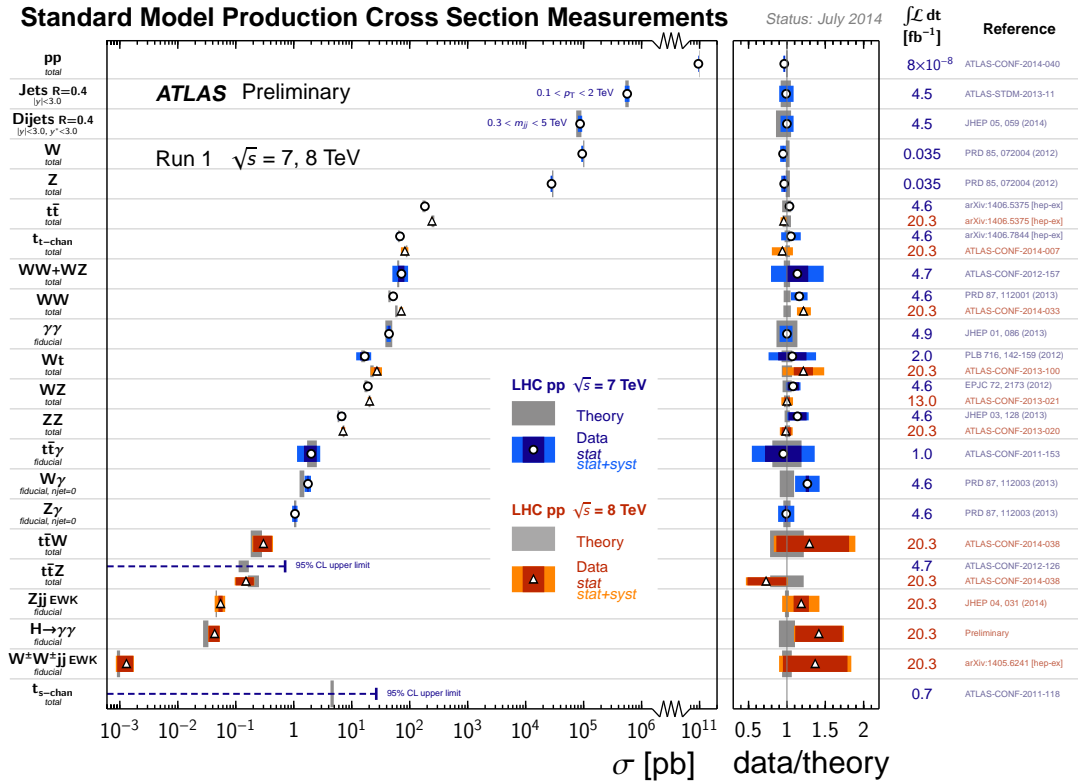


Figure 3.5: Summary of Standard Model total and fiducial production cross section measurements, corrected for leptonic branching fractions, compared to the corresponding theoretical expectations [55]. All theoretical expectations were calculated at NLO or higher.

Chapter 4

The ATLAS detector

Figure 4.1 shows a 3D view of the ATLAS detector, which is characterized by the hybrid system of superconducting magnets: a central solenoid surrounded by two endcap toroids and a barrel toroid. The ATLAS detector is 22 m in height, 44 m in length and its weight is about 7000 tons. The ATLAS detector was designed as follows to cover a broad spectrum of detailed physics studies at the LHC [57]:

- Precise electromagnetic calorimetry for electron and photon identifications and measurements;
- Full-coverage hadronic calorimetry for jet and missing energy measurements;
- Precise muon momentum measurements, with the capability of the measurements using the external muon spectrometer alone at high luminosity;
- Efficient tracking for lepton-momentum measurements and particle identifications for electrons, photons, τ -leptons and heavy-flavor decays;
- Large acceptance in pseudorapidity, related to the polar angle from the beam direction, with almost full azimuthal angle coverage everywhere; and
- Efficient triggering for particles of interest on the high total event rate at the LHC.

The identifications and measurements of particles are performed using combined information from various subdetectors. Subdetectors are categorized into three main components; inner tracker, calorimeter and muon spectrometer. The particles from the collisions can be distinguished by differences in their interactions with matters. Figure 4.2 shows a vertical cross section of the ATLAS detector, representing particle's behavior in each subdetector. Charged particles are bent by the solenoid magnet and detected by the inner trackers to measure their momentum. Electrons and photons are detected at the electromagnetic calorimeter through electromagnetic showers and identified by a presence of an associated track together with shapes of the shower. Strongly interacting particles such as pions, neutrons and protons are detected in both the electromagnetic and hadron calorimeters with hadron showers. Muons reach outside of the calorimeters since they deposit a little energy in the the calorimeters and have enough long life time. Muons are bent by the toroid magnets and detected at the muon spectrometers. Neutrinos cannot be detected, but their presence is inferred by observing a missing momentum in an event. Details of each subdetector are explained in this chapter.

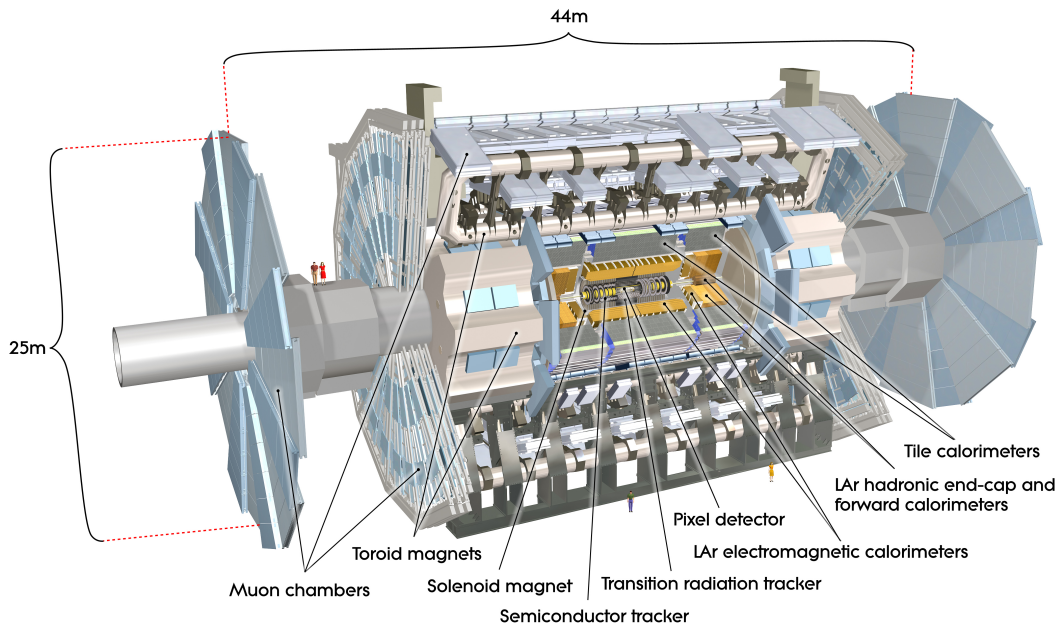


Figure 4.1: Schematic view of the ATLAS detector [56].

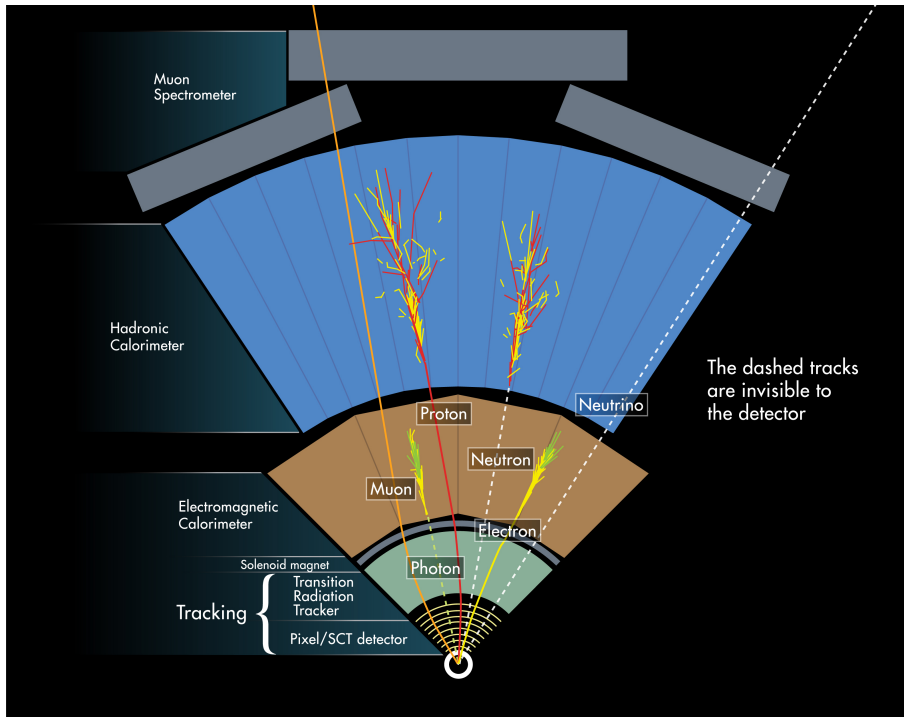


Figure 4.2: Particles's behavior in the ATLAS detector [56].

4.1 Definition of coordinates

A common coordinate system is used throughout the ATLAS. The interaction point is defined as the origin of the coordinate system, and the beam line is defined as z -axis whose positive direction points the LHCb detector. The positive x -axis points the center of LHC ring and the positive y -axis points upward. The x - y plane is referred to as the transverse plane to the beam axis. Particle momentum measured in the transverse plane is referred to as the transverse momentum, p_T . The transverse plane is often described in terms of r - ϕ coordinates. The azimuthal angle ϕ is measured from the x -axis around the beam line. The radial dimension, r , measures the distance from the beam line. The polar angle θ is defined as the angle from the positive z -axis, then pseudorapidity η is defined as $\eta = -\ln(\tan(\theta/2))$. The pseudorapidity is generally used at the hadron colliders since the distribution of number of particles as a function of η is basically flat. The distance ΔR in η - ϕ space is defined as $\Delta R = \sqrt{\Delta\eta^2 + \Delta\phi^2}$. Figure 4.3 illustrates the ATLAS coordinate system.

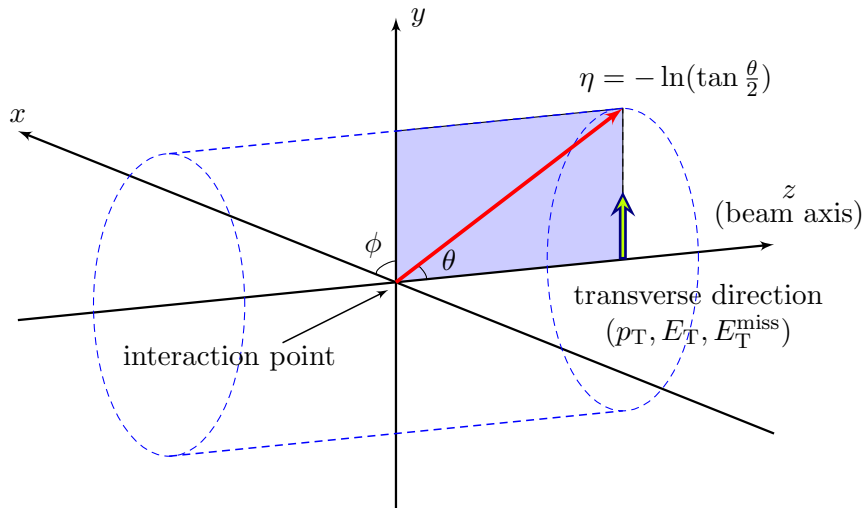


Figure 4.3: The ATLAS coordinate system.

Trajectories of charged particles can be described by five helix parameters in an ideal uniform magnetic field parallel to the z -axis. All quantities are measured at the point of closest approach to the nominal beam axis, $x = 0$ and $y = 0$:

- $1/p_T$: Reciprocal of the transverse momentum with respect to the beam-axis.
- ϕ : Azimuthal angle of the momentum direction in the transverse plane, where $\tan\phi = p_y/p_x$.
- d_0 : Transverse impact parameter, defined as the transverse distance to the beam axis at the point of closest approach.
- $\cot\theta$: Cotangent of the polar angle of the momentum direction, where $\cot\theta = p_z/p_T$.
- z_0 : Longitudinal impact parameter, defined as the z position of the track at the point of closest approach.

4.2 Magnets

The ATLAS magnet system consists of a solenoid, a barrel toroid and two endcap toroids as shown in figure 4.4. Combination of the barrel toroid with two inserted endcap toroids allows to make the magnetic field covering up to $|\eta| = 2.7$. Main parameters of the toroidal and solenoid magnets are summarized in table 4.1.

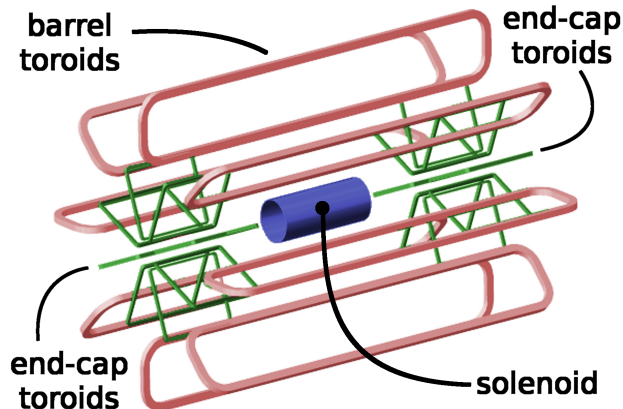


Figure 4.4: Schematic view of the ATLAS magnet system [58].

Table 4.1: Main parameters of the toroidal and solenoid magnets in the ATLAS magnet system [57].

	unit	Central solenoid	Barrel toroid	Endcap toroid
Overall dimensions:				
Inner diameter	m	2.44	9.4	1.65
Outer diameter	m	2.63	20.1	25.3
Axial length	m	5.3	25.3	5
Number of coils	-	1	8	8
Weight	Tons	5.7	830	239
Coils:				
Number of turns per coil	-	1173	120	116
Operating current	kA	7.6	20.5	20
Peak field	T	2.6	3.9	4.1
Conductor:				
(Al : Cu : NbTi)	-	28:1.3:1	19.1.3.1	15.6:0.9:1

4.2.1 Central solenoid

The central solenoid (figure 4.5 (a)) provides approximately 2 Tesla magnetic field with the inner trackers. The solenoid is 5.3 m long with a bore of 2.4 m and has a thickness of 45 mm. Since the central solenoid is installed in front of the electromagnetic calorimeters, it is designed to be as thin as possible to decrease particle scattering effects. Also the solenoid shares its vacuum vessel with the liquid argon calorimeter (see section 4.4.1) to minimize the inactive material. The

iron absorber of the hadron calorimeter (see section 4.4.2) and its girder structure function as a return yoke for this solenoid magnetic field. Figure 4.5 (b) shows the magnetic field provided by the central solenoid as a function of z .

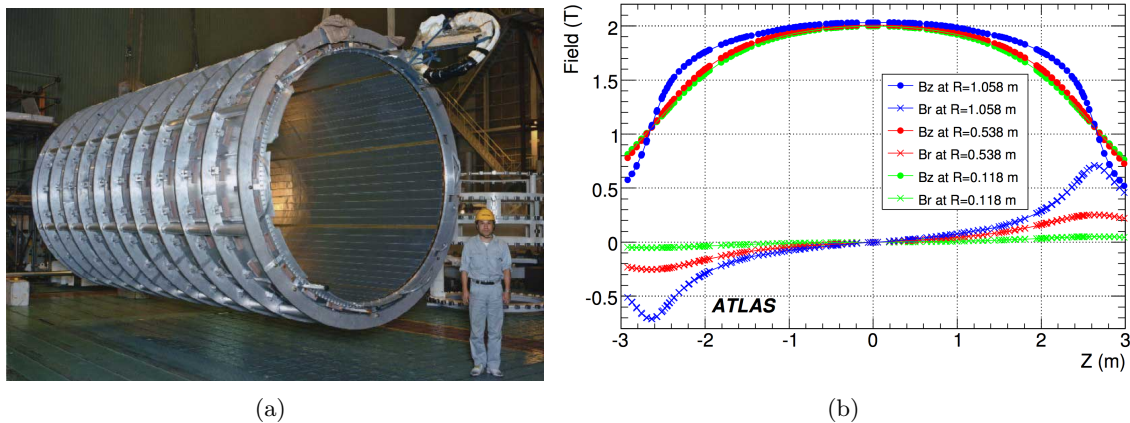


Figure 4.5: (a) Central solenoid magnet [56]. (b) Field (T) data obtained at $\phi = 20\pi/16$ [59].

4.2.2 Barrel and endcap toroids

The toroids magnets are designed to produce a large-volume magnetic field for the muon spectrometers. The open structure of the toroids allows to minimize the contribution of multiple scatterings to the muon momentum resolution. The barrel toroid (figure 4.6 (a)) consists of eight coils assembled radially and symmetrically around the beam axis. The size of the toroid is 25.3 m in length, with inner and outer diameters of 9.4 m and 20.1 m, respectively. Each endcap toroid (figure 4.6 (b)) also consists of eight coils, which are rotated in azimuth by an angle of 22.5 degree with respect to the barrel toroid coils to optimize the bending power, i.e. integrated magnetic field along a particle track, in the transition regions between the two toroids. The bending power is shown in figure 4.7 as a function of η . Typical bending powers are 3 Tm in the barrel region and 6 Tm in the endcap regions.

4.3 Inner trackers

The inner tracker (figure 4.8) is placed at the center of the ATLAS detector and inside the solenoidal magnetic field. The inner tracker detects the position where the charged particle passes very precisely, then provides robust pattern recognition, excellent momentum resolution, as well as very good vertex resolution (see section 6.1). The inner tracker consists of three detectors: silicon-pixel vertex-detector (Pixel), semi-conductor tracker (SCT) and transition radiation tracker (TRT). These three detectors are divided into a barrel part and two endcaps. The barrel parts consist of several cylindrical layers of sensors. The endcaps are composed of a series of disks or wheels of sensors. A layout of the Pixel, SCT and TRT is shown in figure 4.9. Main characteristics, including resolutions, of the detectors are given in table 4.2.

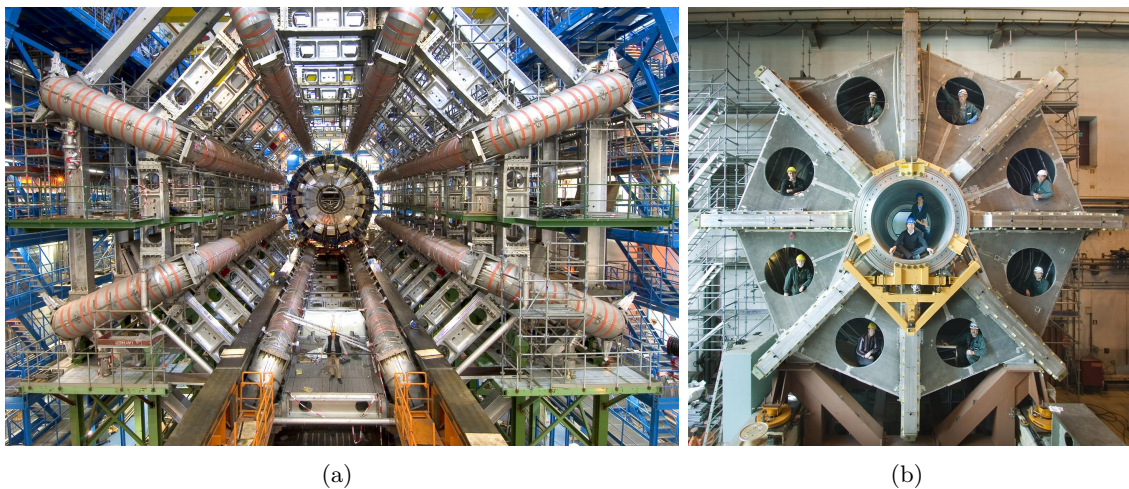


Figure 4.6: Toroid magnets for the barrel region (a) and endcap regions (b) [56].

Table 4.2: Main parameters of the ATLAS inner trackers [62].

	Element size	Resolution [μm]	Hits in barrel	radius of barrel layers [mm]
Pixel	$50 \mu\text{m} \times 400 \mu\text{m}$	10×115	3	50.5, 88.5, 122.5
SCT	$80 \mu\text{m}$	17	8	299, 371, 443, 514
TRT	4 mm	130	~ 30	from 554 to 1082

4.3.1 Silicon-pixel vertex-detector

The Pixel detector is designed to provide a very high granularity and high precision set of measurements at the position close to the interaction point, and determines impact parameter and vertex position resolutions. The Pixel detector is mechanically composed of modules, which is shown in figure 4.10 (a). One module is $16.4 \text{ mm} \times 60.4 \text{ mm}$, and consists of approximately 46,000 silicon sensors, $50 \mu\text{m} \times 400 \mu\text{m}$ each. Each module is read out by 16 front-end chips (FE in the figure). The Pixel modules form three barrel layers at radii of ~ 5 , 9 and 12 cm (1456 modules), respectively, and three endcap layers on each side between radii of 9 to 15 cm (288 modules). This layout provides typically three hits per track pointing to the interaction point. The inner-most barrel layer is called as “b-layer” since it provides the critical information used to reconstruct the vertices from b -quark decays. The thickness of each layer is expected to be about 2.5% of a radiation length at normal incident.

4.3.2 Semi conductor tracker

The SCT system provides typically eight precision measurements per track in the intermediate radial range, contributing to the measurement of momentum, impact parameter and vertex position, as well as providing good pattern recognition. Each SCT module in the barrel region consists of four strip type silicon detectors as shown in figure 4.11 (a). One silicon detector is $6.36 \text{ cm} \times 6.40 \text{ cm}$ with readout strips of $80 \mu\text{m}$ pitch. On each side of the module, two silicon detectors are wire-bonded together to form a 12.8 cm long strip. Two such detector pairs are

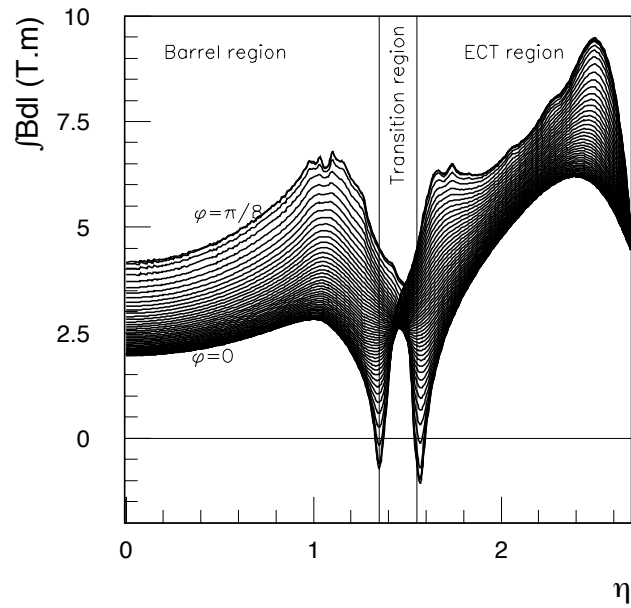


Figure 4.7: Toroid bending power for infinite momentum muons, $\int Bdl$, integrated between the inner and outer muons station as a function of η [61].

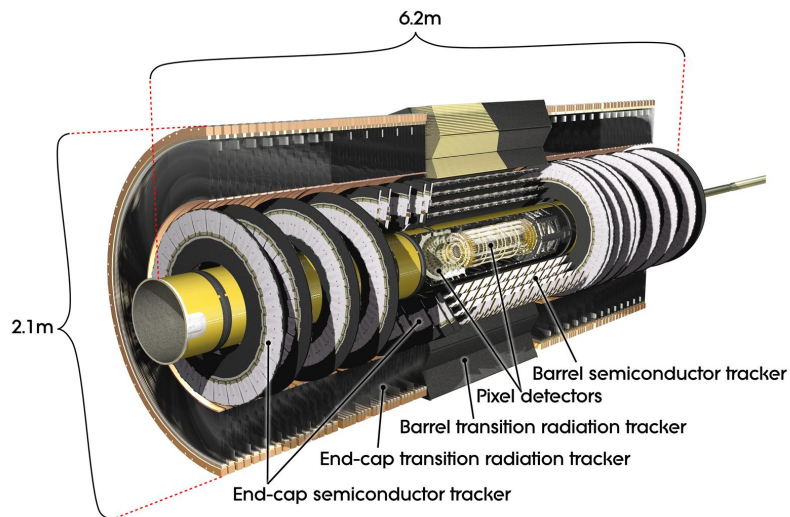


Figure 4.8: Overview of the inner tracker [56].

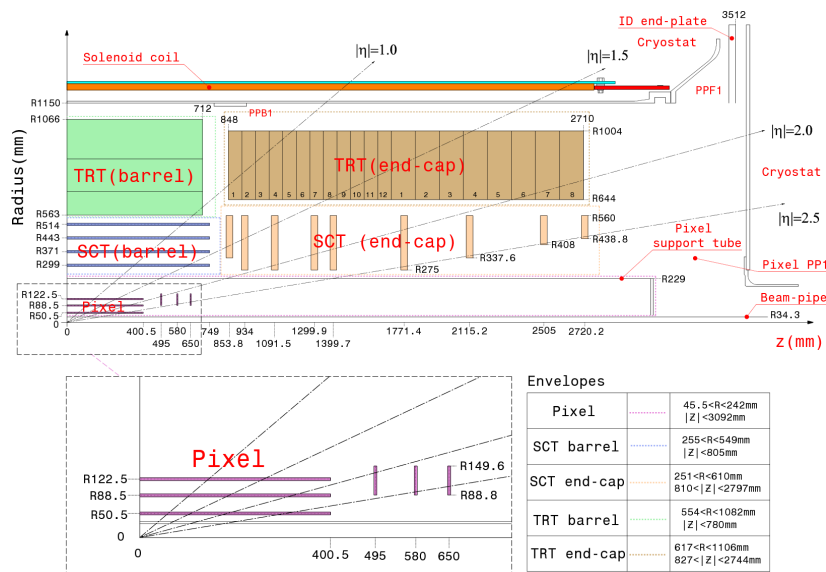


Figure 4.9: A cut-away view of the ATLAS inner detectors. The collision point locates at the left bottom corner of the figure [60].

then glued together back-to-back at a 40 mrad angle to obtain the z coordinate of tracks. These modules form four layers at radii of about 30, 37, 44 and 51 cm in the barrel. The endcap modules are very similar in construction but use tapered strips with one set aligned radially, and form nine layers as shown in figure 4.9. The SCT system contains 61 m² of silicon detectors, with 6.2 million readout channels.

4.3.3 Transition radiation tracker

The TRT is based on the use of straw detectors, which can operate at the expected high rates because of their small diameter and the isolation of the sense wire within individual gas volumes, then provide a good pattern recognition. Each straw is 4 mm in diameter and equipped with a 30 μ m diameter gold-plated tungsten wire. The barrel section contains about 50,000 straws, shown in figure 4.12, and the endcaps contain 320,000 radial straws. In addition to the tracking ability, TRT provides an electron identification capability by employing Xenon gas to detect transition radiation photons created in a radiator between the straws. A pion rejection factor at $p_T = 20$ GeV, for example, is 20 to 90 (depends on the η) with a 90% electron efficiency. Each channel provides two thresholds. This allows the detector to discriminate hits between the tracking, which pass the lower threshold, and the transition radiation, which pass the higher one.

4.4 Calorimeters

The ATLAS calorimeter (figure 4.13) is installed at outside of the inner tracker. The calorimeter measures the energy and position of charged and neutral particles. It consists of metal plates (absorber) and sensitive elements. Particles interact with the absorbers, then produce bunch of many particles, called shower (see figure 4.2), which is detected by the sensitive elements. Characteristics of the shower provide an identification of electrons, photons and hadron jets. The

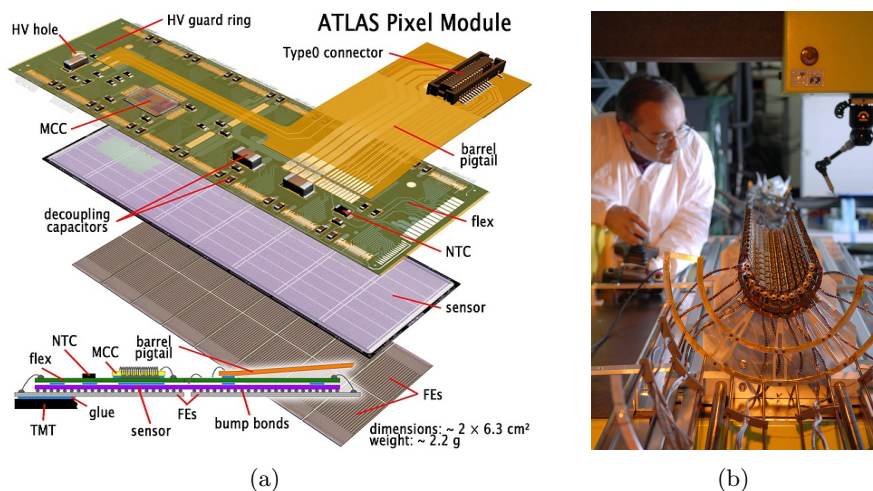


Figure 4.10: (a) Sketch of a ATLAS Pixel module [60]. (b) Picture of the b-layer in the Pixel detector [56].

calorimetry consists of an electromagnetic (EM) calorimeter covering the region $|\eta| < 3.2$ and a hadronic calorimeter covering $|\eta| < 5$. Each calorimeter is divided into several subsystem with different techniques and devices. Tables 4.3 summarizes basic parameters for the calorimeters.

4.4.1 Electromagnetic calorimeter

The ATLAS electromagnetic calorimeter is a sampling calorimeter with lead as the absorber and liquid argon as the sensitive elements, and measures the energy and position of electromagnetically interacting particles, electrons and photons being main examples. The lead and liquid argon are in layers with an accordion geometry as shown in figure 4.14. This geometry provides a complete ϕ coverage without azimuthal cracks. Each sampling cell point towards the interaction point over the η -coverage. The electromagnetic calorimeter is divided into a barrel part ($|\eta| < 1.475$) and two endcaps parts ($1.375 < |\eta| < 3.2$). The barrel part consists of two identical half-barrels, separated by a small gap (6 mm) at $\eta = 0$. The endcap calorimeter is mechanically divided into two coaxial wheels: outer wheel covering the region $1.375 < |\eta| < 2.5$ with three samplings in the longitudinal direction and an inner wheel covering the region $2.5 < |\eta| < 3.2$ with two samplings. The thickness of the absorber is optimized as a function of η in terms of the performance in energy resolution. The total thickness of the electromagnetic calorimeter is > 24 radiation length (X_0) in the barrel and $> 26 X_0$ in the endcaps. Typically achieved resolutions of the energy and direction are given as follows:

$$\frac{\Delta E}{E} = \frac{11.5\%}{\sqrt{E} \text{ (GeV)}} \oplus 0.5\%, \quad \Delta\theta = \frac{50 \text{ mrad}}{\sqrt{E} \text{ (GeV)}}. \quad (4.1)$$

4.4.2 Hadronic calorimeter

The ATLAS hadronic calorimeter is designed to measure the energy of hadrons, such as protons, neutrons and pions. The system is divided into three subdetectors: the iron scintillating-tile calorimeter (Tile) covering $|\eta| < 1.7$, the liquid argon calorimeter (HEC) covering $1.5 < |\eta| < 3.2$ and the high density calorimeter (FCAL) with a range $3.1 < |\eta| < 4.9$.

Table 4.3: Main parameters of the ATLS calorimeters [57]. Segmentation shows number of samplings along the longitudinal direction. Granularity is $\Delta\eta \times \phi$ plane.

EM Calo.	Barrel	Endcap	
Coverage	$ \eta < 1.475$	$1.375 < \eta < 3.2$	
Segmentation	3 samplings	3 samplings ($1.5 < \eta < 2.5$) 2 samplings (other)	
Granularity:			
Sampling1	0.003×0.1	0.025×0.1 ($1.375 < \eta < 1.5$) 0.003×0.1 ($1.5 < \eta < 1.8$) 0.004×0.1 ($1.8 < \eta < 2.0$) 0.006×0.1 ($2.0 < \eta < 2.5$) 0.1×0.1 ($2.5 < \eta < 3.2$)	
Sampling2	0.025×0.025	0.025×0.025 ($1.375 < \eta < 2.5$) 0.1×0.1 ($2.5 < \eta < 3.2$)	
Sampling3	0.05×0.025	0.05×0.025 ($1.5 < \eta < 2.5$)	
Radiation length (X_0)	> 24	> 26	
Hadronic Calo.	Barrel (Tile)	Endcap (HEC)	Forward (FCAL)
Coverage	$ \eta < 1.7$	$1.5 < \eta < 3.2$	$3.1 < \eta < 4.9$
Segmentation	3 samplings	4 samplings	3 samplings
Granularity:			
	0.1×0.1 (sampling1 and 2)	0.1×0.1 ($1.5 < \eta < 2.5$)	$\sim 0.2 \times 0.2$
	0.2×0.1 (sampling3)	0.2×0.1 ($2.5 < \eta < 3.2$)	
Interaction length (λ)	> 10	> 10	> 11

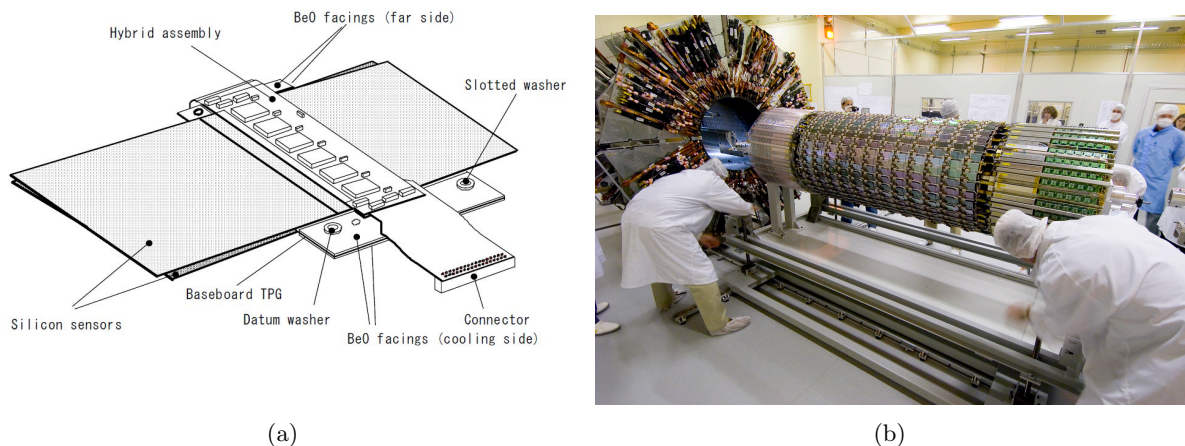


Figure 4.11: (a) Sketch of a ATLAS SCT module [60]. (b) Picture of the SCT detector [56].

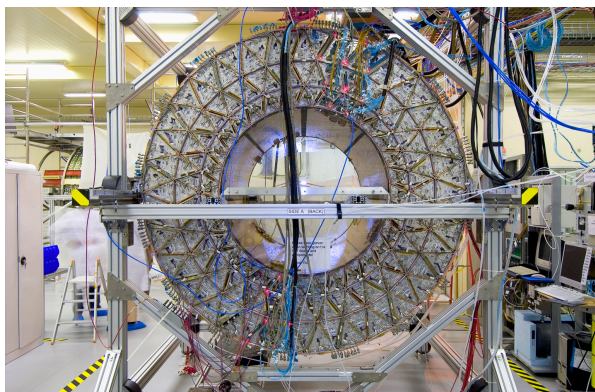


Figure 4.12: Picture of the TRT detector in the barrel region [56].

The Tile is composed of one barrel and two extended barrels. The gaps between the barrel and extend-barrels provide space for cabling and services from the inner-most detector. The scintillating tiles are inserted to an iron matrix as seen in figure 4.15 (a). The structure is periodic along the z axis. Both sides of the scintillating tiles are read out by wavelength shifting fibers into photo-multiplier tubes.

In the range up to $|\eta| = 4.9$, the liquid argon calorimeters, HEC and FCAL, take over the calorimetry due to the high radiation levels in the forward region. The geometrical design of the HEC is simpler than the electromagnetic calorimeter. One module of the HEC is shown in figure 4.15 (b); it has parallel copper plates as the absorber placed perpendicular to the beam line. The HEC consists of two equal-diameter independent wheels. The inner wheel uses 25 mm copper plates, while outer wheel uses the plates of 50 mm. The FCAL consists of a metal matrix with regularly spaced longitudinal channels filled with rods. The sensitive element (liquid argon) fills the gap between the rod and the matrix. This geometry, shown in figure 4.15 (c), allows for an excellent control of the gaps, which is required to be very small in the high rate environment in order to achieve the fast response to minimize noise effects. The FCAL consists of three longitudinal sections: the first one is made of copper matrix, while the other two are

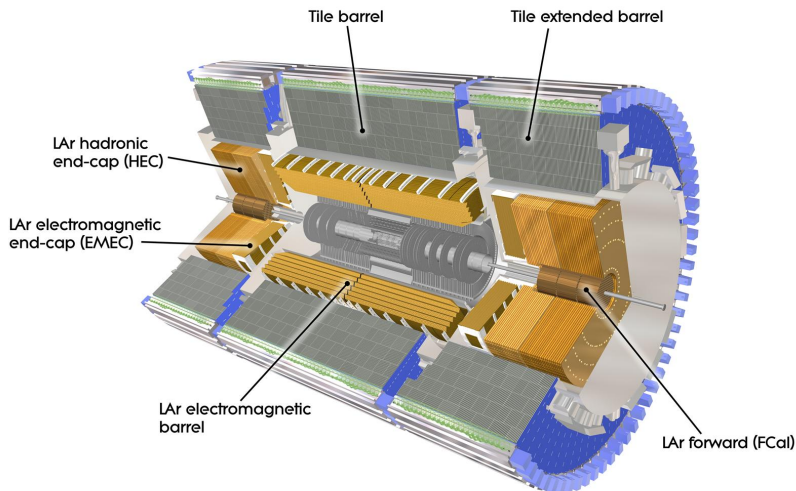


Figure 4.13: Overview of the calorimeters [56].

made out of tungsten matrix.

The total thickness is 11 interaction lengths (λ) at $\eta = 0$, including about 1.5λ from the outer support. The thickness of active calorimeter being close to 10λ is adequate to provide a good resolution for high energy jets. Together with the large η coverage, a good measurement of the missing transverse energy can be performed. The average jet energy resolution is given as follows:

$$\frac{\Delta E}{E} = \frac{50\%}{\sqrt{E \text{ (GeV)}}} \oplus 3\%. \quad (4.2)$$

4.5 Muon spectrometers

The muon spectrometer is designed to measure positions where muons pass through, then they provide direction, charge and momentum of muons by combining the hits as a track. Magnetic bending power to measure the momentum is provided by the barrel toroid and two endcap toroids. The muon spectrometer is composed of four sub systems: Monitored Drift Tube (MDT), Cathode Strip Chamber (CSC), Resistive Plate Chamber (RPC) and Thin Gap Chamber (TGC). The layout of the detectors are shown in figure 4.16 and 4.17. The MDT and CSC provide precise measurements of muon tracks. However, these chambers must operate at high levels of occupancy at the LHC. Thus, the RPC and TGC are designed to have fast response and low-occupancy for the level 1 trigger purpose (see section 4.6.1). The RPC and TGC also provide a second coordinate ϕ , which is orthogonal to the bending direction of muons. The table 4.4 summarizes the parameter of each subdetector.

4.5.1 Monitored Drift Tube

The MDT performs the precision measurement of the coordinate in the bending direction of muons. It covers area of $|\eta| < 2.7$. The basic detection elements of the MDT chamber are a cylindrical aluminum drift tube of 30 mm diameter and a tungsten-rhenium central wire of

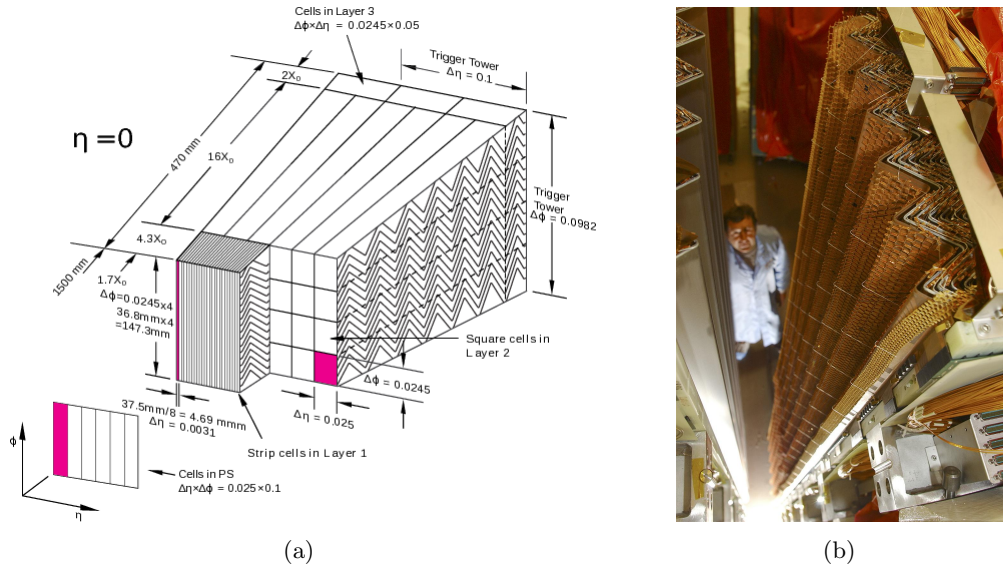


Figure 4.14: (a) Sketch of an module of the electromagnetic calorimeter [60]. (b) Picture of the accordion geometry [56].

Table 4.4: Overview of the muon detector instrumentation. Area covered refers to the total area of the sensitive region of each subsystem [57].

	Precision chamber		Trigger chamber	
	MDT	CSC	RPC	TGC
Number of chambers	1194	32	596	192
Number of readout channels	370,000	67,000	355,000	440,000
Area covered (m^2)	5500	27	3650	2900

$50\ \mu\text{m}$ diameter. The tubes are operated with a non flammable mixture of 93% Ar and 7% CO_2 at 3 bar absolute pressure, and have a total volume of $800\ \text{m}^3$. The wire is at a potential of 3080 V. The operating point is optimum with regard to the requirement of linearity in the drift space-time relation, a small occupation time and a small Lorentz angle. The single-wire resolution is approximately $80\ \mu\text{m}$.

The MDT chamber is an assembly of six or eight parallel layers of the tubes as shown in figure 4.18. This structure improves the resolution of the momentum beyond the single-wire limit. The support structure provide an accurate positioning of the drift tubes with respect to each other. Its deformations are monitored by a built-in optical system. This explains the name of “Monitored” drift tube. The MDT chambers form three stations in both barrel and endcap regions as shown in figure 4.17. The chamber of eight layers is used in the inner station, while six layers are used in the middle and outer stations.

4.5.2 Cathode Strip Chamber

The MDTs well satisfy the requirement for the precise measurement of muons, but the limit for its safe operation is at the counting rate of about $150\ \text{Hz}/\text{cm}^2$, which is exceeded in the region

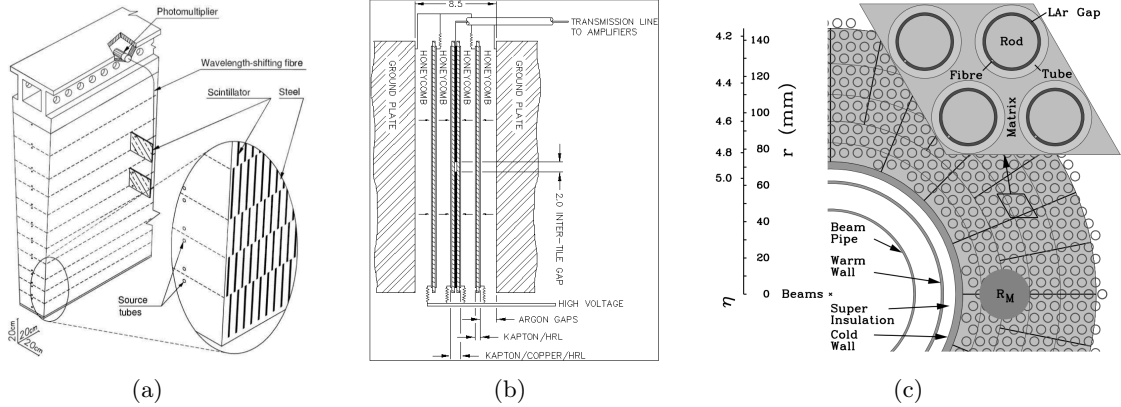


Figure 4.15: (a) Sketch of a module of the Tile [60]. (b) A module of the HEC [60]. (c) The structure of the FCAL [60].

$|\eta| > 2.0$ in the first layer of the endcaps. In this region, CSCs are used and covering up to $|\eta| < 2.7$ as shown in figure 4.17. Their operation is considered safe up to the counting rate of about 1000 Hz/cm^2 . The CSCs are multiwire proportional chambers with the anode wires oriented in the radial direction and with two types of readout cathode strips: one is perpendicular to the wires for providing the precision coordinate and the other parallels to the wires providing the transverse coordinate. The position of tracks is obtained by interpolation between charges on the neighboring cathode strips induced by the avalanche formed on the anode wire. The cathode readouts for the precision coordinate are segmented with pitch of 5.08 mm. Figures 4.19 shows a schematic view of the CSC chamber. The whole CSC system consists of two disks with eight chambers each. A chamber contains four CSC planes resulting in four independent measurements in η and ϕ for each track. A CSC plane reaches a resolution of about $60 \mu\text{m}$, to be compared with the $80 \mu\text{m}$ resolution of a MDT tube.

4.5.3 Resistive Plate Chamber

The RPC is a gas filled detector providing a typical space-time resolution of 1 cm and 1 nsec. The basic RPC unit (figure 4.20) has narrow gas gaps of 2 mm formed by two parallel resistive Bekelite plates. The electric field of about 4.9 kV/mm between the plates allows avalanches of ionization electrons. The signal is read out via capacitive couplings by metal strips on the outside of the plates. The strips are orthogonal to them on the other side: the η strips parallel to the MDT wires and provide the bending view for the trigger and the ϕ strips orthogonal to the MDT wires provide the second coordinate measurement for the offline pattern recognition. The RPC is operated with a gas mixture of $\text{C}_2\text{H}_2\text{F}_4/\text{Iso-C}_4\text{H}_{10}/\text{SF}_6$, which achieves relatively low operation voltage, non-flammability and low cost. The RPC has a simple mechanical structure, using no wires, therefore it is simple to manufacture, which is important for large detectors.

The RPC chambers form three trigger station as shown in figure 4.17. Each station consists of two independent layers, each measuring η and ϕ positions. The middle station is called the pivot plane, where the Level 1 trigger procedure starts.

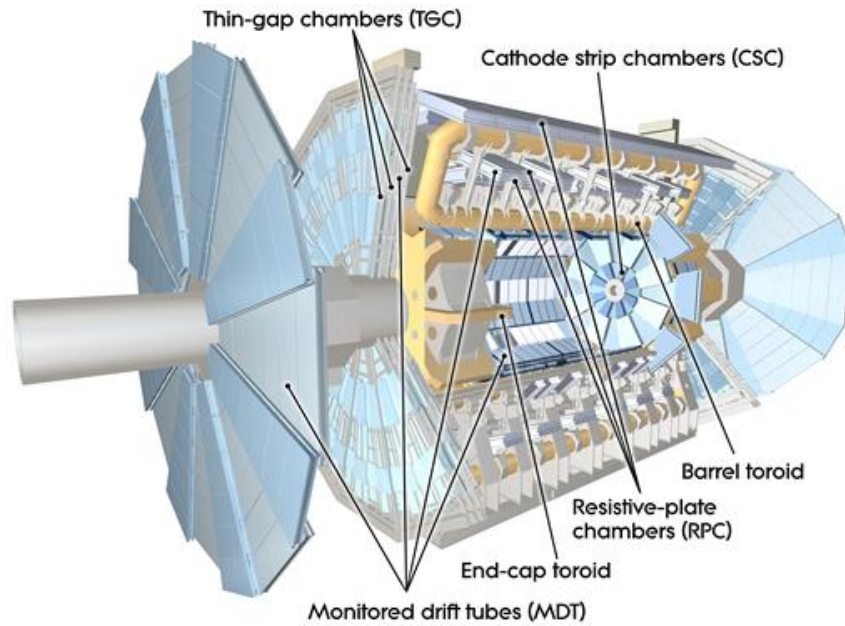


Figure 4.16: Overview of the muon spectrometer [56].

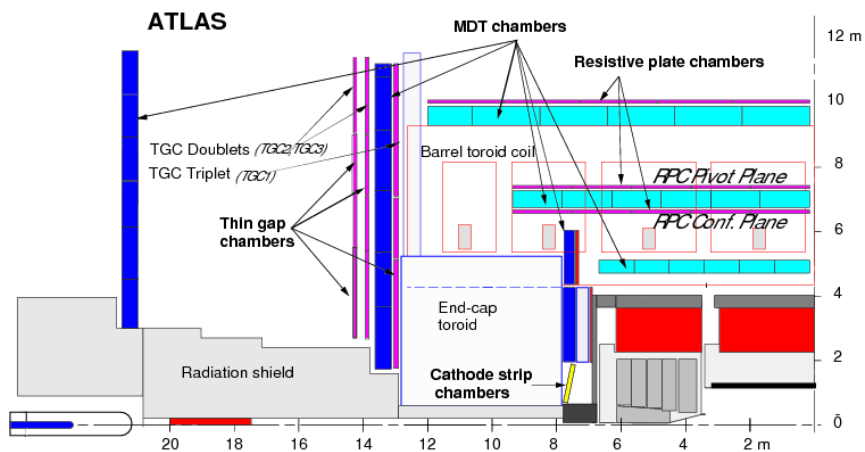


Figure 4.17: Schematic view of the muon spectrometer in the z - y projections [61].

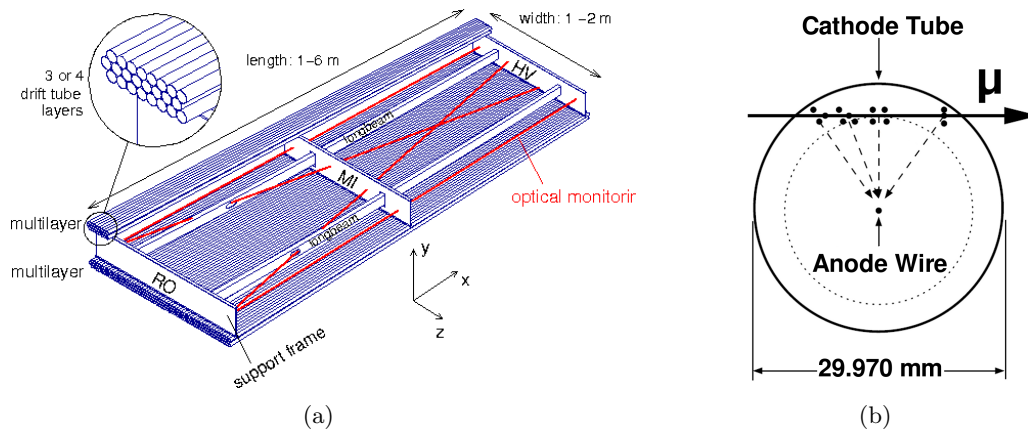


Figure 4.18: (a) Sketch of a chamber of the MDT [60]. (b) Illustration of a muon drift path in an MDT tube [58].

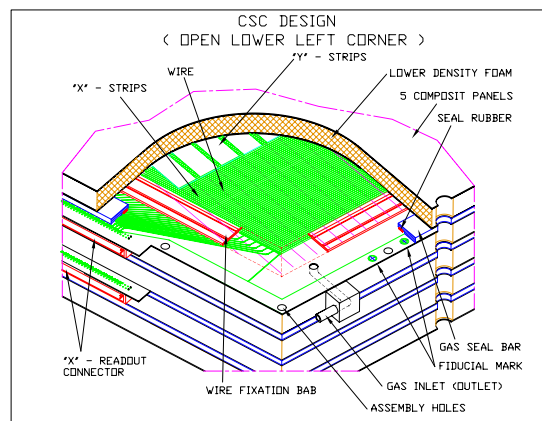


Figure 4.19: Schematic view of CSC [60].

4.5.4 Thin Gap Chamber

The TGC is similar to multi wire proportional chambers, except that the anode-to-anode pitch is larger than the cathode-to-cathode distance. The anode wires are arranged in parallel to the MDT wires, and the cathodes strips arranged orthogonal to the wires. The main dimensional characteristics of the TGC chamber are a cathode-to-cathode distance of 2.8 mm, a wire pitch of 1.8 mm and a wire diameter of $50 \mu\text{m}$ as shown in figure 4.21. The high electric field around the TGC wires and the small distance between the wires reduce the drift component of ionization clusters, and provides a very good time resolution. With the use of a highly quenching gas mixture of CO_2 (55 %) and $n\text{-C}_5\text{H}_{12}$ (45 %), the TGC allows the operation in saturated mode. This mode has number of advantages, for example,

- Small sensitivity to mechanical deformations;
- Small dependence on the incident angle up to 40 degree;
- Small Landau tails of the pulse-height distribution.

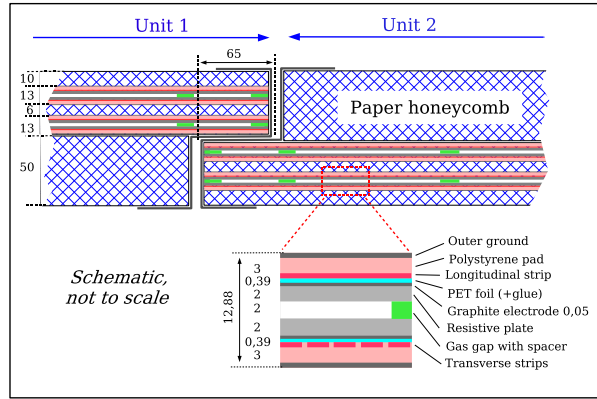


Figure 4.20: Cross section through a RPC chamber, where two units are joined to form a chamber [60].

The signals are read out by both wires and strips, and provide the information for the trigger. The strips are also used to measure the second coordinate for the offline reconstruction. The chamber resolutions are 2–6 mm in the R direction and 3–7 mm in the ϕ direction.

There are three stations with seven layers for the trigger propose as shown in figure 4.17. They are called TGC1, TGC2 and TGC3 from the inner side, respectively. The layers are arranged in one triplet (TGC1) and two doublet (TGC2 and TGC3). The TGC3 is referred as the pivot plane. The Level 1 trigger looks for tracks in a cone opening backwards from the hit on the pivot plane.

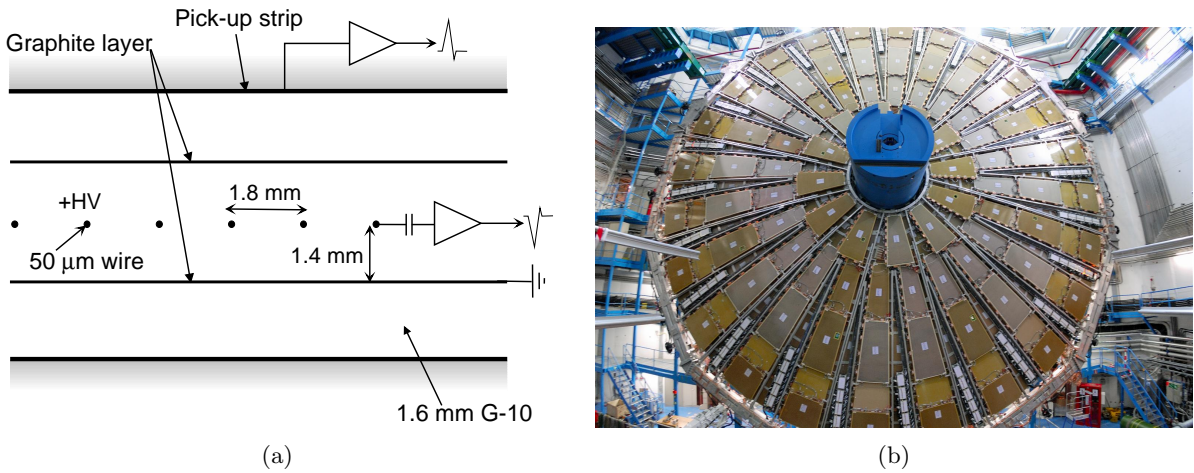


Figure 4.21: (a) Cross section through a TGC chamber [60]. (b) Overview of TGC system [56].

4.6 Trigger and data acquisition system

The interaction rate of protons at the design luminosity is expected to be about 1 GHz. The trigger system is required to select interesting events effectively over the background events.

The ATLAS trigger system consists of three levels of event selections: Level 1, Level 2 and Event filter. The Level 2 and Event filter together form the High Level Trigger (HLT). The Level 1 trigger is a hardware-based trigger by using custom-made electronics, while the HLT is a software trigger, which uses the information of Region of Interest (RoI) from the Level 1 trigger. The Data Acquisition System (DAQ) receives and buffers the event data from the dedicated readout electronics at the Level 1 trigger rate, and transfers the data to permanent event storages based on the HLT decision. Figure 4.22 shows a block diagram of the trigger and DAQ system. These trigger and DAQ systems are explained in this section.

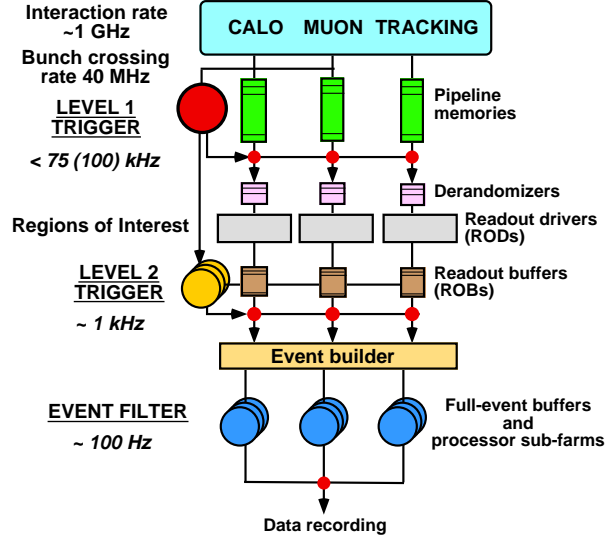


Figure 4.22: Block diagram of the ATLAS trigger and data acquisition system [57].

4.6.1 Level 1 trigger system

The Level 1 trigger performs the initial event selection and is designed to reduce the 40 MHz bunch-bunch crossing rate to 75 kHz (upgradable to 100 kHz). The latency, which is the time from the collision to the Level 1 trigger decision, is required to be less than $2.5 \mu\text{sec}$. The figure 4.23 shows a block diagram of the Level 1 trigger scheme. The Level 1 trigger decisions are performed based on the information from the calorimeters and muon spectrometers.

- **Calorimeter trigger:** All calorimeters (electromagnetic and hadronic; barrel, endcap and forward) are used for the Level 1 calorimeter triggers. The Level 1 calorimeter trigger aims to identify high transverse energy (E_T) electrons, photons and jets, as well as events with a large missing energy (E_T^{miss}) and a large total transverse energy. The Level 1 calorimeter trigger uses information from about 7000 trigger towers of reduced granularity (0.1×0.1 in $\Delta\eta \times \Delta\phi$ in most parts, but larger at high η). The system consists of three main components. The pre-processor digitizes the analogue signal, calculates transverse energies using the look up table, and transmit the data to the Cluster Processor (CP) and Jet/Energy-sum Processor (JEP) in parallel. The CP identifies electron, photon and τ -lepton candidates using the dedicated algorithm [66], which basically finds the 2×2 trigger tower of the electromagnetic calorimeter satisfying the programmable E_T threshold. The JEP works with jet elements, which are the sums of 2×2 trigger towers in the

electromagnetic calorimeters added to 2×2 trigger towers in the hadronic calorimeters. The energy sums of 2×2 , 3×3 or 4×4 jet elements are then compared to the thresholds. The JEP also provides the initial calculation for the E_T^{miss} and total E_T triggers.

- **Muon trigger:** The Level 1 muon trigger uses information from the RPC and TGC, and aims to identify high p_T muons. The principle of the algorithm to select the muons is based on a coincidence of hits on the different trigger stations. The p_T of muons are evaluated with the look up table, which uses the hit pattern of the pivot plane and the other station as inputs, and compared with six programmable thresholds. The results from the RPC and TGC are combined into one set of multiplicities of candidates for the six thresholds.

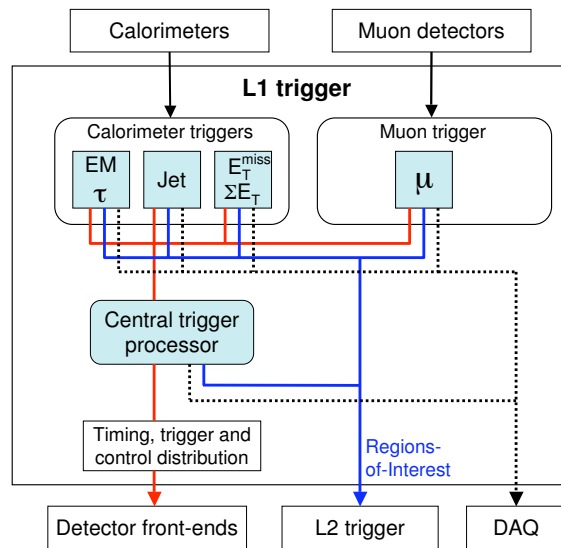


Figure 4.23: Block diagram of the Level 1 trigger system [60].

The Level 1 trigger decision is made by the Central Trigger Processor (CTP), which combines the information from the different trigger systems. Trigger menus can be programmable up to 256 distinct items for various performance and physics studies. The Level 1 trigger decision is distributed to the detector front-end and DAQ system to handle the buffered data. While the Level 1 trigger decision at the CTP is based only on whether the multiplicity of trigger objects satisfy the criteria, information about the geometric position of trigger objects is retained in the calorimeter and muon trigger processor until the trigger decision is made. This information is called as RoI, and sent to the HLT when the Level 1 trigger is accepted.

4.6.2 HLT and DAQ system

Main components of the HLT and DAQ systems are: readout system, Level 2 trigger, event building and Event filter as shown in figure 4.22. As the start of the readout system, the event data are buffered in memories located on the detector-specific front-end electronics during the latency of the Level 1 trigger selection. Event data selected by the Level 1 trigger are read out into the detector-specific readout drivers (RODs) and then into readout buffers (ROBs), where a large number of front-end electronics channels are multiplexed into each ROB. The Level 2

trigger is performed using the information stored in the ROBs, where all detector information is available.

- **Level 2 trigger:** The Level 2 trigger aims to achieve further reduction of the event rate by using the all detector information. The trigger rate of about 3.5 kHz and the average processing time of 40 msec are required. The Level 2 trigger makes use of RoI provided by the Level 1 trigger. The Level 2 trigger thus selectively access the data on the ROBs, which is associated to the RoI. Hence, the process time is reduced since only a few percent of full data is required. It is also possible to access to full event data if needed. In case of the calorimeter triggers, the rejection power at the Level 2 trigger comes from using the full granularity calorimeter information, and requiring a presence of the track in the inner trackers for charged trigger objects. For the muon trigger, high resolution of the muon p_T compared to the Level 1 trigger is available by using the precision muon chamber (MDT) and inner trackers.

Events accepted by the Level 2 trigger are assigned to the event builder. The event builder collects the event data from the readout system and assembles the event as a single formatted data structure so that the ATLAS standard reconstruction and analysis applications can be performed. The full event structure is sent to the Event filter for the final event selection.

- **Event filter:** The final event selection is performed by the Event filter, which reduces the event rate further to 200 Hz by using the ATLAS standard reconstruction algorithms (see chapter 6). The rejection power of the Event filter comes from, for example, the use of complex algorithms and criteria which can not be performed at the Level 2 trigger due to the limited processing time.

The events passed the Event filter are recorded to the mass storage for subsequent full offline analyses. The output data rate is approximately 100 MB/s if the full event data are to be recorded.

Chapter 5

Data samples

The LHC provided the proton-proton collisions for physics analyses during 2010–2012 as described in section 3.3. In this thesis, the Higgs boson production measurement in the $H \rightarrow WW^* \rightarrow l\nu l\nu$ decay channel is performed using the 2012 collision data at $\sqrt{s} = 8$ TeV. A description of this 8 TeV data is presented in this chapter. Monte Carlo samples used to model the signal and background productions in the analysis are also described.

5.1 Collision data

In 2012, the LHC delivered the data corresponding to an integrated luminosity of 22.8 fb^{-1} at $\sqrt{s} = 8$ TeV. The ATLAS succeeded in recording 21.3 fb^{-1} of the delivered luminosity as shown in figure 5.1. The recorded luminosity reflects the data acquisition inefficiency during stable beams. The recorded data are rejected for physics analyses if the relevant detectors are not working correctly. This requirement is called “data quality”. The system of data quality assessment is described in reference [63]. The resulting integrated luminosity is 20.3 fb^{-1} .

The ATLAS experiment records data with triggers as described in section 4.6. In this analysis, the data collected by electron or muon triggers with the lowest p_T thresholds without pre-scaling is used, where “pre-scale” means an artificial random data drop on the trigger decision to reduce the total trigger rate. Table 5.1 summarizes the thresholds of the triggers. To increase the trigger acceptance, the di-lepton triggers, which allow the lower threshold than the single lepton trigger by requiring multiple leptons, are used together with the single lepton triggers. The trigger efficiencies on data are measured using a tag and probe method with $Z \rightarrow ee/\mu\mu$ candidates:

- **Z tag and probe method:** In this method, an electron or a muon pair in an event is required to be opposite charge and have an invariant mass close to the Z boson mass. With this requirement, pure prompt leptons (from the Z decay) are selected. In addition, one of the two leptons (called tag lepton) is required firing the trigger. Then, the other lepton (called probe lepton) becomes an unbiased lepton for the trigger efficiency measurement on the data. The trigger efficiency is defined as follows:

$$\text{Trigger efficiency} = \frac{\text{Number of probe leptons firing the trigger}}{\text{Number of probe leptons}} \quad (5.1)$$

The reconstructed leptons (see chapter 6) are used as the probe leptons. This trigger efficiency thus describes the relative efficiency with respect to the reconstructed leptons.

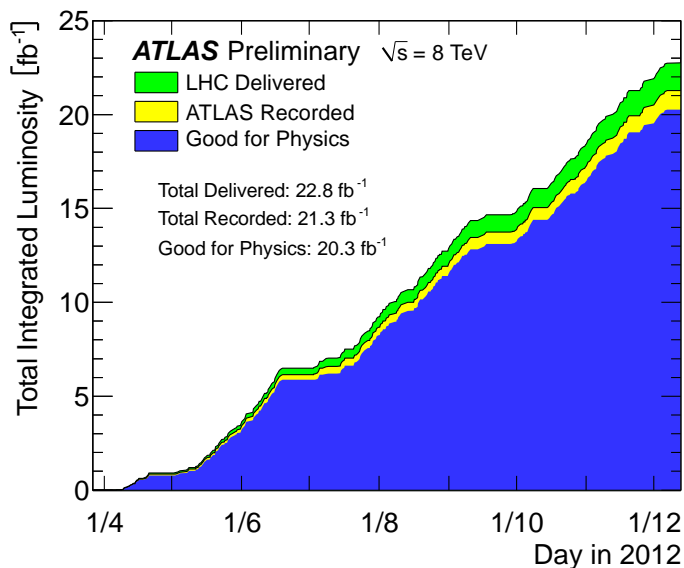


Figure 5.1: Cumulative luminosity versus time delivered by the LHC (green), recorded by ATLAS (yellow), and certified to be good quality data (blue) during stable beams for proton-proton collisions at 8 TeV center-of-mass energy in 2012 [53].

This Z tag and probe method is also used in reconstruction and selection efficiency measurements by changing the probe lepton criteria.

For electrons, the single lepton trigger efficiency is approximately 95%. For muons, the single lepton trigger efficiency varies with η and is approximately 70% for $|\eta| < 1.05$ and 80% for $|\eta| > 1.05$. Figure 5.2 shows the efficiencies for these single lepton triggers.

5.2 Monte Carlo samples

To evaluate the signal and background contributions into the $H \rightarrow WW^* \rightarrow l\nu l\nu$ analysis, detailed theoretical calculations and Monte Carlo simulations are necessary. Generators to produce the Monte Carlo samples are summarized in table 5.2. Events of the W +jets and QCD processes are not listed since these backgrounds are estimated with a data-driven method. For most processes, separate programs are used to generate the hard scattering process (matrix element) and to model the parton shower, which accounts for additional QCD radiations, and hadronization process, which forms hadrons out of quarks and gluons. Figure 5.3 shows the scheme of the simulation for the main generators used in the analysis. The POWHEG generator [67], which is used in most cases, provides the modeling of the hard scattering with NLO calculation, then the parton shower and hadronization processes are modeled using PYTHIA6 [70] or PYTHIA8 [71]. The ALPGEN [68] and SHERPA [69] are also used in case higher parton multiplicities are important. The ALPGEN generates multiparton hard processes at the matrix element level based on LO calculation. Then the partons are passed to HERWIG [72] for the parton shower and hadronization. The SHERPA also can generate multiparton processes with LO calculation, and can treat the parton shower and hadronization processes. Input parton distributions are taken from CT10 [73] for the POWHEG and SHERPA samples and CTEQ6L1 [74] for the ALPGEN. The

Table 5.1: Trigger summary. For single lepton triggers, the “i” means that an isolation requirement of $p_{\text{Tcone}}/p_{\text{T}} < 0.1$ (see section 6.6) which is looser than the offline lepton requirement, is applied at the HLT in order to reduce the trigger rate. For di-lepton triggers, the pair of thresholds corresponds to the leading and sub-leading lepton, respectively.

	p_{T} threshold [GeV]	Name
Single lepton		
electron	24i	EF_e24vhi_medium1
	60	EF_e60_medium1
muon	24i	EF_mu24i_tight
	36	EF_mu36_tight
Di-lepton		
electron + electron	12 and 12	EF_2e12Tvh_loose1
muon + muon	18 and 8	EF_mu18_tight_mu8_EFFS
electron + muon	12 and 8	EF_e12Tvh_tmedium1_mu8

Z +jets samples are weighted to MRSTMCAL PDF set [75]. Finally, the detector response is simulated using either GEANT4 [76] or a GEANT4-based fast simulation [77]. The fast simulation uses a parametrized calorimeter response to reduce the process time.

The total cross section, MC generator and uncertainties for the signal process are described in section 5.2.1. Also the cross section and MC samples for the background processes are described in section 5.2.2. Various methods to obtain event weights to improve the modeling are also provided in section 5.2.3.

5.2.1 Signal samples

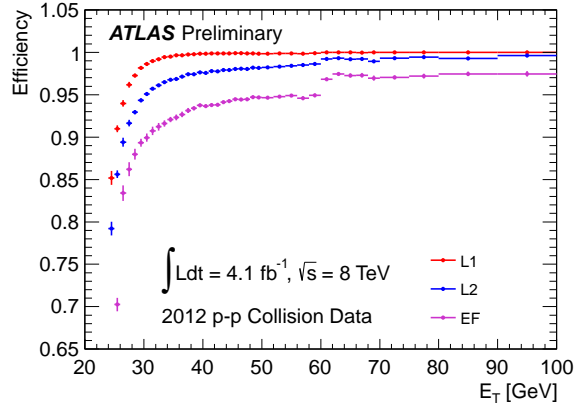
The leading Higgs boson production at the LHC is the ggF production mode as described in 2.1.2. The total cross section of the ggF mode is calculated at next-to-next-to-leading order (NNLO) in QCD, and next-to-leading order (NLO) electroweak corrections are applied, as well as resummation of the soft QCD radiation is performed to next-to-next-to-leading-log (NNLL). These calculations are detailed in references [78–80]. The total production cross section times branching ratio is shown in table 5.2. The uncertainty on the total production cross section is approximately 10% in total, with contributions from the QCD scale variations (7.5%) and the parton distribution function (7.2%) as described in section 2.1.2.

The POWHEG generator matched to the PYTHIA8 is used to simulate the $gg \rightarrow H \rightarrow WW^* \rightarrow \ell\nu\ell\nu$ process, and also used to evaluate the jet multiplicity for the analysis categorization. The POWHEG MC is based on NLO calculation with finite quark masses and includes electroweak corrections at NLO. The Higgs boson p_{T} in POWHEG is reweighted to match the prediction of the NNLO+NNLL calculation given by the HRES2.1 program [81].

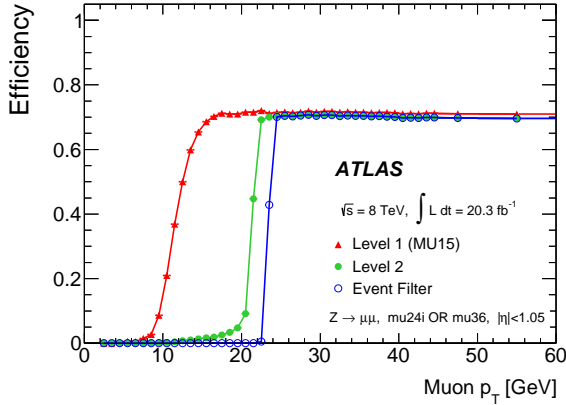
Figure 5.4 shows the simulated jet multiplicity at reconstruction level for $gg \rightarrow H + X$ process, where H decays to $\ell\nu\ell\nu$ and X may contain jets. An uncertainty on this jet multiplicity distribution is evaluated using the jet-veto efficiency (JVE) method [82]. This method assumes the uncertainty on the total cross section, σ_{tot} , is uncorrelated to the uncertainties on JVEs, where the JVEs define the efficiency of no jets being observed in a signal event with a given p_{T} cut, ϵ_0 , and also the efficiency of one jet being observed in an event with $n_j \geq 1$, ϵ_1 . The exclusive jet cross sections in each jet bin, $\sigma_{n=0,1,\geq 2}$, at parton level are given with these JVEs

Table 5.2: Monte Carlo samples used to model the signal and background processes. The corresponding cross section times branching fraction is quoted at $\sqrt{s} = 8$ TeV.

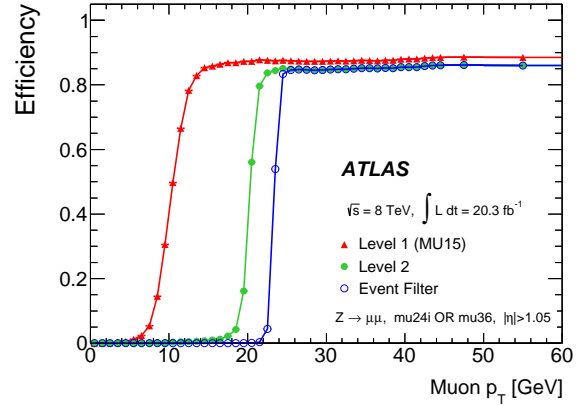
Process	Generator	$\sigma \cdot Br$ (8 TeV) (pb)
Signal		
ggF $H \rightarrow WW^*$	POWHEG+PYTHIA8	0.435
VBF $H \rightarrow WW^*$	POWHEG+PYTHIA8	0.0356
VH $H \rightarrow WW^*$	PYTHIA8	0.0253
WW		
$q\bar{q} \rightarrow WW^*$	POWHEG+PYTHIA6	5.68
$gg \rightarrow WW^*$	GG2WW	0.196
$q\bar{q} \rightarrow WW^*$ (for 2j ggF-enriched)	SHERPA	5.68
VBS $WW^* + 2$ jets	SHERPA	0.0397
Top quarks		
$t\bar{t}$	POWHEG+PYTHIA6	26.6
tW	POWHEG+PYTHIA6	2.35
$tq\bar{b}$	ACERMC+PYTHIA6	28.4
$t\bar{b}$	POWHEG+PYTHIA6	1.82
Other VV		
$W\gamma$ ($p_T^\gamma > 7$ GeV)	ALPGEN+HERWIG	369
$W\gamma^*$ ($m_{\ell\ell} < 7$ GeV)	SHERPA	12.2
WZ ($m_{\ell\ell} > 7$ GeV)	POWHEG+PYTHIA8	12.7
VBS $WZ + 2$ jets ($m_{\ell\ell} > 7$ GeV)	SHERPA	12.2
$Z\gamma$ ($p_T^\gamma > 8$ GeV)	SHERPA	163
ZZ ($m_{\ell\ell} > 4$ GeV)	POWHEG+PYTHIA8	0.733
$ZZ \rightarrow \ell\nu\nu$ ($m_{\ell\ell} > 4$ GeV)	POWHEG+PYTHIA8	0.504
Z+jets		
Z	ALPGEN+HERWIG	16500
VBF $Z + 2$ jets ($m_{\ell\ell} > 7$ GeV)	SHERPA	5.36



(a)



(b)



(c)

Figure 5.2: (a) Efficiencies of e24vhi_medium1 or e60_medium1 triggers at each Level 1, Level 2 and Event Filter with respect to the reconstructed Medium electrons (see section 6.2) as a function of E_T [64]; (b,c) Efficiencies of mu24i_tight or mu36_tight triggers with respect to the reconstructed combined muon (see section 6.3) as a function of p_T , separately for the barrel ($|\eta| < 1.05$) and endcaps ($|\eta| > 1.05$) regions [65].

as follows:

$$\sigma_0 = \epsilon_0 \sigma_{\text{tot}}, \quad \sigma_1 = \epsilon_1 (1 - \epsilon_0) \sigma_{\text{tot}}, \quad \sigma_{\geq 2} = (1 - \epsilon_0)(1 - \epsilon_1) \sigma_{\text{tot}}. \quad (5.2)$$

Three calculations of the jet veto efficiencies are defined based on ratios of cross sections as follows:

$$\epsilon_0^{(a)} = 1 - \frac{\sigma_{\geq 1}^{\text{NLO}}}{\sigma_{\text{tot}}^{\text{NNLO}}}, \quad \epsilon_0^{(b)} = 1 - \frac{\sigma_{\geq 1}^{\text{NLO}}}{\sigma_{\text{tot}}^{\text{NLO}}}, \quad \epsilon_0^{(c)} = 1 - \frac{\sigma_{\geq 1}^{\text{NLO}}}{\sigma_{\text{tot}}^{\text{LO}}} + \left(\frac{\sigma_{\text{tot}}^{\text{NLO}}}{\sigma_{\text{tot}}^{\text{LO}}} - 1 \right) \frac{\sigma_{\geq 1}^{\text{LO}}}{\sigma_{\text{tot}}^{\text{LO}}}, \quad (5.3)$$

$$\epsilon_1^{(a)} = 1 - \frac{\sigma_{\geq 2}^{\text{NLO}}}{\sigma_{\geq 1}^{\text{NNLO}}}, \quad \epsilon_1^{(b)} = 1 - \frac{\sigma_{\geq 2}^{\text{NLO}}}{\sigma_{\geq 1}^{\text{NLO}}}, \quad \epsilon_1^{(c)} = 1 - \frac{\sigma_{\geq 2}^{\text{NLO}}}{\sigma_{\geq 1}^{\text{LO}}} + \left(\frac{\sigma_{\geq 1}^{\text{NLO}}}{\sigma_{\geq 1}^{\text{LO}}} - 1 \right) \frac{\sigma_{\geq 2}^{\text{LO}}}{\sigma_{\geq 1}^{\text{LO}}}, \quad (5.4)$$

where $\sigma_{\geq 1} = \sigma_1 + \sigma_{\geq 2}$. The comparison of the three calculations at different orders in QCD provides an estimate of the perturbative uncertainty on the jet veto. For the efficiency ϵ_0 of the

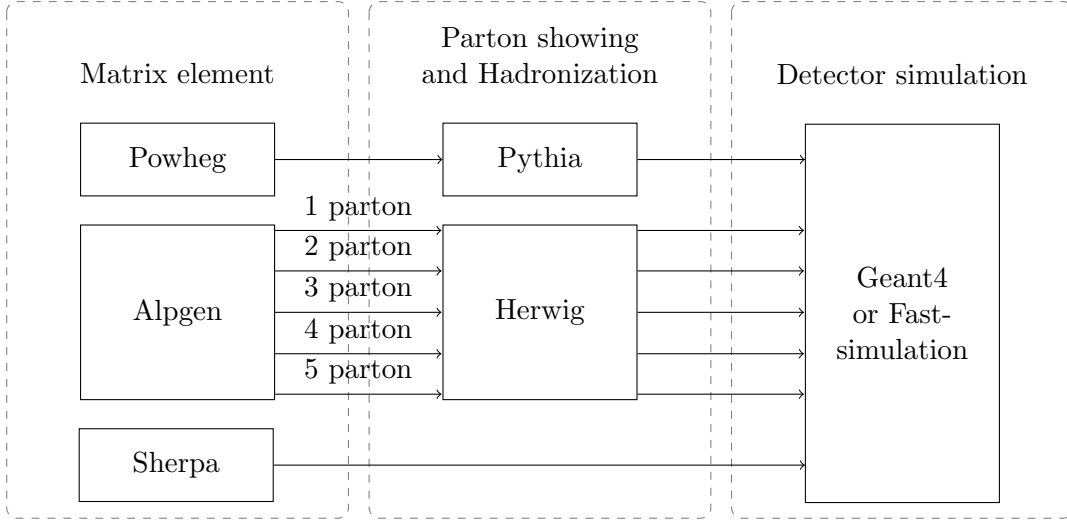


Figure 5.3: Simulation flow. The Alpgen samples are generated for each number of patrons at the matrix element level, and processed separately.

jet veto that defines the $n_j = 0$ category, the central value is evaluated at the NNLO with NNLL resummation. The uncertainty is taken from the maximum difference of the other calculations and the variations by the QCD scale. The obtained results using JETVHETO computation [83] is shown in figure 5.5 (a), along with the POWHEG+PYTHIA8 prediction. The uncertainty is 11% at a jet $p_T = 25$ GeV, which is the threshold used in the analysis. For the efficiency of vetoing an additional jet ϵ_1 , the central value is estimated to be the average of $\epsilon_1^{(b)}$ and $\epsilon_1^{(c)}$ since a full calculation of $\sigma_{\geq 1}^{\text{NNLO}}$ is currently not available. $\epsilon_1^{(b)}$ and $\epsilon_1^{(c)}$ are computed with MCFM program [84]. The maximum QCD scale variation of either calculation is taken as the uncertainty on ϵ_1 . The uncertainty is 15% as shown in figure 5.5 (b). As a result, the uncertainties on the exclusive jet cross sections are obtained through equation 5.2, which are 11%, 25% and 33% for the σ_0 , σ_1 and $\sigma_{\geq 2}$, respectively.

An additional uncertainty on the ggF signal acceptance by event selections in each jet bin is evaluated. A phase space is chosen to be as close as the reconstructed $H \rightarrow WW^* \rightarrow \ell\nu\ell\nu$ event selection (see chapter 7) using truth particles in order to remove the experimental effects. Table 5.3 summarizes the truth-level event selections for each analysis category. The uncertainty is derived from the variation of the acceptance within each jet bin by varying MC conditions. The following uncertainties are considered:

- **Scale:** Uncertainty on the higher order corrections, proved through the variation of the renormalization and factorization scales by factor half and two. The uncertainty is evaluated using the POWHEG+PYTHIA8 for $n_j = 0$ and $n_j = 1$, and using the MCFM for $n_j \geq 2$.
- **PDF:** Uncertainty on the modeling of parton distribution functions. The PDF uncertainty is evaluated by comparing different PDF sets: nominal CT10 and MSTW2008, and adding in quadrature the uncertainty determined using the CT10 error eigenvectors.
- **Generator:** Uncertainty on the implementation of the NLO matrix element and the

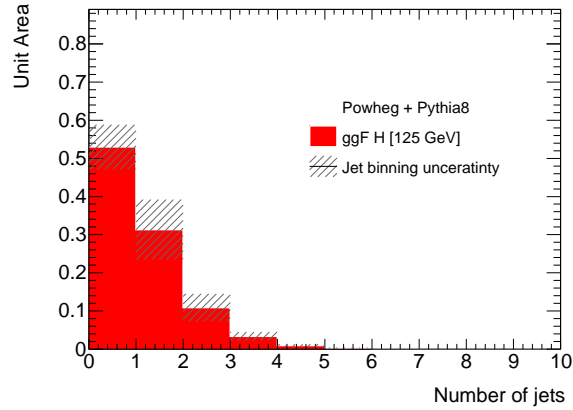


Figure 5.4: Distribution of number of jets in the POWHEG+PYTHIA8 simulation. The distribution is shown for the reconstructed ID jet (see section 6.4) before applying the pre-selection (see section 7.1).

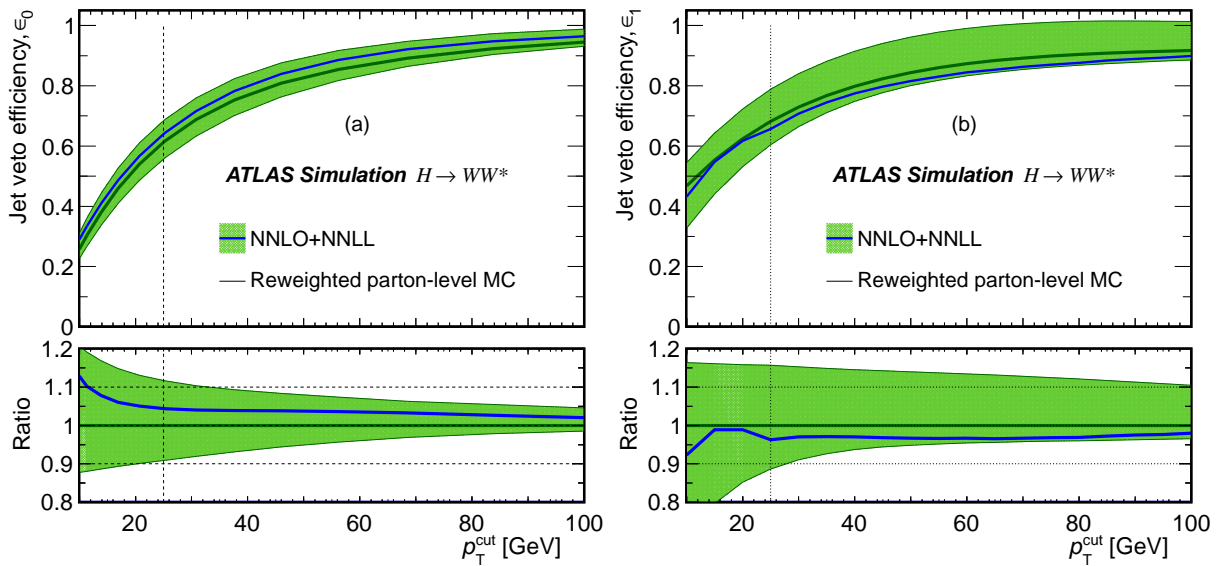


Figure 5.5: The veto efficiency of the (a) first jet and (b) second jet in inclusive ggF production of the Higgs boson, as a function of the veto-threshold p_T [117].

matching of the matrix element to the parton shower. The generator uncertainty is obtained from the comparison between POWHEG+HERWIG and aMC@NLO [85]+HERWIG.

- **UE/PS:** Uncertainties due to the underlying event and parton shower models. They are evaluated by comparing POWHEG+HERWIG and POWHEG+PYTHIA8.

The uncertainties on the ggF signal acceptance are small compared to the uncertainty in number of jets. All uncertainties of the ggF signal modeling, together with the uncertainty on the total cross section of the VBF production mode, are summarized in table 5.4. The uncertainties on the VBF acceptance are not considered since the VBF contribution is small as described in chapter 7.

Table 5.3: Summary of truth-level event selections for the calculation of theoretical uncertainties. The definition of the quantities are described in chapter 7. The missing transverse energy is obtained from the transverse momentum of the two neutrinos, $p_T^{\nu\nu}$.

$n_j = 0$	$n_j = 1$	$n_j \geq 2$ ggF
Exactly two leptons with :		
$p_T > 22$ for the leading lepton ℓ_1		
$p_T > 10$ for the subleading lepton ℓ_2		
Opposite charge leptons		
$m_{\ell\ell} > 10$ for $e\mu$		
$m_{\ell\ell} > 12$ for $ee/\mu\mu$		
$ m_{\ell\ell} - m_Z > 15$ for $ee/\mu\mu$		
$p_T^{\nu\nu} > 20$ for $e\mu$		
$p_{T,\text{rel}}^{\nu\nu} > 40$ for $ee/\mu\mu$		
$p_{T,\text{rel}}^{\nu\nu} > 40$ ($ee/\mu\mu$)	$p_{T,\text{rel}}^{\nu\nu} > 35$ ($ee/\mu\mu$)	—
$p_T^{\ell\ell} > 30$	—	—
$\Delta\phi_{\ell\ell,\text{MET}} > \pi/2$	—	—
—	$m_{\tau\tau} < (m_Z - 25 \text{ GeV})$	$m_{\tau\tau} < (m_Z - 25 \text{ GeV})$
—	$m_T^\ell > 50$ ($e\mu$)	—
$m_{\ell\ell} < 55$	$m_{\ell\ell} < 55$	$m_{\ell\ell} < 55$
$\Delta\phi < 1.8 \text{ rad}$	$\Delta\phi < 1.8 \text{ rad}$	$\Delta\phi < 1.8 \text{ rad}$

5.2.2 Background samples

The Monte Carlo samples used for the modeling of the backgrounds are explained briefly in this subsection. Corrections for the MC samples using the data and uncertainties of their modeling are described in chapter 8.

- **WW:** The inclusive cross section for the $q\bar{q} \rightarrow WW$ production is calculated at NLO with MCFM [84]. The WW kinematics are modeled using POWHEG+PYTHIA6. The small

Table 5.4: Signal yield uncertainty (in %) due to the modeling of the gluon-gluon fusion (ggF) and vector boson fusion (VBF). Uncertainties on the signal acceptance of the event selections (see table 5.3) are divided into the $e\mu$ and $ee/\mu\mu$ cases. For the $e\mu$ sample, uncertainties are evaluated in bins of the mass of di-lepton system, $m_{\ell\ell}$, and the p_T of sub-leading lepton, $p_T^{\ell 2}$, for the fit (see section 9.2). Each uncertainty is treated as a nuisance parameter in the fit.

Uncertainty source	$n_j = 0$		$n_j = 1$		$n_j \geq 2$
ggF					
Total cross section:					
Scale	7.5		7.5		7.5
PDF	7.2		7.2		7.2
Jet binning	11		25		33
Acceptance:					
	$e\mu$	$ee/\mu\mu$	$e\mu$	$ee/\mu\mu$	
Scale	1.0–3.5	1.4	1.4–9.0	1.9	3.6
PDF	3.2–3.3	3.2	2.8–3.3	2.8	2.2
Generator	1.3–3.8	2.5	1.7–6.8	1.4	4.5
UE/PS	2.2–5.7	6.4	1.8–13.5	2.1	1.7
VBF					
Total cross section:					
Scale	0.2		0.2		0.2
PDF	2.7		2.7		2.7

contribution from the quark box diagram, which is not included in POWHEG, is obtained with GG2WW [86]. In the $n_j \geq 2$ ggF-enriched analysis, the WW is modeled in SHERPA because the second jet coming from the parton shower is poorly modeled in POWHEG. For the WW (and WZ) production via non-resonant vector boson scattering (VBS), SHERPA provides the LO cross section and its modeling.

- **Top:** The cross section for the $t\bar{t}$ production is computed at NNLO+NNLL using TOP⁺⁺2.0 [88]. The single top productions are normalized to NNLO+NNLL calculations from references [89], [90] and [91] for the s -channel, t -channel and tW processes, respectively. POWHEG+PYTHIA6 generator is used to model both the $t\bar{t}$ and single top productions, except for the t -channel production, which is modeled with ACERMC [87].
- **Other VV:** The $W\gamma$ process is modeled in ALPGEN+HERWIG. Kinematic cuts are required on particles when in generating events: the photon must have $p_T > 7$ GeV and be separated from the charged leptons by $\Delta R > 0.25$. The $W\gamma$ samples are normalized to the cross section obtained from NLO calculations in MCFM. For the $W\gamma^*$ and WZ productions, there is a boundary at $m_{Z/\gamma^*} = 7$ GeV to avoid the overlap between these samples. The $W\gamma^*$ is modeled with SHERPA with up to one parton. In order to improve the estimation of the jet multiplicity, this SHERPA sample is weighted to reproduce the jet multiplicity of SHERPA sample generated with up to two partons, while the total cross section is normalized to NLO calculation from MCFM. The WZ and ZZ productions are modeled using POWHEG+PYTHIA8 without any corrections on the cross section. The $Z\gamma$ sample is generated using SHERPA. The photon is required to have $p_T > 8$ GeV and $\Delta R > 0.1$ during the generation. The cross section is normalized to NLO calculation from MCFM.

- **Z+jets:** The inclusive Z/γ^* production is generated ALPGEN+HERWIG with a di-lepton invariant mass of $m_{\ell\ell} > 10$ GeV. The samples are normalized to NNLO calculation of DYNNLO [93]. Events with a high- p_T photon emission are removed if they overlap with the kinematics defining the SHERPA $Z\gamma$. The electroweak Z +jets production, which has no QCD couplings, is modeled in SHERPA without the corrections on the cross section.

5.2.3 Monte Carlo event weights

To reproduce experimental conditions as much as possible, some event weights are applied to all simulation samples. The following event weights are considered in this analysis.

- **Pileup:** Pileup interactions are modeled with PYTHIA8, and merged into the signal and background samples. However, the pileup condition was defined before the start of the 2012 proton-proton data-taking. Thus, most MC samples do not describe the number of interactions per bunch crossing distribution in data as shown in figure 5.6 (a). These MC samples are named as mc12a. A few MC samples ($W\gamma^*$, $t\bar{t}$ and VBF Z +jets) were produced after the post-data-taking with a better pileup modeling, which is named as mc12b. The distribution of the number of interactions per bunch crossing in mc12b samples is shown in figure 5.6 (b). The events in samples are weighted to reproduce the data distribution in for both the mc12a and mc12b samples.

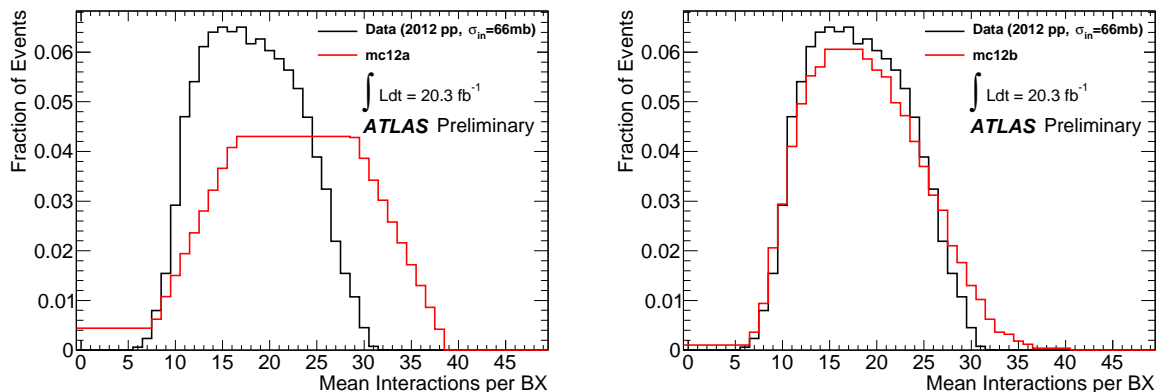


Figure 5.6: Number of interactions per bunch crossing used in mc12a (pre-data-taking production) (a) and mc12b (post-data-taking production) (b) samples.

- **Trigger efficiency:** The triggers listed in table 5.1 were used to collect the data. Events in the MC samples are also required to fire these triggers in its simulations in order to reproduce the data acceptance. The simulations do not describe the detector response perfectly. For example, the detector condition for the triggers changes during the data-taking period. Therefore, a scale factor for the trigger efficiency is introduced. The scale factor is defined as $SF = \epsilon_{\text{data}}/\epsilon_{\text{MC}}$, where ϵ is the trigger efficiency with respect to the reconstructed lepton measured with the tag and probe method (see section 5.1). Figure 5.7 shows the scale factors for the single lepton triggers as an example. The event weight is

calculated from these scale factors as follows:

$$\text{Event weight} = \frac{\epsilon_{\text{data}}^{\text{event}}}{\epsilon_{\text{MC}}^{\text{event}}} \quad (5.5)$$

$$= \frac{1 - (1 - \epsilon_{\text{MC}}^{\text{lead}} \times \text{SF}^{\text{lead}}) \times (1 - \epsilon_{\text{MC}}^{\text{sub}} \times \text{SF}^{\text{sub}})}{1 - (1 - \epsilon_{\text{MC}}^{\text{lead}}) \times (1 - \epsilon_{\text{MC}}^{\text{sub}})}, \quad (5.6)$$

where ϵ^{lead} (SF^{lead}) and ϵ^{sub} (SF^{sub}) are trigger efficiencies (scale factors) for the leading lepton and subleading lepton. In the case of “or-ing” the single lepton triggers and dilepton triggers, additional treatments are required. The trigger efficiency for the event is obtained with individual trigger components (single or di-lepton) as follows:

$$\epsilon^{\text{event}} = \epsilon^{\text{single}} + \epsilon^{\text{di-lepton}} - \epsilon^{\text{single}} \times \epsilon^{\text{di-lepton}}. \quad (5.7)$$

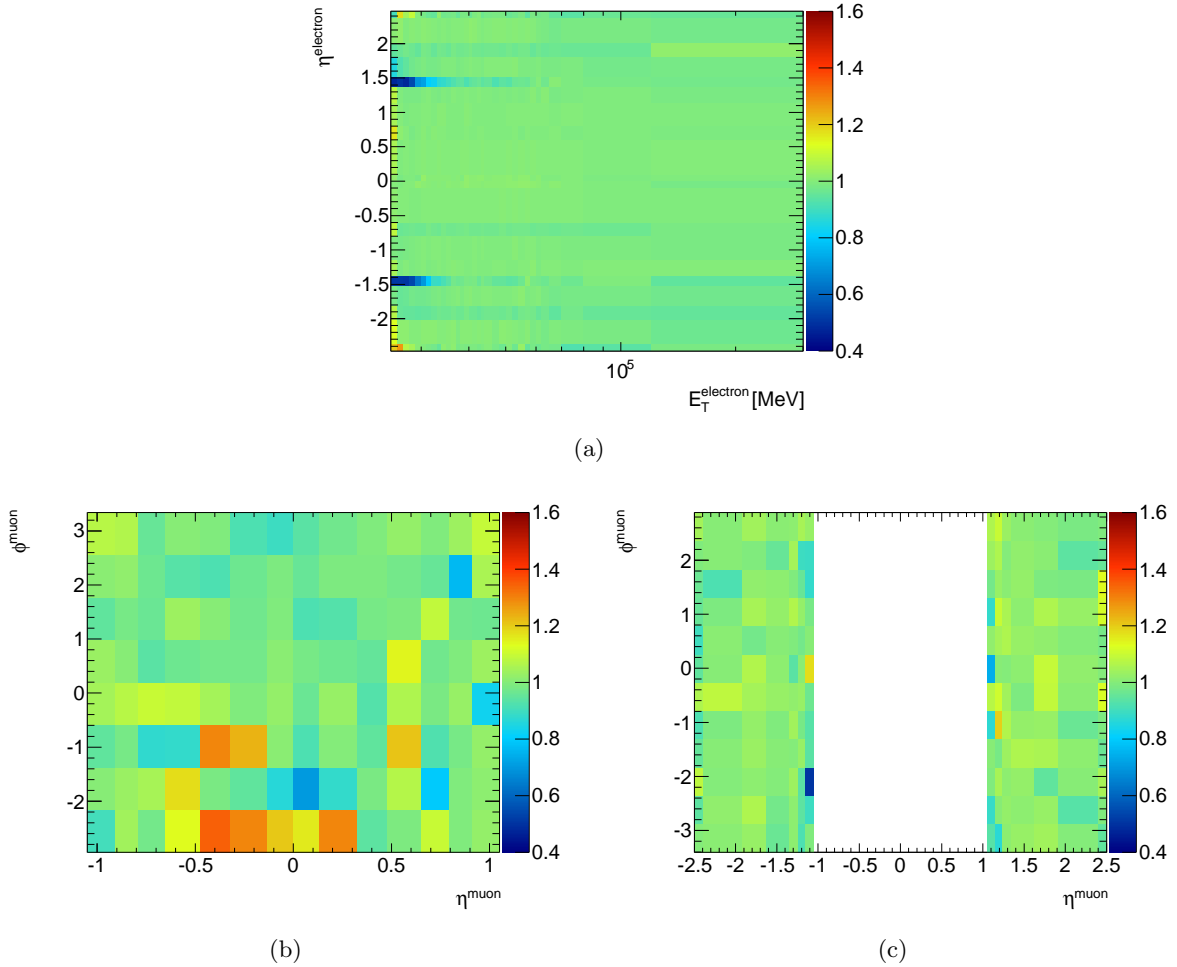


Figure 5.7: Event scale factors for (a) e24vhi_medium1 or e60_medium1 triggers shown in E_T - η plane. (b) Barrel ($|\eta| < 1.05$) and (c) endcaps ($|\eta| > 1.05$) scale factors for mu24i_tight or mu36_tight triggers shown in η - ϕ plane.

- **Lepton selection:** Event weights related to the lepton reconstruction and selection are described in chapter 6. The weights are typically a few percent level.

Figure 5.8 shows the obtained event weights combined with the pileup, trigger efficiency and lepton selection for the signal process before the pre-selection (see chapter 7), separated in $e\mu$ and $ee/\mu\mu$ categories.

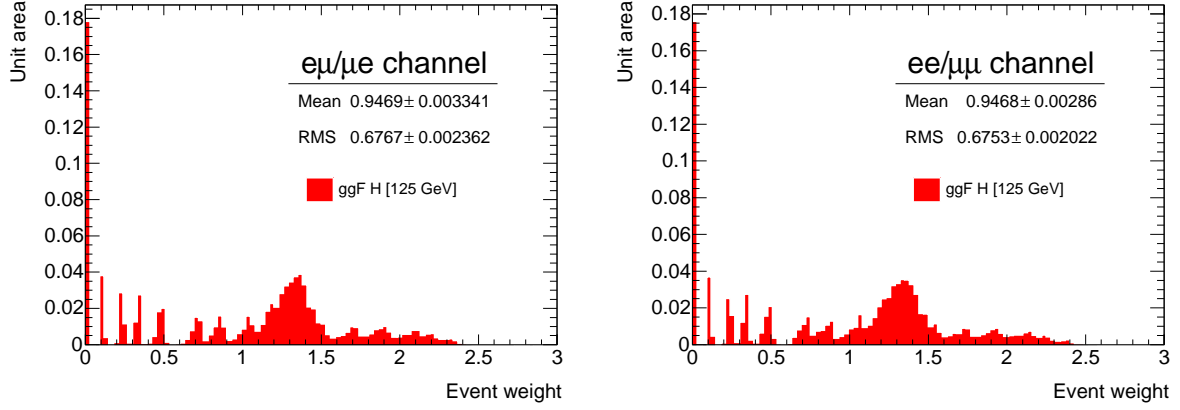


Figure 5.8: Distributions of combined event weights for the pile-up, trigger efficiency and lepton selection. The event weights are extracted from the signal sample (mc12a) before the pre-selection, separately in $e\mu$ (left) and $ee/\mu\mu$ (right) categories. Very small event weights originate from the poor modeling of the pile-up distribution.

Chapter 6

Object reconstruction and selection

By combining information from various subdetectors, the particles originating from the proton-proton collisions are reconstructed using dedicated algorithms. The physics elements listed in figure 6.1 are reconstructed for physics analyses. These reconstructed elements are commonly used throughout the ATLAS, and called “objects”. An object provides essential information for physics analyses: position, momentum, charge and so on. For the $H \rightarrow WW^* \rightarrow \ell\nu\ell\nu$ analysis, electrons, muons, jets and missing energies are the key objects. Reconstruction algorithms and their performances are described in this chapter. Object selections used for the $H \rightarrow WW^* \rightarrow \ell\nu\ell\nu$ analysis are also described.

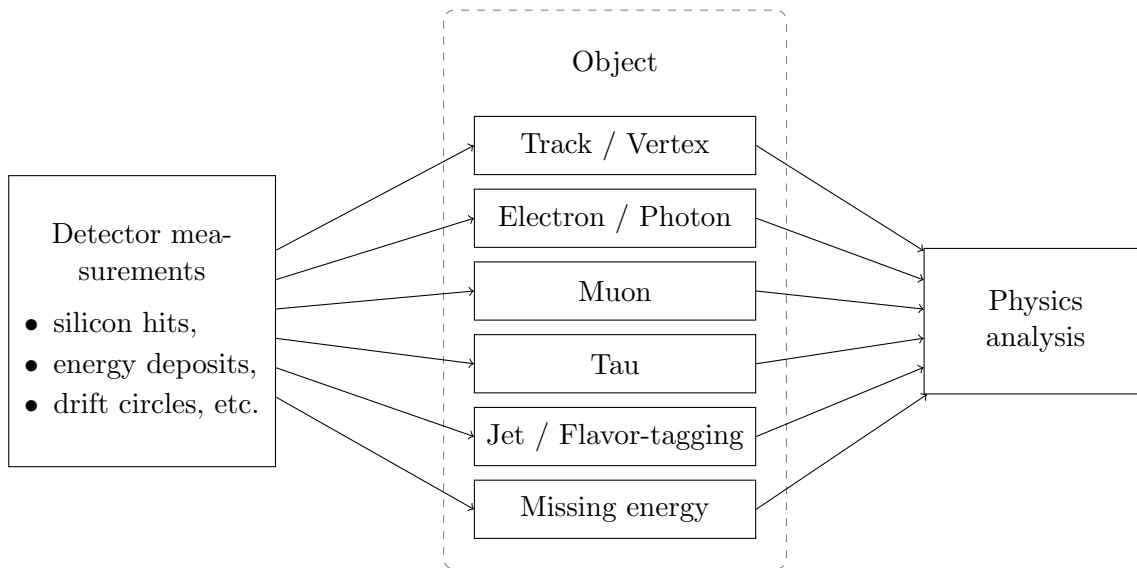


Figure 6.1: Scheme of object reconstructions.

6.1 Charged track and vertex

Charged particles are reconstructed in the inner trackers using a sequence of algorithms [94]. The reconstructed inner tracks become inputs for the other object reconstructions. The baseline algorithm designed for the efficient reconstruction of prompt charged particles is called as “inside-out” algorithm. This algorithm starts with finding a track seed. The track seed is formed

from a combination of space points in the three pixel layers and the inner-most SCT layer. Each hit on the pixel detector directly provides the three dimensional space point, while the space point from the SCT is formed by hits on each side of the module. The track seed is then extended to the outer layers of the SCT by picking up hits using a combinatorial Kalman filter [95]. These track candidates are then fitted based on the scoring strategy [96] to remove incomplete or fake candidates. The selected tracks are extended further to the TRT and associated with the drift circles. Finally, the extended tracks are re-fitted with the full information of three detectors to obtain completed tracks. The reconstructed tracks in an event are shown in figure 6.2 (dark yellow lines), together with the reconstructed muon, electron and jets, which are described later.

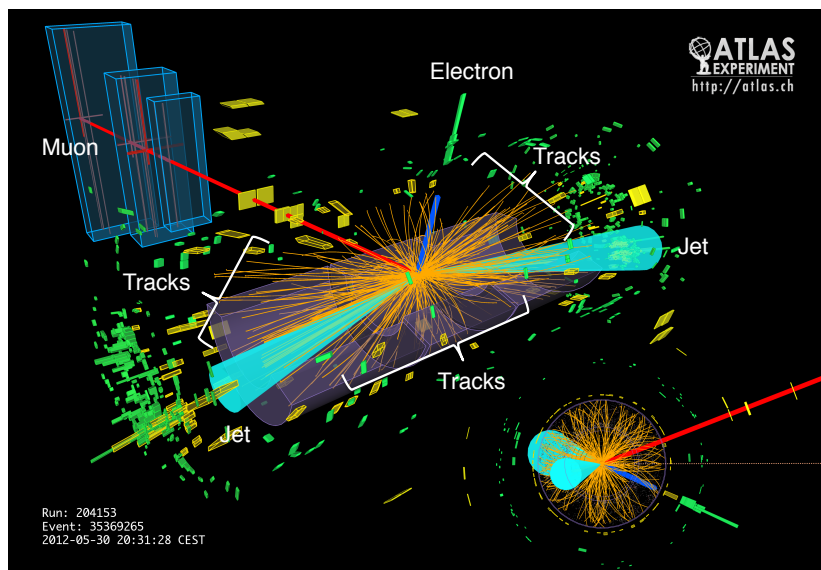


Figure 6.2: Event display for the event number of 35369265 in run number 204153. Tracks reconstructed in the inner trackers are colored dark yellow. Electron track is colored blue and its energy deposit is shown with green box. Muon track is colored red. Jets are shown with light blue cones.

The tracking reconstruction efficiency is evaluated using MC simulations. The efficiency is defined as the ratio of the number of reconstructed tracks to the number of generated charged particles. Figure 6.3 shows the evaluated efficiencies as a function of p_T and η . In the fiducial area for tracking, $p_T > 0.5$ GeV and $\eta < 2.5$, the efficiency of 80–85 % is obtained. The typical track resolution is given as:

$$\Delta p_T / p_T = 0.04 \% \times p_T (\text{GeV}) \oplus 2 \% . \quad (6.1)$$

The hard scattering interaction point as well as positions of additional proton-proton collisions occurring within the same bunch crossing are reconstructed using the tracking information, and are used for precise measurements and identifications of b - and τ -jets. These interaction points in the collisions are called “primary vertex”. The primary vertex reconstruction uses an iterative algorithm [98], where a vertex seed is obtained from the z position at the beam line of the reconstructed track. Nearby tracks are associated to the vertex seed followed by a χ^2 -based fit. Tracks which are displaced by more than 7σ from the vertex seed are used as another seed

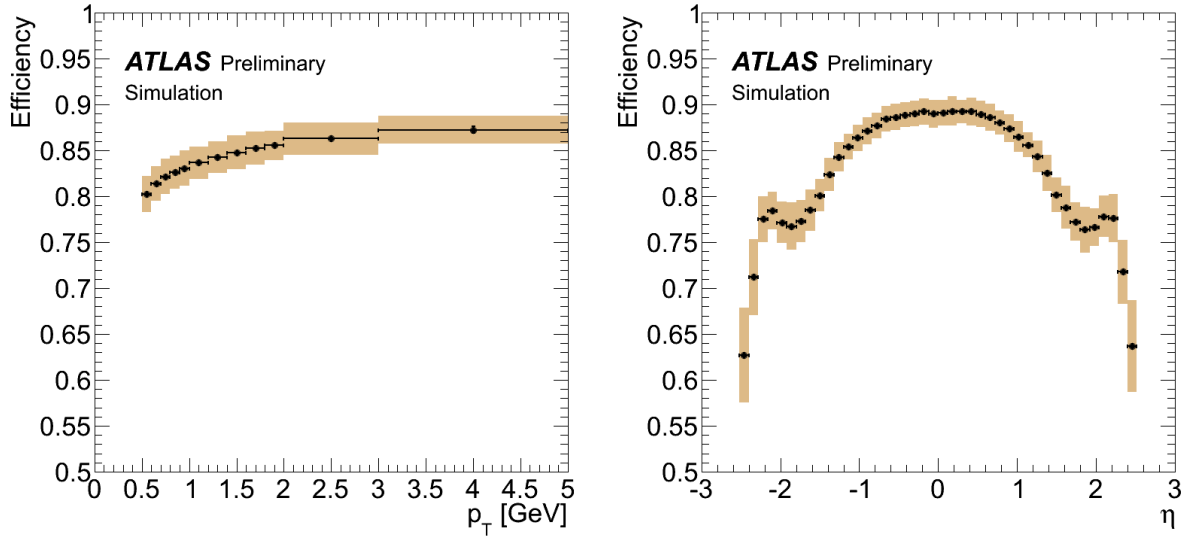


Figure 6.3: Track reconstruction efficiency as a function of p_T (left) and η (right). MC simulation without the pileup is used for the efficiency calculations [97].

of new vertex. This procedure is repeated until no additional vertices can be found. The vertex seeds are required to have at least two tracks to form the primary vertices.

The resolution of primary vertices can be estimated by randomly splitting the associated tracks into two, and fitting these two sets of tracks to two independent vertices. Their separation is used to get an estimate of the resolution of primary vertices. Details of the estimation are described in reference [98]. The results of the measurements are shown in figure 6.4. It can be seen that the resolution of primary vertices strongly depends on the number of associated tracks. The resolutions for a typical number of 50 associated tracks are to be 20–30 μm in x position and 40–50 μm in z position.

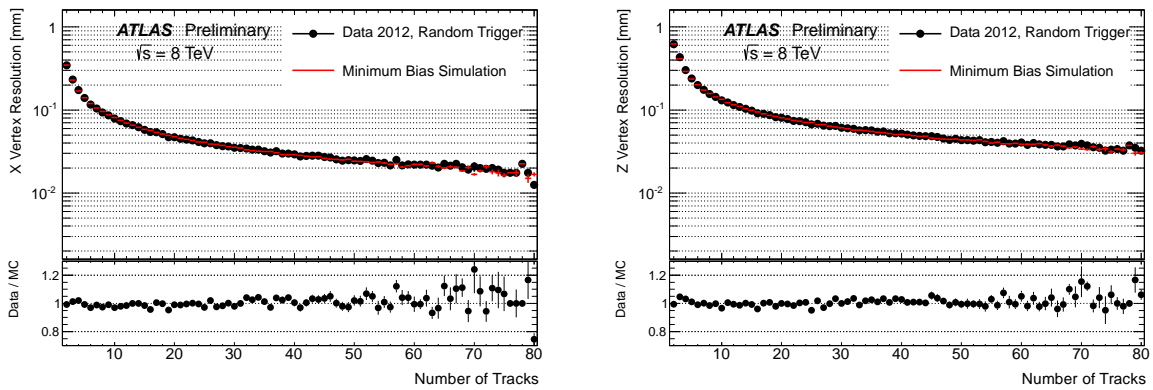


Figure 6.4: Vertex position resolutions in data (black) and MC (blue). The resolutions are shown for the longitudinal (left) and transverse coordinate (right) as a function of the number of tracks in the vertex fit [97].

6.2 Electron reconstruction

Electrons are reconstructed from energy deposits in the electromagnetic calorimeter matched to the track in the inner trackers. The reconstructed electrons are distinguished into several types based on levels of background rejection and signal efficiency. This process for the reconstructed electrons is called “identification”. The identification criteria rely on shapes of electromagnetic showers in the calorimeter as well as track-to-cluster matching quantities.

The reconstruction procedure of electrons is the following. The reconstruction starts from searching for a seed energy deposit (cluster) in the electromagnetic calorimeter. The η - ϕ space of the electromagnetic calorimeter is divided into a grid of towers of size 0.025×0.025 , which corresponds to the granularity of the middle layer of the samplings. The seed cluster is searched for by the sliding-window algorithm [99], and required to have a transverse energy more than 2.5 GeV. This cluster finding is expected to be very efficient for true electrons. In MC simulations, the efficiency is 95 % for electrons with $E_T = 7$ GeV and reaches 99 % at $E_T = 15$ GeV.

The inner tracks are extrapolated from the point of closest approach with respect to the primary vertex to the middle layer of the electromagnetic calorimeter, then the seed cluster is checked whether it matches to the track with the following criteria:

- $|\phi_{\text{cluster}} - \phi_{\text{track}}| < 0.2$ (0.05) for the side of track bending direction (for the other side);
- $|\eta_{\text{cluster}} - \eta_{\text{track}}| < 0.05$.

A specific electron-oriented tracking algorithm, which allows for energy losses at material surfaces with an electron hypothesis, is integrated to the standard track reconstruction in order to improve the performance of the electron reconstructions, which is described in detail in reference [100]. The cluster seed is considered as an electron candidate if there is at least one track is matched. Then, the cluster energy is calibrated in several steps, which is described in reference [101]. Figure 6.5 shows energy resolutions for the reconstructed electrons as a function of E_T . The typical energy resolution is about 3 % for reconstructed electrons with $E_T = 40$ GeV and $\eta = 1.0$. The four-momentum of electrons is computed using information from the final cluster energy (for energy) and matched track (for ϕ and η directions) in most of the cases.

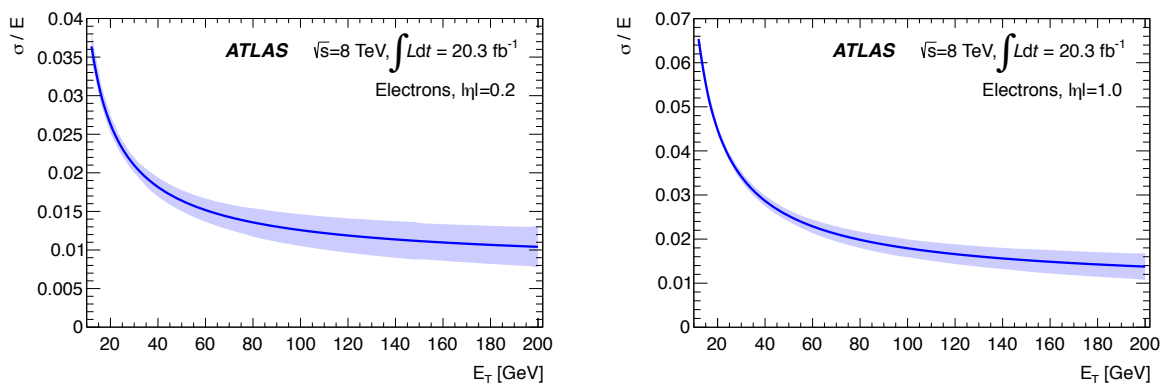


Figure 6.5: Energy resolutions and their uncertainties as a function of E_T for reconstructed electrons with $\eta = 0.2$ (left) and $\eta = 1.0$ (right) [101].

Electron identification is performed to reject backgrounds such as hadronic jets, photon conversions and semi-leptonic decays of heavy flavor hadrons. Two different techniques are

employed for the electron identification; sequential cuts (cut-based) and multivariate analysis using a likelihood (LH). The identification is based on the following discriminant variables:

- Energy leakage to the hadron calorimeter;
- Energy deposit in the third sampling layer of the electromagnetic calorimeter;
- Shower shapes in the first and second sampling layers;
- The matched track quality (number of hits in the inner trackers, etc.);
- The track-to-cluster matching quality ($\Delta\phi$, $\Delta\eta$, etc.);
- Presence of reconstructed photon conversions (conversion bit).

Four (three) reference sets of the cut-based (LH) selections, labelled **Loose**, **Multilepton**, **Medium** and **Tight** (**LooseLH**, **MediumLH** and **VeryTightLH**), have been defined with increasing background rejection power by varying the criteria of the discriminant variables.

The reconstruction and identification efficiencies in data are estimated using the tag and probe method with $Z \rightarrow ee$ and $J/\psi \rightarrow ee$ candidates. By requiring the resonances and strict tag electrons ($E_T > 25$ GeV, **Tight** identification, etc.), pure probe electrons are obtained for the efficiency measurements. For the reconstruction, the efficiency ϵ^{reco} is defined as the ratio of the number of reconstructed electrons to the number of electron clusters. The efficiency of the identification ϵ^{id} is defined as the ratio of the number of the identified electrons to the reconstructed electrons. The combined efficiencies for electrons, $\epsilon = \epsilon^{\text{reco}} \times \epsilon^{\text{id}}$, measured in data and MC simulations ($Z \rightarrow ee$) are shown in figure 6.6. It can be seen that the efficiency is higher in the loose selections compared to the tight selections as designed. The measured data-to-MC ratios are applied to selected electrons in the MC samples for the analysis as scale factors in order to reproduce the data acceptance. Table 6.1 summarizes the identification efficiencies ϵ^{id} in data together with the efficiencies in MC which contains the background processes. It confirms that the high background rejection is achieved in the tight selections.

Table 6.1: Identification efficiencies with respect to the reconstructed electrons for signal and background processes [100]. The signal efficiency is evaluated using the tag and probe method with $Z \rightarrow ee$ candidates in data. The background efficiency is evaluated in the MC simulations which contain non-isolated electrons from heavy flavor decays (1%), electrons from photon conversions (16%) and hadrons (83%). The uncertainty is statistical only.

	Signal eff. in data	Bkg. eff. in MC
Loose	95.7 ± 0.2	4.76 ± 0.04
Multilepton	92.9 ± 0.2	1.64 ± 0.02
Medium	88.1 ± 0.2	1.11 ± 0.02
Tight	77.5 ± 0.2	0.46 ± 0.01
LooseLH	92.8 ± 0.2	0.94 ± 0.02
MediumLH	87.8 ± 0.3	0.51 ± 0.01
VeryTightLH	77.0 ± 0.3	0.29 ± 0.01

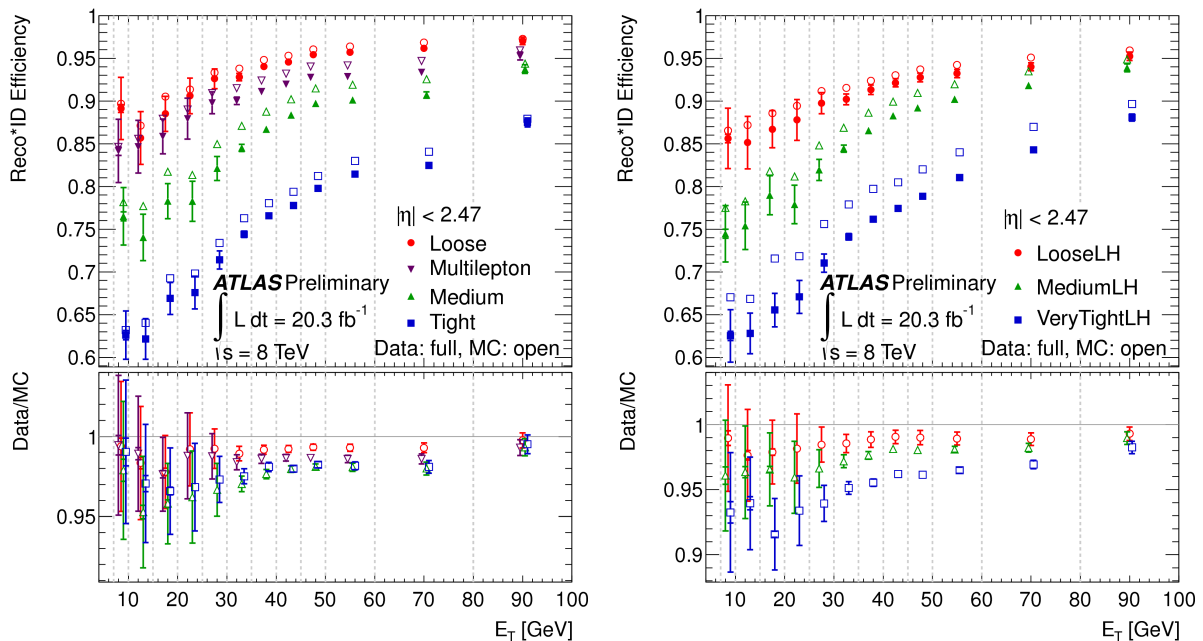


Figure 6.6: Combined reconstruction and identification efficiencies as a function of E_T for the cut-based (left) and LH (right) [97]. The lower panels show the data-to-MC efficiency ratios.

6.3 Muon reconstruction

Muon reconstruction uses the information from the muon spectrometers and the inner trackers. The muon spectrometer has the capability of a stand-alone reconstruction in order to extend the acceptance, where the inner tracker is not installed. The following types of muons are available:

- **Stand-Alone muon (SA):** Muon reconstruction is performed only in the muon spectrometer. The SA muons cover the range up to $|\eta| < 2.7$.
- **Combined muon (CB):** The muon trajectory reconstructed in the muon spectrometer is extrapolated to the inner trackers and combined with the track. The CB muons cover the area of $|\eta| < 2.5$ and have the highest muon purity. This is the main type of the reconstructed muons for physics analyses.
- **Segment Tagged muons (ST):** A track in the inner trackers is classified as a muon if, once extrapolated to the muon spectrometer, it is associated with at least one local track segment in the MDT or CSC chambers. The ST muons allow the low p_T muons crossing only one layer of the chambers.

The reconstruction of SA, CB and ST muons are performed using several types of algorithms [102]. The algorithm named “STACO” for the CB muon is explained below since it is the type of muons used in the $H \rightarrow WW^* \rightarrow \ell\nu\ell\nu$ analysis. The muon reconstruction starts with producing segments in the muon spectrometer. The segment is made from hits in the same chambers with a straight line fit. The segments from the three chamber stations are then fitted to form a track. The obtained track is back-extrapolated to the interaction point through the calorimeter, taking into account the estimated energy loss of the muon in the calorimeter. The extrapolated track (SA track) is matched to the track in the inner tracker and combined into a single track.

STACO performs a statistical combination of the SA track and inner track vectors to obtain a combined track \mathbf{T}_{comb} as follows:

$$(\mathbf{C}_{\text{ID}}^{-1} + \mathbf{C}_{\text{SA}}^{-1})\mathbf{T}_{\text{comb}} = \mathbf{C}_{\text{ID}}^{-1}\mathbf{T}_{\text{ID}} + \mathbf{C}_{\text{SA}}^{-1}\mathbf{T}_{\text{SA}}, \quad (6.2)$$

where \mathbf{T} denotes a vector of five track parameters (defined in section 4.1), and \mathbf{C} is its covariant matrix. The presence of the track in the inner detector rejects most of the muons coming from the pions and kaons, and provides a better momentum resolution. The momentum resolution ranges from 1.7% at central rapidity and $p_{\text{T}} \sim 10$ GeV, to 4% at large rapidity and $p_{\text{T}} \sim 100$ GeV.

The tag and probe method is employed to measure the reconstruction efficiencies of all muon types. For the CB muons, the conditional efficiency that a muon reconstructed in the inner tracker is also reconstructed as a CB muon, $\epsilon(\text{CB}|\text{ID})$, can be measured using the inner tracks as probes. Conversely, the conditional efficiency that a muon reconstructed in the muon spectrometer is also reconstructed in the inner tracker, $\epsilon(\text{ID}|\text{SA})$, can be measured using the SA muons as probes. Then, the muon reconstruction efficiency for the CB muons is obtained approximately as follows:

$$\epsilon(\text{CB}) = \epsilon(\text{CB}|\text{ID}) \times \epsilon(\text{ID}|\text{SA}). \quad (6.3)$$

Figure 6.7 (a) shows the measured reconstruction efficiencies in data and MC as a function of η , together with different muon types. Figure 6.7 (b) shows the data-to-MC ratios of the reconstruction efficiency as a function of η and ϕ , which are used in the analysis to correct the remaining differences between the data and MC simulations. Also the muon momentum in the MC simulations are corrected to data using $J/\psi \rightarrow \mu\mu$ and $Z \rightarrow \mu\mu$ candidates with accuracy of 0.05% to 0.2% depending on rapidity. The procedure of the momentum correction is detailed in reference [103].

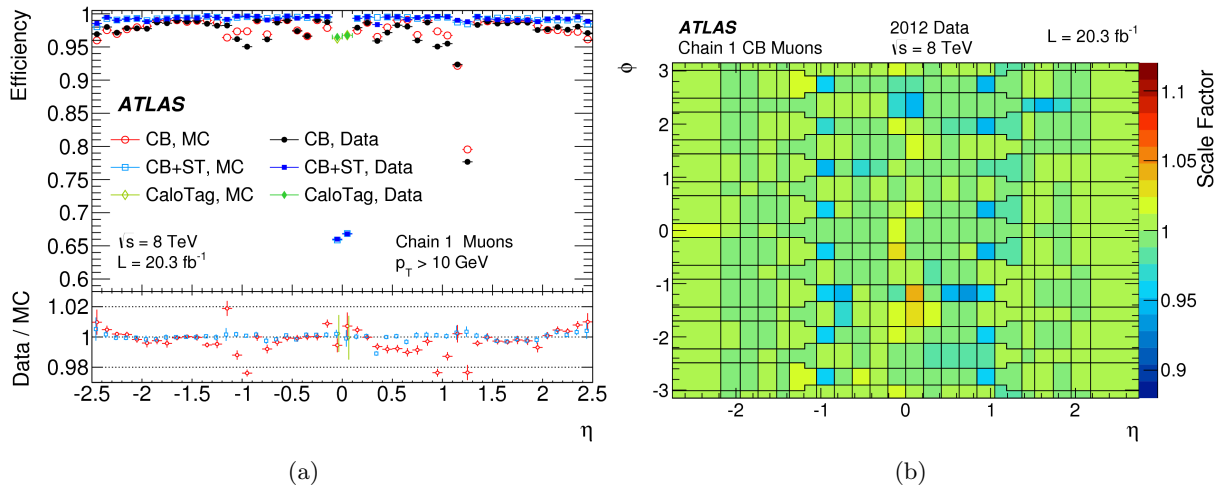


Figure 6.7: (a) Muon reconstruction efficiencies as a function of η measured in $Z \rightarrow \mu\mu$ events for muons with $p_{\text{T}} > 10$ GeV and different muon reconstruction types [103]. (b) Data-to-MC ratio of the muon reconstruction efficiency for the STACO combined muons as a function of η and ϕ for muons with $p_{\text{T}} > 10$ GeV [103].

6.4 Jet reconstruction

Partons produced in the proton-proton collisions become hadrons after the fragmentation. Hadrons make a shower in the calorimeters, and reconstructed as a jet. Since the $H \rightarrow WW^* \rightarrow \ell\nu\ell\nu$ analysis is divided by the number of jets in the final state, reconstruction of jets is a necessary part of the analysis.

Jet reconstruction starts with finding a cluster of energy deposits (topo cluster) in the calorimeters using the three dimensional TopoCluster algorithm [104]. The algorithm finds a seed cell with a energy deposit of more than $4\sigma_{\text{noise}}$, where σ_{noise} is a noise energy from the electronics and pileup. Neighbor cells with a energy deposit of more than $2\sigma_{\text{noise}}$ are clustered to the seed cell iteratively. Finally, all cells neighboring the formed cluster are added. The topo clusters are initially reconstructed at the ‘‘EM scale’’, which correctly measures the energy deposit by particles produced in the electromagnetic showers. The local cluster weighting (LCW) method is aiming to reduce the fluctuations in the response due to the the non-compensating nature of the ATLAS calorimeter (electron/hadron ~ 1.3), energy lost by the clustering and energy lost in dead materials by applying weights. In the $H \rightarrow WW^* \rightarrow \ell\nu\ell\nu$ analysis, this LCW topo clusters are used as the input to the jet reconstruction algorithm.

The jet reconstruction uses the anti- k_t algorithm [105]. The algorithm calculates the following parameters for all i -th and j -th clusters:

$$d_{ij} = \min(k_{t_i}^{-2}, k_{t_j}^{-2}) \frac{\Delta R_{ij}}{R} \quad (6.4)$$

$$d_i = k_{t_i}^{-2}, \quad (6.5)$$

where k_t is the transverse momentum of the cluster. R is the distance parameter, $R = 0.4$ is used in the $H \rightarrow WW^* \rightarrow \ell\nu\ell\nu$ analysis. ΔR_{ij} is the distance between the cluster i and j . If d_{ij} takes the minimum, the cluster i and j are merged into a cluster. If d_i takes the minimum, the cluster i is considered as a reconstructed jet, and removed from the cluster list. This process repeats until no cluster left.

After the reconstruction of jets, the energy of the reconstructed jet is calibrated using MC simulations and in situ techniques. Figure 6.8 shows an overview of the calibration scheme. The procedure consists of four steps [106] as described below:

- **Pileup correction:** Correction to account for the energy offset caused by the pileup interactions. The correction is derived from MC simulations as a function of the number of reconstructed primary vertices and the expected average number of interactions.
- **Origin correction:** Correction to the jet direction. It makes the jet pointing back to the primary vertex instead of the center of the ATLAS detector.
- **Energy and η calibration:** Calibration of the energy and η of the reconstructed jet is derived from MC simulations. The energy response with respect to the truth jet, which is obtained by running the anti- k_t algorithm on truth particles except muons and neutrinos, is defined as follows:

$$R = E_{\text{jet}}^{\text{LCW}} / E_{\text{jet}}^{\text{truth}}. \quad (6.6)$$

The R is the inverse of the jet energy calibration function. Figure 6.9 shows the energy response R as a function η .

- **Residual in situ calibration:** Previous corrections and calibration rely on the MC simulations. Residual data-to-MC differences are assessed using in situ techniques exploiting the transverse momentum balance between the jet and a well-measured reference object.

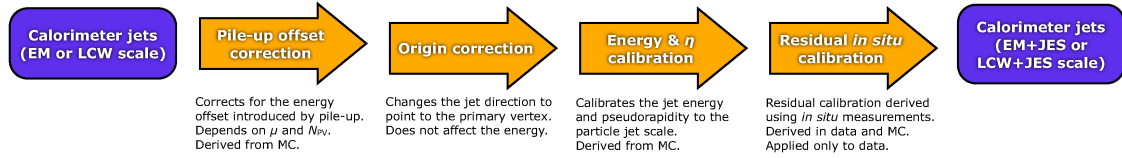


Figure 6.8: Overview of the ATLAS jet calibration scheme [106].

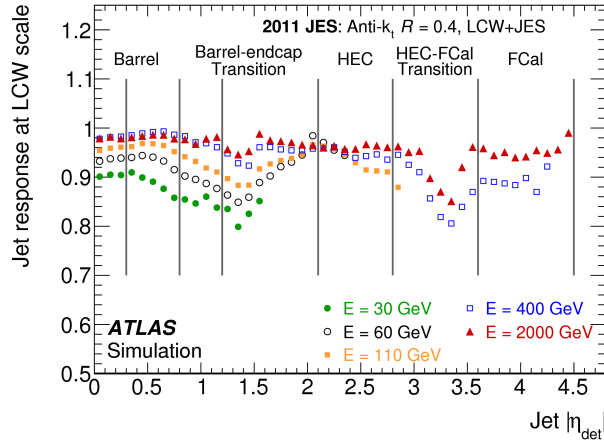


Figure 6.9: Energy response of simulated jets from topo clusters as a function of η [106]. The response is shown separately for various truth jet energies.

The ability to identify the flavor of a reconstructed jet, separating b -quark jet from c -quark and other light flavor jets, is provided by exploiting the characteristics of b -hadrons. This identification of b -quark jets is called “ b -tagging”. Various b -tagging algorithms have been developed in the ATLAS experiment. IP3D is an algorithm based on the impact parameters of tracks associated with the jet. SV1 uses a vertex formed by the decay product of the b -hadrons. JetFilter exploits the topology of the weak b -hadron decays. All algorithms are described in reference [107]. Using the information from the IP3D, SV1 and JetFilter algorithms, the final discrimination based on the neural network is performed with the MV1 algorithm. The MV1 algorithm outputs a “tag weight” for each jet. The fixed cuts on the tag weight (operating point) are tuned to obtain specified b -jet efficiencies in the $t\bar{t}$ sample. For example, the operating point corresponding to the b -jet efficiency of 70% achieves the other-quark jet efficiency of about 10%. In order to consider possible differences of the b -tagging efficiency between the data and MC simulations, scale factors have been measured using the $t\bar{t}$ candidates. The b -tagging efficiency measurement technique using a likelihood function is described in reference [108]. Figure 6.10 shows the measured b -tagging efficiencies and scale factors at the 70% b -jet efficiency operating point as a function of p_T of jets. The scale factors are applied to the events in the MC samples when the b -tagging is required.

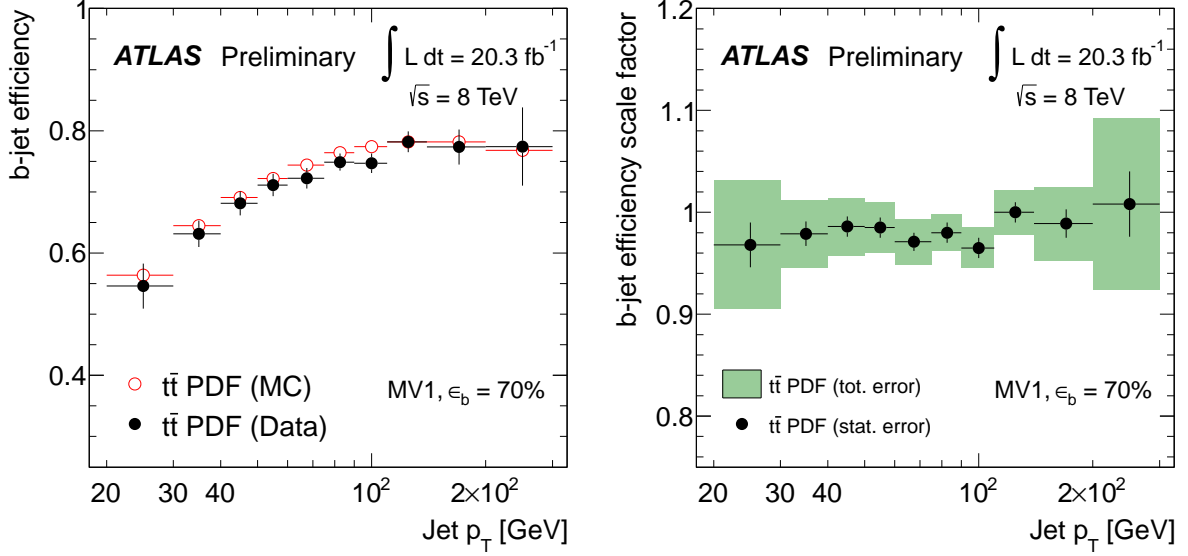


Figure 6.10: b -tagging efficiency (left) and scale factor (right) obtained from the $t\bar{t}$ candidates for the MV1 b -tagging algorithm at the 70% b -jet efficiency operating point [108].

6.5 Missing transverse energy reconstruction

Neutrinos are observed as an energy imbalance in the transverse plane since the transverse energy in the initial state is zero on average. The reconstruction of this missing transverse energy is performed as the negative vector sum of the visible objects. In this analysis, two types of the missing transverse energy are defined: calorimeter-based, $\mathbf{E}_T^{\text{miss}}$, and track-based, $\mathbf{p}_T^{\text{miss}}$. The symbol E_T^{miss} and p_T^{miss} are used for the magnitude of the missing transverse energy.

The calorimeter-based missing transverse energy in an event is computed as follows:

$$\mathbf{E}_T^{\text{miss}} = -(\mathbf{E}_T^{\text{electron}} + \mathbf{E}_T^{\text{gamma}} + \mathbf{E}_T^{\text{tau}} + \mathbf{E}_T^{\text{jet}} + \mathbf{E}_T^{\text{muon}} + \mathbf{E}_T^{\text{cellout}}). \quad (6.7)$$

The various terms in the equation are the vector sum of each physics component. The definitions are:

- E_T^{electron} : Transverse energy from electrons passing Medium identification with $E_T > 10$ GeV. The electron reconstruction and identification are described in section 6.2.
- E_T^{gamma} : Transverse energy from photons passing Tight identification with $E_T > 10$ GeV. The reconstruction and identification of photons are performed by using the energy cluster in the electromagnetic calorimeter without matching tracks, which are described in reference [101].
- E_T^{tau} : Transverse energy from τ -jets reconstructed with Tight identification with $p_T > 10$ GeV. The reconstruction and identification are performed by exploiting the characteristics of τ -jets, which are collimated energy deposits in the calorimeter and low track multiplicity. Details of the reconstruction and identification of τ -jets are described in reference [109].
- E_T^{jet} : Transverse energy from jets with $p_T > 7$ GeV. The jets with $7 < p_T < 20$ GeV are calibrated with only the LCW method. The other jets are fully calibrated. The reconstruction and calibration of the jets are described in section 6.4.

- E_T^{muon} : Transverse momentum from muons. The CB muons are used in the range $|\eta| < 2.5$. The SA muons are used in the range $2.5 < |\eta| < 2.7$. The reconstruction of the muons are described in section 6.3.
- E_T^{cellout} : Transverse energy from the topo clusters not associated to the reconstructed objects described above. In order to consider the low p_T particles that do not reach the calorimeter or make the topo cluster, tracks with $p_T > 0.4$ GeV are added to the E_T^{cellout} if a track is neither associated to the topo cluster nor the reconstructed object. In case the track is associated to the topo cluster, its transverse momentum is added to the calculation and the energy of the topo cluster is removed. The reconstruction of the topo clusters and tracks are described in 6.1 and 6.4.

The calorimeter-based missing transverse energy is commonly used in the ATLAS experiment. In this analysis, another type of missing transverse energies, track-based missing transverse momentum, is defined, which improves the resolution for the Higgs signal process. The track-based missing transverse momentum is computed as follows:

$$\mathbf{p}_T^{\text{miss}} = -(\mathbf{p}_T^{\text{electron}} + \mathbf{p}_T^{\text{muon}} + \mathbf{p}_T^{\text{track}} + \mathbf{p}_T^{\text{corr}}). \quad (6.8)$$

The each component is defined as follows:

- p_T^{electron} : Transverse momentum from electrons satisfying Medium identification, $E_T > 10$ GeV and $|\eta| < 2.47$. The electrons used in the $H \rightarrow WW^* \rightarrow \ell\nu\ell\nu$ analysis (see section 6.6) are also added to the calculation.
- p_T^{muon} : Transverse momentum from CB muons satisfying $p_T > 6$ GeV, $|\eta| < 2.5$ and $|z_0 \times \sin(\theta)| < 1.0$ mm. The muons used in the $H \rightarrow WW^* \rightarrow \ell\nu\ell\nu$ analysis (see section 6.6) are also added to the calculation.
- p_T^{track} : Transverse momentum from tracks which are not associated to the reconstructed electrons and muons described above. The tracks are required to satisfy the following selections:
 - $p_T > 0.5$ GeV, $|\eta| < 2.5$;
 - $|d_0| < 1.5$ mm, $|z_0 \times \sin(\theta)| < 1.5$ mm with respect to the primary vertex, see section 4.1 for the definition of d_0 and z_0 ;
 - number of pixel (SCT) hits > 0 (5).
- p_T^{corr} : Difference of the transverse momentum between $p_T^{\text{jet,calo}}$ and $p_T^{\text{jet,track}}$. $p_T^{\text{jet,calo}}$ is the transverse momentum of the jets used in the $H \rightarrow WW^* \rightarrow \ell\nu\ell\nu$ analysis reconstructed using the calorimeter (ID jets) (see section 6.6). $p_T^{\text{jet,track}}$ is the transverse momentum of the tracks used in p_T^{track} calculation and associated to the ID jets. The tacks are considered to be associated with the ID jet if they are within $\Delta R < 0.4$.

6.6 Object selection

In this section, the objects used in the $H \rightarrow WW^* \rightarrow \ell\nu\ell\nu$ analysis are defined.

Leptons

For reconstructed electrons, the following selections are applied in the analysis in order to reduce the misidentified electrons originating from jets:

- $E_T > 10$ GeV and $|\eta| < 2.47$ (exclude $1.37 < |\eta| < 1.52$);
- VeryTightLH (Medium) identification for $E_T < (>) 25$ GeV;
- $|d_0/\sigma(d_0)| < 3.0$ and $|z_0 \times \sin(\theta)| < 0.4$ mm, see text for the definition of $\sigma(d_0)$;
- $eTcone30/E_T < (0.2, 0.24, 0.28)$ for $E_T = (10\text{--}15, 15\text{--}20, 20\text{--}\infty)$ GeV, see text for the definition of eTcone30;
- $pTcone40/E_T < 0.06$ for $E_T = 10\text{--}15$ GeV, and $pTcone30/E_T < (0.08, 0.10)$ for $E_T = (15\text{--}20, 20\text{--}\infty)$ GeV, see text for the definition of pTcone40 and pTcone30.

Electrons reconstructed with $E_T > 10$ GeV and $|\eta| < 2.47$ are considered as the starting point. The electrons in the range $1.37 < |\eta| < 1.52$ are excluded, where the barrel calorimeter coverage ends and the endcaps start. For reconstructed electrons with $E_T < 25$ GeV, the VeryTightLH identification is required since it provides the highest rejection of the background from non-prompt electrons as shown in table 6.1. On the other hand, the cut-based Medium identification is used for the $E_T > 25$ GeV electrons, where the backgrounds are less significant.

To further reduce the backgrounds, additional requirements are imposed on the impact parameter and isolations. The impact parameter of particles is a quantity related to the distance to the beam axis as defined in section 4.1. The isolation is a parameter defined as the energy or momentum sum around the particle. Two types of the isolation, calorimeter isolation and track isolation, are used in this analysis. The calorimeter isolation represents the sum of the calorimeter cluster energy in a cone around the particle, denoted as eTconeX, where X represents a size of the cone ($X = 30$ if $\Delta R = 0.30$). The energy deposit from the measuring particle is not included. The track isolation is the sum of the transverse momentum of all the tracks in the cone, denoted as pTconeX. The momentum of the track associated to the measuring particle is not included. Then, eTconeX and pTconeX are divided by the electron E_T to obtain the relative size of the quantities. An illustration of the isolation cone is shown in figure 6.11.

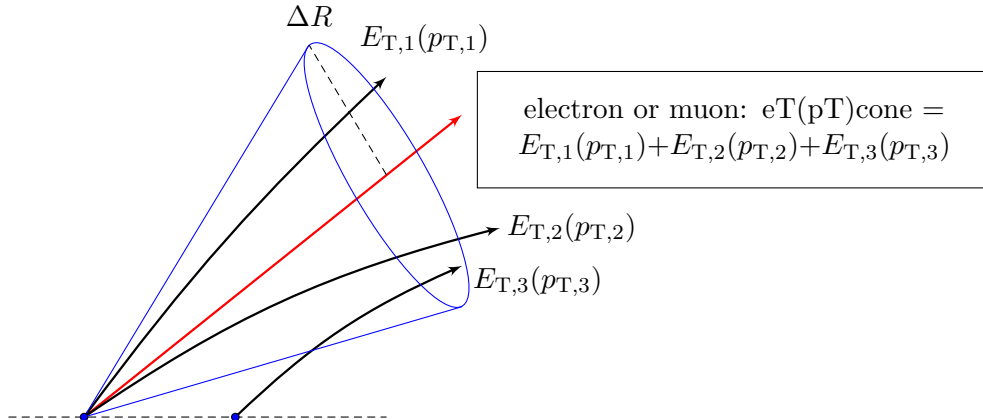


Figure 6.11: Illustration of an isolation cone.

Both the impact parameter and isolation are effective quantities to distinguish prompt leptons from the collision and leptons from the hadron decay. The transverse impact parameter with respect to the primary vertex, d_0 , divided by its estimated uncertainty, $\sigma(d_0)$, is required to satisfy $|d_0/\sigma(d_0)| < 3.0$. The longitudinal impact parameter, z_0 , must satisfy $|z_0 \times \sin(\theta)| < 0.4$ mm. The isolation requirements are varied in the electron E_T , and to be less than 0.20 (0.06) at the lowest E_T to 0.28 (0.10) at the highest E_T for the calorimeter (track) isolation. The distributions of the impact parameters and isolations for the electrons in the Higgs signal and QCD MC samples are shown in figure 6.13. Clear separations between the samples are observed.

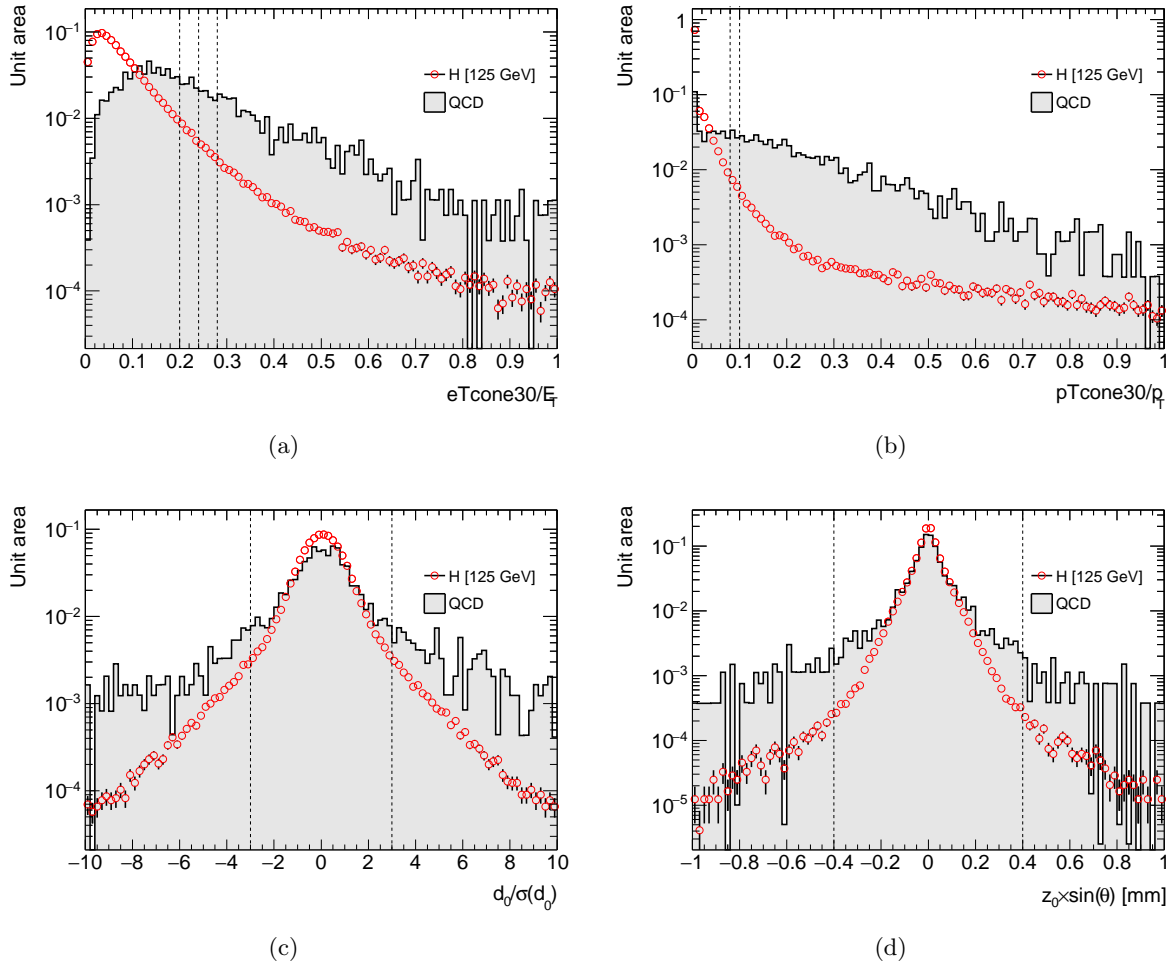


Figure 6.12: The isolation, eT_{cone30}/p_T (a) and pT_{cone30}/p_T (b), and impact parameter, $d_0/\sigma(d_0)$ (c) and $z_0 \times \sin(\theta)$ (d), distributions for the identified electrons in the Higgs signal and multi-jets (QCD) MC samples. The electrons are selected with $E_T > 10$ GeV, $|\eta| < 2.47$ (exclude the gaps) and VeryTightLH (Medium) identification for the $10 < E_T < 25$ GeV ($E_T > 25$ GeV). The dotted lines denote the cut value on the corresponding quantities, which are E_T dependent in case of the isolation parameters.

For reconstructed muons, the following selections are applied:

- $p_T > 10$ GeV and $|\eta| < 2.5$;

- STACO combined muons;
- $|d_0/\sigma(d_0)| < 3.0$ and $|z_0 \times \sin(\theta)| < 1.0$ mm;
- $eTcone30/p_T < (0.06, 0.12, 0.18, 0.30)$ for $p_T = (10\text{--}15, 15\text{--}20, 20\text{--}25, 25\text{--}\infty)$ GeV;
- $pTcone40/p_T < 0.06$ for $p_T = 10\text{--}15$ GeV, and $pTcone30/p_T < (0.08, 0.10)$ for $p_T = (15\text{--}20, 20\text{--}\infty)$ GeV.

Muons reconstructed as the CB muons with $p_T > 10$ GeV and $|\eta| < 2.5$ are used. The CB muons provide the highest purity and resolution for the analysis. The impact parameter and isolation requirements are also applied to the muons in order to suppress the misidentification. For the impact parameters, $|d_0/\sigma(d_0)| < 3.0$ and $|z_0 \times \sin(d_0)| < 1.0$ mm are required. For the isolations, $eTcone30$ ($pTcone40$)/ $p_T < 0.06$ at the lowest p_T and $eTcone30$ ($pTcone30$)/ $p_T > 0.30$ (0.12) at the highest p_T for the calorimeter (track) isolation are imposed.

The leptons satisfying the selections described in this section are denoted as “ID” lepton hereafter. Table 6.2 summarizes the selection of the ID leptons. In order to correct the MC acceptance of the lepton selections, scale factors defined as the difference of the impact parameter and isolation selection efficiencies between the data and MC are evaluated. The selection efficiencies with respect to the reconstructed and identified leptons are calculated with the Z tag and probe method. Figure 6.13 shows the obtained scale factors for ID electrons and muons, which are applied to the leptons in the MC samples.

Table 6.2: The definition of ID lepton.

p_T [GeV]	identification	calorimeter isolation	track isolation	impact parameters
electron				
10–15	VeryTightLH	$eTcone30/E_T < 0.20$	$pTcone40/E_T < 0.06$	$ z_0 \times \sin(\theta) < 0.4$ mm, $ d_0/\sigma(d_0) < 3$
15–20		$eTcone30/E_T < 0.24$	$pTcone30/E_T < 0.08$	
20–25		$eTcone30/E_T < 0.28$	$pTcone30/E_T < 0.10$	
25–	Medium			
muon				
10–15	CB muon	$eTcone30/p_T < 0.06$	$pTcone40/p_T < 0.06$	$ z_0 \times \sin(\theta) < 1.0$ mm, $ d_0/\sigma(d_0) < 3$
15–20		$eTcone30/p_T < 0.12$	$pTcone30/p_T < 0.08$	
20–25		$eTcone30/p_T < 0.18$	$pTcone30/p_T < 0.12$	
25–		$eTcone30/p_T < 0.30$		

Jets

For reconstructed jets, the following criteria are used:

- $p_T > 25$ (30) GeV for $|\eta| < 2.4$ ($2.4 < |\eta| < 4.5$);
- $JVE > 0.5$ for $p_T < 50$ GeV, see text for the definition of JVE;
- 85 % efficiency operating point for the b -tagging.

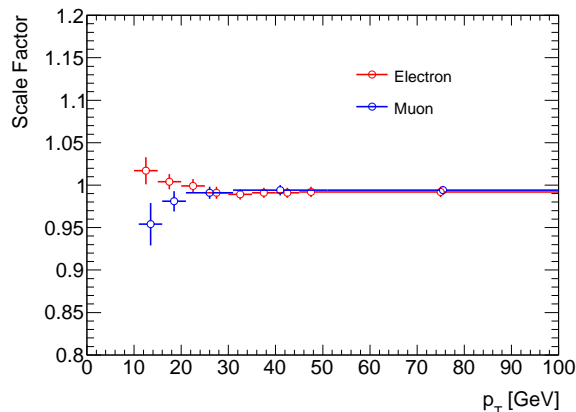


Figure 6.13: Scale factors for ID electrons (red) and muons (blue).

Reconstructed jets are required to have $p_T > 25$ GeV for $|\eta| < 2.4$, and $p_T > 30$ GeV for $2.4 < |\eta| < 4.5$. The higher threshold in the high η regions is to suppress the jets from pileup. A requirement on the jet vertex fraction, JVF, is imposed to further suppress the pileup jets. The JVF is defined for each i -th jet as follows:

$$\text{JVF} = \sum_k p_T(k, \text{PV}_j) / \sum_n \sum_l p_T(l, \text{PV}_n), \quad (6.9)$$

where k runs over all tracks originating from the primary vertex (PV_j), which has the highest track p_T sum, matched to i -th jet. n counts all primary vertices in the event and l runs over all tracks originating from the primary vertex of n matched to i -th jet. Only tracks with $p_T > 500$ MeV are considered in the JVF calculation. $\text{JVF} = 1$ means that all the tracks in the jet is associated with the hard scattering and no contribution from the additional interactions. The JVF is assigned a value of -1 when there are no track associated. Figure 6.14 shows the JVF distribution for the pileup jets and hard-scatter jets. $\text{JVF} > 0.5$ is required for the jet with $p_T < 50$ GeV in this analysis. These selected jets are denoted as ID jet hereafter. The multiplicity of the ID jets is used for the categorization described in section 2.3.

For the b -tagging, 85% efficiency operating point, which is the highest operating point currently available in ATLAS, is used in this analysis since it provides the highest rejection of the top backgrounds by requiring the b -tagging veto.

Missing energy

The calorimeter-based missing transverse energy, E_T^{miss} , and track-based missing transverse momentum, p_T^{miss} , are defined in section 6.5. The p_T^{miss} is used for the m_T calculation since the p_T^{miss} shows a better resolution compared to the E_T^{miss} for the signal process. Figure 6.15 shows the difference of the reconstructed and generated missing transverse energy and m_T in case of using the p_T^{miss} and E_T^{miss} . The distributions are shown for the ggF signal MC samples in the $n_j = 0$ category. The better resolution of p_T^{miss} can be seen.

For the event selection, which is described in section 7, an addition quantity is defined using the E_T^{miss} and p_T^{miss} . The relative missing transverse energy, $E_{T,\text{rel}}^{\text{miss}}$, is defined as follows:

$$E_{T,\text{rel}}^{\text{miss}} = \begin{cases} E_T^{\text{miss}} \times \sin(\Delta\phi_{\text{near}}) & \text{if } \Delta\phi_{\text{near}} < \pi/2 \\ E_T^{\text{miss}} & \text{otherwise} \end{cases} \quad (6.10)$$

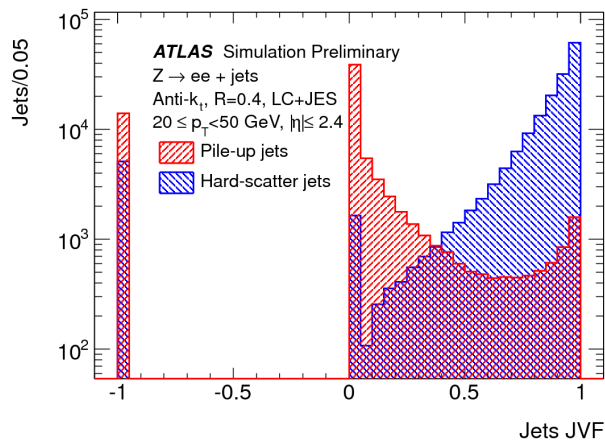


Figure 6.14: JVF distribution for hard-scatter (blue) and pile-up (red) jets with $20 < p_T < 50$ GeV and $|\eta| < 2.5$ in simulated Z +jets events. [110].

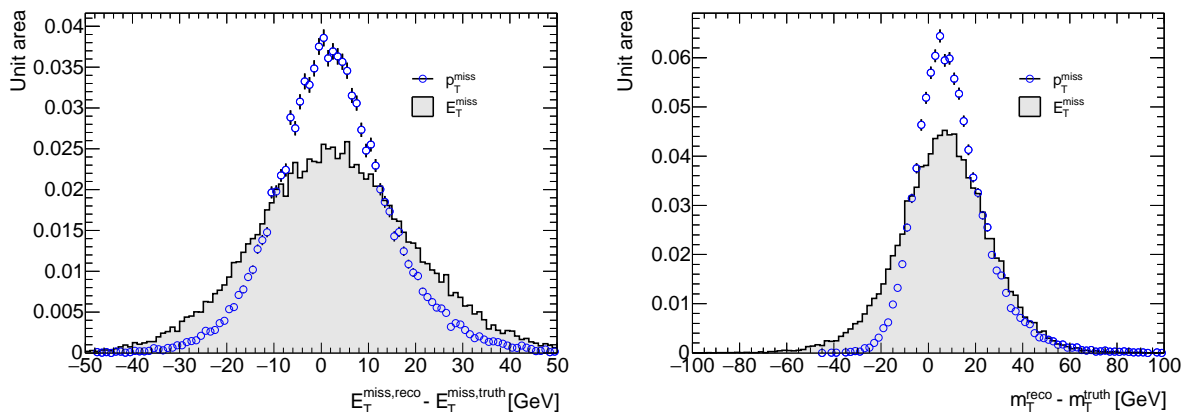


Figure 6.15: Differences of the reconstructed and generated missing transverse energy and m_T for the ggF signal MC in the $n_j = 0$ category. The comparisons are made between the calorimeter-based reconstruction (E_T^{miss}) and track-based reconstruction (p_T^{miss}).

where $\Delta\phi_{\text{near}}$ is the azimuthal angle between the E_T^{miss} and the nearest ID lepton or ID jet. The relative missing transverse energy is effective to reduce the backgrounds originating from a miss-measurement of lepton or jet energies, particularly the Z +jets background. Since there are no neutrinos in the final state of the Z +jets process, the missing transverse energy originates from the miss-measurement of the lepton or jet energy tends to be aligned with this lepton or jet to balance the transverse energy. Thus, the relative missing transverse energy is effective to discriminate the background from the signal, which contains neutrinos in the final state, by pushing the quantity close to zero.

A similar calculation is performed for the p_T^{miss} , except for that p_T^{corr} term (see section 6.5) is not included to the p_T^{miss} calculation because it is found that the rejection power for the Z +jets background increases with this treatment in case of p_T^{miss} . Figure 6.16 shows the $p_{T,\text{rel}}^{\text{miss}}$ distributions of the data without p_T^{corr} and with p_T^{corr} term in a Z +jets enriched region in the $n_j = 1$ category. The Z +jets enriched region is selected with $|m_{\ell\ell} - m_Z| < 15$ GeV requirement after the $m_{\ell\ell} > 12$ GeV cut in the $ee/\mu\mu$ channel (see section 7.1). It can be confirmed that a

better resolution (values close to zero) is available in the $p_{T,\text{rel}}^{\text{miss}}$ without p_T^{corr} term.

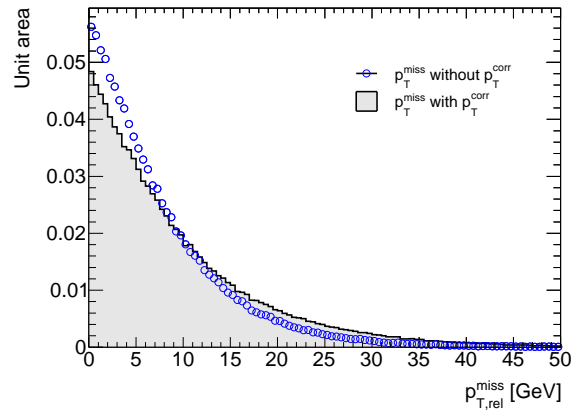


Figure 6.16: $p_{T,\text{rel}}^{\text{miss}}$ distributions without p_T^{corr} and with p_T^{corr} in the Z +jets enriched regions in the $n_j = 1$ category. Comparison is made using the data.

The main idea in the optimization of the missing transverse energy for the event selection are following:

- For the $ee/\mu\mu$ channels, $E_{T,\text{rel}}^{\text{miss}}$ and $p_{T,\text{rel}}^{\text{miss}}$ are used in the advantage of rejecting the Z +jets process, which is the dominant source of the background in this channels.
- For the $e\mu$ channel, only p_T^{miss} , with the best resolution, is used to keep the signal.

Chapter 7

Event selection

Lepton (electron, muon and neutrino) and jet selection criteria have been described in chapter 6. For example, backgrounds arisen from misidentified leptons, W +jets and QCD processes, are reduced and controlled by optimizing the lepton selection criteria. In addition to such object selections, event selections based on the signal and background topologies have been performed in order to increase the sensitivity. Since the background composition depends strongly on different jet multiplicity and lepton flavor, the analysis is categorized as described in section 2.3. Selections applied to all categories, such as requiring to have an opposite charge lepton pair, is called “pre-selection” in this thesis. After the pre-selection, event selections specific to each category are applied. These event selections are optimized for the observed Higgs boson mass of $m_H \sim 125$ GeV. The kinematic spaces after the all event selections are defined as “signal regions (SR)” of the $H \rightarrow WW^* \rightarrow \ell\nu\ell\nu$ analysis. Details of the event selections are described in the following sections.

7.1 Pre-selections

After the initial requirements based on the data quality and triggers, events with exact two identified leptons are selected. Using these two leptons and missing transverse energy, the following pre-sections are performed:

- $p_T > 22$ (10) GeV for the leading lepton ℓ_1 (subleading lepton ℓ_2);
- Opposite-sign (OS) charge leptons;
- $m_{\ell\ell} > 10$ (12) GeV for $e\mu$ ($ee/\mu\mu$) channel, where $m_{\ell\ell}$ is the invariant mass of the di-lepton system;
- $|m_{\ell\ell} - m_Z| > 15$ GeV for $ee/\mu\mu$ channel; and
- $p_T^{\text{miss}} (E_{T,\text{rel}}^{\text{miss}}) > 20$ (40) GeV for $e\mu$ ($ee/\mu\mu$) channel.

The W boson decay is likely to produce a high- p_T lepton, thus $p_T^{\ell_1} > 22$ GeV is required to the leading lepton. Relatively small subleading lepton $p_T^{\ell_2} > 10$ GeV, is required because one of the W boson decays in the signal process is off its mass shell. The lepton pair is required to have OS charge since the SM Higgs boson is a neutral particle. This OS requirement reduces backgrounds such as the *Other* VV process, which may have a same-sign charge lepton pair even at the tree level diagrams. The $m_{\ell\ell} > 10$ (12) GeV for $e\mu$ ($ee/\mu\mu$) channel is required to remove meson resonances. Table 7.2 shows the expected event yields for the signal and backgrounds

Table 7.1: Summary of event selections. Entries specific to the $e\mu$ and $ee/\mu\mu$ lepton-flavor categories are noted as such. Otherwise, they are applied to both categories. All values of dimension or momentum are in GeV.

	$n_j = 0$	$n_j = 1$	$n_j \geq 2$ ggF
Pre-selection:			
select $WW^* \rightarrow \ell\nu\ell\nu$	$\left\{ \begin{array}{l} \text{Exactly two leptons with :} \\ p_T > 22 \text{ for the leading lepton } \ell_1 \\ p_T > 10 \text{ for the subleading lepton } \ell_2 \\ \text{Opposite charge leptons} \end{array} \right. \dots\dots\dots$		
reject mesons	$\left\{ \begin{array}{l} m_{\ell\ell} > 10 \text{ for } e\mu \\ m_{\ell\ell} > 12 \text{ for } ee/\mu\mu \end{array} \right. \dots\dots\dots$		
reject Z + jets	$\left\{ m_{\ell\ell} - m_Z > 15 \text{ for } ee/\mu\mu \dots\dots\dots \right.$		
reject Z + jets	$\left\{ \begin{array}{l} p_T^{\text{miss}} > 20 \text{ for } e\mu \\ E_{T,\text{rel}}^{\text{miss}} > 40 \text{ for } ee/\mu\mu \end{array} \right. \dots\dots\dots$		
Category-specific selection:			
reject Z + jets	$\left\{ \begin{array}{l} p_{T,\text{rel}}^{\text{miss}} > 40 (ee/\mu\mu) \\ f_{\text{recoil}} < 0.1 (ee/\mu\mu) \\ p_T^{\ell\ell} > 30 \\ \Delta\phi_{\ell\ell,\text{MET}} > \pi/2 \\ - \end{array} \right.$	$\left\{ \begin{array}{l} p_{T,\text{rel}}^{\text{miss}} > 35 (ee/\mu\mu) \\ f_{\text{recoil}} < 0.1 (ee/\mu\mu) \\ - \\ - \\ m_{\tau\tau} < (m_Z - 25 \text{ GeV}) \end{array} \right.$	$\left\{ \begin{array}{l} - \\ - \\ - \\ - \\ m_{\tau\tau} < (m_Z - 25 \text{ GeV}) \end{array} \right.$
reject QCD	$\left\{ - \right.$	$m_T^\ell > 50 (e\mu)$	$-$
reject top	$\left\{ - \right.$	$n_b = 0$	$n_b = 0$
select $H \rightarrow WW^*$	$\left\{ \begin{array}{l} m_{\ell\ell} < 55 \\ \Delta\phi < 1.8 \text{ rad} \end{array} \right.$	$\left\{ \begin{array}{l} m_{\ell\ell} < 55 \\ \Delta\phi < 1.8 \text{ rad} \end{array} \right.$	$\left\{ \begin{array}{l} m_{\ell\ell} < 55 \\ \Delta\phi < 1.8 \text{ rad} \end{array} \right.$

at each selection. It can be seen that the $ee/\mu\mu$ sample of 1.6×10^7 events is dominated by the Z +jets process after the $m_{\ell\ell} > 12$ GeV selection, which is significantly reduced by removing the Z boson resonance, $|m_{\ell\ell} - m_Z| > 15$ GeV. Since the signal process has neutrinos in the final state, applying a cut on the missing transverse energy is effective to discriminate the signal from the background processes without neutrinos in their final states, such as the Z +jets and QCD events. The missing transverse energy distributions motivating this selection are shown in figure 7.1. $p_T^{\text{miss}} > 20$ GeV in the $e\mu$ channel and $E_{T,\text{rel}}^{\text{miss}} > 40$ GeV in the $ee/\mu\mu$ channels are required. Among various algorithms to reconstruct the missing transverse energy, p_T^{miss} with the best resolution is chosen for the $e\mu$ channel to keep the signal and $E_{T,\text{rel}}^{\text{miss}}$ with the maximum Z +jets background rejection is used for the $ee/\mu\mu$ channels as described in section 6.6. These Z veto and missing transverse energy requirements achieve a factor of 3×10^3 reduction of the Z +jets background with respect to the initial sample in the $ee/\mu\mu$ channel, with a 30% of the signal efficiency. Table 7.1 summarizes the pre-selection together with the purposes of selections, including the category specific selections described in the following sections. Figure 7.2 shows the distributions of the number of jets after the pre-selection. It can be seen that each jet bin has different background compositions. This motivates the categorization of the data sample based on the jet multiplicity.

Table 7.2: Summary of the expected event yields at the pre-selections. The signal and backgrounds, except for W +jets and QCD, are normalized to the theoretical cross sections (see chapter 5). The W +jets and QCD backgrounds are estimated with the extrapolation factor method (see chapter 8). The signal is shown at $m_H = 125$ GeV. The uncertainties correspond to the statistical uncertainties on the MC simulations.

Pre-selections				
$e\mu$ category				
	Signal	WW	Other VV	Z + jets
lepton p_T	811.1 ± 2.4	11379.5 ± 14.5	4238.6 ± 20.3	45604.7 ± 95.9
OS leptons	785.2 ± 1.9	11340.8 ± 14.5	2125.7 ± 14.4	45150.4 ± 95.3
$m_{\ell\ell} > 12$ GeV	777.6 ± 1.9	11322.6 ± 14.5	2017.0 ± 13.9	45113.1 ± 95.2
$p_T^{\text{miss}} > 20$ GeV	664.6 ± 1.8	9531.5 ± 13.3	1643.9 ± 12.7	13616.2 ± 52.3
	Top	W +jets/QCD	Total Bkg.	Observed
lepton p_T	65091.4 ± 29.6	9684.2 ± 40.1	136065.8 ± 110.9	142993
OS leptons	64847.2 ± 29.5	5944.1 ± 31.2	129473.5 ± 106.5	136073
$m_{\ell\ell} > 12$ GeV	64768.8 ± 29.5	5902.6 ± 31.0	129189.3 ± 106.3	135734
$p_T^{\text{miss}} > 40$ GeV	60637.3 ± 28.5	3494.9 ± 21.6	88976.0 ± 66.0	93789
$ee/\mu\mu$ category				
	Signal	WW	Other VV	Z + jets
lepton p_T	876.8 ± 2.7	11830.4 ± 14.9	9728.2 ± 22.9	16190321.4 ± 8103.1
OS leptons	847.4 ± 2.2	11800.6 ± 14.9	7726.0 ± 18.5	16157185.0 ± 8095.3
$m_{\ell\ell} > 10$ GeV	825.3 ± 2.2	11743.0 ± 14.9	7541.7 ± 17.9	16127853.2 ± 8095.0
Z veto (for $ee, \mu\mu$)	768.1 ± 1.9	9217.3 ± 13.2	2647.0 ± 12.4	1828082.0 ± 1977.4
$E_{T,\text{rel}}^{\text{miss}} > 40$ GeV	248.6 ± 1.0	3733.1 ± 8.4	549.4 ± 6.1	43805.9 ± 279.7
	Top	W +jets/QCD	Total Bkg.	Observed
lepton p_T	66190.1 ± 29.8	26533.1 ± 152.4	16323019.5 ± 8104.7	16570089
OS leptons	65968.1 ± 29.7	25727.7 ± 149.0	16286780.8 ± 8096.8	16535346
$m_{\ell\ell} > 10$ GeV	65708.0 ± 29.6	24598.3 ± 144.9	16255670.4 ± 8096.4	16394493
Z veto (for $ee, \mu\mu$)	51955.3 ± 26.3	10064.0 ± 73.4	1904825.8 ± 1979.0	2014469
$E_{T,\text{rel}}^{\text{miss}} > 40$ GeV	5081.6 ± 8.0	723.5 ± 13.0	53939.2 ± 280.3	53384

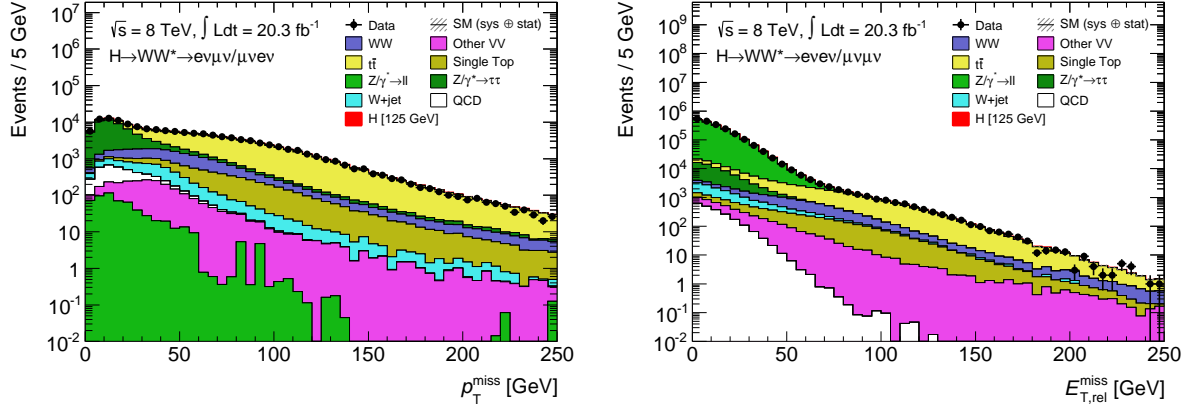


Figure 7.1: The p_T^{miss} distributions for the $e\mu$ channel and the $E_{T,\text{rel}}^{\text{miss}}$ distribution for the $ee/\mu\mu$ channel before the missing energy cut. The signal and backgrounds, except for the W +jets and QCD, are normalized to the theoretical cross sections (see chapter 5). The W +jets and QCD backgrounds are estimated with the extrapolation factor method (see chapter 8).

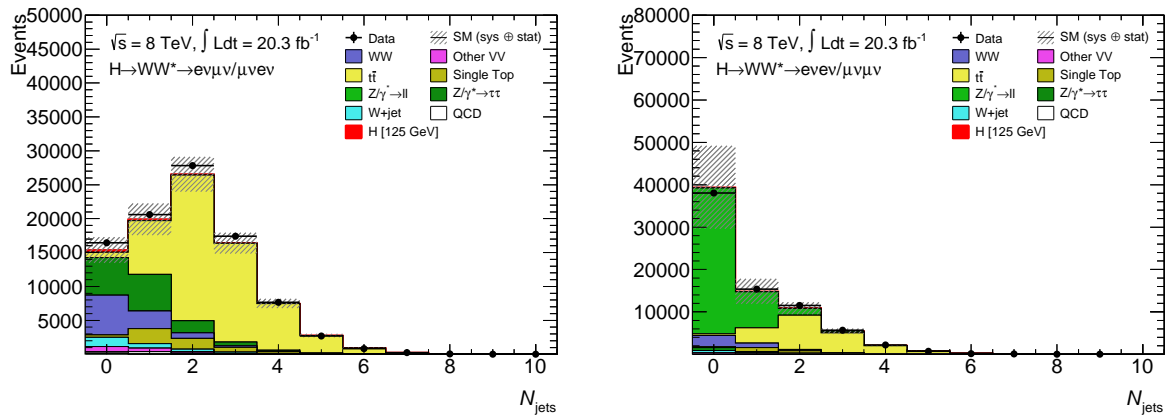


Figure 7.2: The number of jets distributions for the $e\mu$ and the $ee/\mu\mu$ channel after the pre-selections. The signal and backgrounds, except for the W +jets and QCD, are normalized to the theoretical cross sections (see chapter 5). The W +jets and QCD backgrounds are estimated with the extrapolation factor method (see chapter 8).

7.2 Selection for $n_j = 0$ category

The dominant sources of the backgrounds in the $n_j = 0$ category are the WW and Z +jets productions. The following selections aimed at suppressing these backgrounds are performed:

- $\Delta\phi_{\ell\ell,\text{MET}} > \pi/2$, where $\Delta\phi_{\ell\ell,\text{MET}}$ is the azimuthal angle between the di-lepton system and $p_{\text{T}}^{\text{miss}}$;
- $p_{\text{T},\ell\ell} > 30$ GeV, where $p_{\text{T},\ell\ell}$ is the p_{T} of the di-lepton system;
- $p_{\text{T},\text{rel}}^{\text{miss}} > 40$ GeV for $ee/\mu\mu$ channels;
- $m_{\ell\ell} < 55$ GeV;
- $\Delta\phi_{\ell\ell} < 1.8$, where $\Delta\phi_{\ell\ell}$ is the azimuthal angle between the two leptons; and
- $f_{\text{recoil}} < 0.1$, see text for the definition of f_{recoil} .

A potential mis-measurement of the missing transverse momentum is removed by requiring $p_{\text{T}}^{\text{miss}}$ to point away from the momentum of the di-lepton system, $\Delta\phi_{\ell\ell,\text{MET}} > \pi/2$. The p_{T} of the di-lepton system, $p_{\text{T},\ell\ell}$, in the Z +jets process is expected to be small since the di-lepton system need to be balanced without an ID jet in this category. Figure 7.4 (a) (b) show the $p_{\text{T},\ell\ell}$ distributions after the $\Delta\phi_{\ell\ell,\text{MET}}$ cut. $p_{\text{T},\ell\ell} > 30$ GeV is required to both the $e\mu$ and $ee/\mu\mu$ channels to suppress the Z +jets background. An additional requirement on the missing transverse momentum, $p_{\text{T},\text{rel}}^{\text{miss}} > 40$ GeV, is used to provide further reduction of the Z +jets background in the $ee/\mu\mu$ category.

Event selections based on the $H \rightarrow WW^*$ topology are also imposed. The spin-0 nature of the Standard Model Higgs boson combined with the V–A decay of the W bosons leads to a small opening angle between the two leptons in the final state as illustrated in figure 7.3. Thus, $\Delta\phi_{\ell\ell} < 1.8$ is required in order to discriminate the signal from the WW and Z +jets backgrounds effectively. Also the WW background is suppressed by a cut on $m_{\ell\ell}$ since the signal process is mostly distributed in $m_{\ell\ell} < m_H/2$, while the non-resonant WW is continuously distributed over $m_H/2$. A requirement of $m_{\ell\ell} < 55$ GeV is used, which is chosen to keep the signal with the observed mass ($m_H \sim 125$ GeV). The $m_{\ell\ell}$ and $\Delta\phi$ distributions after the $p_{\text{T},\ell\ell} > 30$ GeV cut are shown in figure 7.4 (c) (d). It can be seen that the expected signal (red histogram) is distributed on the selected region defined above.

After these selections, the Z +jets background is sufficiently reduced in the $e\mu$ category. However, it still dominates the $ee/\mu\mu$ samples. In this phase space after requiring the high $p_{\text{T},\ell\ell}$ and low $m_{\ell\ell}$, the di-lepton system in the remaining Z +jets background is expected to be balanced by a hadronic recoil consisting of soft jets, which are not reconstructed as ID jets. To prove the presence of such recoil, jets with $p_{\text{T}} > 10$ GeV are considered within a range of $3\pi/4 < \Delta\phi_{\ell\ell,\text{jet}} < 5\pi/4$, where $\Delta\phi_{\ell\ell,\text{jet}}$ is the azimuthal angle between the di-lepton system and jet. The fraction of the transverse momentum sum of these jets to the di-lepton transverse momentum is defined as follows:

$$f_{\text{recoil}} = \frac{\left| \sum_{\text{soft jets}, i} |\text{JVF}^i| \times p_{\text{T}}^i \right|}{p_{\text{T},\ell\ell}}. \quad (7.1)$$

To reduce the effect of jets originating from the pile-up interactions, the p_{T} of the jets are weighted by the JVF (see section 6.4) value. The f_{recoil} distribution is shown in figure 7.5. The

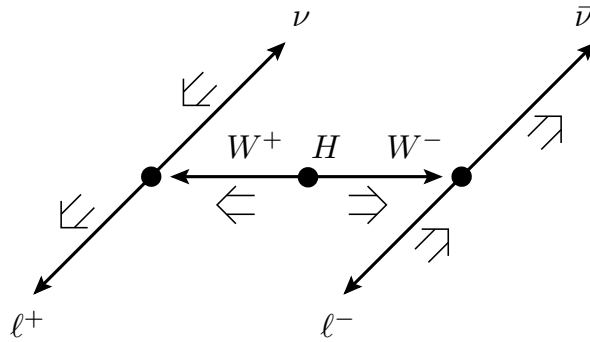


Figure 7.3: Illustration of the $H \rightarrow WW \rightarrow \ell\nu\ell\nu$ decay [117]. The thick small arrows indicate the particle’s direction of motion and the large arrows indicate their spin projections. The spin-0 Higgs boson decays to W bosons with opposite spins, and the spin-1 W bosons decay into leptons aligned their spins.

Z +jets background takes a non-zero value due to the presence of soft jets as expected. Thus, a requirement of $f_{\text{recoil}} < 0.1$ in the $ee/\mu\mu$ channels reduces the Z +jets background significantly. Table 7.3 summarizes the expected event yields for the signal and each background source in the $n_j = 0$ category. Expected signal-to-background ratios in the SRs are about 9% in the $e\mu$ channel and 7% in the $ee/\mu\mu$ channels. About 97% of the expected signal yield originates from the ggF production mode. The remaining background is dominated by the WW production in both the $e\mu$ and $ee/\mu\mu$ channels.

7.3 Selection for $n_j = 1$ category

The presence of a jet in this category increases the top background since the b -quark from the top-quark decay is likely to be reconstructed as a high- p_T jet. The following event selections are performed in this category:

- $n_b = 0$, where n_b is the number of b -tagged jets;
- Maximum $m_T^\ell > 50$ GeV, see text for the definition of m_T^ℓ ;
- $m_{\tau\tau} < (m_Z - 25 \text{ GeV})$ for $e\mu$ channel, see text for the definition of $m_{\tau\tau}$;
- $p_{T,\text{rel}}^{\text{miss}} > 35$ GeV for $ee/\mu\mu$ channels;
- $m_{\ell\ell} < 55$ GeV;
- $\Delta\phi_{\ell\ell} < 1.8$;
- $f_{\text{recoil}} < 0.1$.

To reduce the top background, the reconstructed jets with $p_T > 20$ GeV in the event are required to not be identified as containing a b -quark (see section 6.4), $n_b = 0$. After this requirement, the WW and Z +jets processes become also dominant as with the $n_j = 0$ category.

The production of a high- p_T jet allows for an improved rejection of the $Z \rightarrow \tau\tau$ background, which contributes to the $e\mu$ channel. Since the Z boson is boosted by jets, the τ leptons and its decay products are also boosted; they tend to be emitted close to each other. As a result,

Table 7.3: Summary of the expected event yields in the $n_j = 0$ category. The signal and backgrounds, except for the W +jets and QCD processes, are normalized to the theoretical cross sections (see chapter 5). The WW , Z +jets and Top backgrounds are corrected by normalization factors (NFs) from the data (see chapter 8). For the Z +jets column in the $ee/\mu\mu$ category, separated NFs of 1.05 for the $Z \rightarrow \tau\tau$ and 1.76 for the $Z \rightarrow ee/\mu\mu$ process are used. The W +jets and QCD backgrounds are estimated with the extrapolation factor method (see chapter 8). The expected number of signals is estimated at $m_H = 125$ GeV. The uncertainties correspond to the statistical uncertainties on the MC simulations.

$n_j = 0$ category				
<i>eμ</i> category				
	Signal	<i>WW</i>	Other VV	<i>Z</i> +jets
NFs	-	1.20	-	1.05
0 jet	322.4 ± 0.9	7007.7 ± 12.5	802.3 ± 9.2	5713.0 ± 35.5
$\Delta\phi_{\ell\ell, \text{MET}} > \pi/2$	322.1 ± 0.9	7002.6 ± 12.5	799.6 ± 9.2	5676.6 ± 35.4
$p_{T, \ell\ell} > 30$ GeV	272.6 ± 0.8	5605.6 ± 11.2	619.9 ± 8.1	847.1 ± 15.4
$m_{\ell\ell} < 55$ GeV	232.3 ± 0.6	1645.7 ± 6.0	383.1 ± 6.7	379.2 ± 8.9
$\Delta\phi_{\ell\ell} < 1.8$	208.8 ± 0.6	1480.6 ± 5.7	351.6 ± 6.4	31.0 ± 2.5
	Top	<i>W</i> +jets/QCD	Total Bkg.	Observed
NFs	1.08	-	-	-
0 jet	1218.3 ± 4.0	1571.7 ± 12.9	16314.0 ± 41.0	16423
$\Delta\phi_{\ell\ell, \text{MET}} > \pi/2$	1208.5 ± 4.0	1563.6 ± 12.8	16251.8 ± 40.9	16339
$p_{T, \ell\ell} > 30$ GeV	1085.8 ± 3.8	1082.2 ± 8.9	9241.0 ± 22.9	9339
$m_{\ell\ell} < 55$ GeV	218.2 ± 1.7	439.0 ± 6.4	3065.3 ± 14.2	3411
$\Delta\phi_{\ell\ell} < 1.8$	205.8 ± 1.6	286.8 ± 5.3	2355.9 ± 10.5	2642
<i>ee/μμ</i> category				
	Signal	<i>WW</i>	Other VV	<i>Z</i> +jets
NFs	-	1.20	-	NFs applied
0 jet	171.3 ± 0.6	3207.8 ± 8.6	357.9 ± 5.0	31777.9 ± 230.8
$\Delta\phi_{\ell\ell, \text{MET}} > \pi/2$	171.1 ± 0.6	3204.5 ± 8.6	354.9 ± 5.0	29170.6 ± 218.3
$p_{T, \ell\ell} > 30$ GeV	160.7 ± 0.6	2964.2 ± 8.2	308.9 ± 4.7	6720.8 ± 98.4
$p_{T, \text{rel}}^{\text{miss}} > 40$ GeV	129.1 ± 0.6	2497.7 ± 7.6	204.1 ± 3.6	903.9 ± 38.6
$m_{\ell\ell} < 55$ GeV	121.0 ± 0.5	1080.5 ± 5.0	106.5 ± 2.8	659.9 ± 14.8
$\Delta\phi_{\ell\ell} < 1.8$	117.1 ± 0.5	1051.9 ± 4.9	104.3 ± 2.7	648.4 ± 14.7
$f_{\text{recoil}} < 0.1$	74.8 ± 0.4	774.2 ± 4.2	69.4 ± 2.2	91.6 ± 5.3
	Top	<i>W</i> +jets/QCD	Total Bkg.	Observed
NFs	1.08	-	-	-
0 jet	625.0 ± 2.8	533.1 ± 11.2	36523.2 ± 231.3	38040
$\Delta\phi_{\ell\ell, \text{MET}} > \pi/2$	622.0 ± 2.8	518.4 ± 10.8	33891.4 ± 218.8	35445
$p_{T, \ell\ell} > 30$ GeV	591.5 ± 2.7	398.6 ± 6.7	11000.2 ± 99.1	11660
$p_{T, \text{rel}}^{\text{miss}} > 40$ GeV	519.4 ± 2.6	210.6 ± 4.0	4340.2 ± 39.7	4306
$m_{\ell\ell} < 55$ GeV	156.7 ± 1.4	134.0 ± 3.3	2140.1 ± 16.3	2197
$\Delta\phi_{\ell\ell} < 1.8$	152.3 ± 1.4	122.7 ± 3.2	2082.2 ± 16.1	2127
$f_{\text{recoil}} < 0.1$	71.1 ± 0.9	78.6 ± 2.5	1085.1 ± 7.6	1108

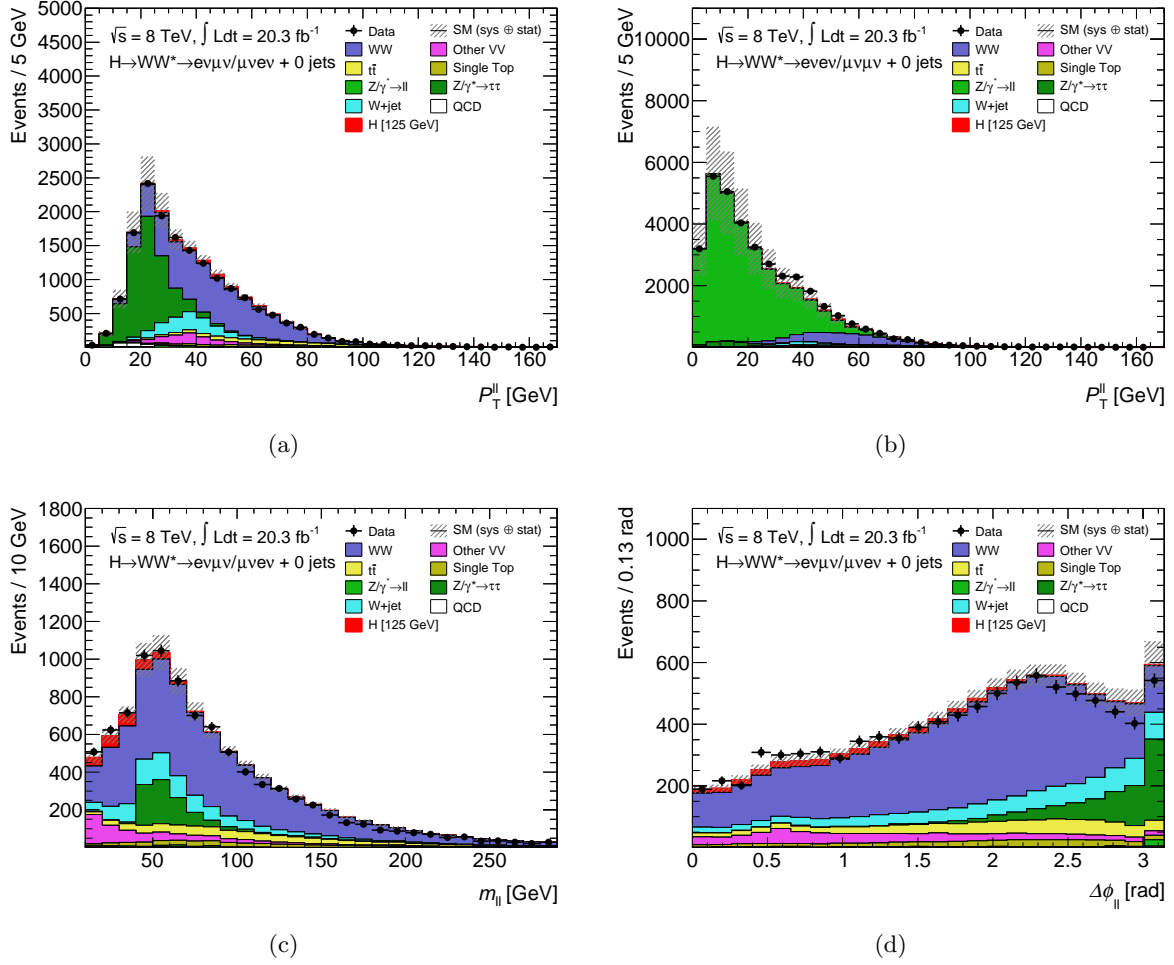


Figure 7.4: The $p_{T, \ell\ell}$ distributions for the $e\mu$ (a) and the $ee/\mu\mu$ (b) channel after the $\Delta\phi_{\ell\ell, MET}$ cut in $n_j = 0$ category; The $m_{\ell\ell}$ (c) and $\Delta\phi_{\ell\ell}$ (d) distributions for the $e\mu$ channel after the $p_{T, \ell\ell}$ cut in $n_j = 0$ category. The normalization factors for the WW , Z +jets and Top processes are applied as given in table 7.3.

the transverse mass constructed for each lepton, m_T^ℓ , becomes a good quantity to separate the $Z \rightarrow \tau\tau$ background and signal. The m_T^ℓ is obtained as follows:

$$m_T^\ell = \sqrt{2p_T^\ell \cdot p_T^{\text{miss}} \cdot (1 - \cos \Delta\phi)}, \quad (7.2)$$

where $\Delta\phi$ is the angle between the lepton momentum and p_T^{miss} . This m_T^ℓ tends to have small values for the $Z \rightarrow \tau\tau$ process since the $\Delta\phi$ is small as mentioned above, and large values for the signal process. The maximum m_T^ℓ is shown in figure 7.6. The maximum $m_T^\ell > 50 \text{ GeV}$ is required. This m_T^ℓ requirement is also effective in removing the QCD background.

The close proximity of the missing transverse momentum to the charged leptons also allows an approximation that the neutrinos are collinear with the visible products of the corresponding τ decay. With this assumption, the fractional momentum of the charged lepton from a given τ

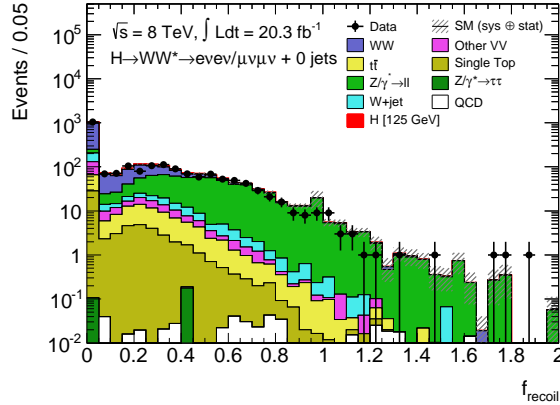


Figure 7.5: The f_{recoil} distribution for the $ee/\mu\mu$ channel after the $\Delta\phi_{\ell\ell} < 1.8$ cut. The normalization factors for the WW , Z +jets and Top processes are applied as given in table 7.3.

decay, x_1 and x_2 , can be calculated as follows:

$$x_{1(2)} = \frac{p_x^{\ell 1} p_y^{\ell 2} - p_y^{\ell 1} p_x^{\ell 2}}{p_x^{\ell 1} p_y^{\ell 2} - p_y^{\ell 1} p_x^{\ell 2} + p_x^{\ell 1(2)} p_y^{\text{miss}} - p_y^{\text{miss}} p_x^{\ell 2(1)}}, \quad (7.3)$$

where p_x and p_y denote the x and y components of the quantity. The mass of the τ lepton pair is thus evaluated as $m_{\tau\tau} = m_{\ell\ell}/\sqrt{x_1 x_2}$, if x_1 and x_2 are positive. A requirement of $m_{\tau\tau} < (m_Z - 25 \text{ GeV})$ reduces the $Z \rightarrow \tau\tau$ background significantly, which can be seen in figure 7.6.

These $Z \rightarrow \tau\tau$ rejections are not performed in the $ee/\mu\mu$ channels since this background is highly suppressed by the relative missing transverse energy cut, $E_{T,\text{rel}}^{\text{miss}} > 40 \text{ GeV}$, in the pre-selection thanks to the small $\Delta\phi$ between the missing energy and leptons. The ($p_{T,\text{rel}}^{\text{miss}}$, f_{recoil} , $m_{\ell\ell}$ and $\Delta\phi_{\ell\ell}$) cuts are applied with the same motivations as the $n_j = 0$ category, except that $p_{T,\text{rel}}^{\text{miss}}$ threshold is reduced to 35 GeV. Table 7.4 summarizes the expected event yields for the signal and each background sources in the $n_j = 1$ category. Expected signal-to-background ratios in the SRs are about 8% in the $e\mu$ channel and 6% in the $ee/\mu\mu$ channels. The ggF production mode dominates 85% of the expected signal yield. The dominant sources of the background are the WW and Top productions in both the $e\mu$ and $ee/\mu\mu$ channels.

7.4 Selection for $n_j \geq 2$ ggF-enriched category

In the $n_j \geq 2$ bins, both the ggF and VBF modes provide sizable contributions. Thus, the analysis is performed separately for ggF and VBF categories. The $n_j \geq 2$ ggF-enriched category is designed to be exclusive to selections of the VBF analysis in order to avoid duplicate events when the ggF and VBF results are combined. In this category, only the $e\mu$ final state is considered due to relatively low sensitivity of the signal strength measurement using the $ee/\mu\mu$ final state. The following event selections are performed in this $n_j \geq 2$ ggF-enriched category:

- $n_b = 0$;
- $m_{\tau\tau} < (m_Z - 25 \text{ GeV})$;
- VBF veto, see text for the definition;

Table 7.4: Summary of the expected event yields in the $n_j = 1$ category. The signal and backgrounds, except for the W +jets and QCD processes, are normalized to the theoretical cross sections (see chapter 5). The WW , Z +jets and Top backgrounds are corrected by the normalization factors from the data (see chapter 8). For the Z +jets column in the $ee/\mu\mu$ category, separated NFs of 1.00 for the $Z \rightarrow \tau\tau$ and 2.40 for the $Z \rightarrow ee/\mu\mu$ process are used. The W +jets and QCD backgrounds are estimated with the extrapolation factor method (see chapter 8). The expected number of signals is estimated at $m_H = 125$ GeV. The uncertainties correspond to the statistical uncertainties on the MC simulations.

$n_j = 1$ category				
$e\mu$ category				
	Signal	WW	Other VV	$Z + \gamma$ /jets
NFs	-	1.04	-	1.00
1 jet	191.8 ± 1.0	2723.3 ± 7.2	517.8 ± 6.8	5685.1 ± 31.5
b -jet veto	164.9 ± 0.9	2380.4 ± 6.7	441.2 ± 6.3	4956.1 ± 29.2
Max. $m_T^\ell > 50$ GeV	140.3 ± 0.8	2238.2 ± 6.5	381.7 ± 5.9	2021.0 ± 20.4
$m_{\tau\tau} < (m_Z - 25$ GeV)	119.4 ± 0.7	1648.8 ± 5.6	287.4 ± 5.2	708.2 ± 11.8
$m_{\ell\ell} < 55$ GeV	99.9 ± 0.6	481.0 ± 3.0	145.4 ± 3.9	387.0 ± 7.9
$\Delta\phi_{\ell\ell} < 1.8$	87.1 ± 0.5	413.3 ± 2.8	124.4 ± 3.6	27.2 ± 2.1
	Top	W +jets/QCD	Total Bkg.	Observed
NFs	1.06	-	-	-
1 jet	10681.0 ± 11.9	996.8 ± 12.2	20616.4 ± 37.2	20607
b -jet veto	2158.6 ± 5.4	803.4 ± 10.8	10749.3 ± 32.9	10859
Max. $m_T^\ell > 50$	2063.1 ± 5.2	539.1 ± 7.2	7247.6 ± 24.0	7368
$m_{\tau\tau} < (m_Z - 25$ GeV)	1489.6 ± 4.4	343.0 ± 5.6	4478.2 ± 15.8	4574
$m_{\ell\ell} < 55$ GeV	406.6 ± 2.3	147.3 ± 4.0	1568.0 ± 10.4	1656
$\Delta\phi_{\ell\ell} < 1.8$	370.2 ± 2.2	94.2 ± 2.9	1029.4 ± 6.2	1129
$ee/\mu\mu$ category				
	Signal	WW	Other VV	$Z + \gamma$ /jets
NFs	-	1.04	-	NFs applied
1 jet	77.4 ± 0.7	1098.8 ± 4.6	191.5 ± 3.5	8369.3 ± 109.6
b -jet veto	66.7 ± 0.6	961.3 ± 4.3	163.2 ± 3.3	6884.2 ± 97.2
$p_{T,\text{rel}}^{\text{miss}} > 35$ GeV	46.6 ± 0.5	733.0 ± 3.8	102.2 ± 2.5	290.1 ± 21.0
$m_{\ell\ell} < 55$ GeV	42.7 ± 0.4	289.2 ± 2.4	49.2 ± 1.8	233.9 ± 9.6
$\Delta\phi_{\ell\ell} < 1.8$	38.6 ± 0.4	262.3 ± 2.3	44.4 ± 1.7	199.9 ± 8.6
$f_{\text{recoil}} < 0.10$ (SF)	23.2 ± 0.3	185.9 ± 1.9	29.5 ± 1.4	27.5 ± 3.0
	Top	W +jets/QCD	Total Bkg.	Observed
NFs	NF = 1.06	-	-	-
1 jet	4750.4 ± 8.0	190.3 ± 6.7	14624.5 ± 110.2	15344
b -jet veto	966.1 ± 3.6	147.5 ± 5.8	9140.4 ± 97.6	9897
$p_{T,\text{rel}}^{\text{miss}} > 35$ GeV	758.3 ± 3.1	68.0 ± 2.5	1953.5 ± 21.9	2095
$m_{\ell\ell} < 55$ GeV	265.0 ± 1.9	37.8 ± 2.0	876.2 ± 10.4	960
$\Delta\phi_{\ell\ell} < 1.8$	246.4 ± 1.8	30.5 ± 1.8	784.5 ± 9.4	889
$f_{\text{recoil}} < 0.10$	141.4 ± 1.4	17.5 ± 1.3	401.9 ± 4.3	467

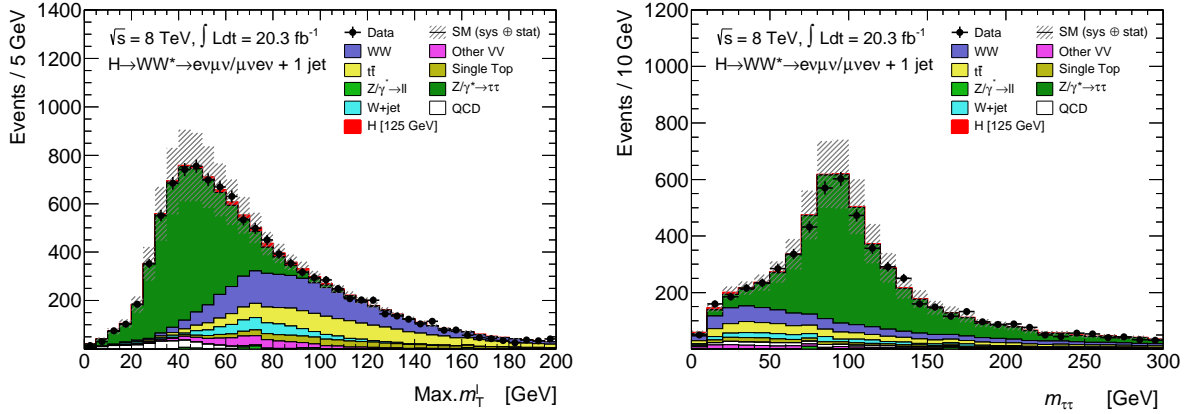


Figure 7.6: The maximum m_T^ℓ and $m_{\tau\tau}$ distributions for the $e\mu$ channel after the $n_b = 0$ cut in the $n_j = 1$ category. The normalization factors for the WW , Z +jets and Top processes are applied as given in table 7.4.

- VH veto, see text for the definition;
- $m_{\ell\ell} < 55$ GeV; and
- $\Delta\phi_{\ell\ell} < 1.8$;

At first, the b -jet veto and $m_{\tau\tau} < (m_Z - 25$ GeV) cut, which are common to the $n_j = 1$ category, are required to suppress the Top and Z +jets backgrounds. At second, a VBF veto is required, which achieves the orthogonality to the VBF analysis. The VBF analysis is performed by exploiting a specific topology. The two quarks scattered at a small angle in the VBF production lead to two energetic jets with a large separation in rapidity, Δy_{jj} , and a large invariant mass, m_{jj} . The Δy_{jj} and m_{jj} distributions after the $n_j \geq 2$ requirement are shown in figure 7.7 in case of the ggF and VBF production modes. With these discriminant variables, a multivariate analysis is performed using the boosted decision tree algorithm (see appendix A.1). Event selections for the VBF-enriched analysis are summarized in table A.1. This ggF-enriched category is thus required to satisfy that at least one of the VBF specific selections fails. The remaining sample still contains a sensitive region for the VH analysis, where the associated W or Z boson decays in hadronically. This region is removed by requiring $\Delta\eta_{jj} > 1.2$ and $|m_{jj} - 85$ GeV| > 15 GeV. Finally, the Higgs topological selections, $m_{\ell\ell} < 55$ GeV and $\Delta\phi_{\ell\ell} < 1.8$, are required. The $m_{\ell\ell}$ and $\Delta\phi_{\ell\ell}$ distributions after the VH veto are shown in figure 7.8. In the signal region of this category, the expected signal-to-background ratio is about 5%, and the Top production is the dominant source of the backgrounds as shown in table 7.5. The expected yield of the ggF production mode is about 74% of the total expected signal yield.

Finally, table 7.4 summarize the event selection efficiencies with respect to the initial data samples (before applying the pre-selection) for all analysis categories. In the $e\mu$ ($ee/\mu\mu$) category, about factor of 1.0×10^1 (1.0×10^3) background rejection compared to the corresponding signal efficiency is achieved.

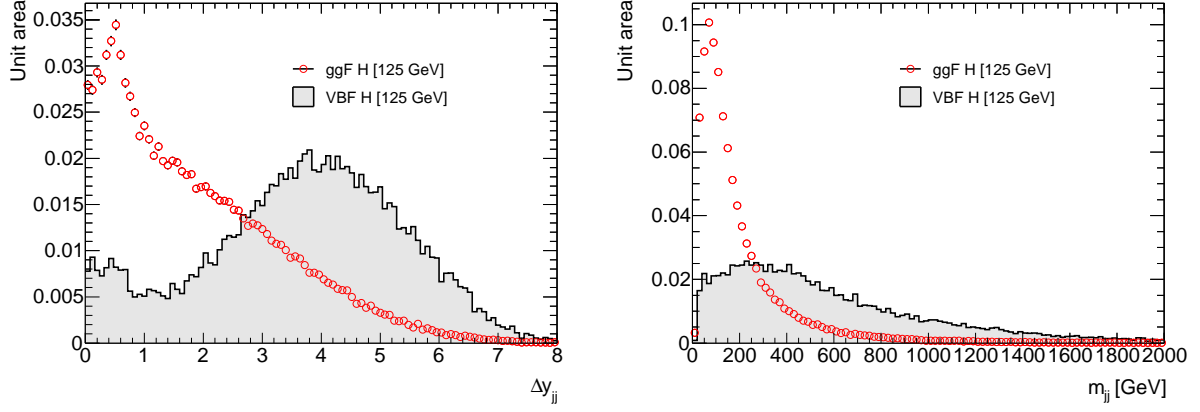


Figure 7.7: The Δy_{jj} and m_{jj} distributions after the $n_j \geq 2$ requirement. Comparisons are made with the ggF and VBF MC samples.

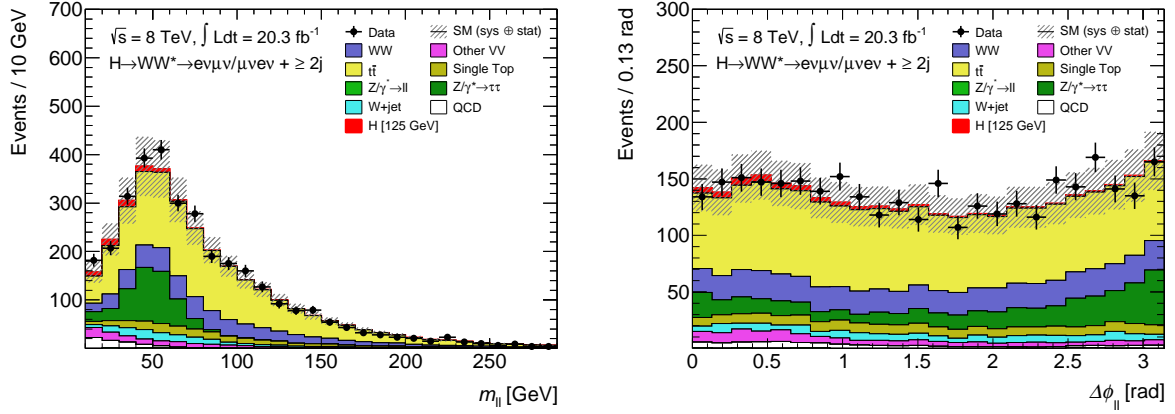


Figure 7.8: The $m_{\ell\ell}^e$ and $\Delta\phi_{\ell\ell}$ distributions for the $e\mu$ channel after the VH veto in the $n_j \geq 2$ ggF-enriched category. The normalization factors for the Z +jets and Top processes are applied as given in table 7.5.

Table 7.5: Summary of the expected event yields in the $n_j \geq 2$ ggF-enriched category. The signal and backgrounds, except for the W +jets and QCD processes, are normalized to the theoretical cross sections (see chapter 5). The Z +jets and Top backgrounds are corrected by the normalization factors from the data (see chapter 8). The W +jets and QCD backgrounds are estimated with the extrapolation factor method (see chapter 8). The signal is shown at $m_H = 125$ GeV. The uncertainties correspond to the statistical uncertainties on the MC simulations.

$n_j \geq 2$ ggF-enriched category				
$e\mu$ category				
	Signal	WW	Other VV	$Z + \gamma$ /jets
NFs	-	-	-	1.00
≥ 2 jets	150.4 ± 1.1	1322.7 ± 4.3	323.8 ± 5.6	2514.1 ± 23.9
b -jet veto	110.3 ± 0.9	961.9 ± 3.7	232.5 ± 4.7	1830.6 ± 20.4
$m_{\tau\tau} < (m_Z - 25 \text{ GeV})$	81.6 ± 0.7	609.6 ± 2.9	152.0 ± 3.9	479.6 ± 9.1
VBF veto	66.5 ± 0.7	592.1 ± 2.9	147.7 ± 3.9	472.7 ± 9.0
VH veto	57.5 ± 0.6	531.1 ± 2.7	131.7 ± 3.7	419.4 ± 8.5
$m_{\ell\ell} < 55 \text{ GeV}$	48.4 ± 0.5	157.6 ± 1.5	65.8 ± 2.7	279.9 ± 6.9
$\Delta\phi_{\ell\ell} < 1.8$	44.2 ± 0.4	140.4 ± 1.4	60.0 ± 2.6	131.8 ± 4.7
	Top	W +jets/QCD	Total Bkg.	Observed
NFs	1.05	-	-	-
≥ 2 jets	52078.2 ± 27.3	959.5 ± 12.3	57237.1 ± 39.0	56759
b -jet veto	3195.9 ± 6.6	407.2 ± 7.5	6651.7 ± 23.5	6777
$m_{\tau\tau} < (m_Z - 25 \text{ GeV})$	2126.7 ± 5.4	247.6 ± 5.6	3620.7 ± 13.0	3826
VBF veto	2094.1 ± 5.4	240.7 ± 5.6	3551.6 ± 12.8	3736
VH veto	1872.9 ± 5.1	211.6 ± 5.2	3170.1 ± 12.1	3305
$m_{\ell\ell} < 55 \text{ GeV}$	572.8 ± 2.8	124.1 ± 4.4	1202.5 ± 9.2	1310
$\Delta\phi_{\ell\ell} < 1.8$	523.3 ± 2.7	98.9 ± 3.8	955.4 ± 7.3	1017

Table 7.6: Summary of the event selection efficiencies with respect to the initial data samples (before applying the pre-selection).

$n_j = 0$ category				
	Signal	WW	Other VV	Z +jets
$e\mu$ SR	24 %	13 %	7 %	6×10^{-2} %
	Top	W +jets/QCD	Total Bkg.	Observed
$e\mu$ SR	3×10^{-1} %	3 %	2 %	2 %
<hr/>				
	Signal	WW	Other VV	Z +jets
$ee/\mu\mu$ SR	8 %	6 %	7×10^{-1} %	6×10^{-4} %
	Top	W +jets/QCD	Total Bkg.	Observed
$ee/\mu\mu$ SR	1×10^{-1} %	2×10^{-1} %	7×10^{-3} %	6×10^{-3} %
<hr/>				
$n_j = 1$ category				
	Signal	WW	Other VV	Z +jets
$e\mu$ SR	10 %	4 %	3 %	5×10^{-2} %
	Top	W +jets/QCD	Total Bkg.	Observed
$e\mu$ SR	6×10^{-1} %	8×10^{-1} %	7×10^{-1} %	7×10^{-1} %
<hr/>				
	Signal	WW	Other VV	Z +jets
$ee/\mu\mu$ SR	3 %	2 %	3×10^{-1} %	2×10^{-4} %
	Top	W +jets/QCD	Total Bkg.	Observed
$ee/\mu\mu$ SR	2×10^{-1} %	5×10^{-2} %	2×10^{-3} %	3×10^{-3} %
<hr/>				
$n_j \geq 2$ ggF-enriched category				
	Signal	WW	Other VV	Z +jets
$e\mu$ SR	5 %	1 %	1 %	2×10^{-1} %
	Top	W +jets/QCD	Total Bkg.	Observed
$e\mu$ SR	8×10^{-1} %	9×10^{-1} %	6×10^{-1} %	6×10^{-1} %

Chapter 8

Background estimation

In order to perform the measurements of the properties of the Higgs boson, it is necessary to understand and estimate the backgrounds precisely. Almost all electroweak and QCD processes presented in the Standard Model could contribute to the $H \rightarrow WW^* \rightarrow \ell\nu\ell\nu$ analysis as backgrounds. The expected yields of the total background in the signal regions (see chapter 7) are about ten times higher than the signal, where the backgrounds mainly consist of WW , other di-bosons (*Other VV*), Top, W +jets, multi-jets (QCD) and Drell-Yan (Z +jets) processes. For a given background, the remaining difference of the prediction of the Monte Carlo simulation (see chapter 5) from data is corrected using the data as much as possible, or the estimation is performed entirely from the data to obtain the precision. The basic ideas of the background estimation are categorized as follows:

- **NORM:** A normalization of the MC is corrected by a data-based normalization factor (NF), while kinematic shapes are still estimated by the MC. The NF is generally defined as the ratio of the data and MC in a background-enriched region (control region, CR). This obtained NF is multiplied to the MC prediction in the SR. A systematic uncertainty is derived from the variation in the ratio α of the number of events in the SR to CR ($\alpha = N^{\text{SR}}/N^{\text{CR}}$) by varying a parameter of MC.
- **DATA:** Both normalization and kinematic shapes are estimated from the data in this category. An extrapolation factor is multiplied to the CR events of the data. This extrapolation factor from the CR to SR is evaluated using a dedicated data sample. A systematic uncertainty is estimated by the difference of properties between the extrapolation factor and the CR.
- **MC:** The MC prediction normalized to the theoretical cross section (see table 5.2) is used. Theoretical uncertainties are assigned.

Since the composition of the background depends on the number of jets and lepton flavors in the final state, the background estimation techniques are performed in different ways in the each analysis category. The dominant sources of the background in each category are generally estimated by the **NORM** technique. The **DATA** technique is also used when a uncertainty on the MC estimation is expected to be a dominant source of systematic uncertainties. Table 8.1 summarizes the methods used for the various background processes and channels. In this chapter, the background estimations using the data are performed in an order as shown in figure 8.1. The MC simulation normalized to the theoretical cross section is used at a step before the corresponding background estimation is fixed. For the final results, NFs of the **NORM** method

are determined simultaneously in the fit (see chapter 9). In the following sections, details of the background estimation for each process are described. Also relevant systematic uncertainties are given.

Table 8.1: Background estimation methods. See text for definitions.

		WW	$Other VV$	Top	$Z \rightarrow \ell\ell$	$Z \rightarrow \tau\tau$	W +jets	QCD
0jet	$e\mu$	NORM	DATA	NORM	MC	NORM	DATA	DATA
	$ee/\mu\mu$	NORM	MC	NORM	NORM	NORM	DATA	DATA
1jet	$e\mu$	NORM	DATA	NORM	MC	NORM	DATA	DATA
	$ee/\mu\mu$	NORM	MC	NORM	NORM	NORM	DATA	DATA
≥ 2 jet	$e\mu e$	MC	MC	NORM	MC	NORM	DATA	DATA



Figure 8.1: Scheme of background determinations before the fit.

8.1 W +jets background

The W +jets background originates from an associated production of a W boson with jets, where one of the jets is misidentified as a prompt lepton. The W +jets background has similar kinematic shapes of the signal, and contributes about 10% of total expected backgrounds. This background is estimated with a data-driven method (categorized into DATA) since it is difficult to model the probability of misidentifications of a jet to a lepton in the simulation precisely. In this section, the background estimation technique and its performance are described.

8.1.1 The extrapolation factor method

The W +jets background is generally estimated with “extrapolation factor method” in the all analysis channels. Part of the W +jets background in the $e\mu$ sample in $n_j = 0$ and $n_j = 0$ categories is estimated with the combination of the “OS-SS method”, which is described in section 8.3. The procedure of the extrapolation factor method is the following:

- 1: Construct a CR from data enriched with the background process. For the W +jets case, one of the two leptons satisfies the full lepton criteria defined at section 6.6 (denoted “ID”), and the other lepton is required an alternative lepton criteria (denoted “anti-ID”) aimed at enhancing misidentified leptons from jets.
- 2: Compute an extrapolation factor defined as $f_l \equiv N_{\text{ID}}/N_{\text{anti-ID}}$ ($l = e$ or μ) also from data samples. In this analysis, two types of data sample, Z +jets and di-jets, are used to obtain the extrapolation factors. The Z +jets (di-jets) sample is used for the W +jets (QCD) estimation since the jet compositions are similar.

- 3: Multiply the extrapolation factor to the control region to estimate the background in the SR:

$$N_{\text{ID+ID}}^{\text{W+jets}} = f \times N_{\text{ID+anti-ID}}^{\text{W+jets}} = \frac{N_{\text{id}}}{N_{\text{anti-ID}}} \times N_{\text{ID+anti-ID}}^{\text{W+jets}}. \quad (8.1)$$

W +jets control region

The W +jets control region is constructed with the ID lepton and anti-ID lepton requirement, but otherwise events in the CR are required to pass the signal selections described in chapter 7. By requiring the same event selections as well as triggers, the CR allows to estimate kinematic shapes of the background process in the SR. The anti-ID lepton definition is designed to preferentially select the non-prompt lepton originated from the decay of hadrons, or a lepton due to the misidentification. This is achieved by loosening the isolation requirements and reverting the **Medium** identification for electrons, and also loosening the isolation requirements and removing the d_0 requirement for muons. In addition, the anti-ID lepton is required to fail the ID lepton selection. The definition of the anti-ID lepton is summarized in table 8.2, with the ID lepton definition in table 6.2. These anti-id lepton selections achieve a good purity of the W +jets process in the CR as designed. However, additional “triggerable” selections are applied in order to avoid a small bias caused by the online selection:

- **Electron:** “EF_{e24vhi,e60}_medium1”, “EF_2e12Tvh.loose1” and “EF_e12Tvh_medium1_mu8” triggers (see section 5.1) are used in the $H \rightarrow WW^* \rightarrow \ell\nu\ell\nu$ analysis, where “medium1” means **Medium** identification criterion is required to electrons at the trigger. “i” means the track isolation, $p_{\text{Tcone20}}/p_{\text{T}} < 0.1$. Since the anti-ID electrons shown in table 8.2 cannot pass the triggers due to **Medium** identification veto, there is a bias by losing the part of acceptance of the CR. Thus, the triggerable anti-ID selections are defined, which require **Medium** identification to avoid the bias as shown in table 8.3. However, it is not feasible to use the triggerable anti-ID definition for the whole events to obtain the CR. The $WZ, W\gamma^{(*)}, ZZ$ and $Z\gamma^{(*)}$ (denoted as “electroweak” process in this section) contaminations to the W +jets CR become so large in the triggerable selection because the prompt leptons are more likely to be selected in this case. Since most events in the W +jets CR are triggered by the leading lepton coming from the W decay satisfying the ID lepton criteria, the bias originating from the anti-ID selection is at a few % level. On the other hand, the bias in the QCD CR (see section 8.2) is considerable since two anti-ID leptons are required in this region. Such events are mainly accepted throughout the di-lepton triggers because the di-lepton triggers require looser selections compared to the single lepton triggers. Thus, the triggerable anti-ID selection is applied to the events firing only the di-lepton triggers to keep the purity of the W +jets process in the W +jets CR and reduce the bias in the QCD CR.
- **Muon:** “EF_{mu24i,mu36}_tight”, “EF_mu18_mu8_EFFS” and “EF_e12Tvh_medium1_mu8” triggers (see section 5.1) are used for muons, where “i” means the track isolation, $p_{\text{Tcone20}}/p_{\text{T}} < 0.1$. The triggerable anti-ID selection is defined with $p_{\text{Tcone30}}/p_{\text{T}} < 0.12$ to avoid the bias, and it is used in events which are fired by only EF_mu24i_tight trigger. The bias is therefore completely removed. The purity of the the W +jets process in the W +jets CR is still kept since most events are triggered by not only EF_mu24i_tight but also EF_mu36_tight.

Figure 8.2 shows different distributions in the W +jets CR after the $\Delta\phi_{\ell\ell}$ cut. The figures contain events collected with both the anti-ID and triggerable anti-ID definitions. The purity of the W +jets process in the CR reaches 88%. The other processes are subtracted from data using the MC expectations when extrapolating the CR to SR.

Table 8.2: The definition of anti-ID leptons. Boldface criteria are those different from the ID lepton.

p_T [GeV]	identification	calorimeter isolation	track isolation	impact parameters
electron				
10–	Fail Medium	$eT_{\text{cone30}}/E_T < \mathbf{0.30}$	$pT_{\text{cone30}}/E_T < \mathbf{0.16}$	$ z_0 \times \sin(\theta) < 0.4$ mm, $ d_0/\sigma(d_0) < 3$
muon				
10–15		$eT_{\text{cone30}}/p_T < \mathbf{0.15}$		$ z_0 \times \sin(\theta) < 1.0$ mm,
15–20	CB muon	$eT_{\text{cone30}}/p_T < \mathbf{0.25}$	removed	d_0 requirement
20–		$eT_{\text{cone30}}/p_T < \mathbf{0.30}$		removed

Table 8.3: The definition of triggerable anti-ID leptons. Boldface criteria are those different from the ID lepton.

p_T [GeV]	identification	calorimeter isolation	track isolation	impact parameters
electron				
10–	Medium	removed	removed	$ z_0 \times \sin(\theta) < \mathbf{1.2}$ mm, $ d_0/\sigma(d_0) < \mathbf{9}$
muon				
10–	CB muon	removed	$pT_{\text{cone30}}/p_T < \mathbf{0.12}$	$ z_0 \times \sin(\theta) < 1.0$ mm, d_0 requirement removed

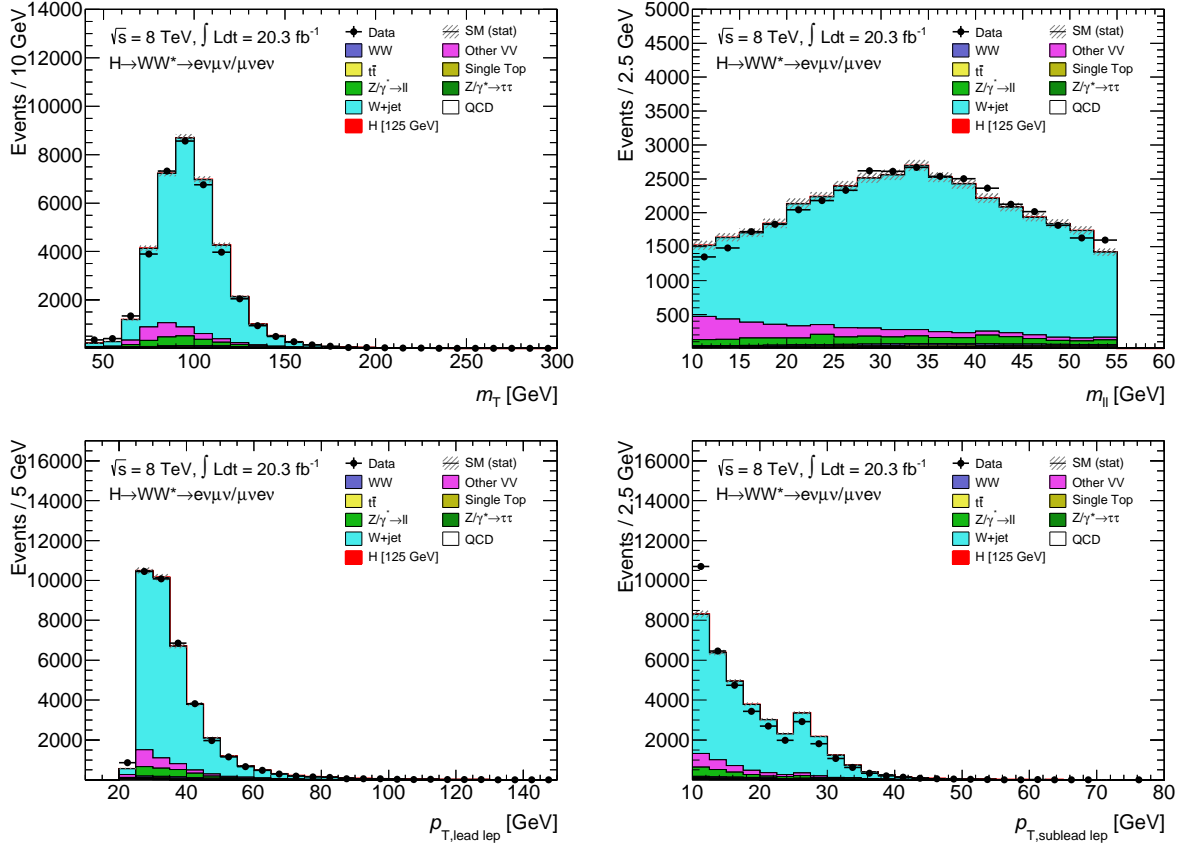


Figure 8.2: The m_T , $m_{\ell\ell}$, $p_T^{\ell 1}$ and $p_T^{\ell 2}$ distributions for the W +jets control region in the $e\mu$ channel after the $\Delta\phi_{\ell\ell}$ cut. The figures show the distributions combined with the $n_j = 0$, $n_j = 1$ and $n_j \geq 2$ ggF-enriched categories. The W +jets process is simulated with the ALPGEN+PYTHIA6, and normalized to data. Only statistical uncertainty is included.

Z+jets extrapolation factor

An extrapolation factor as a function of p_T is measured in data using a Z +jets enriched sample. Ideally, the extrapolation factor should be measured in a W +jets sample to avoid biases, for example differences of the jet composition between the W +jets and measuring sample. However, there are difficulties to measure the extrapolation factor in data using the W +jets sample. A W +jets enriched region would be selected with ID+anti-ID leptons and a missing transverse energy as shown above, and it would be possible to count the number of anti-ID leptons for the denominator of the extrapolation factor. However, also a W +jets enriched region with ID+ID leptons needs to be considered in order to count the numerator. This region is dominated by the WW process, and it is hard to specify which lepton comes from the jet. The Z +jets enriched sample solves these problems since the Z +jets process can be easily selected with the mass of Z boson requirement, and an additional lepton which is not coming from the decay of Z boson can be treated as a lepton from the jet with high purity.

The event selection of the Z +jets samples proceeds as follows:

- Exact one opposite-sign charge lepton pair is required to be in $76 < m_{\ell\ell} < 107$ GeV, with “medium-ID” lepton selection criteria. See text for the definition of medium-ID lepton.
- An event is removed if there is another Z boson candidate in $76 < m_{\ell\ell} < 107$ GeV, with “loose-ID” lepton selection criteria. See text for the definition of loose-ID lepton.
- An event is removed if there is a W boson candidate in $m_T^\ell > 30$ GeV, with “loose-ID” lepton selection criteria.

“medium-ID” leptons are defined by changing the identification from VeryTightLH to Medium for electrons, and loosening the z_0 requirement for muons to gain about 10 % of the Z reconstruction. Exactly one medium-ID lepton pair is required to be in the Z boson mass. ID or anti-ID leptons not matched to the medium-ID leptons from the Z decay are used in the calculation of the extrapolation factor as illustrated in figure 8.3. Also “loose-ID” lepton having $p_T > 7$ GeV without the identification and isolation requirements is defined aimed at finding additional Z or W bosons in the events in order to remove the electroweak process. Events are removed if they satisfy $76 < m_{\ell\ell} < 107$ GeV or $m_T^\ell > 30$ GeV with this loose-ID leptons. Figure 8.4 shows the p_T distributions for the ID and anti-ID leptons in this Z +jets data sample. Remaining electroweak contaminations in the Z +jets sample are subtracted using the MC prediction from data.

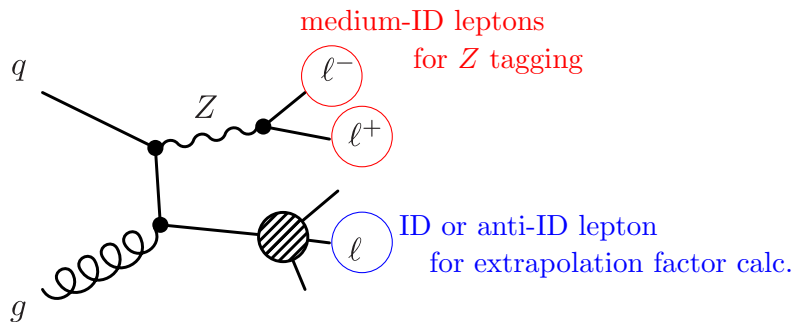


Figure 8.3: Illustration of lepton selections for the Z +jets extrapolation factor calculation.

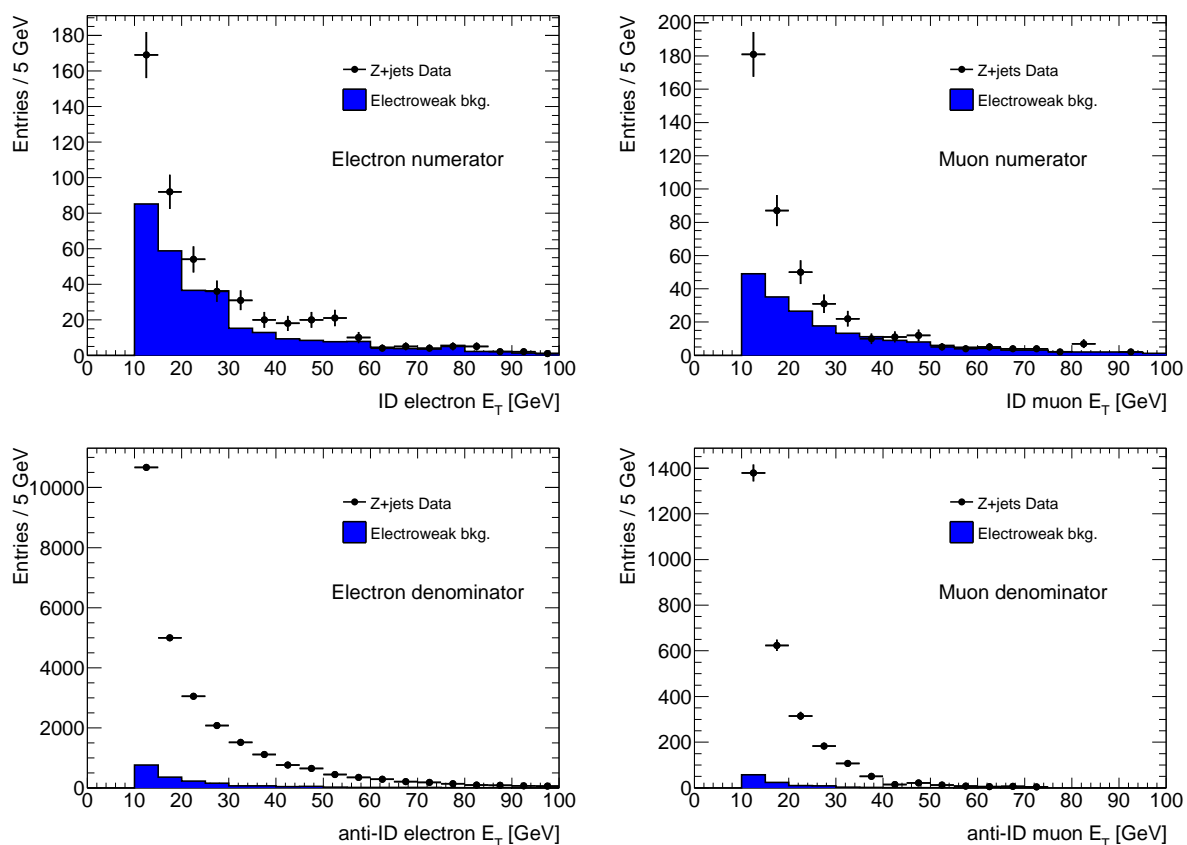


Figure 8.4: The p_T distributions of ID (top row) and anti-ID (bottom row) electrons (right column) and muons (left column) in the Z +jets data sample. The dots are the data, and the histograms are the electroweak process other than the Z +jets process estimated by the MC.

The extrapolation factors need to be calculated for the anti-ID definition and triggerable anti-ID definition separately. Figure 8.5 shows the extrapolation factors for the the anti-ID definition as a function of p_T measured in the Z +jets data. The extrapolation factor depends on not only p_T but also η of leptons. However, it is statistically limited to divide the Z +jets extrapolation factor by η , so the η dependence is derived from the di-jets extrapolation factor described in section 8.2. Also extrapolation factors for the triggerable anti-ID definition are calculated in the di-jets sample since the electroweak contamination in the Z +jets sample increases with the triggerable anti-ID definition.

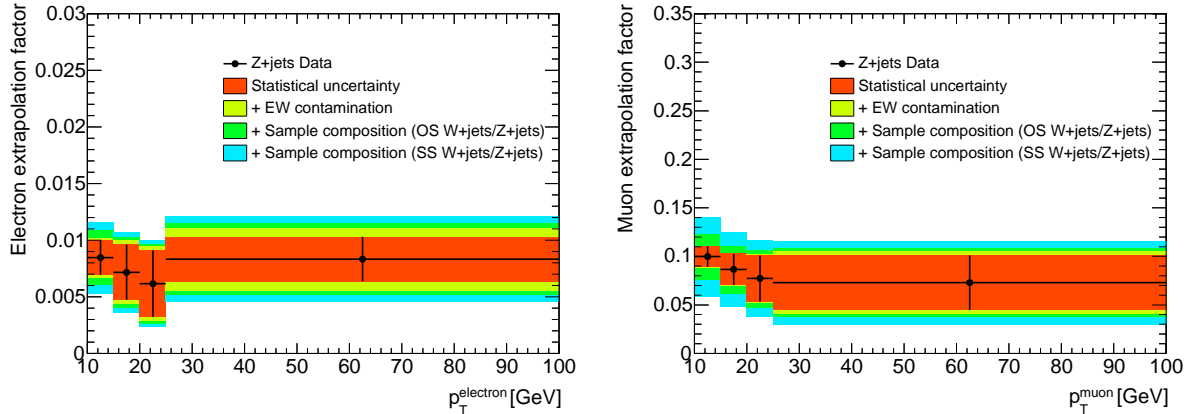


Figure 8.5: Extrapolation factors as a function of p_T for electrons (left) and muons (right). The extrapolation factors are determined in the Z +jets data. The colored bands indicate systematic uncertainties. EW contamination refers to the uncertainty due to the subtraction of the electroweak processes presented in the Z +jets sample. Sample composition refers to the largest variation of the correction factor from ALPGEN+PYTHIA6 to ALPGEN+PYTHIA8 and ALPGEN+HERWIG simulations.

The Z +jets extrapolation factor could be different from that of the W +jets due to differences of the jet kinematics and flavor composition. In particular, a W +jets extrapolation factor is expected to depend on the charge combination of the two leptons in the final state. This is also because of the differences in the jet flavor composition. The W boson production with a c -quark as shown by the left diagram in figure 8.6, where the second lepton comes from the semileptonic decay of a charmed hadron, is likely to result in an opposite-sign pair. On the other hand, the $W + b\bar{b}$ production as shown by the right diagram can be assumed that the process equally go into the opposite-sign (OS) and same-sign (SS) because the lepton production is independent from the charge of b -quarks. Therefore, the Z +jets extrapolation factor measured in data is corrected to both OS W +jets and SS W +jets extrapolation factors using the MC samples. The correction factor for the SS events is later needed for the OS-SS method described in section 8.3. The correction factors, c_{OS} and c_{SS} , are defined as follows:

$$f_{OS} = c_{OS} \times f^{Z+jets,data} = \frac{f_{OS}^{W+jets,MC}}{f^{Z+jets,MC}} \times f^{Z+jets,data}, \quad (8.2)$$

$$f_{SS} = c_{SS} \times f^{Z+jets,data} = \frac{f_{SS}^{W+jets,MC}}{f^{Z+jets,MC}} \times f^{Z+jets,data}, \quad (8.3)$$

where f^{MC} is the extrapolation factor measured in MC, whereas f^{data} is measured in data. The correction factors have been computed in ALPGEN+PYTHIA6 MC simulations: $c_{OS} = 0.99 \pm$

0.05 and $c_{SS} = 1.25 \pm 0.08$ for electrons, $c_{OS} = 1.00 \pm 0.08$ and $c_{SS} = 1.40 \pm 0.14$ for muons. The uncertainties correspond to the statistical uncertainties. Figure 8.7 shows the extrapolation factors for the Z +jets, OS W +jets and SS W +jets measured in the MCs, which are inputs to the correction factors.

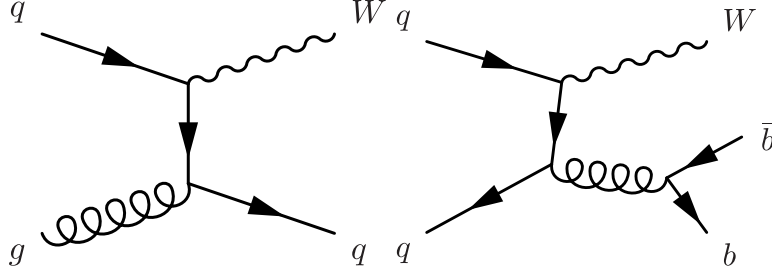


Figure 8.6: Tree diagrams for the $q\bar{q} \rightarrow Wq$ (left) and $q\bar{q} \rightarrow Wg \rightarrow Wb\bar{b}$ (right) productions.

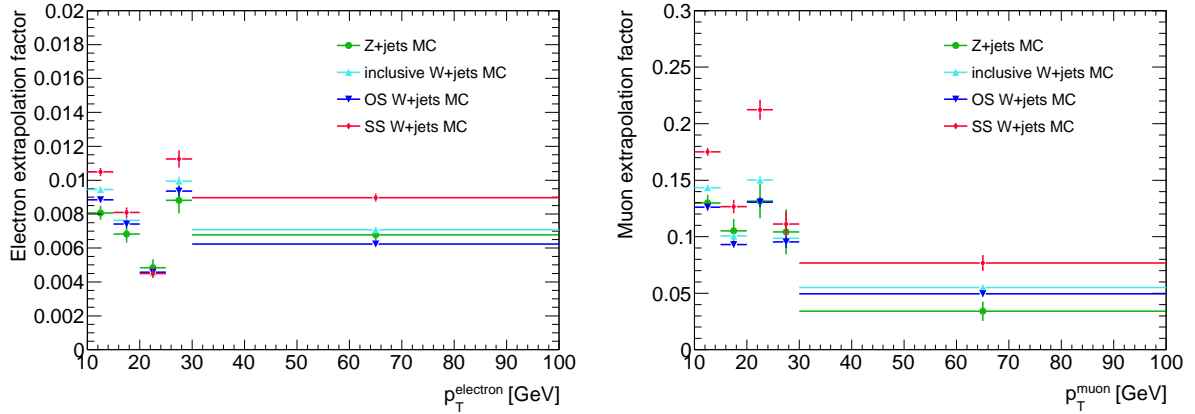


Figure 8.7: Extrapolation factors as a function of anti-ID lepton p_T for electrons (left) and muons (right). The extrapolation factors for Z +jets, opposite-charge W +jets and same-sign W +jets are computed in ALPGEN+PYTHIA6 MC simulations. Only the statistical uncertainty is included.

Systematic uncertainties on the W +jets estimation using the Z +jets extrapolation factor are estimated in the following ways:

- **EW contamination:** Uncertainty associated to the electroweak contamination in the Z +jets sample. The electroweak contamination is almost negligible in the denominator. However, it reaches to about 50% in the numerator as shown in figure 8.4. The uncertainty is evaluated by varying the cross sections of the electroweak processes by 10%.
- **Sample composition:** Uncertainty associated to the sample composition for the correction factors. The uncertainty is determined from comparisons of the correction factor for three MC simulations: ALPGEN+PYTHIA6, ALPGEN+HERWIG and POWHEG+PYTHIA8, to take into account the uncertainties on the matrix element and parton shower modeling. The OS and SS correction factors are partially correlated because they contain the same processes. In order to separate the uncertainty into correlated and uncorrelated parts, all

processes contributing to SS W +jets are assumed to equally contribute to OS W +jets, the $W + b\bar{b}$ being the main example. Other processes like the $W + c$, however, appear almost exclusively in OS W +jets. Thus, the uncertainty on the correction factor, σ_{SS} and σ_{OS} , can be factorized as follows:

$$(\sigma_{\text{SS}})^2 = (\sigma_{\text{SS}}^{\text{corr}})^2 + (\sigma_{\text{SS}}^{\text{stat.}})^2, \quad (8.4)$$

$$(\sigma_{\text{OS}})^2 = (\sigma_{\text{OS}}^{\text{corr}})^2 + (\sigma_{\text{OS}}^{\text{uncorr}})^2 + (\sigma_{\text{OS}}^{\text{stat.}})^2 \quad (8.5)$$

$$= \rho^2 \cdot (\sigma_{\text{SS}}^{\text{corr}})^2 + (\sigma_{\text{OS}}^{\text{uncorr}})^2 + (\sigma_{\text{OS}}^{\text{stat.}})^2, \quad (8.6)$$

where σ^{corr} is a correlated uncertainty between the OS and SS events. σ^{uncorr} is an uncorrelated uncertainty, which contributes to only OS events with the assumption mentioned above. ρ is the fraction of common processes in OS W +jets, which is obtained from the MC simulation: $\rho = 0.48$ for electrons and 0.38 for muons. $\sigma^{\text{stat.}}$ is the MC statistical uncertainty on the correction factor. Equation 8.6 can be solved for the $\sigma_{\text{OS}}^{\text{uncorr}}$. The final fit treats the correlation between the obtained $\sigma_{\text{SS}}^{\text{corr}}$ and $\sigma_{\text{OS}}^{\text{corr}}$.

Table 8.4 summarizes the uncertainties for the W +jets estimation. The statistical and EW contamination uncertainties varies as a function of p_{T} . The uncertainties on the correction factors are obtained at average p_{T} values. The statistical uncertainties on the Z +jets enriched samples with the currently available data are still a dominant source of the uncertainties.

Table 8.4: Systematic uncertainties on the W +jets prediction using the Z +jets extrapolation factor. EW refers to the uncertainty associated to the electroweak contamination in the Z +jets sample. OS(SS) sample refers to the uncertainty associated to the sample composition for the correction factors. They are separated into correlated and uncorrelated parts between OS and SS. The MC statistical uncertainty on the correction factor is included to the uncorrelated part here. These uncertainties are treated as nuisance parameters in the fit (See chapter 9).

electron [GeV]	stat. (%)	EW (%)	OS sample (%)	SS sample (%)
10 – 15	± 18	± 11		
15 – 20	± 34	± 19	± 11 (corr) ± 17 (uncorr)	± 24 (corr) ± 6 (uncorr)
20 – 25	± 52	± 25		
25 –	± 30	± 23		
muon [GeV]	stat. (%)	EW (%)	OS sample (%)	SS sample (%)
10 – 15	± 10	± 3		
15 – 20	± 18	± 5	± 13 (corr) ± 19 (uncorr)	± 34 (corr) ± 10 (uncorr)
20 – 25	± 29	± 9		
25 –	± 34	± 21		

8.1.2 Validation of the method using same-sign lepton sample

Modeling of the W +jets background, together with the *Other VV* background, is validated using the same-sign validation region (SS VR). The same object and event selections as the $H \rightarrow WW^* \rightarrow l\nu l\nu$ analysis except for the lepton charge requirement, which is inverted, are applied to this region. Since the same-sign requirement highly suppresses the WW , Top and Z +jets processes, the W +jets and *Other VV* processes become dominant sources of this

region. Table 8.5 summarizes the expected event yields in the SS VR. The W +jets background is predicted with the extrapolation factor method described above. The total expected yields agree well with the data. This indicates that the extrapolation factor method is working well as designed. Figures 8.8–8.9 show the m_T and $\Delta\phi_{\ell\ell}$ distributions in the SS VRs in each analysis category. The background shapes are also well modeled within the total uncertainties.

8.2 QCD background

The QCD process refers to the multi-jets production, which becomes a background by having two misidentified prompt leptons. The QCD background is expected to be very small contribution in the $H \rightarrow WW^* \rightarrow \ell\nu\ell\nu$ analysis, which is less than 1% of the total background, since the probability of misidentifications of a jet to a leptons is small (< 0.1) as shown in figure 8.5. Due to this small acceptance of the QCD process, it is not feasible to prepare the MC samples, which have reasonable statistical uncertainty on the expected yield in the SR, as well as the background shapes. Thus, a data-driven method (categorized into DATA) has been developed to estimate the normalization and shapes of the QCD background, that resulting in a more robust analysis.

Method of the estimation

The QCD background is estimated in a similar way to the W +jets estimation using the extrapolation factor. In the QCD process, both of the two leptons in the signal region originate from the jets. Therefore, the CR is defined with two anti-ID leptons, then a extrapolation factor is applied twice to the CR with a assumption that the two misidentified leptons are uncorrelated:

$$N_{\text{ID+ID}}^{\text{QCD}} = (f^{\text{di-jets,data}})^2 \times N_{\text{anti-ID+anti-ID}}^{\text{QCD}} = \left(\frac{N_{\text{ID}}}{N_{\text{anti-ID}}}\right)^2 \times N_{\text{anti-ID+anti-ID}}^{\text{QCD}} \quad (8.7)$$

QCD control region

The QCD CR is constructed with two anti-ID leptons aimed at selecting the leptons from multi-jets. The QCD CR is required to pass the signal selections except for that the anti-ID lepton definition is used for both two leptons. The trigger acceptance for the QCD CR is different from the W +jets CR as well as the $H \rightarrow WW^* \rightarrow \ell\nu\ell\nu$ signal regions. Since both two leptons in the QCD CR come from the jets, events in the QCD CR are mainly accepted through the di-lepton triggers, which require looser selections on the leptons compared to the single lepton triggers (i.e. p_T threshold, isolation and identification). The triggerable anti-ID definition for electrons is used in events collected by only the di-lepton triggers to avoid the trigger bias as discussed in section 8.1. The purity of the QCD CR is high at 90% in the $e\mu$ channel, as can be seen in the figure 8.10. The remaining backgrounds in the CR are dominated by the W +jets process, which is subtracted from the data together with the electroweak process using the MCs when extrapolating the CR to SR. The W +jets background estimation with the extrapolation factor method described in previous section is not used since it is not designed to estimate the background in the anti-ID+anti-ID region.

Di-jets extrapolation factor

A extrapolation factor for the QCD prediction is measured in data using a di-jets sample. The di-jets sample is collected with the prescaled triggers given in the table 8.6 instead of the triggers

Table 8.5: Summary of the expected event yields in the SS VRs. The W +jets and QCD backgrounds are estimated with the extrapolation factor method. The other processes are estimated by the MC and normalized to the theoretical cross sections. The uncertainties are statistical only.

$n_j = 0$ category				
$e\mu$ category				
	$W\gamma$	$W\gamma^*$	WZ	ZZ
SS VR	173.9 ± 5.3	115.9 ± 3.1	56.4 ± 1.6	3.8 ± 0.1
	W +jets	Total Bkg.	Observed	Data/MC
SS VR	173.7 ± 4.2	559.0 ± 8.0	533	0.95 ± 0.04
$ee/\mu\mu$ category				
	$W\gamma$	$W\gamma^*$	WZ	ZZ
SS VR	17.4 ± 1.7	18.1 ± 1.2	17.5 ± 0.9	0.7 ± 0.1
	W +jets	Total Bkg.	Observed	Data/MC
SS VR	41.5 ± 1.9	99.2 ± 3.0	89	1.13 ± 0.05
$n_j = 1$ category				
$e\mu$ category				
	$W\gamma$	$W\gamma^*$	WZ	ZZ
SS VR	52.0 ± 2.8	32.2 ± 1.8	34.3 ± 1.3	2.9 ± 0.1
	W +jets	Total Bkg.	Observed	Data/MC
SS VR	62.2 ± 2.6	197.3 ± 4.6	194	0.98 ± 0.07
$ee/\mu\mu$ category				
	$W\gamma$	$W\gamma^*$	WZ	ZZ
SS VR	5.3 ± 0.9	6.4 ± 0.8	10.1 ± 0.7	0.2 ± 0.1
	W +jets	Total Bkg.	Observed	Data/MC
SS VR	13.8 ± 1.2	37.0 ± 1.9	34	0.92 ± 0.16
$n_j \geq 2$ ggF-enriched category				
$e\mu$ category				
	$W\gamma$	$W\gamma^*$	WZ	ZZ
SS VR	25.3 ± 2.0	11.9 ± 1.4	16.1 ± 0.8	2.5 ± 0.1
	W +jets	Total Bkg.	Observed	Data/MC
SS VR	41.6 ± 3.1	124.3 ± 4.2	141	1.13 ± 0.10

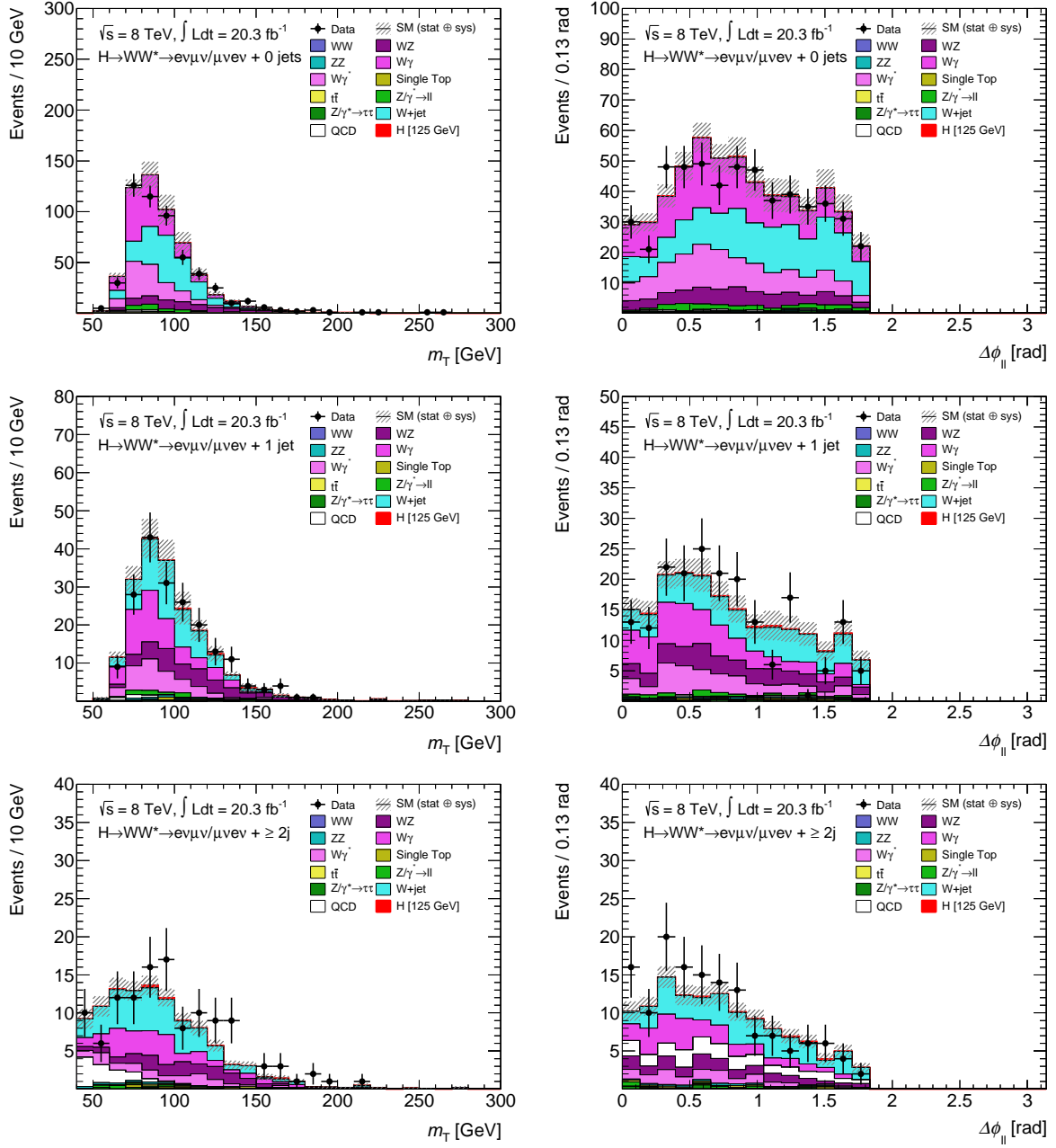


Figure 8.8: The m_T and $\Delta\phi_{\ell\ell}$ distributions in the same-sign validation region after the $\Delta\phi_{\ell\ell}$ cut. The top plots show the distributions in the $n_j = 0$ category, the middle plots are $n_j = 1$ and the bottom plots are $n_j \geq 2$ jets ggF-enriched categories, respectively. The W +jets and QCD backgrounds are estimated with the extrapolation factor method. The other process are modeled with the MC simulations normalized to the theoretical cross sections. Statistical and systematic uncertainties are included.

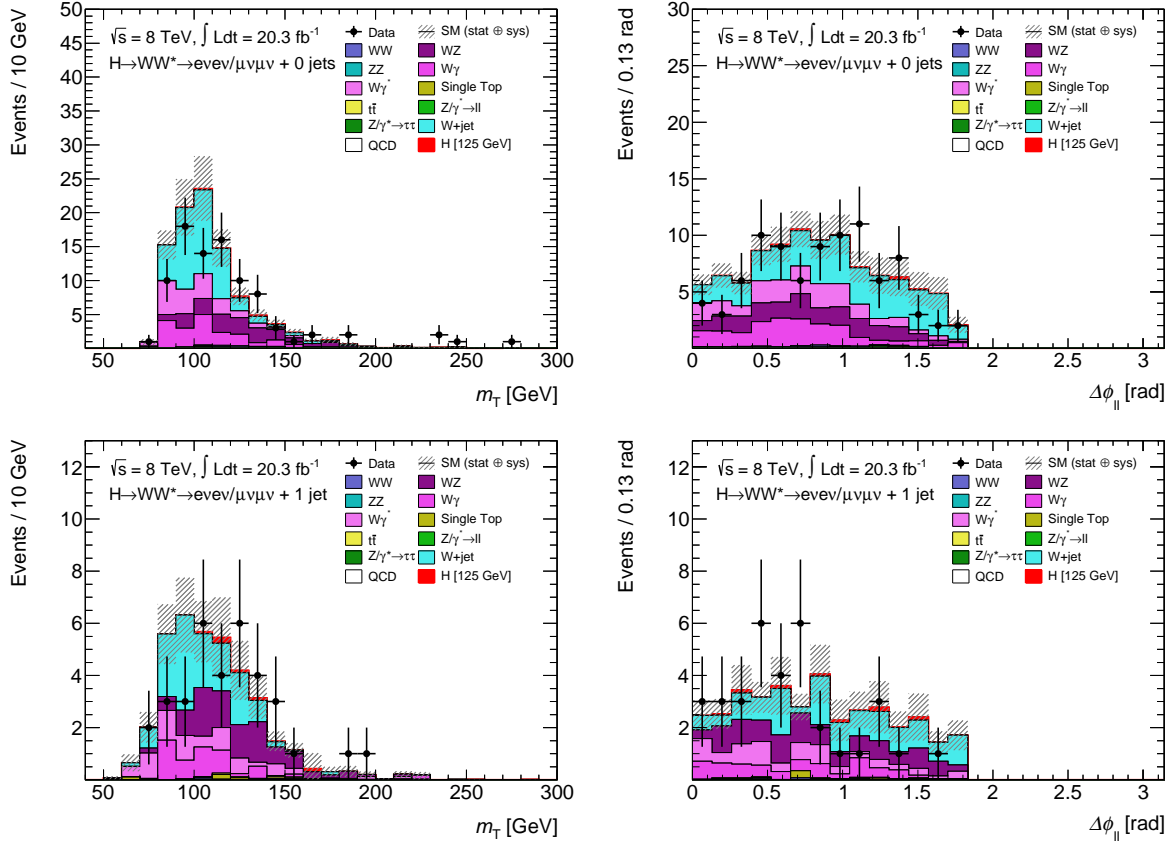


Figure 8.9: The m_T and $\Delta\phi_{\ell\ell}$ distributions in the same-sign validation region after the f_{recoil} cut. The top plots show the distributions in the $n_j = 0$ category and the middle plots show $n_j = 1$ categories, respectively. The W +jets and QCD backgrounds are estimated with the extrapolation factor method. The other process are modeled with the MC simulations normalized to the theoretical cross sections. Statistical and systematic uncertainties are included.

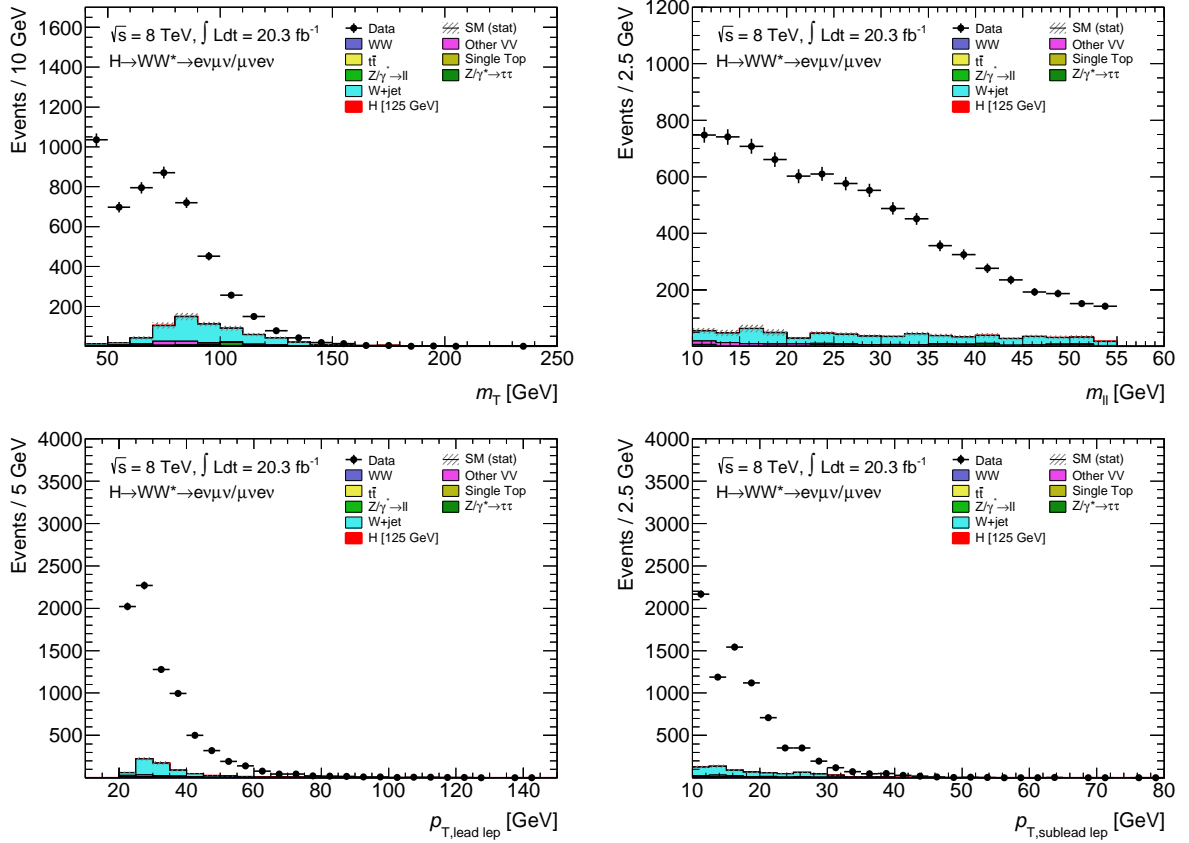


Figure 8.10: The m_T , $m_{\ell\ell}$, $p_T^{\ell 1}$ and $p_T^{\ell 2}$ distributions for the QCD control region in the $e\mu$ channel after the $\Delta\phi_{\ell\ell}$ cut. The figures show the distributions combined with the $n_j = 0$, $n_j = 1$ and $n_j \geq 2$ ggF-enriched categories. The background processes are normalized to their theoretical cross-sections. QCD prediction in simulations are not explicitly shown in the histograms. Only statistical uncertainty is included.

used in the $H \rightarrow WW^* \rightarrow \ell\nu\ell\nu$ analysis to avoid any bias on the online selection. The following event selections are performed to obtain the di-jets sample:

- $m_{\text{T}}^{\ell} > 30$ GeV with the medium-ID lepton;
- $|m_{\ell\ell} - m_Z| < 13$ GeV with the medium-ID lepton;
- $\Delta\phi_{\ell,\text{jet}} > 0.7$ with jet $p_{\text{T}} > 15$ GeV.

In order to suppress the presence of leptons from the W and Z boson decays, the events are vetoed if they have $m_{\text{T}}^{\ell} > 30$ GeV or contain two leptons with $|m_{\ell\ell} - m_Z| < 13$ GeV using the medium-ID leptons. Since the di-jets tends to be produced with back-to-back, a presence of the jet with $p_{\text{T}} > 15$ GeV in away side of the measuring lepton for the extrapolation factor is required, $\Delta\phi_{\ell,\text{jet}} > 0.7$, where $\Delta\phi_{\ell,\text{jet}}$ is the azimuthal angle between the lepton and away side jets. Remaining electroweak contaminations in the di-jets sample are subtracted from data using the MC predictions.

Table 8.6: Supporting triggers for the di-jets sample. eXX (gXX) indicates the E_{T} threshold for electrons (photons), also mu_XX indicates the p_{T} threshold for muons.

electrons	
$E_{\text{T}} < 20$ GeV	e5_etcut, e5_medium1
$E_{\text{T}} > 20$ GeV	g24_etcut
muons	
$p_{\text{T}} < 15$ GeV	mu_6
$p_{\text{T}} > 15$ GeV	mu_15

Figure 8.11 (8.12) shows the extrapolation factors as a function of p_{T} and η of the leptons for the non-triggerable (triggerable) anti-ID definition. The estimated extrapolation factors have biases introduced by different event topologies between the di-jets sample and the QCD CR. The QCD CR requires two leptons, thus there is an ID or (triggerable)anti-ID lepton in the event in addition to the one which the extrapolation is being applied. This bias due to the presence of an additional lepton (denoted as “awayside lepton”) is corrected using a PYTHIA8 di-jets simulation. Some approximations are necessary in calculating the correction factors because the extrapolation factor calculation encounters poor statistics of the MC samples if a awayside lepton is simply required (i.e. two leptons are required in total) to derive the correction. By assuming that the bias is caused by the change in the flavor of jets (b , c or light) producing an ID or anti-ID lepton for the extrapolation factor calculation, this change of flavors is estimated from generic jets in the MC sample by requiring the presence of an awayside lepton. The correction factor, c , is defined with the change of flavors as follows:

$$c = \frac{1}{f} \cdot \frac{N_{\text{light}} \cdot \xi_{\text{light}} + N_b \cdot \xi_b + N_c \cdot \xi_c}{D_{\text{light}} \cdot \xi_{\text{light}} + D_b \cdot \xi_b + D_c \cdot \xi_c} \quad (8.8)$$

$$\xi_{\text{X}} = \frac{J_{\text{X}}^{\text{awayside}} / J_{\text{all}}^{\text{awayside}}}{J_{\text{X}} / J_{\text{all}}}, \quad (8.9)$$

where N is the number of numerators (ID leptons), D is the number of denominators (anti-ID leptons), the suffix denotes the matched quark flavor, and ξ_{X} is the change in fraction of jets of

type X by requiring the presence of awayside lepton. The ξ_X is obtained from the ratio of the fraction of type X jets in generic jets (J_X/J_{all}) and the fraction of type X jets with the awayside lepton ($J_X^{\text{awayside}}/J_{\text{all}}^{\text{awayside}}$). Six patterns of the correction based on the awayside lepton flavor (electron or muon) and the denominator criterion (non-triggerable or triggerable) are estimated. Figure 8.13 shows the obtained correction factors as a function of p_T .

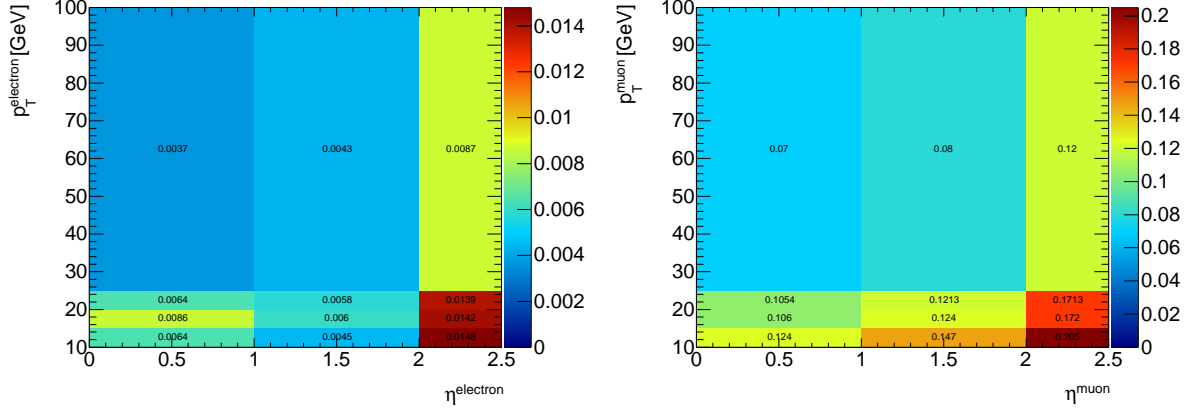


Figure 8.11: Extrapolation factors for electrons (left) and muons (right) in bins of the lepton (η , p_T). The extrapolation factors are measured in data using the di-jets sample. The non-triggerable definition is used for the denominators.

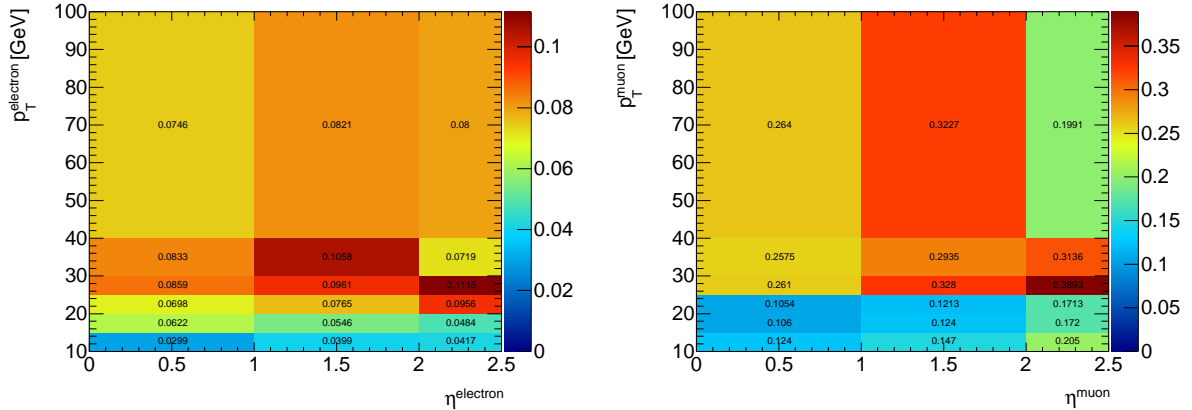


Figure 8.12: Extrapolation factors for electrons (left) and muons (right) in bins of the lepton (η , p_T). The extrapolation factors are measured in data using the di-jets sample. The triggerable definition is used for the denominators.

Systematic uncertainties on the QCD prediction using the di-jets extrapolation factor is split into the following three:

- **EW contamination:** Uncertainty associated to the real lepton contamination (W +jets, Z +jets) in the di-jets sample. The uncertainty is evaluated by varying the cross sections of the W +jets and Z +jets processes by 10 %;

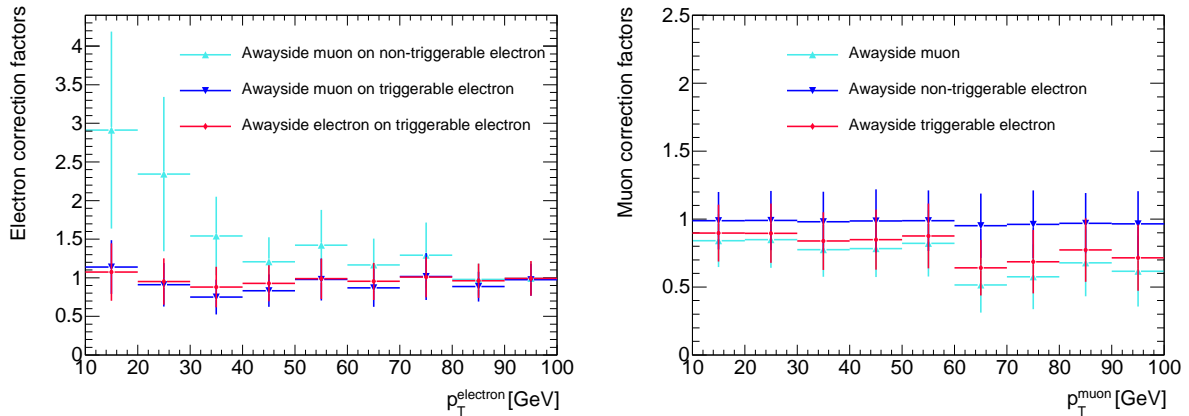


Figure 8.13: Correction factors for the di-jets extrapolation factor for electrons (left) and muons (right) as a function of p_T . The corrections factors are calculated in PYTHIA8 di-jets simulations.

- **Pileup dependence:** Uncertainty aimed at taking into account the difference of the pileup condition due to selecting the di-jets sample with the prescaled triggers. The uncertainty is estimated by evaluating the extrapolation factor as a function of average number of interactions per bunch crossing;
- **Sample correction:** Uncertainty on the jet flavor composition in the correction factor calculation. A 50 % variation applied to the b - and c - jet fractions in the correction factor calculation. The MC statistical uncertainty is also a significant contribution.

Table 8.7 summarizes the estimated uncertainties on the QCD background. The dominant source of the uncertainty is from the sample correction, which is 20–45 %.

In order to validate the QCD background modeled by these extrapolation factors, the QCD contamination in the SS VR (see section 8.1.2) is enhanced by removing the missing transverse energy requirement. Figure 8.14 shows the m_T and $\Delta\phi_{\ell\ell}$ distributions in the SS VR after the $n_j = 0$ requirement, but the missing transverse energy cut is not included. Good agreements between the data and estimated backgrounds within the total uncertainties are observed, which indicates the extrapolation factors for the QCD prediction are working well as designed.

8.3 Other VV background

The di-boson backgrounds, other than the WW background, consist of $W\gamma$, $W\gamma^*$, WZ and ZZ processes. These backgrounds add up to about 10% of the total estimated background, and largely contribute in low $p_T^{\ell_2}$ regions. For the $e\mu$ sample in the $n_j = 0$ and $n_j = 1$ categories, a data-driven method (categorized into DATA) using a merit of symmetries between opposite-sign (OS) and same-sign (SS) events has been developed. For the other channels, the MC predictions are used due to poor data statistics for the data-driven method. The validity of the MC models for the dominant sources of the *Other VV* background are also discussed in this section.

8.3.1 The OS-SS method

The *Other VV* and part of W +jets backgrounds in the $e\mu$ sample in the $n_j = 0$ and $n_j = 1$ categories are estimated directly from the same-sign data by applying the signal selections except

Table 8.7: Systematic uncertainties on the QCD prediction using the di-jets extrapolation factor. (EW+pileup) refers to the uncertainty on the electroweak contamination in the di-jets sample and pileup dependence. The numbers in parentheses for stat. and (EW+pileup) correspond to the case of using the triggerable anti-ID definition. The uncertainties on the correction factor depend on the type of the corrections as shown in figure 8.13. These uncertainties are treated as nuisance parameters in the fit (see chapter 9).

electrons [GeV]	stat. (%)	(EW+pileup) (%)	sample correction (%)
10 – 15	± 3 (7)	± 10 (10)	± 31 –44
15 – 20	± 5 (12)	± 10 (10)	
20 – 25	± 4 (9)	± 10 (10)	
25 –	± 4 (6–11)	± 10 (12–21)	± 21 –33
muons [GeV]	stat. (%)	(EW+pileup) (%)	sample correction (%)
10 – 15	± 1 (1)	± 11 (11)	± 21 –24
15 – 20	± 1 (1)	± 11 (11)	
20 – 25	± 1 (1)	± 11 (11)	
25 –	± 2 (3–17)	± 11 (11–74)	± 23 –42

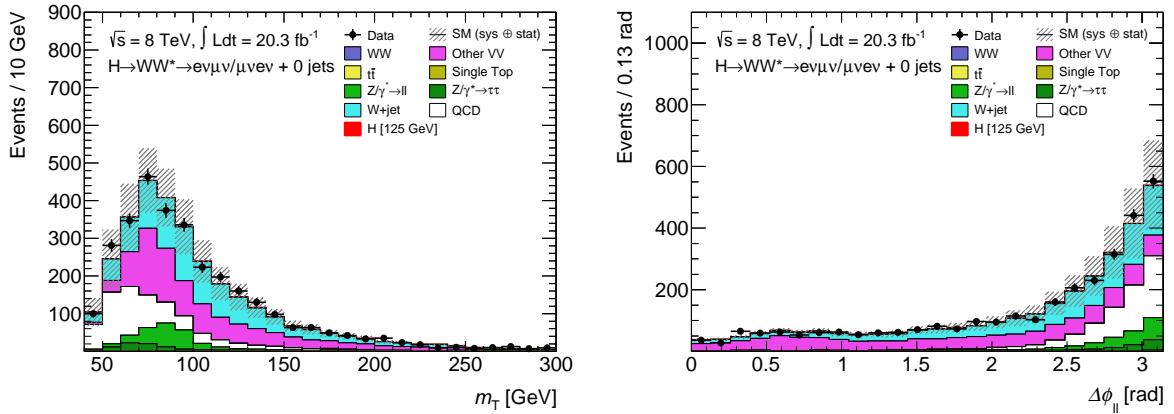


Figure 8.14: The m_T and $\Delta\phi_{\ell\ell}$ distributions in the same-sign validation region after the $n_j = 0$ requirement, but the missing transverse energy cut is not included. The W +jets and QCD backgrounds are estimated with the extrapolation factor method. The other process are modeled with the MC simulations and normalized to the theoretical cross sections. Statistical and systematic uncertainties are included.

that it requires that the two leptons has the same electronic charge (called as “OS-SS method”). Figure 8.15 shows the background composition in the signal region of the $e\mu$ sample for each OS and SS cases. The SS events are dominated by the *Other VV* and W +jets backgrounds because the WW , Top, and Z +jets backgrounds are highly suppressed by the same charge requirement. The rate of the *Other VV* is assumed to be the same between the OS and SS in figure 8.15. This OS = SS assumption for the *Other VV* background is validated in the following section. The number of W +jets events in the opposite-sign is larger than the same-sign because of the charge correlation as described in the section 8.1.

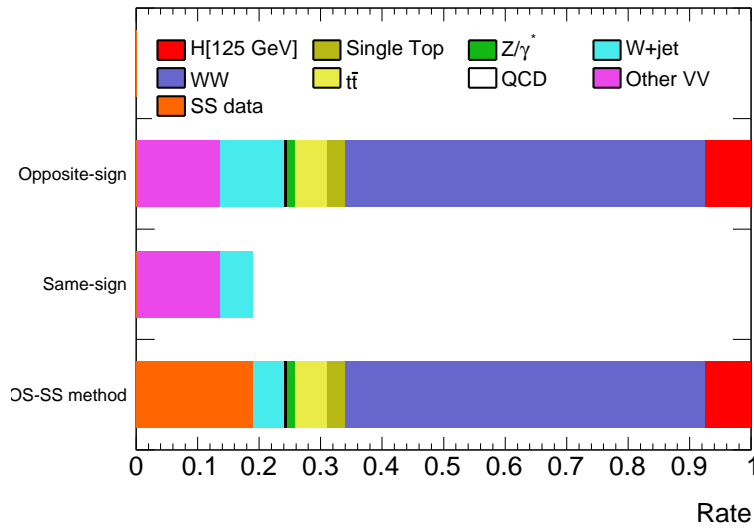


Figure 8.15: The background composition in the signal region of the $e\mu$ sample for the opposite-sign event, same-sign event and OS-SS method.

From the discussions above and figure 8.15, the background estimation of the *Other VV* and W +jets in the signal regions can be described as follows:

$$\begin{aligned}
 N_{\text{OS}}^{\text{OtherVV,SR}} + N_{\text{OS}}^{\text{W+jets,SR}} &= N_{\text{SS}}^{\text{data}} + (N_{\text{OS}}^{\text{W+jets,SR}} - N_{\text{SS}}^{\text{W+jets,SR}}) - N_{\text{SS}}^{\text{other}} \\
 &= N_{\text{SS}}^{\text{data}} + f_{\text{OS}} \times N_{\text{OS}}^{\text{W+jets,CR}} \\
 &\quad - f_{\text{SS}} \times N_{\text{SS}}^{\text{W+jets,CR}} - N_{\text{SS}}^{\text{other}},
 \end{aligned} \tag{8.10}$$

where $N_{\text{SS}}^{\text{data}}$ is the number of observed data with the SS requirement. $N_{\text{OS}}^{\text{W+jets,CR}}$ and $N_{\text{SS}}^{\text{W+jets,CR}}$ are the number of events in the W +jets CR with the corresponding Z +jets extrapolation factor of f_{OS} and f_{SS} (see section 8.1). $N_{\text{SS}}^{\text{other}}$ is other contributions from the WW , Top, Z +jets and QCD processes with the SS requirement, which is $< 5\%$ of the the SS data. The extrapolation factor for the *Other VV* background can be regarded as unity with the OS = SS assumption. All systematic uncertainties on the *Other VV* modeling are removed because the normalization and kinematic shapes of the background are estimated fully taken from the data. Therefore, the OS-SS method improves the precision of the background estimation significantly.

Validation of OS = SS assumption

In the context of the OS-SS method, it is necessary to verify the assumption that the contribution of the *Other VV* is symmetric between the OS and SS in the $e\mu$ sample. This assumption is

based on a fact that the $W\gamma$, $W\gamma^*$ and WZ processes are equally likely to produce a second lepton of either charge relative to the charge of the lepton from the W decay as illustrated in figure 8.16. The contribution of the ZZ is not completely symmetric between the OS and SS because the oppositely-charged leptons are more likely to be selected in the $Z \rightarrow \tau\tau \rightarrow e\nu\mu\nu$ process. However, the ZZ contribution is almost negligible small in the same-sign data: only $< 1\%$ of the total expected other processes.

This OS = SS mechanism is not valid in the $ee/\mu\mu$ samples since the $Z \rightarrow \ell\ell$ decays produce the oppositely-charged leptons with the same flavor, which break the symmetry. Thus, the OS-SS method is not used in the $ee/\mu\mu$ samples.

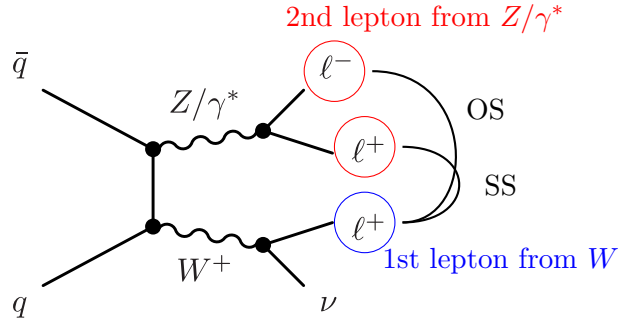


Figure 8.16: OS = SS mechanism.

The assumption is validated in direct comparisons of the OS and SS events using the MC samples. Table 8.8 shows the expected event yields for the *Other VV* background in the OS and SS cases at the several cut stages in the $e\mu$ channel. The expected yields are compatible between the OS and SS within the statistical uncertainties. Figure 8.17 shows different kinematic distributions after the $\Delta\phi_{\ell\ell} < 1.8$ cut. Also good agreements between the OS and SS are found in the kinematic shapes of the *Other VV* process as expected.

OS-SS method vs MC

The modeling of the *Other VV* and W +jets processes with the OS-SS method has been compared to the case using the MC for the *Other VV* process. Table 8.9 summarizes the expected event yields with the statistical and systematic uncertainties for the two methods: OS-SS method and MC prediction. The systematic uncertainty on the *Other VV* prediction comes from the theoretical calculation as summarized in table 8.10. The systematic uncertainty on the W +jets process corresponds to the uncertainty on the extrapolation factor summarized in table 8.4. In the OS-SS method, the statistical uncertainty is larger than that of the MC because the statistics of the SS data is limited. However, the systematic uncertainty on the *Other VV* is removed and also the partial uncertainty on the W +jets, which is correlated between the OS and SS (σ_{OS}^{corr} and σ_{SS}^{corr}), cancels out in $N_{OS}^{W+jets} - N_{SS}^{W+jets}$ term in equation 8.11. In total, the OS-SS method shows better performances compared to the MC: about 15% improvement in the $n_j = 0$ and 39% in the $n_j = 1$ categories. Figure 8.18 shows key distributions used in the fitting procedure. Reasonable agreements are found between the two methods within the total uncertainty.

Table 8.8: The expected event yields for the *Other VV* background in the $e\mu$ channel, separated into OS and SS events. Only statistical uncertainty is included.

	OS <i>Other VV</i>	SS <i>Other VV</i>	OS/SS
$n_j = 0$ category			
jet veto	802.28 ± 9.20	822.44 ± 9.25	0.98 ± 0.02
$\Delta\phi_{\ell\ell, \text{MET}} > 1.57$	799.56 ± 9.19	819.11 ± 9.24	0.98 ± 0.02
$p_{T, \ell\ell} > 30$ GeV	619.86 ± 8.11	635.57 ± 8.12	0.98 ± 0.02
$m_{\ell\ell} < 55$ GeV	383.06 ± 6.66	387.03 ± 6.66	0.99 ± 0.02
$\Delta\phi_{\ell\ell} < 1.8$	351.62 ± 6.41	354.74 ± 6.40	0.99 ± 0.03
$n_j = 1$ category			
one jet	517.76 ± 6.80	510.53 ± 6.73	1.01 ± 0.02
b -jet veto	441.18 ± 6.30	431.78 ± 6.17	1.02 ± 0.02
Maximum $m_T^{\ell} > 50$	381.71 ± 5.85	372.77 ± 5.71	1.02 ± 0.02
$Z \rightarrow \tau\tau$ veto	287.39 ± 5.17	280.65 ± 5.06	1.02 ± 0.03
$m_{\ell\ell} < 50$ GeV	145.36 ± 3.92	138.58 ± 3.81	1.05 ± 0.04
$\Delta\phi_{\ell\ell} < 1.8$	124.44 ± 3.62	122.47 ± 3.60	1.02 ± 0.04

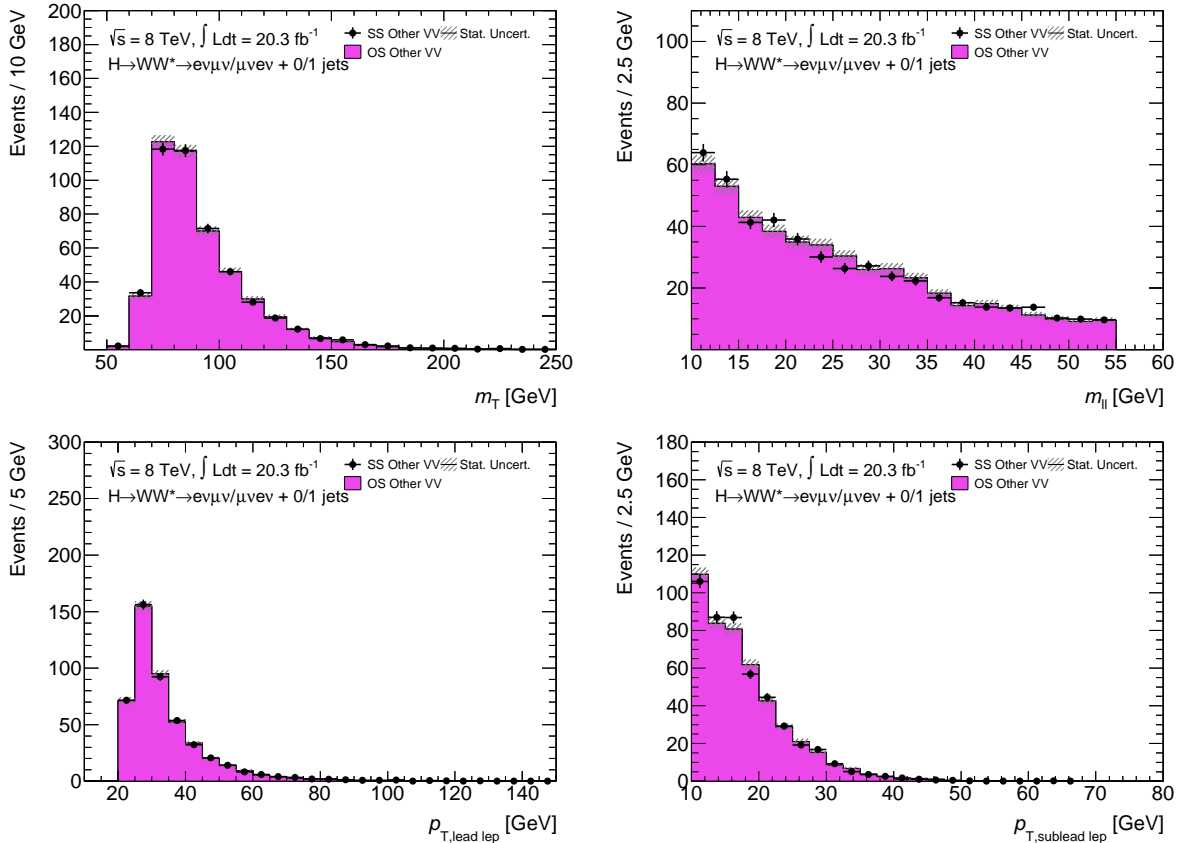

 Figure 8.17: The m_T , $m_{\ell\ell}$, $p_T^{\ell 1}$ and $p_T^{\ell 2}$ distributions for the *Other VV* process in the $e\mu$ sample in the $n_j = 0$ and $n_j = 1$ categories after the $\Delta\phi_{\ell\ell}$ cut. Only statistical uncertainty is included.

Table 8.9: The expected event yields in case of the OS-SS method and using the MC prediction for the *Other VV*. The small contributions of the WW , Top and Z +jets are subtracted from the SS data. The first term of the uncertainties corresponds to the statistical uncertainty, and the second is the systematic uncertainty. The systematic uncertainties are quoted from table 8.4 and 8.10. The total uncertainty is obtained by combining the statistical and systematic uncertainties in quadrature.

	<i>Other VV</i>	W +jets	SS data	Total	Error
$n_j = 0$ category					
OS-SS	-	$103.89 \pm 6.57 \pm 46.77$	$502.52 \pm 23.19 \pm 0.00$	$606.41 \pm 24.10 \pm 46.77$	8.7 %
MC	$351.62 \pm 6.41 \pm 22.51$	$277.63 \pm 5.02 \pm 59.00$	-	$629.45 \pm 8.13 \pm 63.15$	10.1 %
$n_j = 1$ category					
OS-SS	-	$25.95 \pm 3.89 \pm 15.52$	$181.34 \pm 13.97 \pm 0.00$	$207.29 \pm 14.50 \pm 15.52$	10.2 %
MC	$124.44 \pm 3.62 \pm 28.98$	$88.11 \pm 2.89 \pm 19.69$	-	$212.55 \pm 4.63 \pm 35.04$	16.7 %

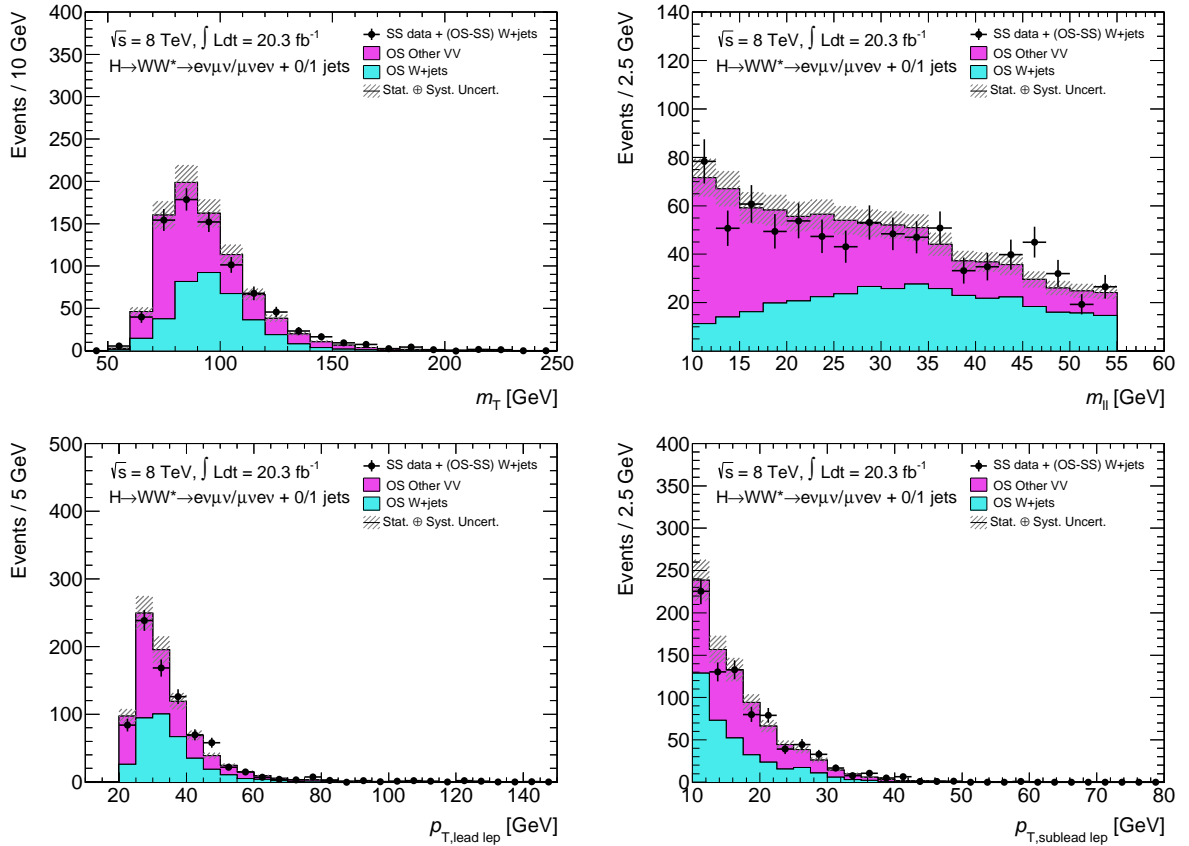


Figure 8.18: The m_T , $m_{\ell\ell}$, $p_T^{\ell 1}$ and $p_T^{\ell 2}$ distributions for the OS-SS method (dots) and using the MC for the *Other VV* process (histograms). The distributions are in the $e\mu$ sample in $n_j = 0$ and $n_j = 1$ categories after the $\Delta\phi_{\ell\ell}$ cut.

8.3.2 Monte Carlo validation

In the $ee/\mu\mu$ and $n_j \geq 2$ ggF-enriched analyses, the MC predictions which are normalized to the NLO cross sections are used to model the *Other VV* background. Therefore, theoretical and experimental uncertainties specific to the *Other VV* background prediction using the MCs are provided in this section. Since the $W\gamma$ and $W\gamma^*$ are dominant sources of the *Other VV* background as shown in figure 8.8 and 8.9 and have larger theoretical uncertainties than the other process, the validities of the $W\gamma$ and $W\gamma^*$ MC models using dedicated validation regions (VRs) are investigated and also given in this section.

MC sample and its theoretical uncertainty

For the $W\gamma$ background, ALPGEN with a normalization factor (k -factor) of 1.15 is used to model the process. The k -factor is obtained by comparing the cross section calculated with MCFM program, which performs the calculation with NLO in QCD. An uncertainty on this k -factor is computed by varying the renormalisation and factorization scales (QCD scales) using the MCFM. This QCD scale uncertainty is split into the jet bins following the procedure so called ‘‘Stewart-Tackmann’’ method described in [111]. They are 11 % in the $n_j = 0$, 53 % in the $n_j = 1$ and 100 % in the $n_j \geq 2$ bins.

The $W\gamma^*$ background is modeled with SHERPA. A k -factor of 0.94 for the $W\gamma^*$ sample is also evaluated in the same way as the $W\gamma$ case. A SHERPA sample with ≤ 2 partons in the matrix element could not be produced in the mass regime; $2m_e < m_{\gamma^*} < 0.5$ GeV, due to technical reasons. Therefore, SHERPA samples produced with ≤ 1 parton are used in the analysis. In order to improve the estimate of the acceptance of each jet bin, reweighting factors for the SHERPA ≤ 1 parton samples as a function of the jet multiplicity are calculated with the events in the $0.5 < m_{\gamma^*} < 7$ GeV mass range by comparing with the SHERPA ≤ 2 partons sample. The obtained reweighting factors are 0.85 ± 0.09 , 1.03 ± 0.32 and 1.84 ± 0.50 for the $n_j = 0$, $n_j = 1$, and $n_j \geq 2$ jet bins, respectively, where the uncertainties correspond to the QCD scale variations only. An additional PDF uncertainty of 3.1 % is assigned to the $W\gamma$ and $W\gamma^*$ processes.

The WZ and ZZ components are modeled with POWHEG+PYTHIA8 without any additional k -factor, since these are calculated at NLO in QCD. Table 8.10 summarizes the scale uncertainties on the normalizations of the *Other VV* process.

Table 8.10: The QCD scale uncertainties on the normalizations of the *Other VV* process. These uncertainties are treated as nuisance parameters in the fit (see chapter 9)

Process	0 jet	1 jet	≥ 2 jets
$W\gamma$	11%	53%	100%
$W\gamma^*$	9.9%	31%	27%
WZ	5%	5%	5%
ZZ	5%	5%	5%

Validation region for $W\gamma$ background

The $W\gamma$ background originates from an asymmetric $\gamma \rightarrow e^+e^-$ conversion in combination with the $W \rightarrow \ell\nu$ decay, where the one of the converted electron (or positron) with higher p_T tends to

be reconstructed as an electron candidate. In order to construct the VR with events containing electrons from photon conversions, two identification criteria of electrons (see section 6.2) are reverted: the conversion bit and the b-layer hit, which indicates whether the electron is matched to a photon conversion vertex [101] and if it has a hit in the inner detector layer closest to the interaction point. The electron from the photon conversion tends to be associated to the conversion vertex and have no hit on the b-layer as illustrated in figure 8.19. Only the muon triggers are used in the VR since the electron triggers require the b-layer hit at the online selection. Additionally, only same sign events are chosen to suppress the contamination from other backgrounds. The other object and event selections to construct the VR are the same with the $H \rightarrow WW^* \rightarrow l\nu l\nu$ analysis.

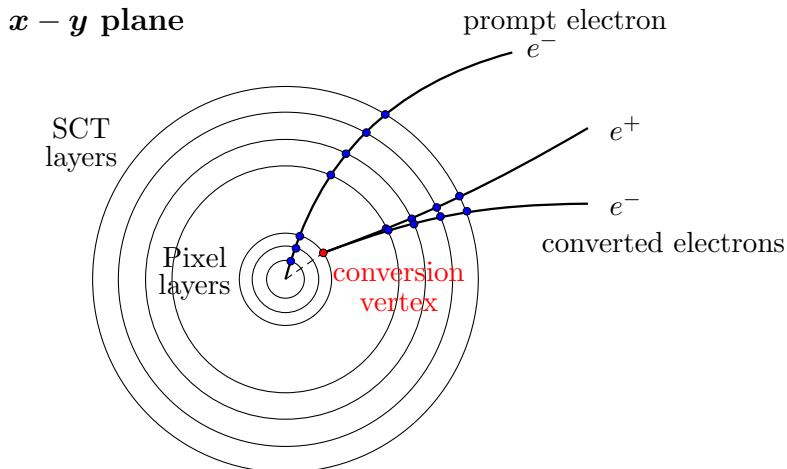


Figure 8.19: Illustration of a photon conversion.

The resulting data and MC events in the $W\gamma$ VR after the $\Delta\phi_{\ell\ell}$ cut are summarized in table 8.11. The purity of the $W\gamma$ process reaches 80% in all jet bins. The remaining other contributions predominantly consist of the $Z\gamma$ and W +jets processes. The $Z\gamma$ process is modeled with SHERPA. The W +jets process is estimated using the data-driven method (see section 8.1) with an extrapolation factor, which is obtained by reverting the conversion bit and b-layer hit requirements in the numerator. Figure 8.20 shows the m_T and $m_{\ell\ell}$ distributions after the $\Delta\phi_{\ell\ell}$ cut. The figure shows reasonable agreements between the data and theoretical prediction within the total uncertainties, which indicate that the $W\gamma$ process and its uncertainties in the MC simulation are well understood. An uncertainty on the modeling of the photon conversion is included in the figure. This systematic uncertainty is discussed in the next subsection.

Systematic uncertainty on the photon conversion

A $Z\gamma$ enriched region is used to derive a systematic uncertainty on the photon conversion because it has a factor of 2.2 more statistics compared to the $W\gamma$ VR as well as more than 99% purity. The Z boson reconstructed in the $\mu^+\mu^-$ and an electron reverted the conversion bit and b-layer hit criteria, described in the text above, are selected to obtain the $Z\gamma$ enriched region. The invariant mass of the $\mu^+\mu^- + e^\pm$ system is required to be within $82 < m_{\mu\mu e} < 95$ GeV to suppress contributions from the associated production of a Z boson and hadronic jets. Figure 8.21 (a) shows the $m_{\mu\mu e}$ distribution before applying this $m_{\mu\mu e}$ cut. It can be confirmed that the Z +jets

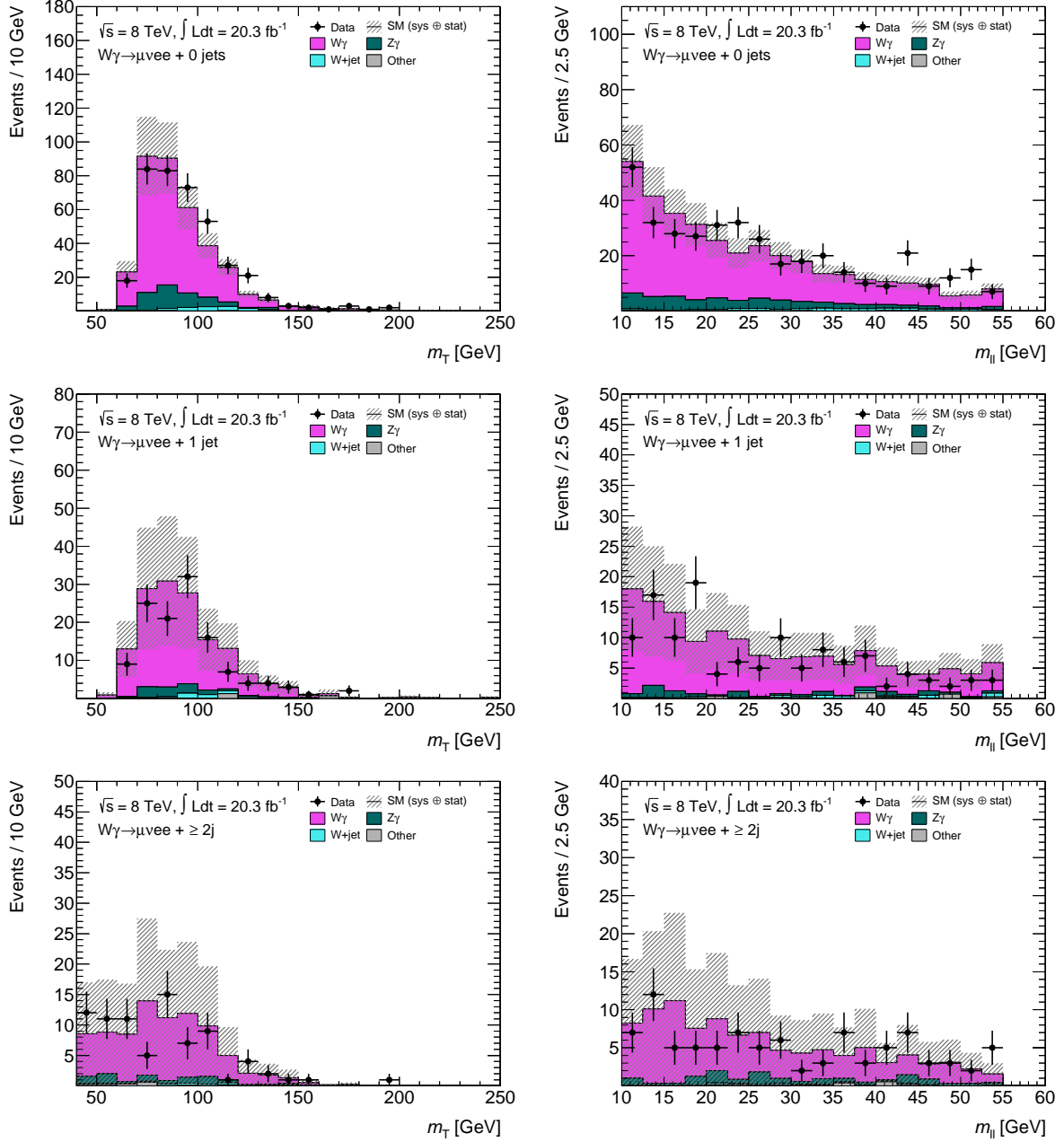


Figure 8.20: The m_T and $m_{\ell\ell}$ distributions in the $W\gamma$ validation region after the $\Delta\phi_{\ell\ell}$ cut. The top plots show the distributions in the $n_j = 0$, the middle plots are $n_j = 1$ and the bottom plots are $n_j \geq 2$ categories, respectively. Statistical, theoretical and p_T dependent uncertainties are included.

Table 8.11: Summary of the expected event yields in the $W\gamma$ validation regions after the $\Delta\phi_{\ell\ell}$ cut. Only statistical uncertainty is included.

	$W\gamma$	$Z\gamma$	W +jets	Total Bkg.	Observed	Data/MC
0 jet	297.83 ± 7.00	46.84 ± 2.93	12.04 ± 0.63	357.85 ± 7.62	380	1.06 ± 0.06
1 jet	144.48 ± 4.84	13.60 ± 1.61	5.63 ± 0.53	166.49 ± 5.27	140	0.84 ± 0.08
≥ 2 jets	83.48 ± 3.62	11.30 ± 1.43	2.53 ± 0.37	99.10 ± 3.95	92	0.93 ± 0.10

process (light green histogram) is distributed in the region of $m_{\mu\mu e} > 95$ GeV. Figure 8.21 (b) shows the electron p_T distribution in the obtained $Z\gamma$ enriched region. About 20% discrepancy between the data and MC prediction is observed in the region of $10 < p_{T,\text{electron}} < 20$ GeV. This indicates that the simulation is more efficient at finding the conversion vertices, or less efficient at finding the b-layer hits due to detector mismodelings. From the differences between the data and MC, a p_T dependent uncertainties, 25% for $10 < p_T < 15$ GeV, 18% for $15 < p_T < 20$ GeV and 5% for $p_T > 20$ GeV are assigned to the efficiency for finding the electrons originated from the photon conversions. This p_T dependent uncertainty is a dominant source of uncertainties on the prediction of the $W\gamma/Z\gamma$ background shapes.

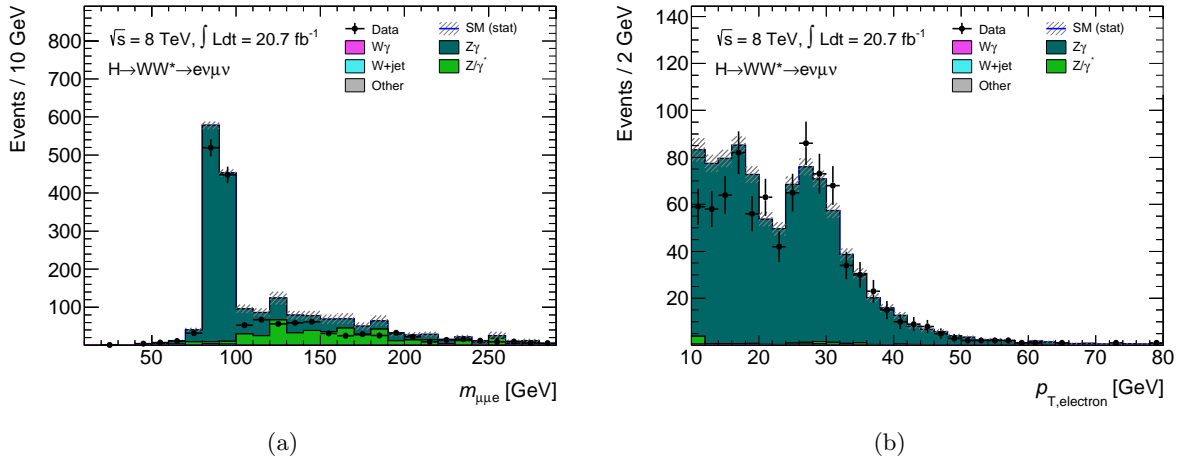


Figure 8.21: (a) The $m_{\mu\mu e}$ distribution before applying the $m_{\mu\mu e}$ cut. (b) p_T of electrons in the $Z\gamma$ enriched region. All process are estimated with the MC simulations and normalized to the theoretical cross sections, Only statistical uncertainty is included.

Validation region and shape uncertainty for $W\gamma^*$ background

The $W\gamma^*$ background originates from the associated production of a W boson with a virtual photon, where the photon internally converts to a pair of charged leptons. Unlike the conversion of real photons, $\gamma^* \rightarrow \mu\mu$ and $\gamma^* \rightarrow \tau\tau$ can also occur, although the latter production is negligible. The modeling of the $W\gamma^*$ background is checked with a validation region aimed at selecting $W\gamma^* \rightarrow e\nu\mu\mu$ candidates. In this process, the muons from the γ^* are likely emitted very close each other. If there are other identified muons (ID-muon) in $\Delta R < 0.3$, the track

isolation parameter (pTcone30) is redefined as follows:

$$\text{pTcone30}' = \text{pTcone30} - p_{\text{T}}^{\text{ID-muon}} \quad (8.11)$$

Also the calorimeter isolation cut is loosend to $e\text{Tcone30}/p_{\text{T}} < 0.4$ to allow low p_{T} muons closely. The following event selections are performed to construct the $W\gamma^*$ VR:

- One election and two muons with opposite charge;
- $p_{\text{T}}^{\ell_1} > 22$ GeV, $p_{\text{T}}^{\ell_2} > 10$ GeV and $p_{\text{T}}^{\ell_3} > 3$ GeV;
- $p_{\text{T}}^{\text{miss}} > 20$ GeV;
- $m_{\ell_2\ell_3} < 7$ GeV;
- $|m_{\ell_2\ell_3} - m_{J/\psi}| > 0.1$ GeV;
- Maximum $\Delta\phi_{\ell_1\ell_i} < 2.8$,

where ℓ_1 denotes the electron from the W boson decay and ℓ_2 (ℓ_3) is the leading (subleading) muon from the γ^* decay. The common p_{T} and $p_{\text{T}}^{\text{miss}}$ selections to the $H \rightarrow WW^* \rightarrow \ell\nu\ell\nu$ analysis are applied first. For an additional muon ℓ_3 , $p_{\text{T}}^{\ell_3} > 3$ GeV is required to allow very low- p_{T} muon from the γ^* decay. $m_{\ell_2\ell_3} < 7$ GeV cut is aimed at rejecting the WZ process. Also $m_{\ell_2\ell_3}$ is required to be not within 0.1 GeV to the mass of J/ψ meson in order to suppress contributions from the associated production of a W boson and J/ψ . The maximum azimuthal angle between the electron and muons, $\Delta\phi_{\ell_1\ell_i}$, is required to be less than 2.8 to suppress the $Z\gamma^*$ process. Table 8.12 shows the expected MC yields and observed data in the $W\gamma^*$ VR. The purity of the $W\gamma^*$ process reaches 87% of the total predictions. The second contribution comes from the $Z\gamma^*$ process, which is also modeled with SHERPA. Figure 8.22 shows various distributions in the $W\gamma^*$ VR. Good agreements between the data and MC are found within the total uncertainties. Especially, the agreement of the jet multiplicity indicates that the reweighting procedure for the $W\gamma^*$ MC is working well.

A shape uncertainty of the m_{T} distribution is calculated using MCFM by varying the QCD scale. The maximum deviation of the variations is taken into account. Figure 8.23 shows the results of the variations. They are $< 12\%$ at the whole m_{T} range.

Table 8.12: Summary of the expected event yields in the $W\gamma^*$ validation regions after the maximum $\Delta\phi_{\ell_1\ell_i}$ cut. Only statistical uncertainty is included.

	$W\gamma^*$	$Z\gamma^*$	Total Bkg.	Observed	Data/MC
incl. jets	88.41 ± 3.04	6.67 ± 0.64	101.48 ± 3.23	114	1.12 ± 0.11

8.4 Z +jets background

The Drell-Yan production (Z +jets) has two oppositely charged leptons in the events. If such events are accompanied with a significant missing transverse energy, either because of the neutrinos in the leptonic τ decay or the degradation of the missing energy resolution with the pile-up,

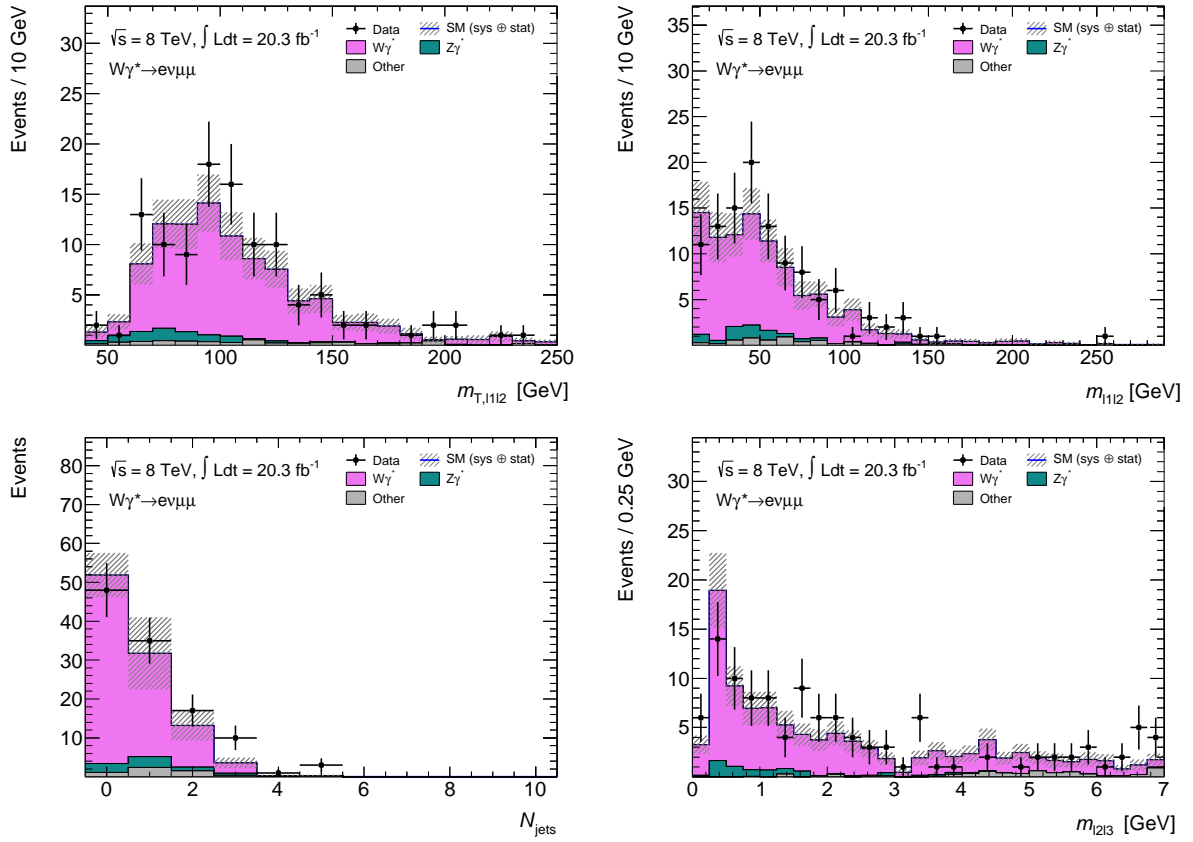


Figure 8.22: The m_T with ℓ_1 and ℓ_2 , $m_{\ell_1\ell_2}$, n_j and $m_{\ell_2\ell_3}$ distributions in the $W\gamma^*$ validation region. Statistical and theoretical uncertainties are included.

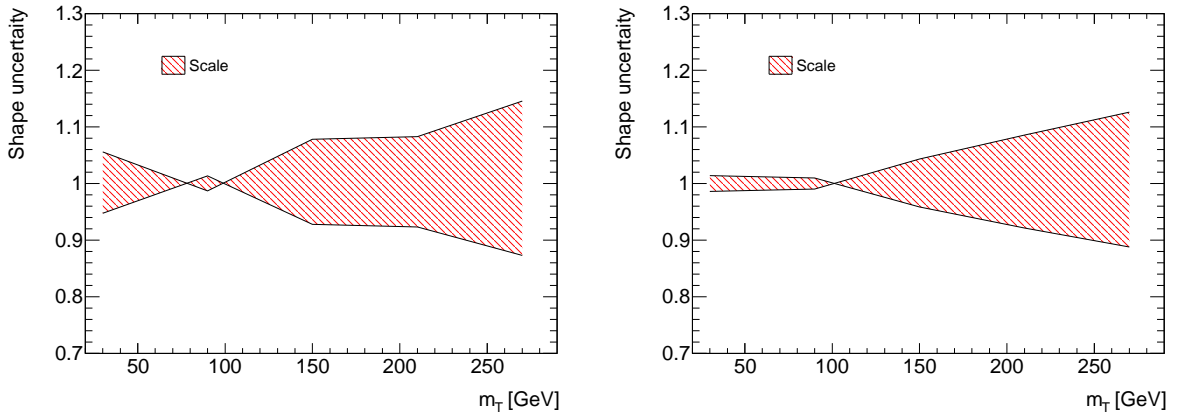


Figure 8.23: Scale uncertainties in the shape of the $W\gamma^*$ m_T distribution.

these may remain in the signal sample. Since the Z +jets production has a large cross section compared to the other SM production, the Z +jets is a significant source of the background in the analysis, especially for the $ee/\mu\mu$ channel. The Z +jets background is separated by its decay mode, $Z \rightarrow \tau\tau$ and $Z \rightarrow ee/\mu\mu$, for which different estimation techniques (NORM category) are used. The $Z \rightarrow ee/\mu\mu$ process contributes to the $ee/\mu\mu$ channels with about 10% of the total expected background, while the $Z \rightarrow \tau\tau$ process mainly contributes to the $e\mu$ channel in the $n_j > 2$ ggF-enriched category and amounts to 14% of the background.

In the following subsections, a reweighting in the p_T of Z bosons for the $n_j = 0$ category is described in section 8.4.1. The background estimation techniques for the $Z \rightarrow \tau\tau$ and $Z \rightarrow ee/\mu\mu$ processes are presented in section 8.4.2 and 8.4.3, respectively.

8.4.1 p_T^Z reweighting

The Z +jets production is modeled with ALPGEN+HERWIG for all analysis categories. However, a mismodeling of the p_T of Z bosons, p_T^Z , reconstructed as $p_{T,\ell\ell}$, has been observed in a Z enriched region in the $n_j = 0$ category. The Z enriched region is obtained by requiring $|m_{\ell\ell} - m_Z| < 15$ GeV after the $m_{\ell\ell} > 10,12$ GeV cut in the pre-selection. Figure 8.24 (a) shows the $p_{T,\ell\ell}$ distribution in the Z enriched region in inclusive jet bins. A reasonable level of agreements between the data and predictions can be seen. However, a severe discrepancy is observed when the $n_j = 0$ is required as shown in figure 8.24 (b).

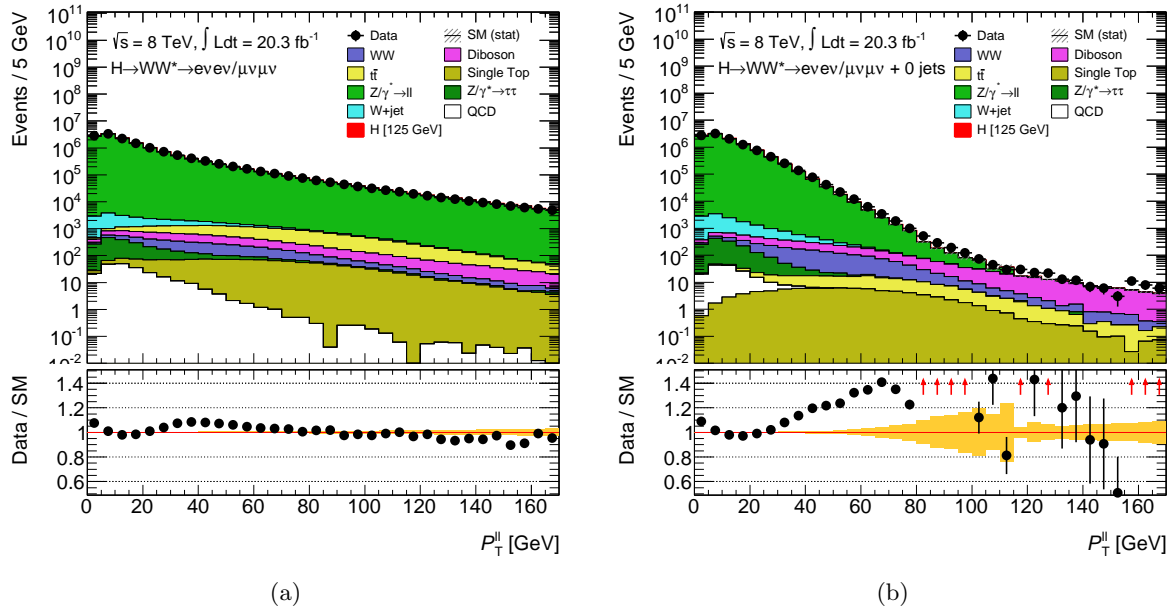


Figure 8.24: The $p_{T,\ell\ell}$ distributions in the Z enriched region in inclusive (a) and $n_j = 0$ (b). The W +jets and QCD processes are estimated with the data-driven method. The other processes are normalized to the theoretical cross section. The bottom part of the plot shows the ratio of the data to prediction.

Since many kinematic variables used in the analysis, such as the p_T of leptons, missing transverse energy, m_T and $\Delta\phi_{\ell\ell}$, are correlated to the p_T^Z , a reweighting procedure is applied in order to obtain a better modeling. The reweighting factor is extracted from the data to Z +jets MC ratio in the Z enriched region in the $n_j = 0$ category. Only the $\mu\mu$ channel is

used to extract the reweighting factor because of the good resolution of reconstructed muons. The obtained reweighting factors are then applied to all $e\mu$ and $ee/\mu\mu$ channels in the $n_j = 0$ category. Figure 8.25 shows the reweighting factor as a function of $p_{T,\ell\ell}$. The modeling of the Z+jets background has been improved in general with this reweighting factor. The $\Delta\phi_{\ell\ell}$ distributions in the Z enriched sample before and after the reweighting are shown in figure 8.26 as an example. A better agreement between the data and predictions can be seen after the reweighting. To take into account a potential difference between the reweighting factor on the Z enriched sample and on actual signal regions, a systematic uncertainty is estimated. For that, another reweighting factor is computed from the Z enriched sample with an additional requirement of $p_T^{\text{miss}} > 20$ GeV. Differences between the two reweighting factors are assigned as the systematic uncertainty. The uncertainty is up to 25% at low $p_{T,\ell\ell}$.

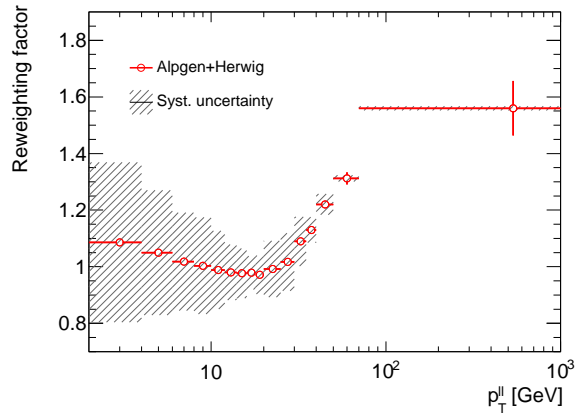


Figure 8.25: Reweighting factor for the Z+jets background in the $n_j = 0$ category.

8.4.2 $Z \rightarrow \tau\tau$ background

The normalization of the $Z \rightarrow \tau\tau$ background is derived from the ratio of data to MC in a CR, where the $Z \rightarrow \tau\tau$ process is enriched. Dedicated CRs for each n_j category are defined after the pre-selection using the $e\mu$ sample. Event selections for the CRs are given as follows:

- **$n_j = 0$:** In this $n_j = 0$ category, the leptons coming from the τ decays are likely emitted back-to-back, which results in a large $\Delta\phi_{\ell\ell}$. This event topology, together with the invariant mass of the di-lepton system, is exploited to construct the CR. Figure 8.27 shows the $m_{\ell\ell}$ and $\Delta\phi_{\ell\ell}$ distributions after the $n_j = 0$ selection. $m_{\ell\ell} < 80$ GeV and $\Delta\phi > 2.8$ are required.
- **$n_j = 1$:** In this $n_j = 1$ category, the CR is defined after the maximum $m_T^\ell > 50$ GeV requirement but before the $Z \rightarrow \tau\tau$ veto. The $Z \rightarrow \tau\tau$ discrimination is based on the $m_{\ell\ell}$ and $m_{\tau\tau}$ with the collinear approximation method (see section 7.3). Figure 8.35 shows the $m_{\ell\ell}$ and $m_{\tau\tau}$ distributions after the maximum m_T^ℓ selection. $m_{\ell\ell} < 80$ GeV and $m_{\tau\tau} > 60$ GeV are required to define the CR.
- **$n_j \geq 2$ ggF-enriched:** The CR in the $n_j \geq 2$ ggF-enriched category is defined in the similar way as in the $n_j = 0$ category. $m_{\ell\ell} < 70$ GeV and $\Delta\phi_{\ell\ell} > 2.8$ are required after the $n_b = 0$ selection in order to build the CR.

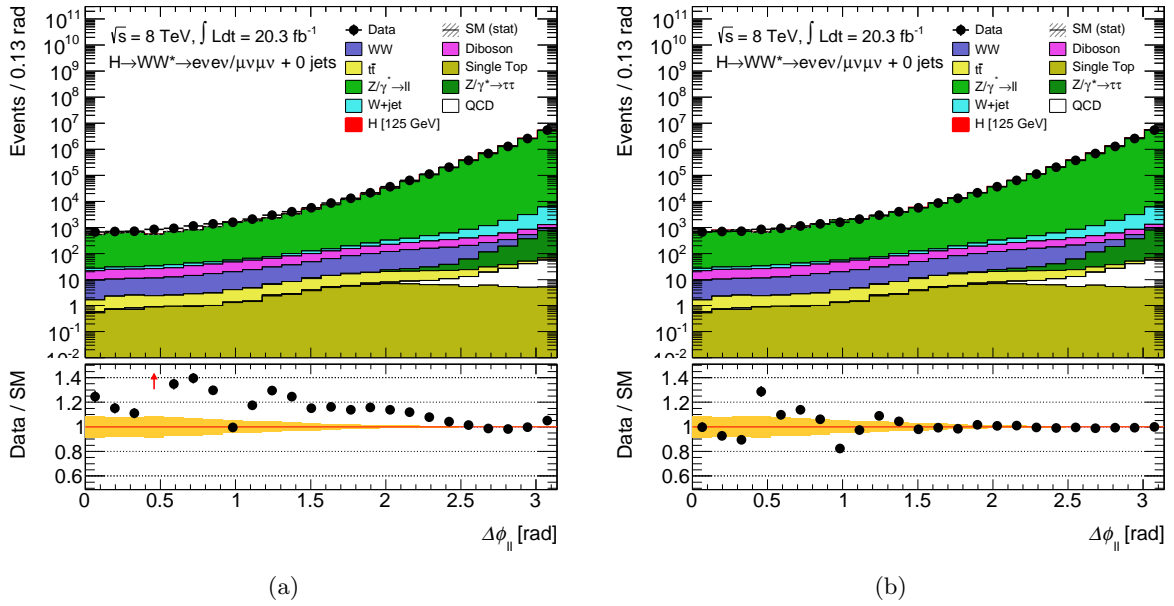


Figure 8.26: The $\Delta\phi_{\ell\ell}$ distributions before (a) and after (b) applying the p_T^Z reweighting. The distributions are shown in the Z enriched region in the $n_j = 0$ category. The backgrounds are estimated with the same methods as figure 8.24. The bottom part of the plot shows the ratio of the data to prediction.

Table 8.13 summarizes the expected event yields in the $Z \rightarrow \tau\tau$ CRs. The purities of the $Z \rightarrow \tau\tau$ process are 91%, 84% and 73% for the $n_j = 0$, $n_j = 1$ and $n_j \geq 2$ ggF-enriched categories, respectively. The normalization factor (NF) is computed using the predicted and observed event yields as follows:

$$\text{NF} = \frac{N^{\text{obs}} - N^{\text{non-}Z \rightarrow \tau\tau}}{N^{Z \rightarrow \tau\tau}}, \quad (8.12)$$

where $N^{(\text{non-})Z \rightarrow \tau\tau}$ is the number of expected events for the (non-) $Z \rightarrow \tau\tau$ process. The estimated NFs are 1.00 ± 0.02 (stat.), 1.05 ± 0.04 (stat.) and 1.00 ± 0.09 (stat.) for the $n_j = 0$, $n_j = 1$ and $n_j \geq 2$ ggF-enriched categories, respectively. Figure 8.28 shows the m_T and $\Delta\phi_{\ell\ell}$ distributions in the $Z \rightarrow \tau\tau$ control regions. Good agreements of the background shapes between the data and predictions are observed.

An uncertainty on the extrapolation from the CR to SR is evaluated from the difference in the parameter of $\alpha = N^{SR}/N^{CR}$ in various conditions using simulations. The following sources of the uncertainty are considered:

- **Scale:** Uncertainty due to the higher perturbative orders in QCD not included in the MC. The uncertainty is evaluated by varying the renormalization and factorization scales in ALPGEN by factor half and two. The maximum deviation is taken as the uncertainty;
- **PDF:** Uncertainty on the modeling of the parton distribution functions. The MC events generated with the default CTEQ6L1 are reweighted to CT10, MSTW2008 and NNPDF2.3 [112] PDF sets, then the uncertainty is obtained by taking the largest deviation between

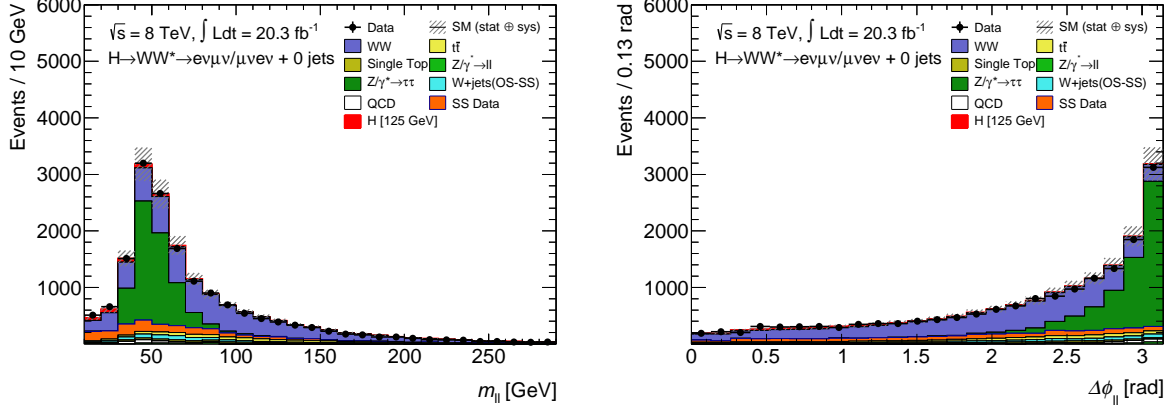


Figure 8.27: The $m_{\ell\ell}$ and $\Delta\phi_{\ell\ell}$ distributions after the $n_j = 0$ selection in the $e\mu$ sample. The W +jets and QCD processes are estimated with the extrapolation method. The *Other VV* process is estimated using the OS-SS method. The other processes are estimated using the MC. The normalization factors for the WW , Z +jets and Top processes are applied to the MC predictions, including the $Z \rightarrow \tau\tau$ process.

Table 8.13: Summary of the expected event yields in the $Z \rightarrow \tau\tau$ control regions. The W +jets and QCD backgrounds are estimated with the extrapolation factor method. The *Other VV* background in the $n_j = 0$ and 1 categories are estimated using the OS-SS method. The other processes are normalized to the theoretical cross sections, except for the Top process in the $n_j > 2$ ggF-enriched category, which is corrected with the normalization factor (see section 8.5). The uncertainty is the statistical only.

$n_j = 0$ category				
	WW	Z +jets	Top	W +jets (OS-SS)
$Z \rightarrow \tau\tau$ CR	116.92 ± 1.47	4137.53 ± 28.65	16.47 ± 0.49	73.20 ± 8.56
	QCD	SS Data	Total Bkg.	Observed
$Z \rightarrow \tau\tau$ CR	93.01 ± 1.31	82.14 ± 12.56	4519.28 ± 32.50	4557
$n_j = 1$ category				
	WW	Z +jets	Top	W +jets (OS-SS)
$Z \rightarrow \tau\tau$ CR	99.15 ± 1.34	1170.46 ± 12.96	74.66 ± 1.02	29.65 ± 4.56
	QCD	SS Data	Total Bkg.	Observed
$Z \rightarrow \tau\tau$ CR	20.26 ± 0.52	67.93 ± 9.39	1462.10 ± 16.74	1540
$n_j \geq 2$ ggF-enriched category				
	WW	<i>Other VV</i>	Z +jets	Top
$Z \rightarrow \tau\tau$ CR	12.66 ± 0.42	4.06 ± 0.66	192.36 ± 5.79	34.03 ± 0.70
	W +jets	QCD	Total Bkg.	Observed
$Z \rightarrow \tau\tau$ CR	10.20 ± 2.00	8.32 ± 0.61	262.82 ± 6.25	266

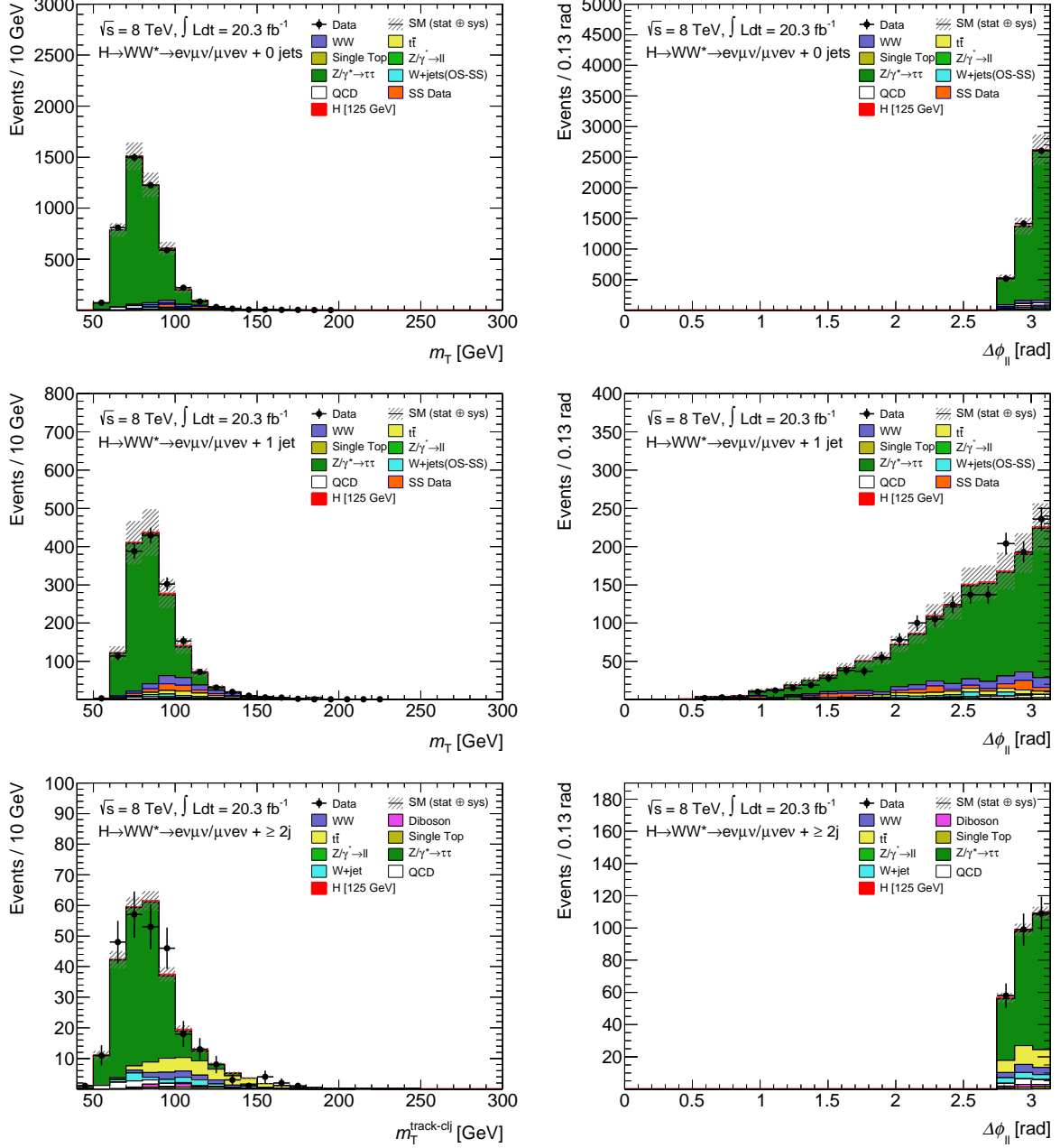


Figure 8.28: The m_T and $\Delta\phi$ distributions in the $Z \rightarrow \tau\tau$ control regions in the $n_j = 0$ (top), $n_j = 1$ (middle) and $n_j \geq 2$ ggF-enriched (bottom) categories. The backgrounds are estimated with the same configuration as table 8.13, but the $Z \rightarrow \tau\tau$ normalization factor is applied in the plots.

the CT10 and either the MCTW2008 or the NNPDF2.3, and adding in quadrature the uncertainty determined using the CT10 error eigenvectors;

- **UE/PS:** Uncertainties for the underlying event and parton shower models. The underlying and showering effects are quantified by comparing the ALPGEN+HERWIG and ALPGEN+PYTHIA6;
- **p_T^Z reweighting:** Uncertainty on the p_T^Z reweighting for the $n_j = 0$ category. Two sets of the reweighting (described in section 8.4.1) are compared to evaluate the uncertainty. Since this reweighting is correlated to the UE/PS modeling, previous UE/PS uncertainty is recalculated after the reweighting (residual uncertainty) for the $n_j = 0$ category.

Table 8.14 summarizes the evaluated uncertainties on the extrapolation from the $Z \rightarrow \tau\tau$ CR to SR.

Uncertainty source		$n_j = 0$	$n_j = 1$	$n_j \geq 2$
Scale		-1.6	4.7	-10.3
PDF		1.4	1.8	1.1
UE/PS	p_T^Z	19	-2	10.4
	residual	5.7		

Table 8.14: Summary of the uncertainties (in %) on the extrapolation from the $Z \rightarrow \tau\tau$ CR to SR. The signed uncertainty means the correlation among the categories. These uncertainties are treated as nuisance parameters in the fit (see chapter 9).

8.4.3 $Z \rightarrow ee/\mu\mu$ background

The $Z \rightarrow ee/\mu\mu$ processes largely contribute to the $ee/\mu\mu$ channels. The f_{recoil} variable (defined in equation 7.1) is used to reduce the $Z \rightarrow ee/\mu\mu$ background in the $ee/\mu\mu$ channels because it shows a clear shape difference between the Z +jets and all other processes with neutrinos in the final state. The f_{recoil} requirement is the final event selection to construct the SR in the $ee/\mu\mu$ channels. A data-driven estimation of the selection efficiency reduces the systematic uncertainty on this cut since the f_{recoil} uses soft jets and the MCs are not expected to be precise in these modeling.

The number of observed events after ($N_{\text{SR}}^{\text{obs}}$) and before ($N_{\text{pre-SR}}^{\text{obs}}$) the f_{recoil} cut are written as follows:

$$N_{\text{SR}}^{\text{obs}} = N_{\text{SR}}^{Z+\text{jets}} + N_{\text{SR}}^{\text{non-}Z+\text{jets}}, \quad (8.13)$$

$$N_{\text{pre-SR}}^{\text{obs}} = \frac{N_{\text{pre-SR}}^{Z+\text{jets}}}{\epsilon^{Z+\text{jets}}} + \frac{N_{\text{pre-SR}}^{\text{non-}Z+\text{jets}}}{\epsilon^{\text{non-}Z+\text{jets}}}, \quad (8.14)$$

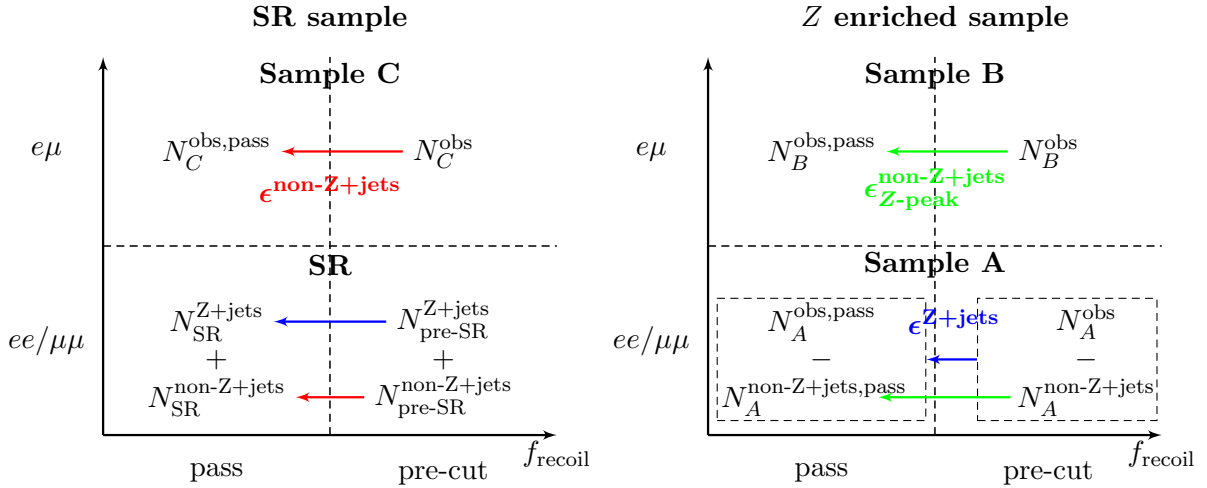
where the observed events are divided to the Z +jets contribution, $N^{Z+\text{jets}}$, and the other contribution, $N^{\text{non-}Z+\text{jets}}$. The $\epsilon^{Z+\text{jets}}$ and $\epsilon^{\text{non-}Z+\text{jets}}$ are the efficiencies of the f_{recoil} selection for the Z +jets and the other processes, respectively. Combining equation 8.13 and 8.14, $N_{\text{SR}}^{Z+\text{jets}}$ is given as follows:

$$N_{\text{SR}}^{\text{Z+jets}} = \epsilon^{\text{Z+jets}} \times \frac{N_{\text{SR}}^{\text{obs}} - \epsilon^{\text{non-Z+jets}} \times N_{\text{pre-SR}}^{\text{obs}}}{\epsilon^{\text{Z+jets}} - \epsilon^{\text{non-Z+jets}}}, \quad (8.15)$$

which gives the fully data-driven estimate of the Z +jets yield by measuring $\epsilon^{\text{Z+jets}}$ and $\epsilon^{\text{non-Z+jets}}$ from the data. $\epsilon^{\text{Z+jets}}$ is calculated using the $ee/\mu\mu$ sample satisfying $|m_{\ell\ell} - m_Z| < 15$ GeV after the $p_{\text{T,rel}}^{\text{miss}}$ selection (sample A). The non- Z +jets contribution in this region, $N_A^{\text{non-Z+jets}}$, is not negligible in measuring the efficiency; this contribution is subtracted with the MC and data-driven predictions described in previous sections. An additional f_{recoil} efficiency, $\epsilon_{\text{Z-peak}}^{\text{non-Z+jets}}$, is evaluated by considering the efficiency of the subtraction component. $\epsilon_{\text{Z-peak}}^{\text{non-Z+jets}}$ is obtained from the $e\mu$ sample satisfying the Z selection defined above (sample B). Now, $\epsilon^{\text{Z+jets}}$ is given by:

$$\epsilon^{\text{Z+jets}} = \frac{N_A^{\text{obs,pass}} - \epsilon_{\text{Z-peak}}^{\text{non-Z+jets}} \times N_A^{\text{non-Z+jets}}}{N_A^{\text{obs}} - N_A^{\text{non-Z+jets}}}, \quad \epsilon_{\text{Z-peak}}^{\text{non-Z+jets}} = \frac{N_B^{\text{obs,pass}}}{N_B^{\text{obs}}}, \quad (8.16)$$

where $N_{A(B)}^{\text{obs}}$ is number of observed events in sample A(B), and also $N_{A(B)}^{\text{obs,pass}}$ is number of events in sample A(B) passing the f_{recoil} cut. The remaining $\epsilon^{\text{non-Z+jets}}$ is calculated simply as the fraction of events in the $e\mu$ sample passing the f_{recoil} cut in the SR (sample C). The relations between the f_{recoil} efficiencies and measuring samples are summarized in figure 8.29. Figure 8.30 shows the f_{recoil} distributions in the sample A, B and C. Good purities of the Z +jets process in sample A and the non- Z +jets process in sample B and C can be seen.


 Figure 8.29: f_{recoil} efficiency method.

Since the $\epsilon^{\text{Z+jets}}$ is calculated in the sample A and applied to the SR, the sample A to SR extrapolation uncertainty is evaluated with MCs by comparing the f_{recoil} selection efficiency between the sample A and SR. The largest difference using ALPGEN+HERWIG and ALPGEN+PYTHIA samples is taken as the uncertainty. Also uncertainties on the sample B and C to the $ee/\mu\mu$ sample extrapolation are assigned to the $\epsilon^{\text{non-Z+jets}}$ and $\epsilon_{\text{Z-peak}}^{\text{non-Z+jets}}$. The largest difference of the f_{recoil} selection efficiency between the $e\mu$ sample and $ee/\mu\mu$ sample by varying the yield of each source of the non- Z +jets process by its uncertainty is evaluated with

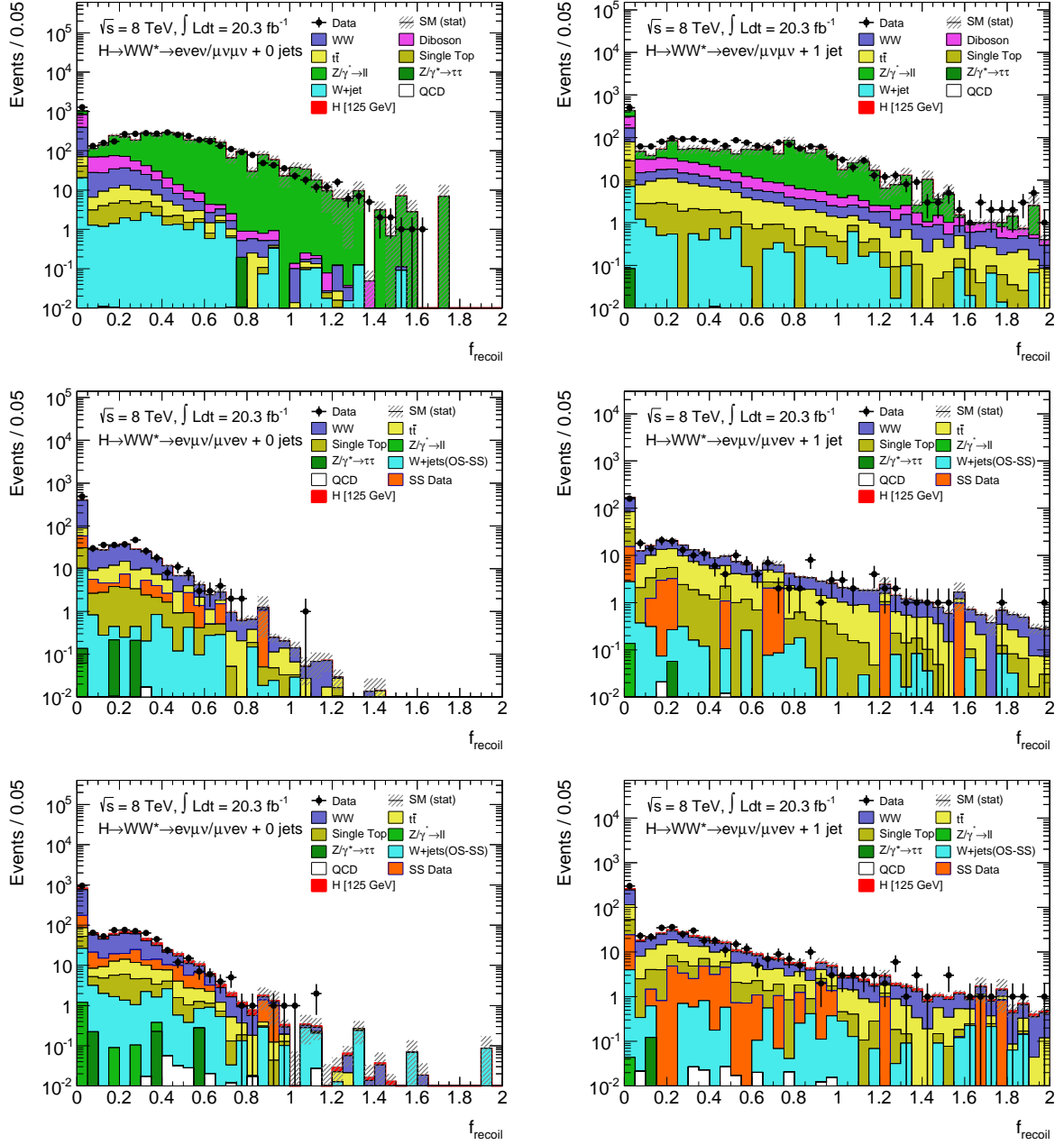


Figure 8.30: The f_{recoil} distribution is sample A (top), B (middle) and C (bottom). The left plots show the distribution in the $n_j = 0$ category and the right is the $n_j = 1$ category. The W +jets and QCD processes are estimated with the extrapolation factor method. The *Other VV* process in the $e\mu$ sample is estimated with the OS-SS method. The other processes are normalized to the theoretical cross sections without any data-based normalization factors.

the MC, and taken as the uncertainty. The uncertainty from the generator comparison is not assigned to the $\epsilon^{\text{non-}Z+\text{jets}}$ and $\epsilon_{Z\text{-peak}}^{\text{non-}Z+\text{jets}}$ since it is confirmed that differences between different generators are within the statistics uncertainty.

Table 8.15 summarizes the obtained efficiencies and their uncertainties. The normalization factor is evaluated from the ratio of $N_{\text{SR}}^{Z+\text{jets}}$ to the number of $Z+\text{jets}$ events in the SR estimated by the MC. The obtained normalization factors for the $Z \rightarrow ee/\mu\mu$ background are 2.18 ± 0.33 (stat.) for the $n_j = 0$ category and 1.62 ± 0.50 (stat.) for $n_j = 1$ category. These normalization factors are applied to only the $ee/\mu\mu$ channels. The MCs without data-based corrections are used in the $e\mu$ channel since the f_{recoil} cut is not required.

Table 8.15: Summary of the f_{recoil} efficiencies and uncertainties. These uncertainties are treated as nuisance parameters in the fit (see chapter 9)

Efficiency type	$n_j = 0$	$n_j = 1$
$\epsilon^{Z+\text{jets}}$, efficiency of sample A	0.14	0.13
sample A to SR extrapolation	32 %	16 %
statistical	9.4 %	16 %
$\epsilon_{Z\text{-peak}}^{\text{non-}Z+\text{jets}}$, efficiency of sample B	0.68	0.66
sample B to $ee/\mu\mu$ extrapolation	2.5 %	2.4 %
statistical	1.9 %	3.9 %
$\epsilon^{\text{non-}Z+\text{jets}}$, efficiency of sample B	0.69	0.64
sample C to $ee/\mu\mu$ extrapolation	0.8 %	1.2 %
statistical	1.8 %	3.0 %
Total uncertainty on yield estimate	49 %	45 %

8.5 Top background

Top quarks are mostly produced in its pair or in association with a W boson or quarks. The leptonic decay of a top quark, $t \rightarrow Wb \rightarrow \ell\nu b$, leads a lepton and b -quark in the final state. Thus, the top production tends to contribute to the $n_j \geq 1$ categories, about 35 % ($n_j = 1$) and 55 % ($n_j \geq 2$ ggF-enriched) of the total background in the signal regions. The Top production is modeled using POWHEG+PYTHIA6, except for the t -channel production, which is modeled with ACERMC. The Top background yields predicted by the MC are corrected by data-based normalization factors (NORM category). The normalizations for the $n_j = 0$ and $n_j = 1$ categories are obtained with specific treatments, which are described in the following section 8.5.1 and 8.5.2. For the $n_j \geq 2$ ggF-enriched category, the normalization is computed from the ratio of the data and MC in a control region, which is described in section 8.5.3.

8.5.1 Estimation of background normalization for $n_j = 0$ category

In the $n_j = 0$ category, the top quark productions contribute as backgrounds when all jets produced with the top quarks are not identified. Therefore, the modeling of the jets highly affects the prediction of the Top background in this category. A method to obtain the normalization (called ‘‘Jet veto extrapolation method’’) based on this jet veto probability thus has been developed.

The number of Top events after the $n_j = 0$ requirement but including $\Delta\phi_{\ell\ell} < 2.8$ cut can be expressed using the data as follows:

$$N_{\text{Top},0j}^{\text{data}} = (N^{\text{obs}} - N^{\text{non-Top}}) \times P_2^{\text{data}}, \quad (8.17)$$

where N^{obs} is the number of events in data before the $n_j = 0$ requirement but also including $\Delta\phi_{\ell\ell} < 2.8$ cut (defined as ‘‘Top 0j CR’’). The $\Delta\phi_{\ell\ell} < 2.8$ requirements are applied to suppress the Z +jets contribution in the CR. In addition, the CR is defined using only the $e\mu$ events to achieve a further suppression of the the Z +jets contribution. $N^{\text{non-Top}}$ is the remaining contribution from the non-Top process, which is estimated with the MCs and data-driven methods described in previous sections. Figure 8.31 (a) and (b) show the m_T and $\Delta\phi_{\ell\ell}$ distributions in the Top 0j CR. The purity of the Top process in the CR reaches about 60%. The quantity of P_2 corresponds to the fraction of the Top events passing the $n_j = 0$ requirement. The P_2 can be computed by the Top MC samples.

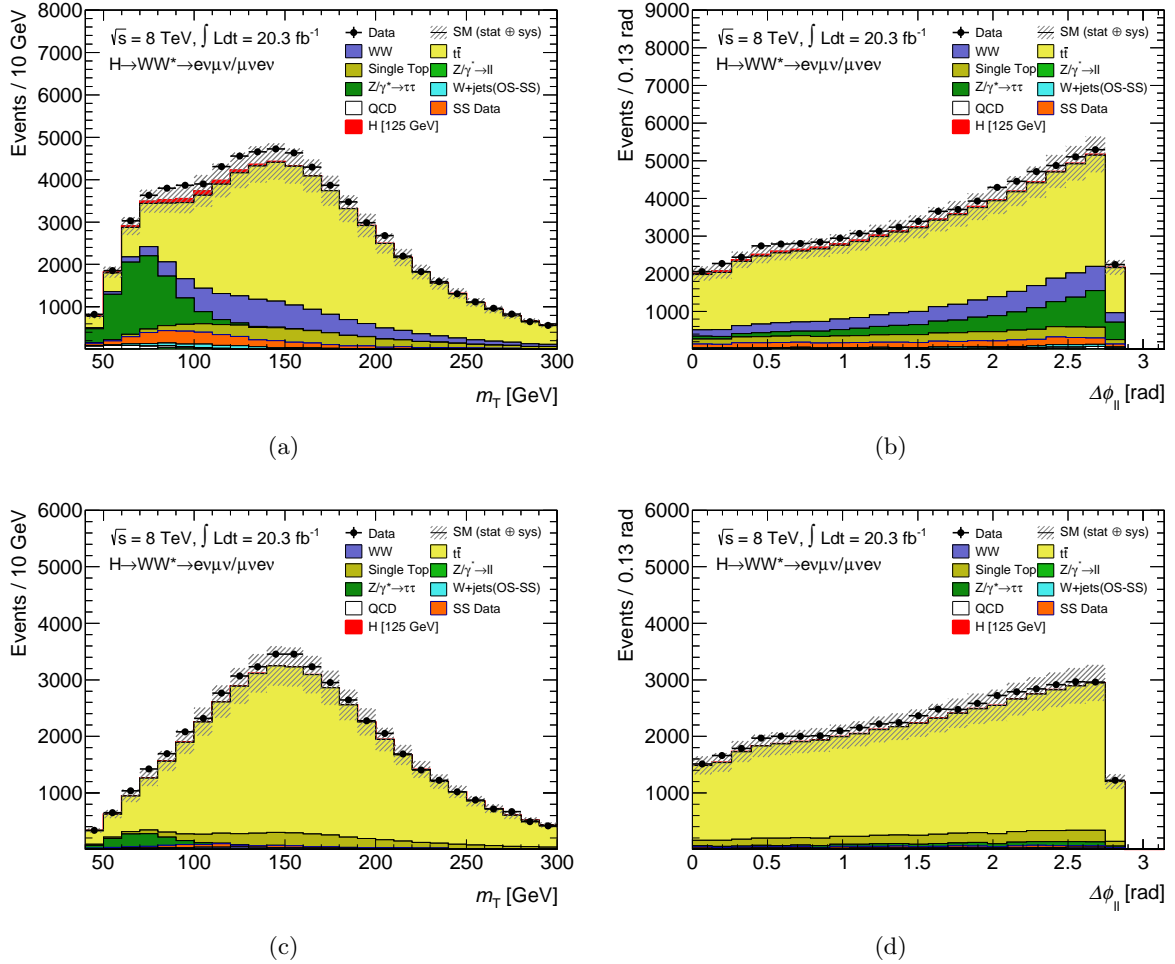


Figure 8.31: The m_T and $\Delta\phi_{\ell\ell}$ distributions in the Top 0j CR (top) and b -tagged CR (bottom). The W +jets, QCD and *Other* VV processes are estimated with the data-driven methods. The Z +jets process is estimated with the MC, and corrected by the normalization factor from the data. The other processes are normalized to the theoretical cross sections.

The P_2 estimated with the MC is corrected by data to take into account a possible mis-

modeling of the jets. The correction is obtained from a control sample (b -tagged CR) that requires at least one b -tagged jet with $p_T > 20$ GeV at the Top 0j CR. The b -tagged CR is dominated by the $t\bar{t}$ production as shown in figure 8.31 (c) and (d). The b -tagged jet with the largest tag weight is defined as the tag jet. Now, the P_2^{data} can be written with the correction as follows:

$$P_2^{\text{data}} = P_2^{\text{MC}} \times \left(\frac{P_1^{\text{btag,data}}}{P_1^{\text{btag,MC}}} \right)^2, \quad (8.18)$$

where P_1^{btag} is a single jet veto survival probability, which is defined as the fraction of events with no probe jet in addition to the tag jet over the total number of events in the b -tagged CR. The probe jets are defined as jets satisfying $\Delta R(\text{jet}, \text{tag jet}) > 1$. This quantity of P_1 basically denotes a jet veto efficiency, where the presence of one jet is expected. The square is applied to account for the presence of two jets in the Born-level $t\bar{t}$ production. Figure 8.32 shows the number of probe jets in the b -tagged CR.

Table 8.16 summarizes the results for this Jet veto extrapolation method. The normalization factor is evaluated from the ratio of $N_{\text{Top},0j}^{\text{data}}$ to the number of Top events estimated with the MC after the $n_j = 0$ and $\Delta\phi_{\ell\ell} < 2.8$ requirements, $N_{\text{top},0j}^{\text{MC}}$. The normalization factor of 1.08 ± 0.02 (stat.) is obtained.

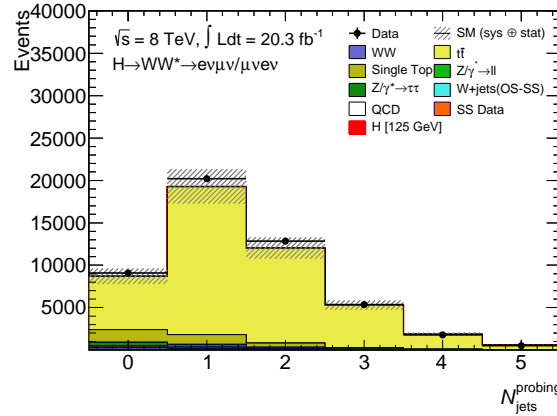


Figure 8.32: The number of probe jets for the P_1 calculation in the Jet veto extrapolation method. The backgrounds are estimated with the same methods as figure 8.31.

Since the calculation of the Jet veto extrapolation method is not performed in the final fitting procedure, the obtained normalization factor is inserted to the fitting as a constant value. Thus, all uncertainties on the normalization factor, including experimental uncertainty (see section 9.3), are estimated. Uncertainties for the term $P_2^{\text{MC}} / (P_1^{\text{btag,MC}})^2$ in equation 8.18, which relies on the MC modeling, are evaluated from the difference of the term by varying the experimental and theoretical conditions. Also uncertainties related to the extrapolation from the jet veto stage to the SR are derived from the variation of $\alpha_{\text{top},0j} = N_{\text{Top},0j}^{\text{MC,SR}} / N_{\text{Top},0j}^{\text{MC}}$ in the MCs, where $N_{\text{Top},0j}^{\text{MC,SR}}$ is the number of Top events in the SR. The following theoretical uncertainties on these parameters are assigned:

- **Scale:** Uncertainty due to the higher perturbative orders in QCD not included in the MC. The uncertainty is evaluated by varying the renormalization and factorization scales in MC@NLO by factor half and two. The maximum deviation is taken as the uncertainty;

Table 8.16: Summary of the results for the Jet veto extrapolation for the $n_j = 0$ category. The uncertainties shown are statistical only.

$P_1^{\text{btag,data}}$	0.1699 ± 0.0018
$P_1^{\text{btag,MC}}$	0.1686 ± 0.0002
P_2^{data}	0.01815 ± 0.00040
P_2^{MC}	0.01808 ± 0.00007
N^{obs}	76013
$N^{\text{non-Top}}$	20414.5 ± 76.8
$N_{\text{Top},0j}^{\text{data}}$	1009.2 ± 23.0
$N_{\text{Top},0j}^{\text{MC}}$	939.2
Ratio (NF)	1.08 ± 0.02

- **PDF:** Uncertainty on the modeling of the parton distribution functions. The uncertainty is obtained by taking the largest deviation between the nominal CT10 and either the MCTW2008 or the NNPDF2.3, and adding in quadrature the uncertainty determined using the CT10 error eigenvectors;
- **Generator and UE/PS:** Uncertainties for the generator, underlying event and parton shower models. The generator effects are evaluated by comparing MC@NLO+HERWIG and POWHEG+HERWIG. The underlying and showering effects are quantified by comparing the POWHEG+PYTHIA6 and POWHEG+HERWIG;
- **Single top:** In the Top background estimation, the $t\bar{t}$ and single-top productions are treated together. The cross sections of the single-top productions are varied by $\pm 20\%$ to take into account a potential difference of the jet veto survival probabilities (P_1 and P_2) between the two processes;
- **Interference:** The $t\bar{t}$ and tW processes share the same final state and interference between the two processes are expected. The overlap removal is performed at the event generations. The uncertainty is obtained by comparing different schemes of removing the interference [113].

The table 8.17 summarizes the uncertainties on the $P_2^{\text{MC}}/(P_1^{\text{btag,MC}})^2$ and $\alpha_{\text{top},0j}$. The total uncertainty amounts to 8.3%.

8.5.2 b -tag extrapolation for $n_j = 1$ category

In the $n_j = 1$ category, the Top production is the second largest background after the WW production. A normalization factor method (called “ b -tag extrapolation method”) is used to estimate the Top background in this category. This method is designed to reduce the experimental uncertainties on the b -tagging. The normalization is obtained from the only $e\mu$ channel, then applied to both the $e\mu$ and $ee/\mu\mu$ channels.

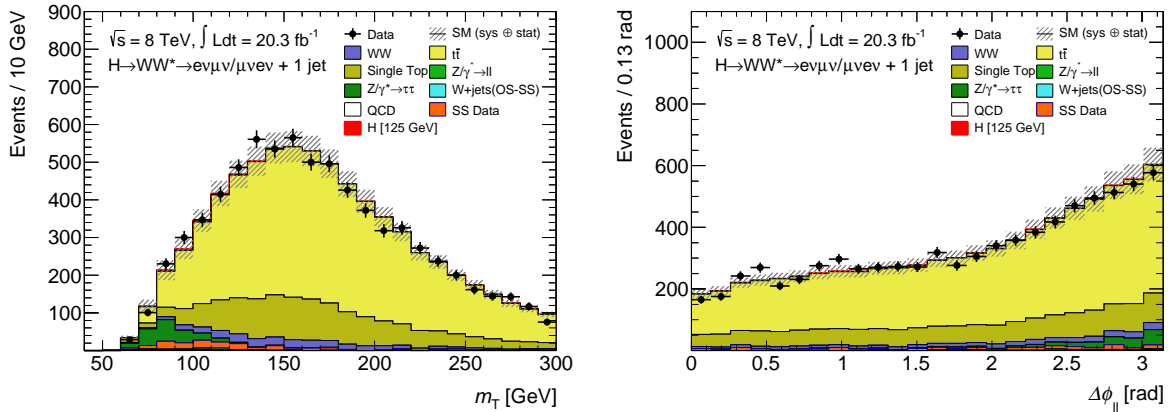
The number of Top events after the maximum $m_T^\ell > 50$ GeV cut but with no $n_b = 0$ requirement in the $n_j = 0$ category can be written using the data as follows:

$$N_{\text{Top},1j}^{\text{data}} = (N^{\text{obs}} - N^{\text{non-Top}}) \times \frac{(1 - \epsilon_{\text{tag}}^{\text{data},1j\text{CR}})}{\epsilon_{\text{tag}}^{\text{data},1j\text{CR}}}, \quad (8.19)$$

Table 8.17: Summary of the uncertainties for the Jet veto extrapolation for the $n_j = 0$ category. Each uncertainty is treated as a nuisance parameter in the fit (see chapter 9)

Uncertainty source	$P_2^{\text{MC}} / (P_1^{\text{btag,data}})^2$	$\alpha_{\text{top},0j}$
Experimental	4.4	0.9
Non-top subtraction	2.7	-
Theoretical:		
Scale	1.6	0.8
PDF	0.7	1.1
Gen. and UE/PS	3.5	4.1
Single top	0.4	1.2
Interference	0.2	0.2
Statistical	2.6	0.9
Total	6.8	4.7

where N^{obs} is the number of events after the maximum $m_T^\ell > 50$ GeV cut, but the b -tagging requirement is reverted (defined as “Top 1j CR”). $N^{\text{non-top}}$ is the other contributions from the non-Top production, which are estimated with the MCs and data-driven methods as described previous sections. $\epsilon_{\text{tag}}^{\text{1jCR}}$ corresponds to the efficiency of the b -tagging in the Top 1j CR. The Top 1j CR achieves a good purity, as shown in figure 8.33, by revering the b -tagging requirement. Also fairly good agreements on the shape estimations are observed. The $\epsilon_{\text{tag}}^{\text{1jCR}}$ can be computed using the MC samples. However, a systematic uncertainty of 5% on the b -tagging would induce an uncertainty of about 30% in the estimated yield in the SR. In order to reduce this uncertainty, the $\epsilon_{\text{tag}}^{\text{1jCR}}$ is estimated with the data.


 Figure 8.33: The m_T and $\Delta\phi_{\ell\ell}$ distributions in the Top 1j CR. The W +jets and QCD processes are estimated with the extrapolation factor method. The *Other VV* process is estimated using the OS-SS method. The Z +jets and Top backgrounds are corrected by the normalization factors from the data.

To measure the b -tagging efficiency in a phase space as close to the SR, a control sample after the pre-selection with the $n_j = 2$ and maximum $m_T^\ell > 50$ GeV requirements are selected, where exact one jet is required to be the b -tagged jet. The selected sample is dominated by the

$t\bar{t}$ process with reconstructed jets from b quarks. Then, b -tagging efficiency, $\epsilon_{\text{tag}}^{\text{data},2\text{jCR}}$, is defined as the fraction of events with the other jet being b -tagged. A correction factor based on the MC, $\epsilon_{\text{tag}}^{\text{MC},1\text{jCR}}/\epsilon_{\text{tag}}^{\text{MC},2\text{jCR}}$, is introduced to take into account the bias which originates from the the b -tagging efficiency difference between the two jets and one jet events. Finally, the $\epsilon_{\text{tag}}^{\text{data},1\text{jCR}}$ is given with the data as follows:

$$\epsilon_{\text{tag}}^{\text{data},1\text{jCR}} = \epsilon_{\text{tag}}^{\text{data},2\text{jCR}} \times \frac{\epsilon_{\text{tag}}^{\text{MC},1\text{jCR}}}{\epsilon_{\text{tag}}^{\text{MC},2\text{jCR}}}. \quad (8.20)$$

Table 8.18 summarizes the values used for the b -tag extrapolation for the $n_j = 1$ category. The normalization factor is evaluated from the ratio of $N_{\text{Top},1\text{j}}^{\text{data}}$ to the number of Top events estimated with the MC after the maximum $m_T^\ell > 50$ GeV cut but with no $n_b = 0$ requirement, $N_{\text{top},1\text{j}}^{\text{MC}}$. The normalization factor of 1.06 ± 0.03 (stat.) is obtained.

A theoretical uncertainty is considered for the correction term $\epsilon_{\text{tag}}^{\text{MC},1\text{jCR}}/\epsilon_{\text{tag}}^{\text{MC},2\text{jCR}}$, which fully relies on the MC. Also an uncertainty on the extrapolation from the Top 1j CR to the SR is evaluated. For the correction term, the uncertainty amounts to be 0.8% by summing up the theoretical uncertainties defined in section 8.5.2. Also the theoretical uncertainty of 3.6% is assigned to the extrapolation by comparing $\alpha = N_{\text{Top},1\text{j}}^{\text{MC},\text{SR}}/N_{\text{Top},1\text{j}}^{\text{MC}}$ with scale, PDF, generator and UE/PS uncertainties, where $N_{\text{Top},1\text{j}}^{\text{MC},\text{SR}}$ is the number of Top events in the SR predicted by the MC. These theoretical uncertainties are treated as nuisance parameters in the fit (see chapter 9).

Table 8.18: Summary of results for the b -tag extrapolation for the $n_j = 1$ category. The uncertainties shown are statistical only.

$\epsilon_{\text{tag}}^{\text{MC},1\text{jCR}}$	0.748 ± 0.001
$\epsilon_{\text{tag}}^{\text{MC},2\text{jCR}}$	0.694 ± 0.000
$\epsilon_{\text{tag}}^{\text{data},2\text{jCR}}$	0.692 ± 0.003
$N^{\text{obs}} - N^{\text{non-Top}}$	6091.4 ± 83.5
$N_{\text{Top},1\text{j}}^{\text{data}}$	2063.1 ± 49.2
$N_{\text{Top},1\text{j}}^{\text{MC}}$	1954.3 ± 5.0
Ratio (NF)	1.06 ± 0.03

8.5.3 Control region for $n_j \geq 2$ ggF-enriched category

In the $n_j > 2$ ggF-enriched category, the Top background remains large even with the $n_b = 0$ requirement. A CR with a high $m_{\ell\ell}$ selection is defined to derive a normalization factor for the Top estimation in the SR. The CR is constructed after the VBF veto and with $m_{\ell\ell} > 80$ GeV requirement to distinguish it from the SR (see figure 7.8). Table 8.19 summarizes the expected yields for each process in the CR. The purity of Top process in the CR reaches approximately 70%. The normalization factor (NF) is calculated as follows:

$$\text{NF} = \frac{N^{\text{obs}} - N^{\text{non-Top}}}{N^{\text{Top}}}, \quad (8.21)$$

where $N^{(\text{non-})\text{Top}}$ is the number of expected events for the (non-)Top process in the CR. The normalization factor of 1.05 ± 0.03 (stat.) is obtained. It is possible to increase the purity by

reverting the b -tag requirement as the $n_j = 1$ category. However, the systematic uncertainty on the extrapolation of the b -tagged CR to b -veto SR becomes large in this case. The figure 8.34 shows the m_T and $\Delta\phi_{\ell\ell}$ distributions in the high $m_{\ell\ell}$ CR. Fairly good agreements are found.

Table 8.19: Summary of the expected event yields in the high $m_{\ell\ell}$ control regions for the Top background. The W +jets and QCD backgrounds are estimated with the extrapolation factor method. The other processes are normalized to the theoretical cross sections. The uncertainty is the statistical only.

$n_j \geq 2$ category				
	WW	$Other VV$	Z +jets	Top
Top high $m_{\ell\ell}$ CR	559.35 ± 2.79	100.42 ± 2.97	52.78 ± 6.86	1726.80 ± 4.72
	W +jets	QCD	Total Bkg.	Observed
Top high $m_{\ell\ell}$ CR	111.65 ± 3.16	16.86 ± 0.43	2569.84 ± 9.81	2664

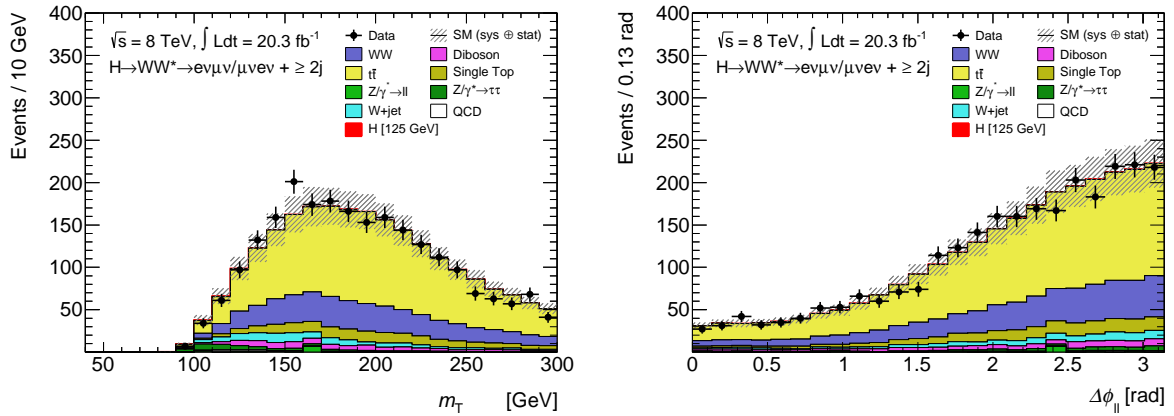


Figure 8.34: The m_T and $\Delta\phi_{\ell\ell}$ distributions in the high $m_{\ell\ell}$ CR. The W +jets and QCD processes are estimated with the extrapolation factor method. The normalization factors for the Z +jets and Top backgrounds are applied. The other processes are normalized to the theoretical cross sections.

Theoretical uncertainty on the extrapolation of the CR to SR are 3.2% from the generator, 1.2% from the UE/PS, 1% from the scale and 0.3% from the PDF. These theoretical uncertainties are treated as nuisance parameters in the fit (see chapter 9).

8.6 WW background

The WW process, with subsequent decay $W \rightarrow \ell\nu$, has the same final state with the signal. As a result, the WW process becomes the leading background in the $n_j = 0$ and $n_j = 1$ categories contributing 66% and 42% of the total backgrounds, respectively. The main contribution of the WW process is modeled using POWHEG+PYTHIA6 MC samples in the $n_j = 0$ and $n_j = 1$ categories. Normalizations of the MC samples are obtained from the WW control regions (NORM category). For the $n_j > 2$ ggF-enriched category, the WW process is modeled with SHERPA

because the second jet coming from the parton shower is poorly modeling in POWHEG. The SHERPA sample is normalized to the NLO inclusive calculation, since it is difficult to construct a control region in this category because of the large Top background contamination.

8.6.1 WW control region

The normalization factor of the WW background is taken from the ratio of data and MC in the CR. The lepton selections for the WW CR are the same as the SRs, except for the p_T of the subleading lepton. $p_T^{\ell 2} > 15$ GeV is required to reduce the W +jets and *Other VV* contaminations into the WW CR. The WW CR is divided into the $n_j = 0$ and $n_j = 1$ categories to improve the estimation of the jet multiplicity. The $ee/\mu\mu$ channels are not used to obtain the normalization factors because of lower statistics and purity. The normalization factors obtained from the $e\mu$ category are thus also applied to the $ee/\mu\mu$ category. Event selections for the WW CRs are given as follows:

- $n_j = 0$: In the $n_j = 0$ category, the CR is defined after the requirement of the $p_{T,\ell\ell} > 30$ GeV. To reduce the Z +jets background, $\Delta\phi_{\ell\ell} < 2.6$ is required. An additional requirement is $55 < m_{\ell\ell} < 110$ GeV. The lower bound of the $m_{\ell\ell}$ selection is determined by the SR selection. The upper bound is chosen to maximize the accuracy of the background prediction taking into account the statistical uncertainty on the CR sample and the systematic uncertainty on the extrapolation. The $\Delta\phi_{\ell\ell}$ and $m_{\ell\ell}$ distributions before applying the WW CR selections are shown in figure 7.4.
- $n_j = 1$: In the $n_j = 1$ category, the CR is defined after the maximum m_T^ℓ requirement. While $m_{\tau\tau} < (m_Z - 25$ GeV) is required in the SR, this threshold is not used in the CR since it removes about 30% of the WW background at high $m_{\tau\tau}$. An alternative cut, $|m_{\tau\tau} - m_Z| > 25$ GeV, is used. Additionally a cut on $m_{\ell\ell} > 80$ GeV is applied in order to exclude the signal regions and the Z +jets background. The $m_{\tau\tau}$ and $m_{\ell\ell}$ distributions before applying the WW CR selections are shown in figure 8.35.

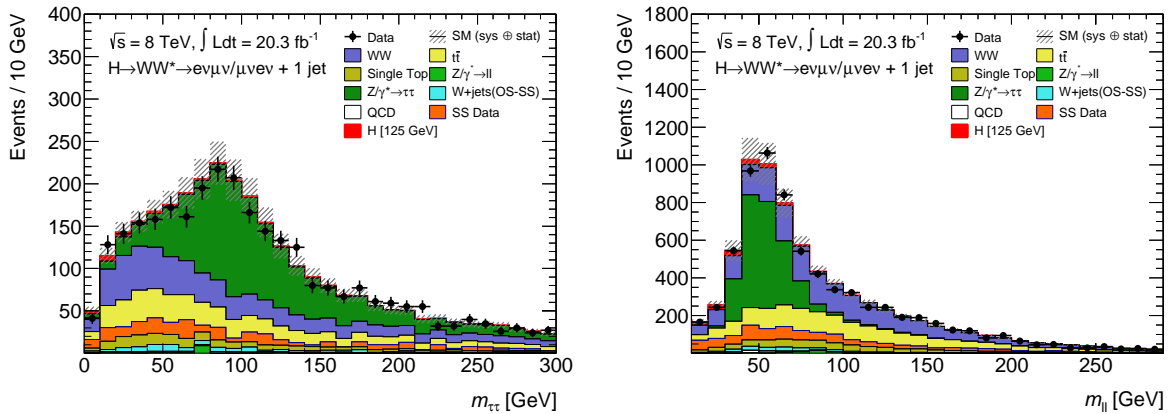


Figure 8.35: The $m_{\tau\tau}$ and $m_{\ell\ell}$ distributions for the $e\mu$ category after the maximum m_T^ℓ cut. The W +jets and QCD backgrounds are estimated with the extrapolation factor method. The *Other VV* background is estimated using the OS-SS method. The other processes, including the WW , are corrected by the normalization factors from the data.

Table 8.20 summarizes the expected event yield in the WW CRs. The purity of the control regions are 68 % in the $n_j = 0$ category and 42 % in the $n_j = 1$ category. The other backgrounds which contribute to the WW CR are corrected by the data-based normalization factors, or estimated with data-driven methods defined in the previous sections. The estimated normalization factor (NF) is determined using the predicted and observed event yields as follows:

$$\text{NF} = \frac{N^{\text{obs}} - N^{\text{non-WW}}}{N^{\text{WW}}}, \quad (8.22)$$

where $N^{(\text{non-})\text{WW}}$ is the number of expected events for the (non-)WW process in the CR. The normalization factor of 1.20 ± 0.03 (stat.) for the $n_j = 0$ category and $\text{NF} = 1.03 \pm 0.05$ (stat.) for the $n_j = 1$ category are obtained. Figure 8.36 shows the m_T and $\Delta\phi_{\ell\ell}$ distributions in the WW control regions with the estimated normalization factors. The shapes of these distributions agree well between the data and predictions.

Table 8.20: Summary of the expected event yields in the WW control regions. The W +jets and QCD backgrounds are estimated with the extrapolation factor method. The *Other VV* background is estimated using the OS-SS method. The Z +jets and Top background are corrected by the normalization factors from data. Other processes are normalized to the theoretical cross sections. The uncertainties correspond to the statistical uncertainty.

$n_j = 0$ category				
	WW	Z +jets	Top	W +jets (OS-SS)
WW CR	1602.73 ± 5.48	115.10 ± 4.42	332.47 ± 2.11	94.27 ± 3.74
	QCD	SS Data	Total Bkg.	Observed
WW CR	1.98 ± 0.48	211.66 ± 15.07	2358.20 ± 17.19	2713
$n_j = 1$ category				
	WW	Z +jets	Top	W +jets (OS-SS)
WW CR	1097.93 ± 4.50	96.99 ± 9.34	1100.03 ± 3.80	46.00 ± 4.27
	QCD	SS Data	Total Bkg.	Observed
WW CR	12.81 ± 0.43	248.42 ± 16.59	2602.19 ± 20.38	2647

8.6.2 Theoretical uncertainty in extrapolation

The CR to SR extrapolations for the $n_j = 0$ and $n_j = 1$ categories have uncertainties due to the limited accuracy of the MC prediction. The uncertainty is derived from the variation of the $\alpha = N^{\text{SR}}/N^{\text{CR}}$ ratios in the following comparisons:

- **Scale:** Uncertainty due to the higher perturbative orders in QCD not included in the MC. The uncertainty is evaluated by varying the renormalization and factorization scales in aMC@NLO by factor half and two. The maximum deviation is taken as the uncertainty.
- **PDF:** This uncertainty is evaluated with the same procedure as the Top production (section 8.5.1).

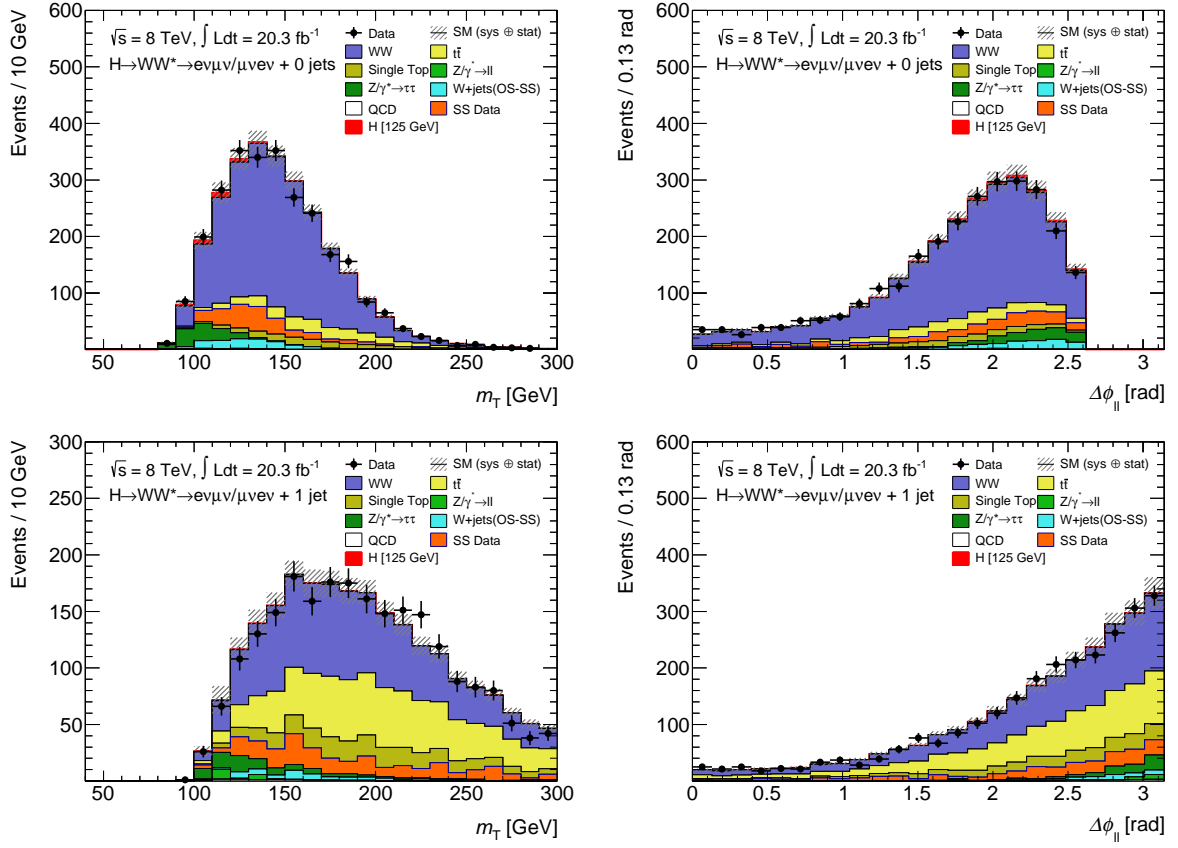


Figure 8.36: The m_T and $\Delta\phi_{\ell\ell}$ distributions in the WW control regions for the $n_j = 0$ (top) and $n_j = 1$ (bottom) categories. The backgrounds are estimated with the same methods as figure 8.35.

- **EW:** Uncertainty due to higher-order electroweak correction is determined by reweighing the MC to the NLO electroweak calculation [92] and taking the difference without the reweighing as the uncertainty.
- **Generator and UE/PS:** These uncertainties are evaluated with the same procedure as the ggF signal production (section 5.2.1).

Table 8.21 summarizes the uncertainties on the WW extrapolation for $n_j = 0$ and $n_j = 1$ categories. The extrapolation uncertainties are subdivided by the $m_{\ell\ell}$ and $p_T^{\ell\ell 2}$ as shown in the table since these divisions are performed in the fit (see section 9.1).

An additional uncertainty related to the m_T shape modeling is considered since the m_T distributions is used in the signal extraction (see chapter 9). The uncertainty is evaluated by comparing the m_T distributions in the scale, generator and UE/PS variations defined above. For each m_T shape comparison, envelopes are constructed as shown in figure 8.37. This uncertainty is up to 10% at high m_T . The generator and UE/PS uncertainties for this shape estimation and extrapolation are treated as fully correlated in the fit since the same generators are used. The theoretical uncertainty on the WW prediction is one of dominant sources of uncertainties on the signal strength measurement due to the large contamination in the SRs.

$n_j = 0$ category							
	SR1, $e\mu$			SR2, $e\mu$			SR, $ee/\mu\mu$
	a	b	c	a	b	c	
Scale	0.7	1.2	0.7	0.7	0.8	0.8	0.8
PDF	1.0	0.8	0.6	0.8	0.7	0.7	1.1
Generator	0.4	0.9	3.1	0.5	1.0	3.9	2.4
EW	1.2	0.7	-0.3	0.8	0.5	-0.4	0.1
UE/PS	2.2	1.7	-1.9	1.5	1.0	-2.4	-1.2
Total	2.8	2.6	3.8	2.1	2.0	4.8	2.9
$n_j = 1$ category							
	SR1, $e\mu$			SR2, $e\mu$			SR, $ee/\mu\mu$
	a	b	c	a	b	c	
Scale	3.1	1.6	1.0	3.2	1.5	1.3	0.6
PDF	0.6	0.5	0.6	0.5	0.4	0.6	0.9
Generator	-3.4	0.7	5.3	1.9	2.4	5.6	3.8
EW	-0.9	-1.5	-2.8	-0.9	-1.6	-2.7	-2.1
UE/PS	-2.4	-3.0	-3.6	-2.0	-3.0	-3.1	-2.3
Total	5.4	3.9	7.1	4.5	4.5	7.1	5.1

Table 8.21: Summary of the WW theory uncertainties (in %) on the extrapolation for $n_j = 0$ and $n_j = 1$ categories. The uncertainty in the $e\mu$ category is divided by the $m_{\ell\ell}$ and $p_T^{\ell\ell 2}$: SR1 (SR2) corresponds to the region with $m_{\ell\ell} < (>) 30$ GeV, and (a) is the region with $10 < p_T^{\ell\ell 2} < 15$ GeV, (b) is $15 < p_T^{\ell\ell 2} < 20$ GeV and (c) is $p_T^{\ell\ell 2} > 20$ GeV, respectively. The negative sign indicates anti-correlation with respect to the unsigned uncertainty in the same line. Each source of the uncertainty is treated as a nuisance parameter in the fit (see chapter ??).

For the $n_j > 2$ ggF-enriched analysis, the WW background is estimated using SHERPA. The SHERPA samples are split between the cases where final-state jets results from QCD vertices or from electroweak vertices. Uncertainty from the missing higher order in the MC samples are

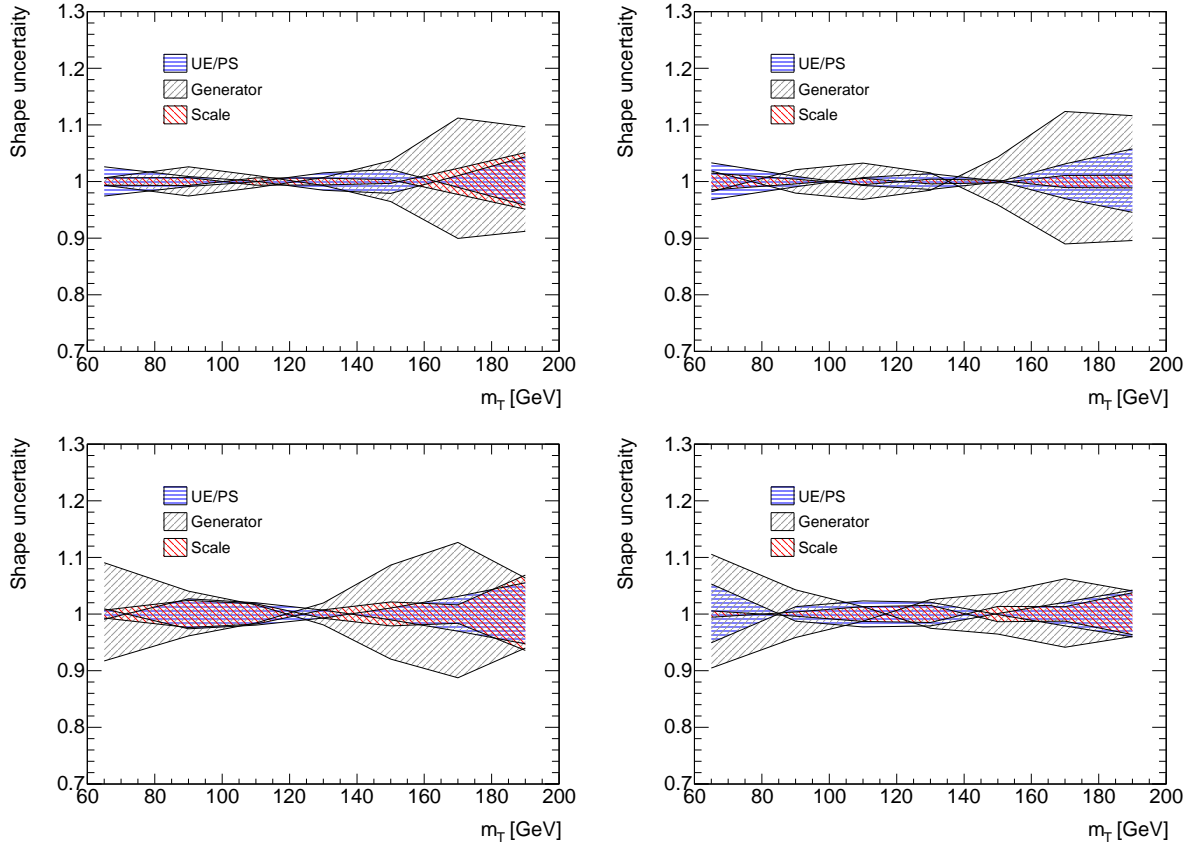


Figure 8.37: UE/PS, Generator and Scale envelopes in $n_j = 0$ (top) and $n_j = 1$ (bottom), SR1 (left) and SR2 (right). SR1 is the region with $m_{\ell\ell} < 30$ GeV and SR2 is the region with $m_{\ell\ell} > 30$ GeV. A piecewise linear interpolation is used for each individual source of uncertainty.

obtained by varying the renormalization and factorization scales in MadGraph and found to be 19% and 10% for the QCD and electroweak samples, respectively. Difference between SHERPA and MadGraph on the m_T distribution are taken as the shape uncertainty. They are 1–7% for the QCD sample and 5–17% for the electroweak sample.

8.7 Other backgrounds

Backgrounds considered to be smaller contributions than those already studied in the $H \rightarrow WW^* \rightarrow \ell\nu\ell\nu$ analysis are investigated.

$W + J/\psi$ background

The W boson production associated with a J/ψ meson contributes as a background when one of the leptons from the J/ψ decay is not identified. The presence of the $W+J/\psi$ production is confirmed in the $W\gamma^*$ validation region. Figure 8.38 shows the $m_{\ell_2\ell_3}$ distribution after the p_T^{miss} requirement for the $W\gamma^*$ VR. A data excess due to the $W+J/\psi$ background is observed around $m_{\ell_2\ell_3} \sim 3$ GeV, which corresponds to the mass of J/ψ meson. This $W+J/\psi$ contribution to the SR is evaluated by scaling up the $W\gamma^*$ MC sample to observed data in the $W\gamma^*$ VR with $2 < m_{\ell_2\ell_3} < 4$ GeV. The scale factor (SF) is obtained as follows:

$$\text{SF} = \frac{N^{\text{obs}} - N^{\text{non-}W\gamma^*}}{N^{W\gamma^*}} - 1, \quad (8.23)$$

where $N^{(\text{non-})W\gamma^*}$ is the number of expected events for the (non-) $W\gamma^*$ process. Then, the SF is multiplied to the $W\gamma^*$ events generated by the MC with $2 < m_{\ell_2\ell_3} < 4$ GeV requirement. This $W\gamma^*$ sample is regarded as the $W+J/\psi$ process with an assumption that the $W+J/\psi$ process has similar kinematics with the $W\gamma^*$ process. The estimated yield in the SR of the $n_j = 0$ category in the $e\mu$ sample is 15.2 ± 1.4 (stat.) events, which corresponds to 0.6% of the total expected background. The $W+J/\psi$ background is not included to the background estimation explicitly since the contribution is small and the $W+J/\psi$ background is already estimated in the OS-SS method because of the charge symmetry of this process.

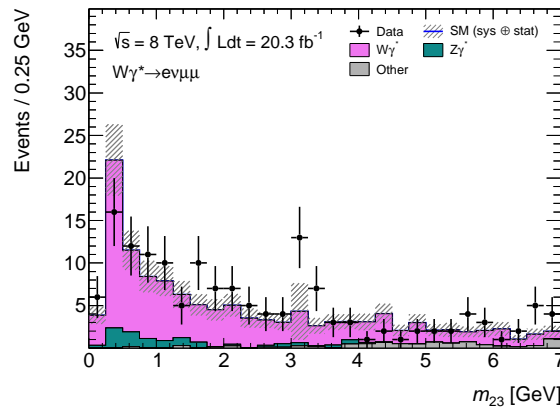


Figure 8.38: The $m_{\ell_2\ell_3}$ distribution after the p_T^{miss} cut in the $W\gamma^*$ VR.

Tri-boson, $t\bar{t} + W$ and same-sign WW backgrounds

Contributions of the tri-boson productions (WWW and $WW\gamma^*$), W boson production associated with a pair of top quarks ($t\bar{t} + W$) and same-sign WW scattering process (SS WW) [115] are also investigated using the MC samples. Table 8.22 summarizes the generators used for these processes. It is confirmed that contributions of these processes are less than 0.1% of the total expected background yield. These backgrounds are not included to the background estimation of the $H \rightarrow WW^* \rightarrow \ell\nu\ell\nu$ analysis since the contributions are negligible.

Table 8.22: Monte Carlo samples used to model the other background processes. MadGraph generator is described in reference [116].

Process	Generator	$\sigma \cdot Br$ (8 TeV) (pb)
WWW	MadGraph	0.00510
$WW\gamma^*$	MadGraph	0.001
$t\bar{t} + W$	MadGraph	0.235
SS WW	SHERPA	0.235

Chapter 9

Signal extraction and uncertainties

The extraction of the signal yield is the result of a statistical analysis of the data samples described through chapter 5–8. The signal strength parameter μ , defined as the ratio of the observed signal yield to the expected value with SM, is one of the central results of this thesis. The μ is measured using a maximum likelihood function, designed to simultaneously model the yields of various samples.

In this chapter, distributions and their range used in the fit are described in section 9.1 followed by details of the implementation in the likelihood in section 9.2. Section 9.3 explains the experimental uncertainties used in the fit.

9.1 Fit regions

The fit is simultaneously performed over the signal and control regions. The event selections for the SRs are described in chapter 7. The SRs in the $e\mu$ channels are subdivided in bins of $m_{\ell\ell}$ and $p_T^{\ell_2}$. The divisions are performed with boundaries of [10, 30, 55] GeV for $m_{\ell\ell}$ and [10, 15, 20, ∞] GeV for $p_T^{\ell_2}$. Figure 9.1 (a) and (b) show the $m_{\ell\ell}$ and $p_T^{\ell_2}$ distributions in the SR of the $n_j = 0$ category with these boundaries. The W +jets and *Other VV* backgrounds, which are denoted as W +jets(OS-SS) and SS Data in the figures, tend to be distributed in low $m_{\ell\ell}$ and low $p_T^{\ell_2}$ regions. These quantities thus are effective to distinguish the signal from the backgrounds in the fit. In addition, the SRs of the $e\mu$ sample are separated by the flavor of the subleading lepton (electron or muon) because the $W\gamma$ background tends to be reconstructed with a low- p_T electron. The m_T distributions with $\ell_2 = \text{electron}$ and $\ell_2 = \text{muon}$ are shown in figure 9.1 (c) and (d). The $n_j \geq 2$ ggF-enriched category uses single SR due to the limited statistics. Table 9.1 summarizes the SR categories in the fit.

The m_T distribution is used to fit all SR categories. For the $n_j \leq 1$ categories, variable bin widths on the m_T distribution are used to maximize the expected signal significance. This is accomplished by maintaining an approximate constant signal yield in each bin (ten bins for $e\mu$ and six bins for $ee/\mu\mu$). Figure 9.2 shows the m_T distribution in the most sensitive region: $n_j = 0$, $e\mu$, $m_{\ell\ell} > 30$ GeV and $p_T^{\ell_2} > 20$ GeV, with this binning. For the $n_j \geq 2$ ggF category, four bins specified by the range [0, 50, 80, 130, ∞] GeV on the m_T are used.

The control regions (defined in chapter 8) determine the normalizations of the corresponding backgrounds through a Poisson term in the likelihood. The background estimations without a floating normalization parameter, such as the data-driven W +jets, are not added into the Poisson term and the estimated event yields are used. Table 9.2 summarizes the background estimation using the data. The background estimations marked by solid circles in the table enter the fit with a Poisson term. These CRs are called “profiled CR” in this chapter.

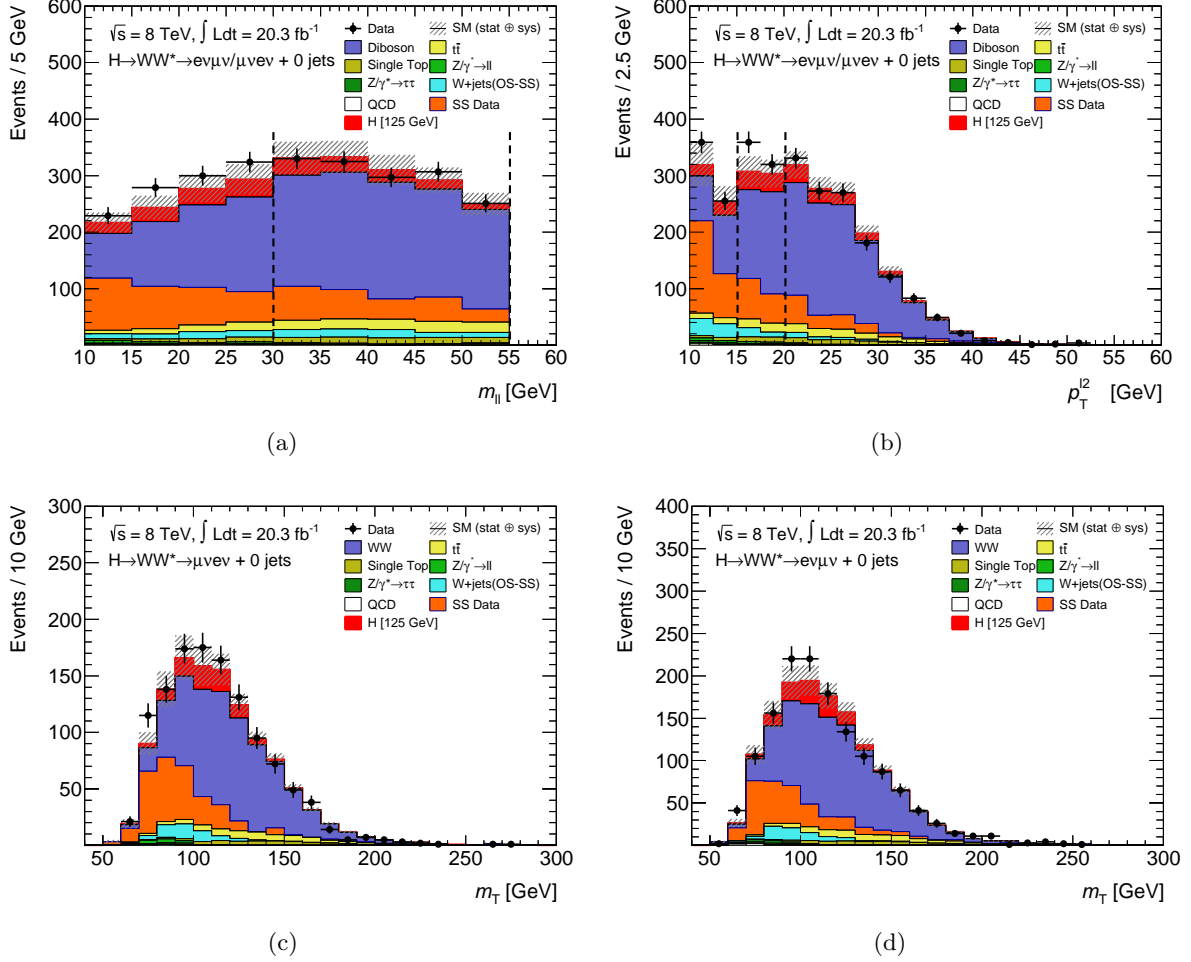


Figure 9.1: The $m_{\ell\ell}$ (a) and $p_T^{\ell_2}$ (b) distributions in the SR of the $n_j = 0$ category with the $e\mu$ sample. The dotted lines denote the SR boundaries in the fit. The m_T distributions are also shown, separated in $\ell_2 = \text{electron}$ (c) and $\ell_2 = \text{muon}$ (d) cases. The W +jets and QCD backgrounds are estimated with the extrapolation method. The *Other VV* background is estimated using the OS-SS method. The other backgrounds are modeled with the MCs, and normalized to the theoretical cross sections. The WW , Z +jets and Top backgrounds are corrected with the normalization factors from the data. The signal is shown at $m_H = 125$ GeV.

	SR category in fit i			bins b
	$\otimes m_{\ell\ell}$	$\otimes p_{\text{T}}^{\ell_2}$	$\otimes \text{flavor}$	
$n_j = 0$				
$e\mu$	$\otimes [10, 30, 55]$	$\otimes [10, 15, 20, \infty]$	$\otimes [e, \mu]$	10 bins on m_{T}
$ee/\mu\mu$	$\otimes [12, 55]$	$\otimes [10, \infty]$		6 bins on m_{T}
$n_j = 1$				
$e\mu$	$\otimes [10, 30, 55]$	$\otimes [10, 15, 20, \infty]$	$\otimes [e, \mu]$	10 bins on m_{T}
$ee/\mu\mu$	$\otimes [12, 55]$	$\otimes [10, \infty]$		6 bins on m_{T}
$n_j \geq 2$				
$e\mu$	$\otimes [10, 55]$	$\otimes [10, \infty]$		4 bins on m_{T}

Table 9.1: Signal region definition in the likelihood fit. Energy-related quantity is in GeV.

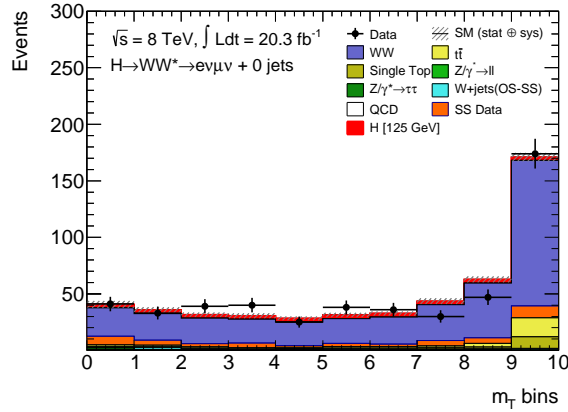


Figure 9.2: The $m_{\ell\ell}$ distributions in the most sensitive category in the fit: $n_j = 0$, $e\mu$, $m_{\ell\ell} > 30$ GeV and $p_{\text{T}}^{\ell_2} > 20$ GeV. Configuration is the same as figure 9.1. The binning is optimized so that the signal yield becomes an approximate constant in each bin. The bin boundaries are $[0, 93.2, 100.2, 105.0, 109.2, 113.0, 116.9, 121.1, 126.4, 135.4, \infty]$ GeV.

	Estimation technique	Reference	Profiled sample
$n_j = 0$			
WW	WW control region	section 8.6.1	• $e\mu$
$Other VV$	OS-SS method	section 8.3.1	○
Top	Jet veto extrapolation	section 8.5.1	○
$Z \rightarrow \ell\ell$	f_{recoil} efficiency method	section 8.4.3	• $ee/\mu\mu$
$Z \rightarrow \tau\tau$	$Z \rightarrow \tau\tau$ control region	section 8.4.2	• $e\mu$
W +jets/QCD	Extrapolation method	section 8.1.1	○
$n_j = 1$			
WW	WW control region	section 8.6.1	• $e\mu$
$Other VV$	OS-SS method	section 8.3.1	○
Top	b -tag extrapolation	section 8.5.1	• $e\mu$
$Z \rightarrow \ell\ell$	f_{recoil} efficiency method	section 8.4.3	• $ee/\mu\mu$
$Z \rightarrow \tau\tau$	$Z \rightarrow \tau\tau$ control region	section 8.4.2	• $e\mu$
W +jets/QCD	Extrapolation method	section 8.1.1	○
$n_j \geq 2$ ggF			
Top	Top control region	section 8.5.3	• $e\mu$
$Z \rightarrow \tau\tau$	$Z \rightarrow \tau\tau$ control region	section 8.4.2	• $e\mu$
W +jets/QCD	Extrapolation method	section 8.1.1	○

Table 9.2: Summary of the background estimations using data. The background CRs marked by solid circles enter the fit as a profiled CR. The backgrounds marked by open circles use the estimated yields without the profiling in the fit.

9.2 Likelihood function and test statistic

The likelihood $\mathcal{L}(\mu, \boldsymbol{\theta})$ used in the analysis is a function of the signal strength parameter μ and a set of nuisance parameters $\boldsymbol{\theta} = \{\theta_a, \theta_b, \dots\}$. The likelihood function consists of four probability functions, and given as follows:

$$\begin{aligned}
 \mathcal{L} = & \overset{\text{Table 9.1}}{\prod_{i,b}} f(N_{ib}|\mu \cdot S_{ib} \cdot \overset{\text{Syst.}}{\prod_r} \nu(\theta_r) + \overset{\text{Table 2.2}}{\sum_k} \beta_k \cdot B_{kib} \cdot \overset{\text{Syst.}}{\prod_s} \nu(\theta_s)) \left\{ \begin{array}{l} \text{Poisson for SR with} \\ \text{signal strength } \mu. \end{array} \right. \\
 & \times \overset{\text{Table 9.2}}{\prod_l} f(N_l | \overset{\text{Table 2.2}}{\sum_k} \beta_k \cdot B_{kl}) \dots \dots \dots \left\{ \begin{array}{l} \text{Poisson for profiled} \\ \text{CR with } \beta. \end{array} \right. \\
 & \times \overset{\text{Syst. (r,s)}}{\prod_t} g(\tilde{\theta}_t | \theta_t, 1) \dots \dots \dots \left\{ \begin{array}{l} \text{Gaussian for} \\ \text{sys. constrain} \end{array} \right. \\
 & \times \overset{\text{Table 2.2}}{\prod_k} f(\tilde{\theta}_k | \theta_k \cdot \xi_k) \dots \dots \dots \left\{ \begin{array}{l} \text{Poisson for} \\ \text{stat. constrain} \end{array} \right.
 \end{aligned} \tag{9.1}$$

1. The first term of the \mathcal{L} is a product of Poisson functions f for the probability of observing N events given λ expected events, $f(N|\lambda) = e^{-\lambda} \lambda^N / N!$, in each SR category and bin (i, b) summarized in table 9.1. The λ consists of the number of signal events S and background events $\sum_k B_k$, where k denotes the type of the background processes in table 2.2. The parameter of interest μ is multiplied to S , and the B is scaled by β , which is a normalization factor for the background yield constrained in a profiled CR (described in 2.). The signal and background yields are also scaled by the response functions, ν , which parametrize the impact on the yields by the systematic uncertainty (described in 3. and 4.).
2. The second component constrains the background yields with Poisson terms by the measurements in the CR. The poisson function is given for each profiled CRs in table 9.2. In a simple case of the CR (e.g. WW CR), the poisson function is $f(N_l | \beta \cdot B)$, where N_l is the number of observed events in l , and B is the predicted yield with a float normalization parameter of β . The β parameters are the same as those in the previous paragraph. For the f_{recoil} efficiency (see section 8.4.3) and b -tag extrapolation methods (see section 8.5.2), the specific treatments are needed as follows:
 - f_{recoil} efficiency method: The selection efficiency of f_{recoil} is introduced to the poisson function as a floating parameter. The poisson function of the SR is divided into the two cases, which pass or fail the f_{recoil} selection as follows:

$$f(N_{SR}^{\text{pass}} \mid \beta \cdot \epsilon^{\text{Z+jets}} \cdot B_{SR}^{\text{Z+jets}} + \epsilon^{\text{non-Z+jets}} \cdot B_{SR}^{\text{non-Z+jets}}), \tag{9.2}$$

$$f(N_{SR}^{\text{fail}} \mid \beta \cdot (1 - \epsilon^{\text{Z+jets}}) \cdot B_{SR}^{\text{Z+jets}} + (1 - \epsilon^{\text{non-Z+jets}}) \cdot B_{SR}^{\text{non-Z+jets}}), \tag{9.3}$$

where β is the variable of interest for the background constrain. The $\epsilon^{\text{Z+jets}}$ and $\epsilon^{\text{non-Z+jets}}$ are constrained by Poisson functions of the sample A, B and C as described in section 8.4.3. The $\epsilon^{\text{non-Z+jets}}$ is parametrized to the signal and other non- Z +jets process by introducing an additional nuisance parameter θ since the f_{recoil} efficiency is expected to be different between the signal and other non- Z +jets process.

- b -tag extrapolation: The normalization of the b -tagging efficiency, $\beta^{b\text{-tag}}$, is constrained with the $n_j = 2$ control sample (see section 8.5.2) as follows:

$$f(N_{n_j=2}^{2b} \mid \beta^{2j} \cdot (\beta^{b\text{-tag}})^2 \cdot B^{2b,\text{Top}} + B^{2b,\text{non-Top}}), \quad (9.4)$$

$$f(N_{n_j=2}^{1b} \mid \beta^{2j} \cdot \beta^{b\text{-tag}}(B^{1b,\text{Top}} + (1 - \beta^{b\text{-tag}})B^{2b,\text{top}}) + B^{2b,\text{non-Top}}), \quad (9.5)$$

where N^{2b} (N^{1b}) corresponds to the number of observed events with one (two) b -tagged jets, and B^{2b} (B^{1b}) is the predicted yields with one (two) b -tagged jets. β^{2j} is a float parameter for the normalization on the top yields in the $n_j = 2$ sample. Then, the poisson function of the Top 1j CR is given as follows:

$$f(N_{n_j=1}^{1b} \mid \beta^{1j} \cdot \beta^{b\text{-tag}} \cdot B^{1b,\text{top}} + B^{1b,\text{non-Top}}). \quad (9.6)$$

The β^{1j} is a variable of interest for the top yield estimation in the $n_j = 1$ category.

3. The third term constraints the systematic uncertainties with unit Gaussian functions. The function of each systematic uncertainty t is written as $g(\tilde{\theta}_t|\theta_t, 1) = e^{-(\tilde{\theta}_t - \theta_t)^2/2}/\sqrt{2\pi}$, where $\tilde{\theta}$ is the central value of the measurement, and the $\tilde{\theta}$ has an associated nuisance parameter of θ . Then, the effects on the event yields by these systematic uncertainties in the first term are taken into account through the response function ν . For the flat systematics, which do not change the m_T shape, the response function takes the form $\nu = (1 + \epsilon)^\theta$. In this notation, if the uncertainty, that corresponds to one standard deviation $\theta = \pm 1$, affects the event yield by $\pm 3\%$, $\epsilon = 3\%$ is obtained. In this case, the ν follows a log-normal probability density function, which is a suitable for positively defined observable like, cross section, cut efficiency, luminosity and so on. For the shape systematics, the shape variation is separated into a flat component and a pure shape component. The flat component is treated in the same way described above, and the shape component uses the response function of $\nu = 1 + \epsilon \cdot \theta$ in each bin. Detail of the choice of the response function is described in reference [114].
4. The fourth term constraints the statistical uncertainties from the MC or data-driven method with Poisson functions. The Poisson function is given as $f(\tilde{\theta}|\theta \cdot \xi)$, where ξ is the number of events in the corresponding sample, i.e. the number of generated events in case of the MC. The ξ can be written as $\xi = (B/\sigma)^2$, where the B is the estimated yield and σ is its statistical uncertainty. For the expectations in the first term, the $\tilde{\theta}$ takes the value of ξ and the linear response function $\nu = \theta$ is used.

This likelihood is maximized to determine the μ . To calculate the p_0 , the probability to obtain the observed results when the $\mu = 0$ hypothesis is actually true, the test statistic is defined as follows:

$$\tilde{q}_\mu = -2 \ln \frac{\mathcal{L}(\mu, \hat{\theta}_\mu)}{\mathcal{L}_{\max}}, \quad (9.7)$$

where the denominator \mathcal{L}_{\max} is the maximum possible value of the \mathcal{L} . The numerator is maximized over θ for a given value of μ , the obtained θ is denoted as $\hat{\theta}_\mu$. The probability density functions of \tilde{q}_μ , $f(\tilde{q}_\mu|\mu)$, as shown in figure 9.3 can be constructed by generating pseudo-data with Monte Carlos. The p_0 is evaluated by a integral of the probably density function from the observed \tilde{q}_0 to the larger values under the background-only hypothesis ($\mu = 0$).

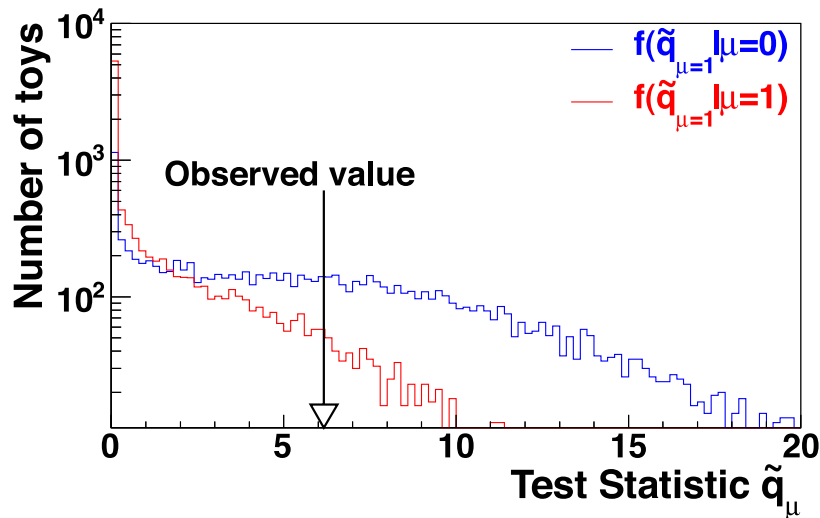


Figure 9.3: An example of test statistic distributions for ensembles of pseudo-data generated for signal+background and background-only hypotheses [114].

9.3 Uncertainties

Systematic uncertainties are treated with the Gaussian term in the Likelihood function of equation 9.1. Theoretical and experimental uncertainties specific to individual processes have been described in chapter 5 and 8. Experimental uncertainties common to the signal and backgrounds are described in this section. The dominant sources of the uncertainty are the follows:

- **Integrated luminosity:** Uncertainty on the integrated luminosity in the 2012 data is estimated with the same method described in reference [51], where over ten systematic sources are considered, such as the beam sizes $\sum_{x,y}$, the detector response, etc. The total size of the uncertainty is 2.8%.
- **Lepton efficiency:** Uncertainty on the lepton efficiency consists of the reconstruction, identification, selection and trigger efficiencies, as well as their momentum scales and resolutions. The uncertainties are generally obtained from the variation of the measurements by varying conditions, such as the pileup modeling, event selections, etc. The uncertainty on the electron identification varies between 0.2% and 2.7% as a function of p_T and η . The uncertainty on the selection also varies in p_T , 1.6% and 2.7% at the $p_T = 10\text{--}15$ GeV for the electrons and muons, respectively. The other uncertainties on the lepton modeling are all smaller than 1%.
- **Jet energy scale:** Uncertainty on the jet energy calibration consists of modelings and statistics on the method for the η calibration of jets from the central region to the forward region, high p_T jet behavior, impact from the pileup jets and so on. The full description of the individual uncertainty can be found in reference [105]. The total uncertainty of the jet energy scale for the jets with $p_T > 25$ GeV and $|\eta| < 4.5$ is 1–7% depending on p_T and η .
- **b-tagging efficiency:** Uncertainty related to the b -tagging efficiency is decomposed to six components using so called eigenvector method [108]. For each source of uncertainties

such as jet energy scale, one covariance matrix is constructed with a dimension of number of p_T bins (six). The total covariance matrix is obtained as a sum of these individual component matrices. The variations of the eigenvalue of the total covariance provide the uncertainties, which range $< 1\%$ to 7.8% . The uncertainty on light jet misidentified as b -jets are η and p_T dependent, which ranges 9% to 19% . Also the uncertainty on c -jets reconstructed as b -jets ranges between 6% to 14% .

- **Missing transverse energy:** Variations of the lepton momentum and jet energy described above are propagated to the E_T^{miss} and p_T^{miss} calculations. The systematic sources specific to the E_T^{miss} and p_T^{miss} are briefly summarized below. The uncertainty on E_T^{cellout} term in the E_T^{miss} calculation is obtained by exploiting the balance between the E_T^{cellout} and the total momentum of the hard objects, p_T^{hard} , in $Z \rightarrow \mu\mu$ events. The p_T^{hard} can be regarded as the true value of E_T^{cellout} and allow to evaluate uncertainties on scales and resolutions of the E_T^{cellout} . Variations in terms of the p_T^{hard} and average number of interactions per bunch crossing are $0.2\text{--}0.3$ GeV on the scales and are $1\text{--}4\%$ on the resolutions, which are taken as the uncertainties. The uncertainty on the p_T^{track} in the p_T^{miss} calculation is evaluated from the comparison of the properties of p_T^{miss} in $Z \rightarrow ee/\mu\mu$ events in the data and simulated samples. Scale variations range $0.3\text{--}1.4$ GeV and the uncertainties on the resolution are between $1.5\text{--}3.3$ GeV.

Chapter 10

Results

Object and event selections, background estimation techniques and procedure for signal extraction are provided in the previous chapters. This chapter summarizes the estimated event yields in the signal regions before the fit (called “pre-fit” hereafter) in section 10.1, and gives the result of the signal strength measurement using the fit in section 10.2.

10.1 Event yields and distributions

Tables 10.1–10.3 summarize the expected event yields in the $n_j = 0$, $n_j = 1$ and $n_j \geq 2$ ggF-enriched categories, respectively. The background predictions are performed with the pre-fit normalization factors and the data-driven methods described in chapter 8. The signal regions of the $n_j = 0$ and $n_j = 1$ categories with the $e\mu$ sample are subdivided by the $m_{\ell\ell} = 30$ GeV and $p_T^{\ell\ell} = 15$ GeV in the tables. SR1 (SR2) in the tables denotes the regions of $m_{\ell\ell} < (>) 30$ GeV, and lowpt (hipt) denotes the regions of $p_T^{\ell\ell} < (>) 15$ GeV. Different compositions of the signal and backgrounds can be seen in each region of these divisions, which are part of the boundaries in the fit. For example, the SR1 with the low $p_T^{\ell\ell}$ region is dominated by the *Other VV* (SS Data) and W +jets backgrounds, while the other three regions are dominated by the WW background. The expected signal contribution is large in the SR2 with the hipt requirement. The estimated ratios of the observed data to the estimated backgrounds are greater than one in all signal regions. This implies that the observed data have excesses over the backgrounds because of the existence of the signal.

Figure 10.1 (a) shows the m_T distribution in the signal region of the $n_j = 0$ and $n_j = 1$ combined sample, and figure 10.1 (b) shows the same distribution but the estimated backgrounds are subtracted from the data. A clear excess of the data is observed in these plots. The agreement of the prediction to the data can not be achieved without the presence of the Higgs boson signal. The figures 10.2, 10.3 and 10.4 show the individual m_T distributions in the $n_j = 0$, $n_j = 1$ and $n_j \geq 2$ ggF categories, respectively.

10.2 Fit results

The profiled likelihood fit described in section 9.2 has been performed to extract the signal yield. All signal production modes are treated together with one parameter of interest in the fit. The observed signal strength of the Higgs boson, μ^{obs} , using all signal regions described in this thesis is to be:

Table 10.1: Summary of the estimated and observed event yields in the $n_j = 0$ signal regions. The W +jets and QCD backgrounds are estimated with the extrapolation factor method. The *Other VV* background in the $e\mu$ category is estimated with the OS-SS method. The other backgrounds are modeled with the MCs, and normalized to the theoretical cross sections. The WW , Z +jets and Top backgrounds are corrected with the pre-fit normalization factors from the data. For the Z +jets column in the $ee/\mu\mu$ category, separated NFs of 1.00 for the $Z \rightarrow \tau\tau$ process and 2.40 for the $Z \rightarrow ee/\mu\mu$ process are used. The signal is shown at $m_H = 125$ GeV. The uncertainty is statistical only.

$n_j = 0$ category						
$e\mu$ category						
	Signal	WW	Z +jets	Top	W +jets (OS-SS)	
NFs	-	1.20	1.00	1.08	-	
SR	208.8 ± 0.6	1480.6 ± 5.7	31.0 ± 2.5	205.8 ± 1.6	103.9 ± 6.6	
SR1, hipt	78.2 ± 0.4	414.6 ± 3.0	8.2 ± 1.2	53.3 ± 0.8	13.55 ± 2.6	
SR2, hipt	87.6 ± 0.4	883.8 ± 4.4	7.8 ± 1.3	122.8 ± 1.3	35.5 ± 2.7	
SR1, lowpt	25.5 ± 0.2	91.0 ± 1.4	9.5 ± 1.4	12.1 ± 0.4	28.2 ± 3.8	
SR2, lowpt	17.5 ± 0.2	91.2 ± 1.4	5.5 ± 1.0	17.6 ± 0.5	26.6 ± 3.8	
	QCD	SS Data	Total Bkg.	Observed	Ratio (Obs./Bkg.)	
NFs	-	-	-	-	-	
SR	9.2 ± 1.6	502.5 ± 23.2	2332.9 ± 25.0	2642	1.13 ± 0.03	
SR1, hipt	1.5 ± 0.4	130.2 ± 11.8	621.3 ± 12.6	762	1.23 ± 0.05	
SR2, hipt	2.0 ± 0.3	130.9 ± 11.8	1182.8 ± 13.0	1266	1.07 ± 0.03	
SR1, lowpt	4.9 ± 0.5	158.4 ± 13.1	304.1 ± 13.8	370	1.22 ± 0.08	
SR2, lowpt	0.8 ± 1.5	83.1 ± 9.3	224.8 ± 10.3	244	1.09 ± 0.09	
$ee/\mu\mu$ category						
	Signal	WW	<i>Other VV</i>	Z +jets	Top	
NFs	-	1.20	-	NFs applied	1.08	
SR	74.8 ± 0.4	774.2 ± 4.2	69.4 ± 2.2	91.6 ± 5.3	71.1 ± 0.9	
	W +jets	QCD	Total Bkg.	Observed	Ratio (Obs./Bkg.)	
NFs	-	-	-	-	-	
SR	78.5 ± 2.5	0.04 ± 0.2	1085.1 ± 7.6	1108	1.02 ± 0.03	

Table 10.2: Summary of the estimated and observed event yields in the $n_j = 1$ signal regions. The configuration is the same as the $n_j = 0$ category in table 10.1.

$n_j = 1$ category					
$e\mu$ category					
	Signal	WW	Z +jets	Top	W +jets (OS-SS)
NFs	-	1.04	1.05	1.06	-
SR	87.1 ± 0.5	413.3 ± 2.8	27.2 ± 2.2	370.2 ± 2.2	26.0 ± 3.9
SR1, hipt	33.7 ± 0.3	113.4 ± 1.5	2.3 ± 0.6	99.7 ± 1.1	8.2 ± 1.6
SR2, hipt	39.6 ± 0.3	253.2 ± 2.2	16.6 ± 1.7	225.4 ± 1.7	13.0 ± 2.1
SR1, lowpt	8.0 ± 0.2	21.0 ± 0.6	3.4 ± 0.8	18.1 ± 0.5	1.1 ± 2.1
SR2, lowpt	5.9 ± 0.1	25.6 ± 0.7	4.8 ± 0.9	27.0 ± 0.6	3.7 ± 2.0
	QCD	SS Data	Total Bkg.	Observed	Ratio (Obs./Bkg.)
Scale factors	-	-	-	-	-
SR	6.1 ± 0.4	181.3 ± 14.0	1024.1 ± 15.1	1129	1.10 ± 0.04
SR1, hipt	1.2 ± 0.2	65.8 ± 8.3	290.6 ± 8.7	318	1.09 ± 0.07
SR2, hipt	1.8 ± 0.2	61.1 ± 8.2	571.1 ± 9.0	615	1.08 ± 0.05
SR1, lowpt	1.9 ± 0.2	31.3 ± 5.9	76.9 ± 6.3	82	1.07 ± 0.15
SR2, lowpt	1.2 ± 0.2	23.2 ± 5.0	85.5 ± 5.6	114	1.33 ± 0.15
$ee/\mu\mu$ category					
	Signal	WW	<i>Other VV</i>	Z +jets	Top
NFs	-	1.04	-	NFs applied	1.06
SR	23.2 ± 0.3	185.9 ± 1.9	29.5 ± 1.4	27.5 ± 3.0	141.4 ± 1.4
	W +jets	QCD	Total Bkg.	Observed	Ratio (Obs./Bkg.)
NFs	-	-	-	-	-
SR	17.4 ± 1.3	0.02 ± 0.03	401.9 ± 4.3	467	1.16 ± 0.06

 Table 10.3: Summary of the estimated and observed event yields in the signal region of the $n_j \geq 2$ ggF-enriched category. The W +jets and QCD backgrounds are estimated with the extrapolation factor method. The other backgrounds are modeled with the MCs, and normalized to the theoretical cross sections. The Z +jets and Top backgrounds are corrected with the pre-fit normalization factors from the dedicated control regions. The signal is shown at $m_H = 125$ GeV. The uncertainty is statistical only.

$n_j \geq 2$ category					
$e\mu$ category					
	Signal	WW	<i>Other VV</i>	Z +jets	Top
NFs	-	-	-	1.00	1.05
SR	44.2 ± 0.4	140.4 ± 1.4	60.0 ± 2.6	131.8 ± 4.7	523.3 ± 2.7
	W +jets	QCD	Total Bkg.	Observed	Ratio (Obs./Bkg.)
NFs	-	-	-	-	-
SR	49.7 ± 3.7	49.2 ± 0.9	802.3 ± 9.2	5713.3 ± 35.5	1.06 ± 0.03

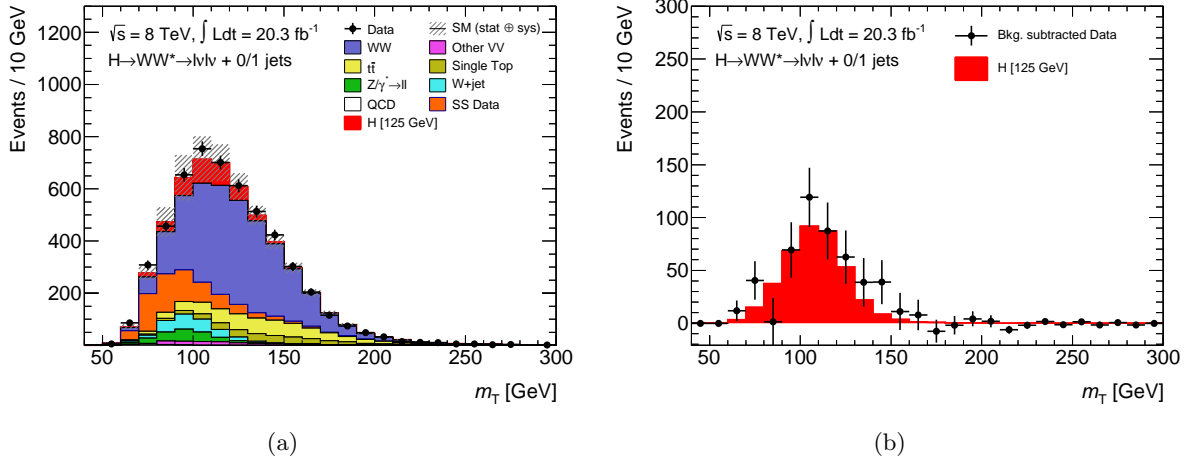


Figure 10.1: The m_T distributions for the $n_j = 0/1$ category. Both the $e\mu$ and $ee/\mu\mu$ channels are included. The configuration of the background estimate is the same as those described in the caption of the table 10.1. The W +jets histogram consists of the W +jets (OS-SS) estimate in the $e\mu$ channel and the W +jets estimate in the $ee/\mu\mu$ channel. On the right plot: the points show the residuals of the data with respect to the estimated background. The red histogram shows the expected distribution of the SM Higgs boson at the $m_H = 125$ GeV. This signal process is normalized to the theoretical cross section.

$$\begin{aligned}
 \mu^{\text{obs}} &= 1.07^{+0.18}_{-0.18} \text{ (stat.) }^{+0.12}_{-0.12} \text{ (expt.) }^{+0.18}_{-0.15} \text{ (theo.) } \pm 0.03 \text{ (lumi.)} \\
 &= 1.07^{+0.18}_{-0.18} \text{ (stat.) }^{+0.22}_{-0.19} \text{ (syst.)} \\
 &= 1.07^{+0.29}_{-0.26}.
 \end{aligned} \tag{10.1}$$

The μ^{obs} is measured at the $m_H = 125.36$ GeV from the ATLAS measurement [47]. The uncertainties are divided according to their source. The statistical uncertainty accounts for the number of observed events in the signal region and profiled control regions. The statistical uncertainty on the MC samples and non-profiled CR methods are included in the experimental uncertainty, as well as the other experimental uncertainties. The theoretical uncertainty counts the uncertainties on the cross section and normalization of the simulated samples. The obtained signal strength is consistent with the SM expectation within the total uncertainty.

Table 10.4 summarizes the obtained normalization factors β in the profiled control regions in comparisons to the pre-fit values. No significant differences between the two values are observed. The profiled control regions thus work well as designed.

Table 10.5 shows the highest ranked top fifteen nuisance parameters that affect the signal strength measurement together with its pull value. The impact of single systematic source θ is evaluated with the following equation:

$$\Delta\hat{\mu} = \hat{\mu}(\hat{\theta} \pm \Delta\hat{\theta}) - \hat{\mu}(\hat{\theta}). \tag{10.2}$$

The $\hat{\mu}$ is the observed (post-fit) value of the signal strength, and the $\hat{\theta}$ is the post-fit value of the nuisance parameter. The uncertainty on $\hat{\theta}$, $\Delta\hat{\theta}$, is found by scanning the points where the ratio of the likelihood, $-\ln(\mathcal{L}(\hat{\theta} \pm \Delta\hat{\theta})/\mathcal{L}(\hat{\theta}))$, takes values of one. The leading uncertainties on the

Table 10.4: Summary of the normalization factors before (pre) and after (post) the fit. The uncertainties on the pre-fit values are statistical only.

Category	WW		Top		$Z \rightarrow \tau\tau$	
	pre-fit	post-fit	pre-fit	post-fit	pre-fit	post-fit
$n_j = 0$	1.20 ± 0.03	1.18	-	-	1.00 ± 0.02	0.98
$n_j = 1$	1.03 ± 0.05	1.08	1.06 ± 0.03	1.02	1.05 ± 0.04	1.03
$n_j \geq 2$ ggF	-		1.05 ± 0.03	1.13	1.00 ± 0.09	0.96

signal strength measurement are from the limited accuracy of the MC predictions (QCD scale, PDF and generator).

 Table 10.5: Impact on the observed signal strength $\hat{\mu} = 1.07$ and nuisance parameters $\hat{\theta}$. The pulls are given in unit of standard deviation, and $\Delta\hat{\theta}$ of unity means no constraint.

Systematic source	Impact on $\hat{\mu}$		Impact on $\hat{\theta}$			Reference
	+	-	Pull, $\hat{\theta}$	$+\Delta\hat{\theta}$	$-\Delta\hat{\theta}$	
ggF, QCD scale on total cross section	0.07	0.06	-0.09	0.70	0.69	section 5.2.1
WW , generator modeling on m_T shape	0.07	0.06	0.01	0.99	1.00	section 8.6
ggF, PDF variations on total cross section	0.06	0.06	0.00	1.00	0.99	section 5.2.1
W +jets, OS uncorr. correction on electron f	0.05	0.04	0.64	0.70	0.64	section 8.1
Top, generator modeling on α	0.04	0.04	-0.38	0.88	0.88	section 8.5
W +jets, OS uncorr. correction on muon f	0.03	0.03	0.46	0.76	0.76	section 8.1
Integrated luminosity	0.03	0.03	0.16	1.00	1.00	section 9.3
Muon isolation efficiency	0.03	0.03	0.22	0.99	0.98	section 9.3
ggF, PDF variations on acceptance	0.03	0.03	0.01	1.00	1.00	section 5.2.1
QCD, correction on f	0.02	0.02	0.54	0.88	0.81	section 8.2
ggF, QCD scale on jet veto efficiency ϵ_1	0.01	0.03	-0.21	0.93	0.94	section 5.2.1
WW , QCD scale on acceptance	0.02	0.02	0.19	0.99	0.99	section 8.6
ggF, QCD scale on acceptance	0.02	0.02	-0.02	1.00	1.00	section 5.2.1
ggF, UE/PS on acceptance	-	0.02	0.00	0.95	0.95	section 5.2.1
f_{recoil} efficiency parameterization for signal θ	0.02	0.02	-0.23	0.98	0.98	section 9.2

Also the signal strength has been measured at different Higgs boson mass points. Figure 10.5 (a) shows the measured signal strengths as a function of m_H . This figure indicates that the observed signal yield is consistent with the SM expectation with $m_H \sim 125$ GeV hypothesis. This $m_H \sim 125$ GeV is consistent with the other Higgs boson mass measurement using the $H \rightarrow ZZ^* \rightarrow 4\ell$ and $H \rightarrow \gamma\gamma$ decay channels at the ATLAS as described in section 2.2.

The test statistics \tilde{q}_0 defined in section 9.2 is used to calculate the significance of the observed excess. The observed and expected p_0 , the probability to obtain the signal yields by the background fluctuations with $\mu = 0$ hypothesis, are shown in figure 10.5 (b) as a function of m_H . A broad minimum is observed around $m_H = 125$ GeV, reflecting the analysis is optimized at that mass and the branching ratio of the Higgs to WW^* as a function of m_H . The observed local significance is 4.5 standard deviation at $m_H = 125.36$ GeV. This result establishes the evidence

of the Higgs boson production in the $H \rightarrow WW^* \rightarrow \ell\nu\ell\nu$ channel alone. The scale factors for the Higgs boson coupling constants are also measured to assess possibilities of couplings of the Higgs boson to new particles beyond the SM, which are described in section [11.4](#).

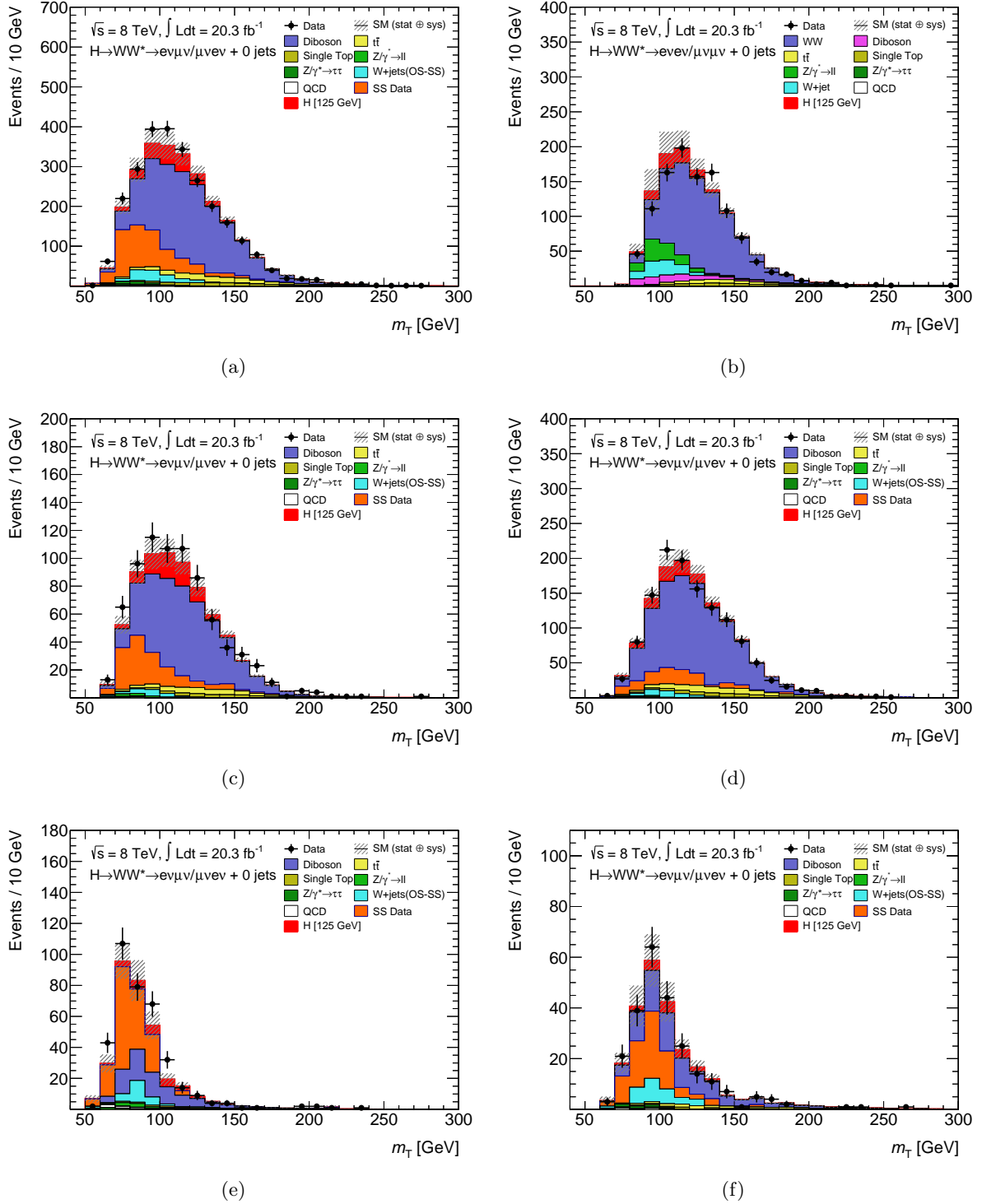


Figure 10.2: The m_T distribution in the SR of the $n_j = 0$ category with the $e\mu$ sample (a) and $ee/\mu\mu$ sample (b). The distributions in the subdivided SRs with the $e\mu$ sample are shown in figures (c) (SR1, hipt), (d) (SR2, hilt), (e) (SR1, lowpt) and (f) (SR2, lowpt). The signal and background configurations are the same with the figure 10.1.

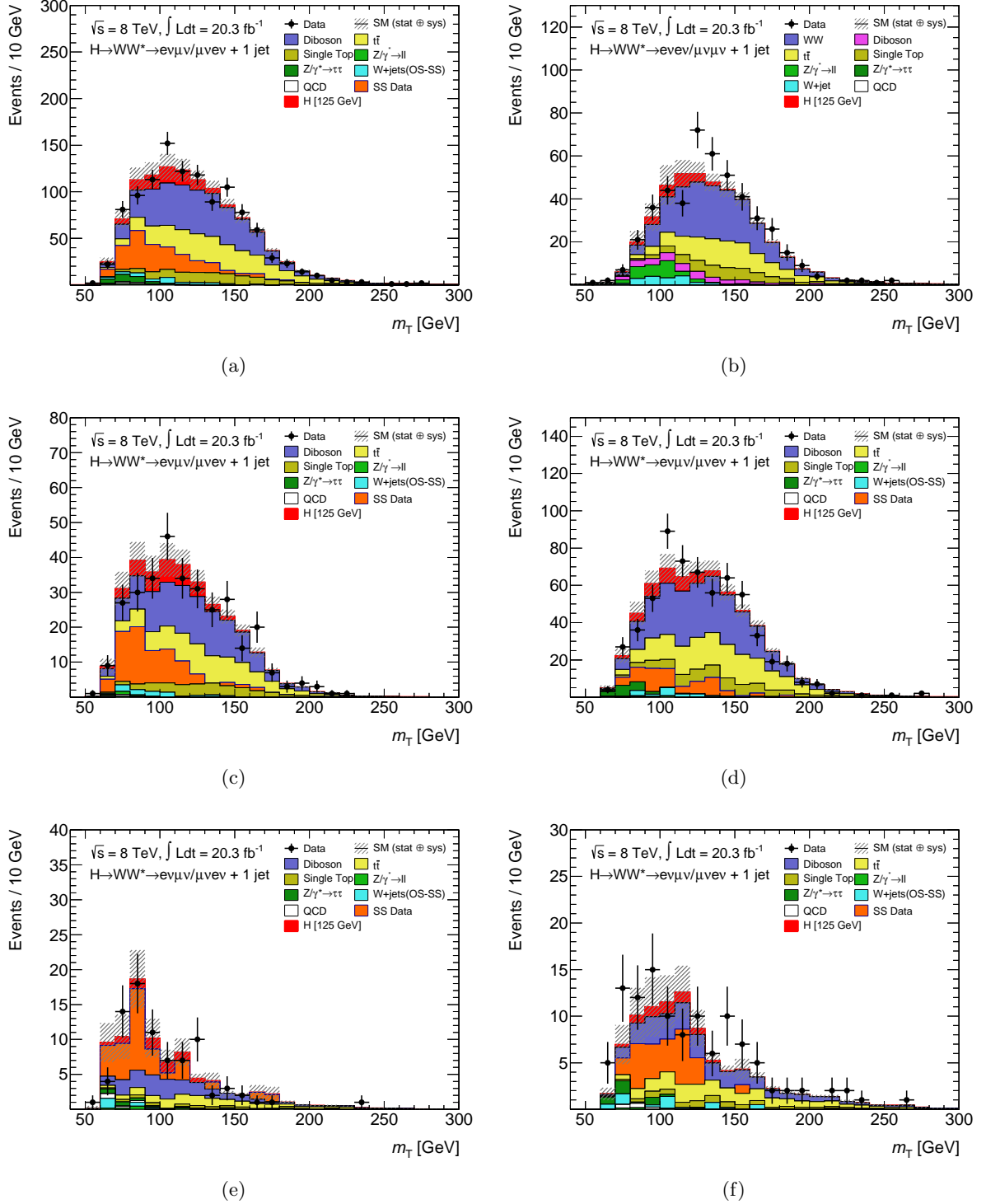


Figure 10.3: The m_T distribution in the SR of the $n_j = 1$ category with the $e\mu$ sample (a) and $ee/\mu\mu$ sample (b). The distributions in the subdivided SRs with the $e\mu$ sample are shown in figures (c) (SR1, hipt), (d) (SR2, hilt), (e) (SR1, lowpt) and (f) (SR2, lowpt). The signal and background configurations are the same with the figure 10.1.

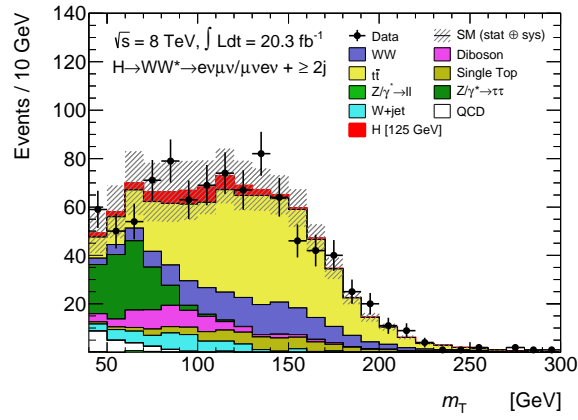


Figure 10.4: The m_T distribution in the SR of the $n_j \geq 2$ ggF-enriched category. The configurations of the signal and background estimates are described in the caption of the table 10.3.

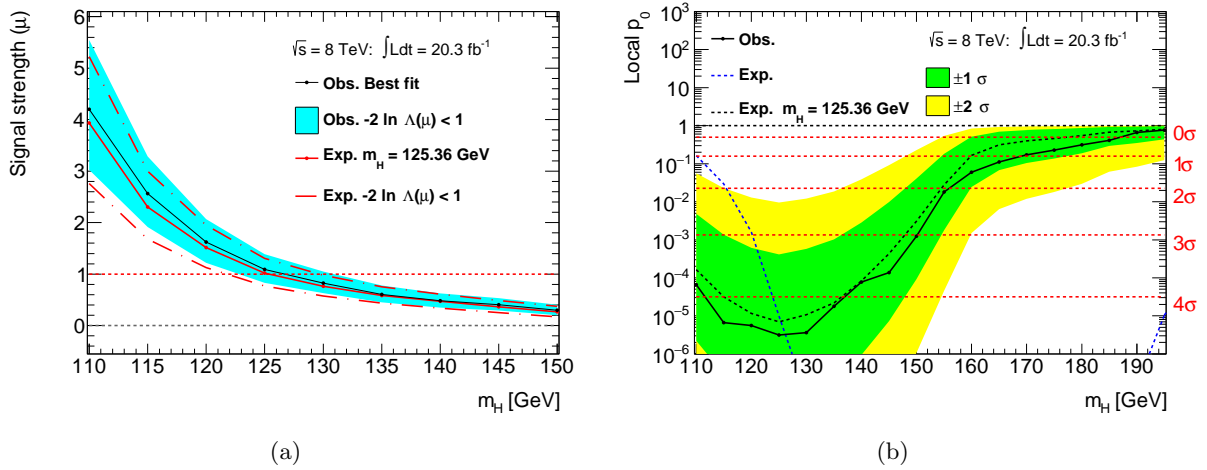


Figure 10.5: (a) μ as a function of m_H . The observed values are shown with a black line. The expected values are one by definition at all mass points. The $m_H = 125.36$ GeV curve shows the expectation given the presence of a signal at that mass. (b) The p_0 as a function of m_H . The observed values are shown with a black solid line. The expected values are shown with a blue dotted line. The $m_H = 125.36$ GeV curve shows the expectation given the presence of a signal at that mass.

Chapter 11

Discussion

This thesis measured the Higgs boson production using the gluon-gluon fusion enriched sample in the 8 TeV data. The ATLAS collaboration also performed the analysis with a different background estimation technique using the same data set. Comparisons with these results are shown in section 11.1. As described in section 2.3, the ggF analysis using another set of the data collected in year 2011 at $\sqrt{s} = 7$ TeV, and another analysis category based on the vector boson fusion topology are defined. These analyses have been also performed by the ATLAS collaboration. The ggF 7 TeV analysis and its results are explained in section 11.2, also the VBF analysis (7 TeV + 8 TeV data) is described in section 11.3. Then, the results combined with the ggF and VBF analyses with the full data sets are discussed in section 11.4, and compared with the results of the CMS experiment at the LHC in section 11.5.

11.1 Comparison with the different background estimation

The analysis described in this thesis uses the OS-SS method (see section 8.3.1) to estimate the *Other VV* and part of the *W+jets* backgrounds in the $e\mu$ sample in the $n_j = 0$ and $n_j = 1$ categories. A different technique to estimate the *Other VV* background is used in the ATLAS measurement [117], where the *Other VV* background is modeled with the MC samples and a normalization factor is obtained from a dedicated control region. The same sign validation region defined in section 8.1.2 is treated as the control region (called as “SSCR method”) for the *Other VV* background. The normalization factors of 0.92 ± 0.07 for the $n_j = 0$ and 0.96 ± 0.12 for the $n_j = 1$ categories are obtained with this method. Figure 11.1 shows the m_T distributions estimated with the SSCR method and OS-SS method. Both methods show a similar m_T distribution. In the SSCR method, an additional Poisson term is implemented to the likelihood function to constrain the normalization of the *Other VV* background.

Table 11.1 shows the observed and expected signal strengths in case of the two methods. The results are shown only in the $e\mu$ sample in the $n_j = 0$ and the $n_j = 1$ combined category since the other part of the analysis is the same between the two cases. The observed signal strengths are consistent within a few percent level between the OS-SS and SSCR methods. The total uncertainties on the signal strength are also at the same level, but compositions of the uncertainties are different. The statistical uncertainty in the OS-SS method is larger than those in the SSCR method. The systematic uncertainty shows an opposite tendency; it is larger in the SSCR method. Since the OS-SS method uses the same sign data directly to estimate the normalization and m_T shape of the background without the systematic uncertainty, the performance is driven by the statistics of the same sign data. On the other hand, the SSCR method relies on the MC to predict the m_T shape. Thus, the relatively high statistics is available

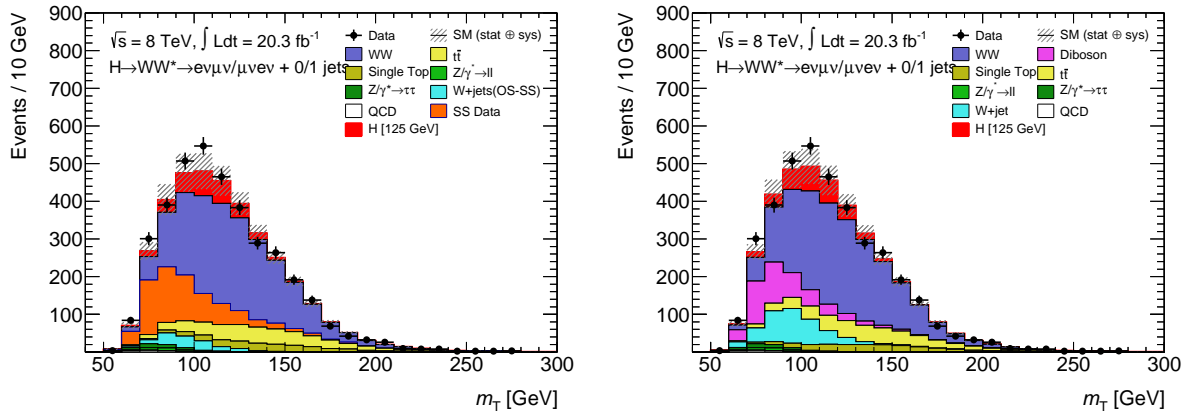


Figure 11.1: The m_T distributions with the OS-SS method (left) and SSCR method (right) in the signal regions of the $n_j = 0/1$ category in the $e\mu$ sample.

in the SSCR method, while the systematic uncertainty is required on the MC prediction. With the available statistics of the Run1 data, the SSCR shows slightly better performance in the total uncertainty. In the future analysis where higher statistics are available (i.e. upcoming $\sqrt{s} = 13$ TeV collisions), the OS-SS method will be an essential technique to improve the results by reducing the systematic uncertainty. If the statistical uncertainty on the same sign data is switched off (i.e. infinite same sign data is available) in the current analysis, the expected signal strength with the OS-SS method shows a value of $\mu = 1 +0.281/-0.250$ (total), which can be compared with those in table 11.1.

Table 11.1: Observed and expected signal strength μ in the $e\mu$ sample in $n_j = 0$ and $n_j = 1$ combined category. Only 8 TeV data is used. The statistical uncertainties account for the number of data and MC in the signal region and profiled control region. The systematic uncertainties include theoretical and experimental uncertainties.

	Observed μ	Expected μ
OS-SS method	$1.23^{+0.329}_{-0.298}$ (total)	$1^{+0.301}_{-0.271}$ (total)
	$1.23^{+0.230}_{-0.231}$ (stat.) $+0.235^{+0.235}_{-0.188}$ (syst.)	$1^{+0.219}_{-0.218}$ (stat.) $+0.207^{+0.207}_{-0.161}$ (syst.)
SSCR method	$1.27^{+0.333}_{-0.295}$ (total)	$1^{+0.297}_{-0.265}$ (total)
	$1.27^{+0.224}_{-0.222}$ (stat.) $+0.247^{+0.247}_{-0.195}$ (syst.)	$1^{+0.211}_{-0.209}$ (stat.) $+0.208^{+0.208}_{-0.164}$ (syst.)

11.2 7 TeV (2011) analysis

In 2011, a dataset corresponding to an integrated luminosity of 4.46 fb^{-1} at $\sqrt{s} = 7$ TeV (7 TeV data) is collected by ATLAS for physics analyses. The analyses using the 7 TeV data are designed to use common selections and method with the 8 TeV data analysis where possible. In this section, $H \rightarrow WW^* \rightarrow \ell\nu\ell\nu$ analysis based on the ggF-enriched sample with the 7 TeV

data is reviewed.

The analysis is performed on the $n_j = 0$ and $n_j = 1$ categories. The $n_j > 2$ ggF-enriched category is not included because of the limited statistics of the 7 TeV data. MC generators used in the analysis are summarized in table 5.2. For data and object selections, main differences with respect to the 8 TeV analysis are summarized as follows:

- Only single lepton (electron and muon) trigger;
- Cut-based Tight identification for electrons;
- Tight isolation and impact parameter requirement for leptons;
- Tight JVF requirement for jets.

The 7 TeV data are selected using single lepton triggers with a muon p_T threshold of 18 GeV and with varying electron E_T thresholds (20–22 GeV depending data taking period). The cut-based Tight identification is used for electrons in all E_T range. The OS-SS or SSCR methods are not used with the 7 TeV data due to the poor statistics. Thus, tight isolation and impact parameter are required in order to suppress the W +jets and *Other* VV backgrounds. Since the JVE requirement can be tighten without a signal loss due to less severe pile-up condition (see figure 3.3 (b)), $|JVE| > 0.75$ is used. For event selections, there are the following changes:

- $n_j = 0$:
 - The threshold of $p_{T,\ell\ell}$ in $ee/\mu\mu$ channel is changed to 40 GeV;
 - The threshold of f_{recoil} in $ee/\mu\mu$ channel is changed to 0.2;
- $n_j = 1$:
 - The threshold of $E_{T,\text{rel}}^{\text{miss}}$ in $ee/\mu\mu$ channel is changed to 35 GeV;
 - The $p_{T,\text{rel}}^{\text{miss}}$ requirement in $ee/\mu\mu$ channel is removed;
 - $p_{T,\ell j} > 35$ GeV requirement for $ee/\mu\mu$ channel is added;
 - The threshold of f_{recoil} in $ee/\mu\mu$ channel is changed to 0.5.

The size of Z +jets background in $ee/\mu\mu$ channel depends on the missing transverse energy resolution. A better resolution of the missing transverse energy is available in the 7 TeV data due to the lower level of pileup, that reduces the Z +jets background. Therefore, the thresholds of $E_{T,\text{rel}}^{\text{miss}}$ and f_{recoil} are loosened, and the $p_{T,\text{rel}}^{\text{miss}}$ requirement is removed in order to increase the signal efficiency. The reduced thresholds are partially compensated by an increased $p_{T,\ell\ell}$ threshold and an additional requirement on $p_{T,\ell j}$, where $p_{T,\ell j}$ is the p_T of the dilepton + jet system. In the $e\mu$ channel, the same event selection with the 8 TeV analysis is used.

The SRs of the $e\mu$ samples are split by the $p_T^{\ell 2}$ and $m_{\ell\ell}$ in the final fit, while there is no further division in the $ee/\mu\mu$ samples. Figure 11.2 shows the m_T distributions in the SRs of 7 TeV data analysis. The Misid (W +jets/QCD) background is estimated with the extrapolation factor method described in section 8.1. The WW , DY (Z +jets) and Top backgrounds are modeled with the MC samples, and corrected by data-based normalization factors. The VV background is estimated entirely from the MC simulations. Details of the background treatments are described in reference [117].

A Likelihood fit to extract the signal yield is performed on the m_T distribution. The observed Higgs signal strength μ^{obs} in the ggF-enriched sample with the 7 TeV data is:

$$\mu^{\text{obs}} = 0.61^{+0.50}_{-0.48} \text{ (stat.) }^{+0.37}_{-0.33} \text{ (syst.) } = 0.61^{+0.62}_{-0.59}. \quad (11.1)$$

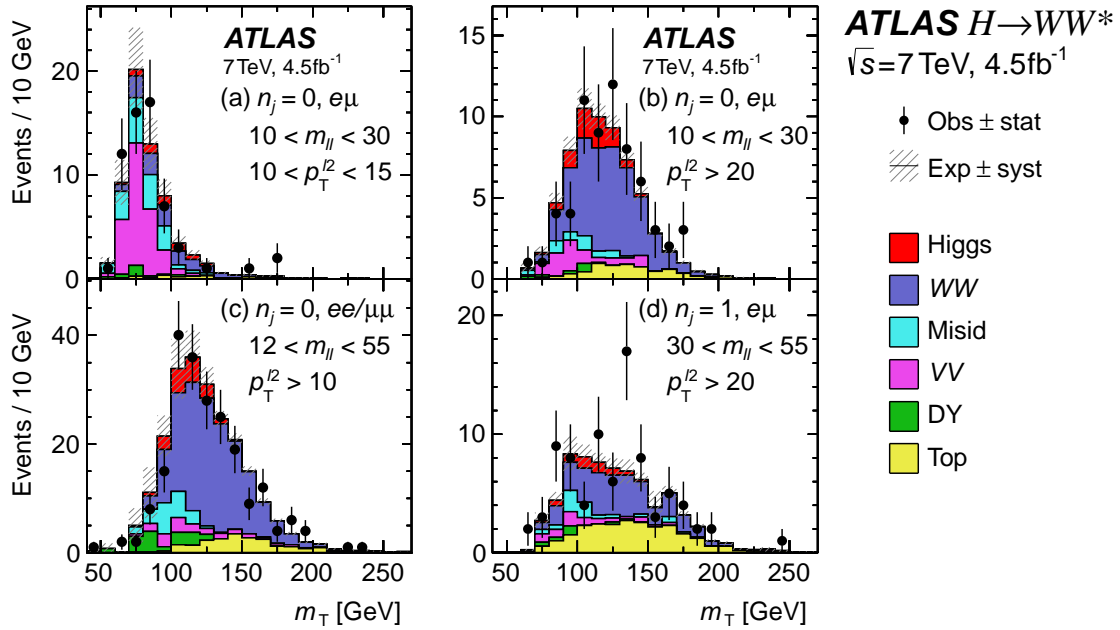


Figure 11.2: The m_T distribution in the SR of the $n_j = 0$ and $n_j = 1$ categories in the 7 TeV data analysis, for specific m_ℓ and $p_T^{\ell 2}$ range [117].

The signal strength is measured at $m_H = 125.36$ GeV. The result is consistent with the SM expectation within larger uncertainties, which is dominated by the statistical uncertainty. This result is combined with the result of 8 TeV data analysis in section 11.4.

11.3 VBF analysis

The VBF process (figure 2.3 (b)) has a specific topology. The two quarks scattered at a small angle lead to two energetic jets with a large separation in rapidity and a large invariant mass. To maximize the sensitivity by exploiting these event characteristics, a boosted decision tree (BDT) algorithm [118, 119] is used in the VBF analysis. This is one of the main differences compared to the ggF analysis. The BDT is trained using the MC samples so that the BDT can classify events as signal-like or background-like. This trained BDT outputs a value (BDT Score) between -1 and 1 for a given event, where a value of 1 indicates that the event is signal-like. The event selections using this BDT Score are described in appendix A.1.

In the VBF analysis, there are no differences of the event selection and background estimation method between the 7 TeV and 8 TeV data. The object selections for the 7 TeV (8 TeV) data are the same as the ggF analysis described in section 11.2 (section 6.6). The BDT is trained with the 8 TeV samples since much higher statistics are available, and it is used in the 7 TeV samples. Figure 11.3 shows the BDT score distributions in the signal regions. The Misid (W +jets /QCD) background is estimated with the extrapolation factor method described in section 8.1. The Top and DY (Z +jets) backgrounds are modeled by the MCs with data-based normalization factors. The other backgrounds are fully estimated with the MCs and normalized to the theoretical cross section. Details of the background treatments are described in reference [117].

The observed Higgs signal strength μ^{obs} in the VBF-enriched sample combined with the 7

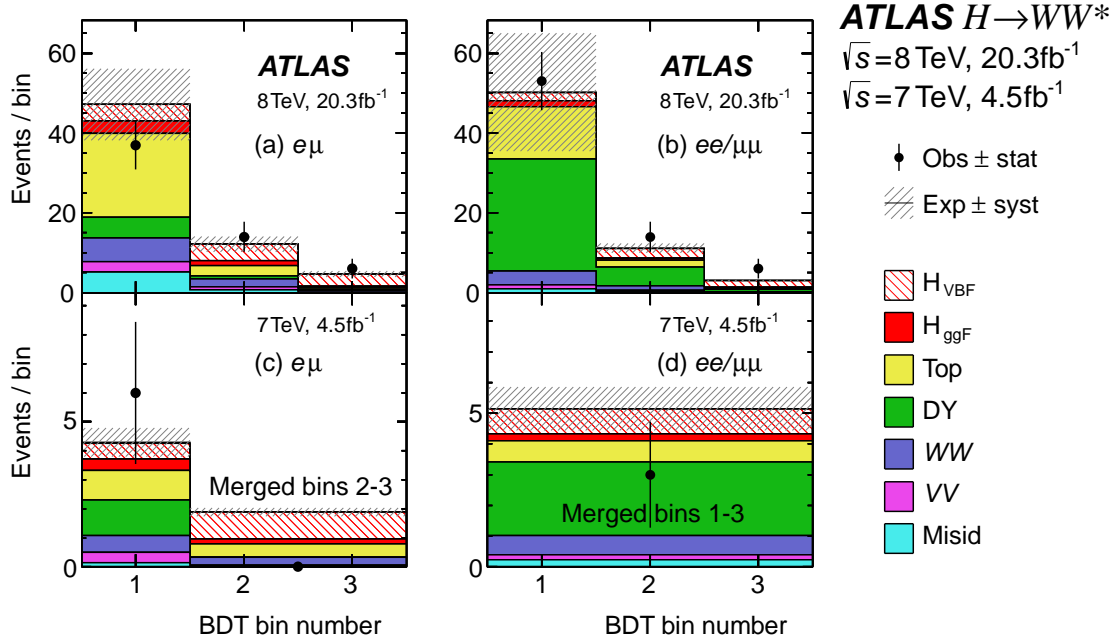


Figure 11.3: BDT score distributions in the signal regions of the $n_j \geq 2$ VBF-enriched category [117]. The 8 TeV (7 TeV) data is shown on the top (bottom), the $e\mu$ ($ee/\mu\mu$) on the left (right). Bin boundaries are at BDT score = $[-0.48, 0.3, 0.78, 1.0]$.

TeV and 8 TeV data sets is:

$$\mu^{\text{obs}} = 1.21 \begin{matrix} +0.37 \\ -0.33 \end{matrix} (\text{stat.}) \begin{matrix} +0.29 \\ -0.20 \end{matrix} (\text{syst.}) = 1.21 \begin{matrix} +0.46 \\ -0.39 \end{matrix}. \quad (11.2)$$

The signal strength is measured at $m_H = 125.36$ GeV. This VBF analysis is still dominated by the statistical uncertainty. The observed local significance corresponds to 3.8 standard deviation. The signal regions of the $n_j \geq 2$ VBF-enriched category are optimized for the sensitivity to the VBF production mode. However, the ggF contamination is not negligible (about 40 % of the total signal). In order to discuss the compatibility with the SM prediction of the VBF production process, separated signal strength of μ_{ggF} and μ_{VBF} are simultaneously determined through a fit on the ggF and VBF combined category. This combined results are discussed in the next section.

11.4 Combined results

The $H \rightarrow WW^* \rightarrow l\nu l\nu$ analysis using the ggF-enriched sample in 8 TeV data, which is described through this thesis, is combined with the 7 TeV data analysis and VBF analysis. A likelihood fit is performed with all analysis categories to extract a global signal strength followed by the procedure described in reference [117]. The correlation of nuisance parameters among the analysis category is assumed to be 100 % except for those that are statistical in origin or have a different source for the two datasets. For example, the QCD scale uncertainty on the signal is treated as correlated among the category, while the luminosity uncertainty is treated

as uncorrelated. The global signal strength μ is calculated at $m_H = 125.36$ GeV, and it is:

$$\mu^{\text{obs}} = 1.05^{+0.15}_{-0.15} (\text{stat.})^{+0.16}_{-0.14} (\text{syst.}) = 1.05^{+0.22}_{-0.20}. \quad (11.3)$$

The result is consistent with the SM expectation within the uncertainty. The μ is obtained with accuracy of 20%, which is precise than the measurements using the other decay modes ($H \rightarrow ZZ^*$, $H \rightarrow \gamma\gamma$, etc) with the Run1 dataset [48]. The observed local significance p_0 reaches 5.9 standard deviation, that establish the evidence of the Higgs boson production in the $H \rightarrow WW^* \rightarrow \ell\nu\ell\nu$ decay.

In order to assess the compatibility with the SM prediction of the ggF and VBF production processes individually, the signal strengths of μ_{ggF} and μ_{VBF} are simultaneously determined through the fit, which can be performed thanks to the different sensitivity to these processes in ggF-enriched and VBF-enriched categories. The μ_{ggF} and μ_{VBF} are introduced to λ in the first term of the Likelihood function as $\mu_{\text{ggF}} \cdot S_{\text{ggF}} + \mu_{\text{VBF}} \cdot S_{\text{VBF}}$, where S_{ggF} and S_{VBF} are the number of expected ggF and VBF events, respectively. The corresponding two dimensional scan of μ_{ggF} and μ_{VBF} is shown in figure 11.4 (a). The obtained best fit values are:

$$\mu_{\text{ggF}} = 0.96^{+0.28}_{-0.25} (\text{total.}) \quad (11.4)$$

$$\mu_{\text{VBF}} = 1.25^{+0.52}_{-0.44} (\text{total.}) \quad (11.5)$$

With these results, it is confirmed that both the ggF and VBF production modes are compatible with the SM predictions within the uncertainties.

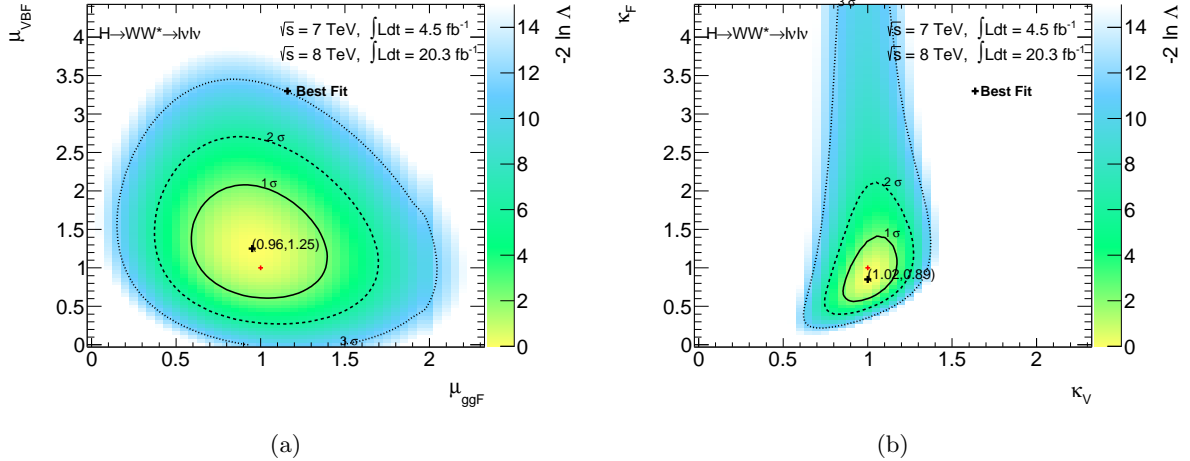


Figure 11.4: Likelihood scan as a function of (a) μ_{ggF} and μ_{VBF} , (b) κ_V and κ_F . All analysis categories (ggF-enriched and VBF-enriched with 7 TeV and 8 TeV data) are used. 1, 2 and 3 standard deviation are shown.

The μ_{ggF} and μ_{VBF} can be translated to scale factors of Higgs boson couplings to the fermions, κ_F , and bosons, κ_V , using a framework [12] motivated by the tree level interactions. For example, the coupling strength at the hWW vertex (see equation 2.20) is parametrized with κ_V as follows:

$$g_{hWW} = \frac{1}{2}(\kappa_V \cdot g)^2 v. \quad (11.6)$$

Accordingly, the μ_{ggF} and μ_{VBF} can be written as follows:

$$\mu_{\text{ggF}} \propto \frac{\kappa_{\text{F}}^2 \cdot \kappa_{\text{V}}^2}{\kappa_{\text{H}}^2} = \frac{\kappa_{\text{F}}^2 \cdot \kappa_{\text{V}}^2}{(Br_{H \rightarrow f\bar{f}})\kappa_{\text{F}}^2 + (Br_{H \rightarrow VV})\kappa_{\text{V}}^2} \quad (11.7)$$

$$\mu_{\text{VBF}} \propto \frac{\kappa_{\text{V}}^4}{\kappa_{\text{H}}^2} = \frac{\kappa_{\text{V}}^4}{(Br_{H \rightarrow f\bar{f}})\kappa_{\text{F}}^2 + (Br_{H \rightarrow VV})\kappa_{\text{V}}^2}, \quad (11.8)$$

where κ_{H} is a scale factor of the total decay width, which is divided into κ_{F} and κ_{V} with an assumption that there are no non-SM decay mode. $Br_{H \rightarrow VV(f\bar{f})}$ is the branching ratio to the vector bosons (fermions). The κ_{F} and κ_{V} take values of one if observed coupling constants are the same as the expected values in the SM. Figure 11.4 (b) shows a Likelihood scan as a function of κ_{F} and κ_{V} . The low discrimination among high values of κ_{F} is due to the functional behavior of the total ggF yield. The κ_{F} dependence in equation 11.7 decreases when $\kappa_{\text{F}} > \kappa_{\text{V}}$ since the branching ratio of $Br_{H \rightarrow f\bar{f}}$ is larger than $Br_{H \rightarrow VV}$ in the SM, but the ratio is still sensitive to κ_{F} . As a result, the degradation of discrimination power is observed since the measurement of κ_{F} is driven by μ_{VBF} . The best fit values are:

$$\kappa_{\text{F}} = 0.89^{+0.22}_{-0.17} \text{ (stat.) } ^{+0.19}_{-0.13} \text{ (syst.)} = 0.89^{+0.30}_{-0.23} \quad (11.9)$$

$$\kappa_{\text{V}} = 1.02^{+0.07}_{-0.08} \text{ (stat.) } ^{+0.07}_{-0.07} \text{ (stat.)} = 1.02^{+0.10}_{-0.11} \quad (11.10)$$

The obtained κ_{F} and κ_{V} are also consistent with the SM prediction. The coupling to the vector bosons has been measured with accuracy of 10%, which confirms that the measurement using $H \rightarrow WW^* \rightarrow \ell\nu\ell\nu$ channel provides a strong constraint on the Higgs boson couplings to the vector bosons.

11.5 Comparisons with the CMS results

The Higgs signal strength measurement using the $H \rightarrow WW^* \rightarrow \ell\nu\ell\nu$ decay channel is also performed in the CMS experiment [120] using the LHC Run1 data. Figure 11.5 summarizes the signal strength measured in ATLAS and CMS. The results in both experiments are consistent within the total uncertainty. However, the signal strengths measured in CMS tend to be smaller than the SM prediction. Since the statistical uncertainty is still large (comparable with the systematic uncertainty), the update measurements with the expected 13 TeV data are hoped. A better precision is achieved in ATLAS compared to CMS experiment. This could be explained by the high signal efficiency by optimizing the object and event selections, and including the $n_j \geq 2$ ggF-enriched category, as well as smaller uncertainties on the background estimations. The BDT algorithm also provides a better discrimination of the signal in the VBF-enriched category.

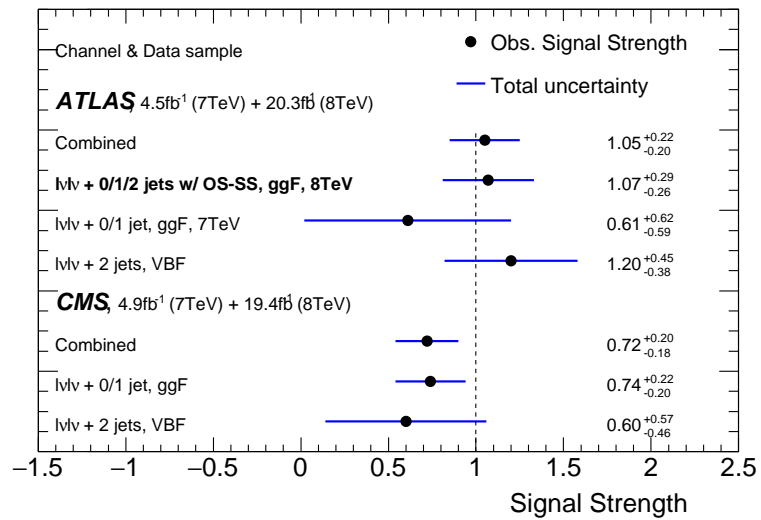


Figure 11.5: Summary of the observed signal strengths. Signal strength are measured at $m_H = 125.36$ GeV in ATLAS and $m_H = 125.6$ GeV in CMS [120]. The CMS combined result includes VH analyses.

Chapter 12

Conclusion

Measurement of the Higgs boson production in the $H \rightarrow WW^* \rightarrow \ell\nu\ell\nu$ decay with the ATLAS detector at the LHC has been presented. The Higgs signal strength measured by focusing the gluon-gluon fusion production mode with the 8 TeV collision data taken in 2012, which corresponds to an integrated luminosity of 20.3 fb^{-1} , is:

$$\mu_{\text{ggF}}^{8\text{TeV}} = 1.07^{+0.18}_{-0.18} \text{ (stat.) }^{+0.22}_{-0.19} \text{ (syst.)}.$$

The result is consistent with the Standard Model expectation. The measurement is performed with the following studies:

- Development of the OS-SS method,
- Construction of the validation regions for the *Other VV* background.

The OS-SS method estimates the *Other VV* and part of W +jets backgrounds fully from the data, that resulting in the reduction of the systematic uncertainties. This method is unique and will provide further information in upcoming $\sqrt{s} = 13 \text{ TeV}$ collisions at the LHC since the statistics of the same-sign data will be improved. The validation methods for the *Other VV* background estimated by the MC simulations have been established by developing the validation regions.

In order to achieve a precise measurement, the analysis is combined with the other analyses using the 7 TeV collision data taken in 2011, which corresponds to an integrated luminosity of 4.46 fb^{-1} , and focusing the vector boson fusion production mode. The Higgs signal strength and scale factors to the coupling constants, measured in the combined sample, are:

$$\begin{aligned}\mu^{\text{obs}} &= 1.05^{+0.15}_{-0.15} \text{ (stat.) }^{+0.16}_{-0.14} \text{ (syst.)} = 1.05^{+0.22}_{-0.20} \\ \kappa_{\text{F}} &= 0.89^{+0.22}_{-0.17} \text{ (stat.) }^{+0.19}_{-0.13} \text{ (syst.)} = 0.89^{+0.30}_{-0.23} \\ \kappa_{\text{V}} &= 1.02^{+0.07}_{-0.08} \text{ (stat.) }^{+0.07}_{-0.07} \text{ (stat.)} = 1.02^{+0.10}_{-0.11}\end{aligned}$$

These results are also consistent with the Standard Model predictions. The statistical and systematic uncertainties contribute approximately equal. The signal and background productions are well understood though this analysis, which will be essential inputs to the future analysis.

Acknowledgements

I would like to first thank the staffs of Kobe University for helping my research activities. I am thankful to Prof. Hisaya Kurashige for providing me with a great opportunity to participate in the ATLAS experiment. His leadership always led me to the right direction so that I can accomplish researches throughout my long undergraduate, master and doctoral programs in Kobe University. I am also grateful to Prof. Yuji Yamazaki. He taught me a lot of things about the collider physics, how to research in a large international collaboration, how to write theses as well. Without his comments, my thesis couldn't have got into shape. I also learned data analyses at the collider experiment from Prof. Takashi Matsusita. His advices were very constructive, and influenced my research style. He made an occasion to participate in the $H \rightarrow WW^* \rightarrow \ell\nu\ell\nu$ analysis group for me, so I really appreciate that. I would like to express my thanks to Dr. Li Yuan, who helped me to do researches in this $H \rightarrow WW^* \rightarrow \ell\nu\ell\nu$ analysis group. Discussions about the analysis with her were very instructive, and improved my English. I also would like to express my gratitude to Prof. Kiyotomo Kawagoe. He gave me an environment to learn the particle physics as a leader of the Kobe particle physics group when I was a master student. I learned particle detectors from Prof. Atsuhiko Ochi through open end conversations, I appreciate it. I would like to extend my thanks to Prof. Akimasa Ishikawa, Prof. Shima Shimizu and Prof. Junpei Maeda, who provided useful comments in Kobe meetings. I shared a good research life at CERN with them. Yumi Yokoyama is another member of the staffs, who I would like to thank. She supported my research activities as a secretary of the Kobe particle physics group.

My appreciations go to the $H \rightarrow WW^* \rightarrow \ell\nu\ell\nu$ analysis team. Prof. Tatsuya Masubuchi is a wonderful expert of the analysis, and gave me a lot of ideas and advices. I really appreciate him, and am so lucky I could research with him in the group. I am grateful to Dr. Keisuke Yoshihara for guiding me with his energetic research style. I learned background estimation techniques from him. I feel truly grateful to Jianming Qian, Pierre Savard, Biagio Di Micco, Christian Schmitt, Corrinne Miles and Olivier Arnaez. They led us to a great achievement of the Higgs boson measurement as conveners of the group. I am also grateful to Chris Hays, Joe Kroll, Magda Chelstowska and Doug Schaefer. I received very useful comments and suggestions from them through the rate measurement and W +jets background subgroup meetings. Also I would like to express my appreciation to Jonathan Long, Christian Meinech, Johanna Bronner and Joana Machado Miguénd for helping maintenances of the skimming and analysis frameworks. I learned the statistical treatment on data from Hee Yeun Kim, Stefan Gadatsch and Aaron Armbruster. Without their helps and works, I would be counting the signal and background by hand.

I would like to extend my appreciations to the ATLAS Japan group. I am thankful to Prof. Katsuo Tokusyuku, Prof. Kunihiro Nagano, Prof. Osamu Sasaki, Prof. Masato Aoki, Prof. Masaya Ishino, Prof. Toshi Sumida, Prof. Makoto Tomoto and Prof. Susumu Oda. Their organization and supports were essential for my research activities in the TGC trigger group.

I learned a lot of things in the TGC group, detector operations, analyses using the data and simulations, the Athena framework as well. Physics analyses performed in the ATLAS are completely based on their achievements of the detector and trigger operations. Also my research life is supported by a lot of colleagues, Kohei Kessoku, Yu Suzuki, Takashi Hayakawa, Takeshi Domae, Toyonobu Okuyama, Yoichi Ninomiya, Wataru Okamura, Nobe Takuya, Ryo Nagai, Katsuya Yamauchi, Takuya Tashiro, Masahiro Morinaga, Chikuma Kato and Dai Kobayashi. I could survive on a long stay at CERN thanks to companionships with them. The regular BBQs at the Ferney base are unforgettable memories for me.

Finally, I would like to express my deepest thanks to my family. Obviously, I could not spend my research life without their supports.

Tomoe Kishimoto
January, 2015

Bibliography

- [1] UA1 Collaboration, “Experimental observation of isolated large transverse energy electrons with associated missing energy at $\sqrt{s} = 540$ GeV”, Phys. Rev. Lett. B **122**, 103-116 (1983).
- [2] UA2 Collaboration, “Observation of Single Isolated Electrons of High Transverse Momentum in Events with Missing Transverse Energy at the CERN anti-p p Collider”, Phys. Rev. Lett. B **122**, 476-485 (1983).
- [3] F. Englert and R. Brout, “Broken Symmetry and the Mass of Gauge Vector Mesons”, Phys. Rev. Lett. **13**, 321 (1964).
- [4] Peter W. Higgs, “Broken Symmetries and the Masses of Gauge Bosons”, Phys. Rev. Lett. **13**, 508 (1964).
- [5] Steven Weinberg, “A Model of Leptons”, Phys. Rev. Lett. **19**, 1264 (1967).
- [6] ATLAS Collaboration, “Observation of a new particle in the search for the Standard Model Higgs boson with the ATLAS detector at the LHC”, Phys. Lett. B **716**, 1 (2012).
- [7] CMS Collaboration, “Observation of a new boson at a mass of 125 GeV with the CMS experiment at the LHC”, Phys. Lett. B **716**, 1 (2012).
- [8] H1 Collaboration, “Combined measurement and QCD analysis of the inclusive $e^\pm p$ scattering cross sections at HERA”, J. High Energy Phys. 01 (2010) 109.
- [9] CDF Collaboration, “Measurement of $d\sigma/d\sigma$ of Drell-Yan e^+e^- pairs in the Z Mass Region from $p\bar{p}$ Collisions at $\sqrt{s} = 1.96$ TeV”, arXiv:0908.3914 [hep-ph].
- [10] DØ Collaboration, “Measurement of the shape of the boson rapidity distribution for $p\bar{p} \rightarrow Z/\gamma^* \rightarrow e^+e^- + X$ events produced at \sqrt{s} of 1.96 TeV”, Phys. Rev. D **76**, 012003 (2007).
- [11] LHC Higgs Cross Section Working Group, <https://twiki.cern.ch/twiki/bin/view/LHCPhysics/CrossSections>.
- [12] LHC Higgs Cross Section Working Group, “Handbook of LHC Higgs Cross Sections: 3. Higgs Properties”, arXiv:1307.1347 [hep-ph].
- [13] C. Anastasiou and K. Melnikov, “Higgs boson production at hadron colliders in NNLO QCD”, Nucl. Phys. **B646**, 220 (2002).
- [14] U. Aglietti, R. Bonciani, G. Degrassi, and A. Vicini, “Master integrals for the two-loop light fermion contributions to $gg \rightarrow H$ and $H \rightarrow \gamma\gamma$ ”, Phys. Lett. B **600**, 57 (2004).

-
- [15] S. Actis, G. Passarino, C. Sturm, and S. Uccirati, “NLO Electroweak Corrections to Higgs Boson Production at Hadron Colliders”, *Phys. Lett. B* **670**, 12 (2008).
- [16] S. Catani, D. de Florian, M. Grazzini, and P. Nason, “Soft-gluon resummation for Higgs boson production at hadron colliders”, *J. High Energy Phys.* 07 (2003) 028.
- [17] J M Campbell, J W Huston and W J Stirling, “Hard interactions of quarks and gluons: a primer for LHC physics”, *Rep. Prog. Phys.* 70, 89 (2007).
- [18] A. D. Martin, W. J. Stirling, R. S. Thorne and G. Watt, “Parton distributions for the LHC”, *Eur. Phys. J. C* **63**, 189 (2009).
- [19] P. Bolzoni, F. Maltoni, S.-O. Moch, and M. Zaro, “Higgs Boson Production via Vector-Boson Fusion at Next-to-Next-to-Leading Order in QCD”, *Phys. Rev. Lett.* **105**, 011801 (2010).
- [20] M. Ciccolini, A. Denner, and S. Dittmaier, “Electroweak and QCD corrections to Higgs production via vector-boson fusion at the CERN LHC”, *Phys. Rev. D* **77**, 013002 (2008).
- [21] Oliver Breina, Robert V. Harlanderb, Tom J.E. Zirke, “vh@nnlo Higgs Strahlung at hadron colliders”, *Comput. Phys. Commun.* **184**, 998-1003 (2013).
- [22] S. Dawson, L.H. Orr, L. Reina, D. Wackerroth, “Associated Top Quark-Higgs Boson Production at the LHC”, arXiv:hep-ph/0211438 [hep-ph].
- [23] A. Bredenstein, A. Denner, S. Dittmaier, and M. M. Weber, “Precise predictions for the Higgs-boson decay $H \rightarrow WW/Z Z \rightarrow 4$ leptons”, *Phys. Rev. D* **74**, 013004 (2006).
- [24] A. Djouadi, J. Kalinowski, and M. Spira, “HDECAY: a Program for Higgs Boson Decays in the Standard Model and its Supersymmetric Extension”, *Comput. Phys. Commun.* **108**, 56 (1998).
- [25] ATLAS Collaboration, “Measurements of Higgs boson production and couplings in the four-lepton channel in pp collisions at center-of-mass energies of 7 and 8 TeV with the ATLAS detector”, arXiv:1408.5191 [hep-ph].
- [26] H. Miyazawa, “Baryon Number Changing Currents”, *Prog. Theor. Phys.* 36 no. 6, 1266 (1966).
- [27] P. Ramond, “Dual Theory for Free Fermions”, *Phys. Rev. D* **3**, 2415 (1971).
- [28] Y. Golfand and E. Likhtman, “Extension of the Algebra of Poincare Group Generators and Violation of p Invariance”, *JETP Lett.* **13**, 323 (1971).
- [29] A. Neveu and J. Schwarz, “Factorizable dual model of pions”, *Nucl. Phys.* **B31**, 86 (1971).
- [30] A. Neveu and J. Schwarz, “Quark Model of Dual Pions”, *Phys. Rev. D* **4**, 1109 (1971).
- [31] J.-L. Gervais and B. Sakita, “Field theory interpretation of supergauges in dual models”, *Nucl. Phys.* **B34**, 632 (1971).
- [32] D. Volkov and V. Akulov, “Is the Neutrino a Goldstone Particle?”, *Phys. Lett. B* **46**, 109 (1973).

- [33] J. Wess and B. Zumino, “A Lagrangian Model Invariant Under Supergauge Transformations”, *Phys. Lett. B* **49**, 52 (1974).
- [34] J. Wess and B. Zumino, “Supergauge transformations in four dimensions”, *Nucl. Phys.* **B70**, 52 (1974).
- [35] P. Fayet, “Supersymmetry and Weak, Electromagnetic and Strong Interactions”, *Phys. Lett. B* **64** no. 2, 159 (1976).
- [36] P. Fayet, “Spontaneously broken supersymmetric theories of weak, electromagnetic and strong interactions”, *Phys. Lett. B* **69**, 489 (1977).
- [37] G. R. Farrar and P. Fayet, “Phenomenology of the Production, Decay, and Detection of New Hadronic States Associated with Supersymmetry”, *Phys. Lett. B* **76**, 575 (1978).
- [38] P. Fayet, “Relations Between the Masses of the Superpartners of Leptons and Quarks, the Goldstino Couplings and the Neutral Currents”, *Phys. Lett. B* **84**, 416 (1979).
- [39] S. Dimopoulos and H. Georgi, “Softly broken supersymmetry and SU(5)”, *Nucl. Phys.* **B193**, 150 (1981).
- [40] L. Maiani, A. Polosa, and V. Riquer, “Bounds to the Higgs Sector Masses in Minimal Supersymmetry from LHC Data”, arXiv:1305.2172 [hep-ph].
- [41] A. Djouadi, L. Maiani, G. Moreau, A. Polosa, J. Quevillon, V. Riquer, “The post-Higgs MSSM scenario: Habemus MSSM?”, arXiv:1307.5205 [hep-ph].
- [42] S. Kanemura et al., “Can WIMP dark matter overcome the nightmare scenario?”, *Phys. Rev. D* **82**, 055026 (2010).
- [43] P. J. Fox, R. Harnik, J. Kopp, and Y. Tsai, “Missing Energy Signatures of Dark Matter at the LHC”, *Phys. Rev. D* **85**, 056011 (2012).
- [44] A. Djouadi, O. Lebedev, Y. Mambrini, and J. Quevillon, “Implications of LHC searches for Higgs–portal dark matter”, *Phys. Lett. B* **709**, 65 (2012).
- [45] L. Lopez-Honorez, T. Schwetz, and J. Zupan, “Higgs portal, fermionic dark matter, and a Standard Model like Higgs at 125 GeV”, *Phys. Lett. B* **716**, 179 (2012).
- [46] ATLAS Collaboration, “Search for Dark Matter in Events with a Hadronically Decaying W or Z Boson and Missing Transverse Momentum in pp Collisions at $\sqrt{s} = 8$ TeV with the ATLAS Detector”, *Phys. Rev. Lett.* **112**, 041802 (2014).
- [47] ATLAS Collaboration, “Measurement of the Higgs boson mass from the $H \rightarrow \gamma\gamma$ and $H \rightarrow ZZ^* \rightarrow 4\ell$ channels in pp collisions at center-of-mass energies of 7 and 8 TeV with the ATLAS detector”, *Phys. Rev. D* **90**, 052004 (2014).
- [48] ATLAS Higgs Public Results,
<https://atlas.web.cern.ch/Atlas/GROUPS/PHYSICS/CombinedSummaryPlots/HIGGS/> .
- [49] ATLAS Collaboration, “Measurement of Higgs boson production and couplings in diboson final state with the ATLAS detector at the LHC”, *Phys. Lett. B* **726**, 88 (2013).
- [50] LHC design report, CERN/-2004-004, 4 June 2004.

- [51] ATLAS Collaboration, “Improved luminosity determination in pp collisions at $\sqrt{s} = 7$ TeV using the ATLAS detector at the LHC”, *Eur. Phys. J.C*, **73**:2518 (2013).
- [52] S. van der Meer, “Calibration of the effective beam height in the ISR”, CERN-ISR-PO-68-31 (1968).
- [53] ATLAS Luminosity Public Results, <https://twiki.cern.ch/twiki/bin/view/AtlasPublic/LuminosityPublicResults/> .
- [54] ATLAS Collaboration, “ATLAS Trigger Performance Status Report”, CERN/LHCC/98-15 (1998).
- [55] ATLAS Standard Model Public Results, <https://twiki.cern.ch/twiki/bin/view/AtlasPublic/StandardModelPublicResults> .
- [56] ATLAS experiment photos, <http://www.atlas.ch/photos/>.
- [57] ATLAS Collaboration, “ATLAS DETECTOR AND PHYSICS PERFORMANCE Technical Design Report Volume I”, CERN/LHCC/99-14 ATLAS TDR (1999).
- [58] J.J. Goodson, “Search for Supersymmetry in States with Large Missing Transverse Momentum and Three Leptons including a Z-Boson”, (2012).
- [59] M Aleksa et al, “Results of the ATLAS solenoid magnetic field map”, *J. Phys.: Conf. Ser.* **110** 092018 (2008).
- [60] ATLAS Collaboration, “The ATLAS experiment at the CERN Large Hadron Collider”, JINST **3** S08003 (2008).
- [61] ATLAS Collaboration, “Muon Spectrometer Technical Design Report”, CERN/LHCC/97-22 (1997).
- [62] ATLAS Collaboration, “Alignment of the ATLAS Inner Detector and its Performance in 2012”, ATLAS-CONF-2014-047 (2014).
- [63] T. Golling, H.S. Hayward, P.U.E. Onyisi¹, H.J. Stelzer and P. Waller, “The ATLAS data quality defect database system”, *Eur. Phys. J.C*, **72**: 1960 (2012).
- [64] ATLAS Egamma trigger Public Results, <https://twiki.cern.ch/twiki/bin/view/AtlasPublic/EgammaTriggerPublicResults>.
- [65] ATLAS Collaboration, “Performance of the ATLAS muon trigger in pp collisions at $\sqrt{s} = 8$ TeV”, arXiv:1408.3179 [hep-ph].
- [66] J. Garvey et al., “Use of an FPGA to identify electromagnetic clusters and isolated hadrons in the ATLAS level-1 calorimeter trigger”, *Nucl. instrum. Meth.* **A512**, 506 (2003).
- [67] P. Nason, “A new method for combining NLO QCD with shower Monte Carlo algorithms”, *J. High Energy Phys.* **11** (2014) 040.
- [68] M. L. Mangano, F. Piccinini, A. D. Polosa, M. Moretti, and R. Pittau, “ALPGEN, a generator for hard multiparton processes in hadronic collisions”, *J. High Energy Phys.* **07** (2003) 001.

- [69] T. Gleisberg, S. Hoche, F. Krauss, M. Schonherr, S. Schumann, F. Siegert, and J. Winter, “Event generation with SHERPA 1.1”, *J. High Energy Phys.* 02 (2009) 007.
- [70] T. Sjostrand, S. Mrenna, and P. Skands, “PYTHIA 6.4 physics and manual”, *J. High Energy Phys.* 05 (2006) 026.
- [71] T. Sjostrand, S. Mrenna, and P. Skands, “A brief introduction to PYTHIA 8.1”, *Comput. Phys. Commun.* **178**, 852 (2008).
- [72] G. Corcella, I. G. Knowles, G. Marchesini, S. Moretti, K. Odagiri, P. Richardson, M. H. Seymour, and B. R. Webber, “HERWIG 6.5: an event generator for Hadron Emission Reactions With Interfering Gluons (including supersymmetric processes)”, *J. High Energy Phys.* 01 (2001) 010.
- [73] H.-L. Lai, M. Guzzi, J. Huston, Z. Li, P. M. Nadolsky, J. Pumplin, and C.-P. Yuan, “New parton distributions for collider physics”, *Phys. Rev. D* **82**, 074024 (2010).
- [74] J. Pumplin, D. R. Stump, J. Huston, H.-L. Lai, P. M. Nadolsky, and W.-K. Tung, “New generation of parton distributions with uncertainties from global QCD analysis”, *J. High Energy Phys.* 0207 (2002) 012.
- [75] A. Sherstnev and R. S. Thorne, “Parton distributions for LO generators”, *Eur. Phys. J. C* **55**, 553 (2008).
- [76] GEANT4 Collaboration, “Geant4 a simulation toolkit”, *Nucl. Instr. Meth. A* **506**, 250 (2003).
- [77] ATLAS Collaboration, “The simulation principle and performance of the ATLAS fast calorimeter simulation FastCaloSim”, ATLAS-PHYS-PUB-2010-013.
- [78] C. Anastasiou, R. Boughezal and F. Petriello, “Mixed QCD-electroweak corrections to Higgs boson production in gluon fusion”, *J. High Energy Phys.* 0904 (2009) 003.
- [79] D. de Florian, M. Grazzini, “Higgs production through gluon fusion: updated cross sections at the Tevatron and the LHC”, *Phys. Lett. B* **674**, 291 (2009).
- [80] J. Baglio, A. Djouadi, “Higgs production at the LHC”, *J. High Energy Phys.* 03 (2011) 055.
- [81] D. de Florian, G. Ferrera, M. Grazzini and D. Tommasini, “Higgs boson production at the LHC: transverse momentum resummation effects in the $H \rightarrow \gamma\gamma$, $H \rightarrow WW \rightarrow \ell\nu\ell\nu$ and $H \rightarrow H \rightarrow 4\ell$ decay modes”, *J. High Energy Phys.* 06 (2012) 132.
- [82] LHC Higgs Cross Section Working Group, “Handbook of LHC Higgs Cross Sections: 2. Differential Distributions”, Report No. CERN-2012-00, <https://cds.cern.ch/record/1416519>.
- [83] A. Banfi, P. Monini, G. Salam and G. Zanderighi, “Higgs- and Z-boson Production with a Jet Veto”, *Phys. Rev. Lett* **109**, 202001 (2012).
- [84] J. M. Campbell, R. K. Ellis, and C. Williams, “Vector boson pair production at the LHC”, *J. High Energy Phys.* 07 (2011) 018.
- [85] V. Hirschi, R. Frederix, S. Frixione, M.V. Gazelli, “Automation of one-loop QCD corrections”, *J. High Energy Phys.* 1105 (2011) 044.

- [86] N. Kauer, “Interference effects for $H \rightarrow WW/ZZ \rightarrow \ell\bar{\nu}_\ell\bar{\ell}\nu_\ell$ searches in gluon fusion at the LHC”, *J. High Energy Phys.* **12** (2013) 018.
- [87] B. P. Kersevan and E. Richter-Was, “The Monte Carlo event generator AcerMC versions 2.0 to 3.8 with interfaces to PYTHIA 6.4, HERWIG 6.5 and ARIADNE 4.1”, *Comput. Phys. Commun.* **184**, 919 (2013).
- [88] M. Czakon and A. Mitov, “Top++: a program for the calculation of the top-pair cross-section at hadron colliders”, *Comput. Phys. Commun.* **185**, 2930 (2014).
- [89] N. Kidonakis, “NNLL resummation for s-channel single top quark production”, *Phys. Rev. D* **81**, 054028 (2010).
- [90] N. Kidonakis, “Next-to-next-to-leading-order collinear and soft gluon corrections for t-channel single top quark production”, *Phys. Rev. D* **83**, 091503 (2011).
- [91] N. Kidonakis, “Two-loop soft anomalous dimensions for single top quark associated production with a W^- or H^- ”, *Phys. Rev. D* **82**, 054018 (2010).
- [92] A. Bierweiler, T. Kasprzik and J. H. Kuhn, “Vector-boson pair production at the LHC to $\mathcal{O}(\alpha^3)$ accuracy”, *J. High Energy Phys.* **12** (2013) 071.
- [93] S. Catani, L. Cieri, G. Ferrera, D. de Florian, and M. Grazzini, “Vector boson production at hadron colliders: a fully exclusive QCD calculation at NNLO”, *Phys. Rev. Lett.* **103**, 082001 (2009).
- [94] S. Frixione et al., “Concepts, Design and Implementation of the ATLAS New Tracking (NEWT)”, ATL-SOFT-PUB-2007-007, <https://cdsweb.cern.ch/record/1020106>.
- [95] R. Fruhwirth et al., “Application of Kalman filtering to track and vertex fitting”, *Nucl. Instrum. Meth.* **A262**, 444, (1987).
- [96] D. Wicke, “A New Algorithm For Solving Tracking Ambiguities”, DELPHI 98-163, PROG 236 TRACK 92 (1998).
- [97] ATLAS Inner Tracking Performance Public Results, <https://twiki.cern.ch/twiki/bin/view/AtlasPublic/InDetTrackingPerformanceApprovedPlots>.
- [98] ATLAS Collaboration, “Performance of primary vertex reconstruction in proton-proton collisions at $\sqrt{s} = 7$ TeV in the ATLAS experiment”, ATLAS-CONF-2010-069 (2010).
- [99] W. Lampl et al., “Calorimeter Clustering Algorithms : Description and Performance”, ATL-LARG-PUB-2008-002, <https://cds.cern.ch/record/1099735>.
- [100] ATLAS Collaboration, “Electron efficiency measurements with the ATLAS detector using the 2012 LHC proton-proton collision data”, ATLAS-CONF-2014-032 (2014).
- [101] ATLAS Collaboration, “Electron and photon energy calibration with the ATLAS detector using LHC Run 1 data”, arXiv:1407.5063 [hep-ph].
- [102] ATLAS Collaboration, “Expected performance of the ATLAS experiment - detector, trigger and physics”, arXiv:0901.0512 [hep-ex].

- [103] ATLAS Collaboration, “Measurement of the muon reconstruction performance of the ATLAS detector using 2011 and 2012 LHC proton-proton collision data”, *Eur. Phys. J. C* **74**, 3130 (2014).
- [104] W. Lampl et al., “Calorimeter Clustering Algorithms: Description and Performance”, Tech. Rep. ATL-LARG-PUB-2008-002.
- [105] ATLAS Collaboration, “Jet energy measurement and its systematic uncertainty in proton-proton collisions at $\sqrt{s}=7$ TeV with the ATLAS detector”, *J. High Energy Phys.* 0804 (2008) 063.
- [106] ATLAS Collaboration, “Jet energy measurement and its systematic uncertainty in proton-proton collisions at $\sqrt{s} = 7$ TeV with the ATLAS detector”, arXiv:1406.0076 [hep-ex].
- [107] ATLAS Collaboration, “Commissioning of high performance b-tagging algorithms with the ATLAS detector”, ATLAS-CONF-2011-102 (2011).
- [108] ATLAS Collaboration, “Calibration of b -tagging using dileptonic top pair events in a combinatorial likelihood approach with the ATLAS experiment”, ATLAS-CONF-2014-004 (2014).
- [109] ATLAS Collaboration, “Tau reconstruction and identification performance in ATLAS”, ATLAS-CONF-2010-086 (2010).
- [110] ATLAS Collaboration, “Pile-up subtraction and suppression for jets in ATLAS”, ATLAS-CONF-2013-083 (2013).
- [111] I. W. Stewart and F. J. Tackman, “Theory uncertainties for Higgs mass and other searches using jet bins”, *Phys. Rev. D* **85** 034011 (2012).
- [112] R. D. Bell et al. (NNPDF Collaboration), “Parton distributions with LHC data”, *Nucl. Phys. B* **867**, 244 (2013).
- [113] S. Frixione et al., “Single-top hadroproduction in association with a W boson”, *J. High Energy Phys.* 07 (2008) 029.
- [114] ATLAS and CMS collaborations, “Procedure for the LHC Higgs boson search combination in Summer 2011”, ATLAS-PHYS-PUB-2011-011.
- [115] Bo Zhu, Pietro Govoni, Yajub Mao, Chiara Mariotti, Weimin Wu, “Same Sign WW Scattering Process as a Probe of Higgs Boson in pp Collision at $\sqrt{s} = 10$ TeV”, arXiv:1010.5848 [hep-ex].
- [116] Fabio Maltoni, Tim Stelzer, “MadEvent: Automatic event generation with MadGraph”, arXiv:0208156 [hep-ex].
- [117] ATLAS Collaboration, “Observation and measurement of Higgs boson decays to WW^* with the ATLAS detector”, arXiv:1412.2641 [hep-ex].
- [118] Y. Freund and R. E Schapire, “A Decision-Theoretic Generalization of On-Line Learning and an Application to Boosting”, *J. Comput. Syst. Sci.* **55**, 119 (1997).
- [119] J. Friedman, “Stochastic gradient boosting”, *J. Comput. Stat. Data. Anal.* **38**, 367 (2002).

- [120] ATLAS Collaboration, “Measurement of Higgs boson production and properties in the WW decay channel with leptonic final states”, arXiv:1312.1129 [hep-ex].

Appendix A

A.1 Selection for the VBF analysis

The dominant sources of the backgrounds in the $n_j > 2$ VBF-enriched sample are the Top process for the $e\mu$ channel and Z +jets process for the $ee/\mu\mu$ channel. The following event selections are applied to obtain the signal regions:

- Pre-selections (see section 7.1) without the missing transverse energy requirement;
- $p_T^{\text{miss}} (E_T^{\text{miss}}) > 40$ (45) GeV for $ee/\mu\mu$ channels;
- $m_{\tau\tau} < (m_Z - 25 \text{ GeV})$;
- $n_b = 0$;
- $C_{\ell 1} < 1$ and $C_{\ell 2} < 1$, see text for the definition of $C_{\ell 1(2)}$;
- $C_{j_1} > 1$ for j_3 with $p_T^{j_3} > 20$ GeV; and
- BDT score > -0.48 .

The common pre-selection is applied to select the $WW^* \rightarrow \ell\nu\ell\nu$ events, where the missing transverse energy requirement is removed in the $e\mu$ channels in order to recover the signal acceptance for the statistically-limited analysis. For $ee/\mu\mu$ channels, $p_T^{\text{miss}} (E_T^{\text{miss}}) > 40$ (45) GeV is required to suppress the Z +jets background. $m_{\tau\tau} < (m_Z - 25 \text{ GeV})$ and $n_b = 0$ are used to remove the $Z \rightarrow \tau\tau$ and Top backgrounds, respectively.

The VBF process is characterized by the presence of the pair of jets (j_1, j_2) . The pseudorapidity gap between them is defined as $\Delta\eta_{jj} = \eta_{j_1} - \eta_{j_2}$, where a relatively low level of hadronic activity is expected since the mediating weak boson do not exchange the color, while the Higgs boson products (i.e. leptons) tend to be in the gap. To require such absence of jets from the QCD radiation and presence of leptons between the jets, the following quantity is defined:

$$C_i = |\eta_i - \frac{\sum \eta_{jj}}{2}| / \frac{\Delta\eta_{jj}}{2}, \quad (\text{A.1})$$

where $\sum \eta_{jj} = \eta_{j_1} + \eta_{j_2}$. The value of C_i increases from zero when η_i is centered between the jets to one when η_i is aligned with either jet. $C_{\ell 1} < 1$ and $C_{\ell 2} < 1$ is required for the leading and subleading leptons. $C_{j_1} > 1$ is also required for additional jets with $p_T > 20$ GeV.

Finally, a selection is applied with a boosted decision tree (BDT) multivariate method [118, 119] to exploit the VBF topology. BDTs consists of several decision trees, each tree making a simple cut on single variable, then an event is passed to one of two nodes based on whether it passed or failed the cut. The decision trees are trained on signal and backgrounds MC samples

so that the BDT can classify events as signal-like or background-like. The trained BDT outputs a value (BDT score) between -1 to 1 for given events. In this analysis, values closer to 1 indicate that the event is very signal-like while -1 indicates the event is more background-like. A basic selections are applied to the MC samples, which are used in the BDT training. These selections are the pre-selections described in section 7.1 with removing the missing transverse energy cut and changing the threshold of the $p_T^{\ell 2}$ from 10 GeV to 15 GeV, as well as requiring $n_j \geq 2$ and $n_b = 0$. The following eight variables are used as inputs to the BDT training:

- $m_{\ell\ell}, \Delta\phi_{\ell\ell}, m_T,$
- Δy_{jj} defined as rapidity gap between j_1 and $j_2,$
- p_T^{sum} defined as vector sum of leptons, jets and missing transverse energy,
- m_{jj} defined as mass of j_1 and $j_2,$
- $\sum C_\ell$ defined as $C_{\ell_1} + C_{\ell_2}$ and
- $\sum m_{\ell j}$ defined as $m_{\ell_1, j_1} + m_{\ell_1, j_2} + m_{\ell_2, j_1} + m_{\ell_2, j_2}.$

Figure A.1 shows four of these variables. Clear separations between the VBF signal and other processes can be seen. The BDT score > -0.48 is chosen to maximize expected significance. Table A.1 summarizes the event selections for the $n_j > 2$ VBF-enriched category with the purpose of selections. A cross-check analysis, which is purely cut-based, are also performed using the BDT input variables. Event selections for the cut-based analysis are also summarized in table A.1.

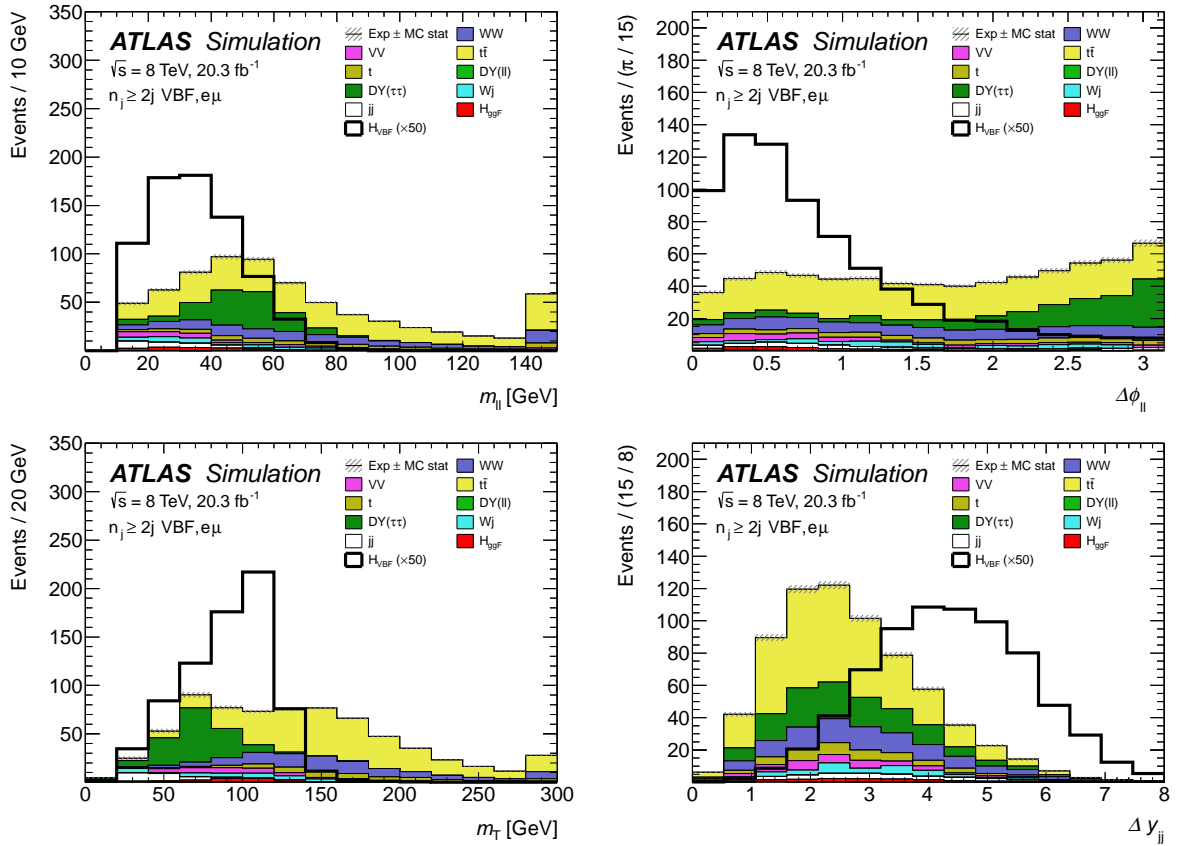


Figure A.1: Distributions of variables used as inputs to the BDT training in the $e\mu$ channel in the 8 TeV data [117]. The variables shown before applying the BDT score cut.

Table A.1: Summary of the event selections in the $n_j \geq 2$ VBF-enriched category. Entries specific to the $e\mu$ and $ee/\mu\mu$ lepton-flavor categories are noted as such, otherwise, they are applied to both categories. All energy related values are in GeV.

$n_j \geq 2$ VBF-enriched		BDT-based	cut-based
Pre-selection:			
select $WW^* \rightarrow l\nu l\nu$	$\left\{ \begin{array}{l} p_T > 22 \text{ for the leading lepton } \ell_1 \\ p_T > 10 \text{ for the subleading lepton } \ell_2 \\ \text{Opposite charge leptons} \end{array} \right.$	
reject mesons		$\left\{ \begin{array}{l} m_{\ell\ell} > 10 \text{ for the } e\mu \\ m_{\ell\ell} > 12 \text{ for the } ee/\mu\mu \end{array} \right.$
reject Z + jets		$\left\{ m_{\ell\ell} - m_Z > 15 \text{ for the } ee/\mu\mu \right.$
Category-specific:			
reject Z + jets	$\left\{ \begin{array}{l} p_T^{\text{miss}} > 40 \text{ (} ee/\mu\mu \text{)} \\ E_T^{\text{miss}} > 45 \text{ (} ee/\mu\mu \text{)} \\ m_{\tau\tau} < (m_Z - 25) \end{array} \right.$	$\left\{ \begin{array}{l} p_T^{\text{miss}} > 50 \text{ (} ee/\mu\mu \text{)} \\ E_T^{\text{miss}} > 55 \text{ (} ee/\mu\mu \text{)} \\ m_{\tau\tau} < (m_Z - 25) \end{array} \right.$	
reject Top	$\left\{ n_b = 0 \right.$	
VBF topology	$\left\{ \begin{array}{l} C_{\ell_1} < 1 \text{ and } C_{\ell_2} < 1 \\ C_{j_3} > 1 \text{ for } j_3 \text{ with } p_T^{j_3} > 20 \\ \text{BDT score} > -0.48 \\ - \\ - \\ - \\ - \\ - \end{array} \right.$	$\left\{ \begin{array}{l} C_{\ell_1} < 1 \text{ and } C_{\ell_2} < 1 \\ C_{j_3} > 1 \text{ for } j_3 \text{ with } p_T^{j_3} > 20 \\ p_T^{\text{sum}} < 15 \text{ GeV} \\ \Delta y_{jj} > 3.6 \\ m_{jj} > 600 \\ m_{\ell\ell} < 50 \\ \Delta\phi_{\ell\ell} < 1.8 \text{ (2.8) for } p_T^{\ell_2} > (<)15 \\ m_T > 80 \end{array} \right.$	